THE UNIVERSITY
of EDINBURGH

Development of a high-throughput drug screening platform for oligodendrocyte myelination (for progressive multiple sclerosis)

Jee Soo (Monica) Kim

Doctor of Philosophy with Integrated Study

Optical Medical Imaging with Healthcare Innovation and Entrepreneurship

The University of Edinburgh and The University of Strathclyde

2019

DECLARATION

I declare that this thesis was composed by myself, that the work contained herein is my own except where explicitly stated otherwise in the text, and that this work has not been submitted for any other degree or professional qualification except as specified.

Jee Soo (Monica) Kim

August 2019

ACKNOWLEDGEMENTS

Firstly, I would like to thank my amazing supervisor Professor Charles ffrench-Constant for the continuous support, motivation, guidance, and knowledge. It has not been the easiest journey but your patience and faith guided me when I needed it most. I would also like to thank my second supervisor Professor Neil Carragher for all your invaluable input into my research and growth as a scientist over the years.

Many thanks to all the past and current members of the CffC and Williams labs – for the years of continuous support, scientific discussions, and cakes for all occasions. Special mentions to Professor Anna Williams, Dr. Veronique Miron, Dr. Marie Bechler, Dr. Matthew Swire, Dr. Steffen Mayerl, and Dr. Peggy Assinck for all your patience and advice. Also, thank you to Sophie Quick and Dr. Laura Wagstaff for all our lunchtime conversations about Harry Potter and feminism, and the other members of SCRM who have made my time so memorable.

I am also extremely grateful for Dr. Bertrand Vernay – you truly went above and beyond as the Head of Imaging at SCRM in supporting my project, and I am grateful for all your advice over the years. Thank you also to Dr. Matthieu Vermeren and Dr. Eoghan O'Duibhir.

Finally, I would like to thank my friends and family who have been invaluable sources of moral and mental support throughout the ups and downs of PhD life. Thank you to my Edinburghers, MedSci, and SCRM families for all the movies and games nights, food, and hugs when I needed them most. Thank you to my brother and sister for being so understanding, and for your support and patience. Lastly, thank you to my parents for always believing in me. I could not have done it without any of you.

ABSTRACT

Aim

As part of the broad strategy in Edinburgh and beyond to discover new treatments for progressive Multiple Sclerosis (MS), the aims for my PhD project were: (1) to address the lack of an *in vitro* phenotypic drug screening platform that is able to fully recapitulate myelin sheath formation, with the long-term goal being to enhance the discovery of pro-remyelination therapies in progressive MS, and target the poor drug discovery rates in brain disorders which is partially due to poor disease modelling, and (2) the exploration of non-linear optical imaging microscopy techniques that targets both the resolution and speed to study myelination.

Background

In multiple sclerosis, an inflammatory autoimmune process destroys the oligodendrocytes that provide neuronal support by forming multi-layered compact myelin sheaths around axons, leading to neurodegeneration. Although there are drugs available to suppress the inflammatory attack to limit the formation of demyelinated lesions, no treatments currently exist to promote the regeneration of these myelin sheaths once the damage has occurred.

Cell based screens have formed an important part of the strategy used to discover such regenerative drugs. The majority of published cell-based phenotypic drug screens to target repair have focused on the differentiation of oligodendrocyte precursor cells into oligodendrocytes rather than their ability to form mature protective myelin sheaths. However, in many MS lesions, pre-myelinating oligodendrocytes are present, and studies on oligodendrocyte biology show that differentiation and myelination are regulated by distinct mechanisms. There is therefore a need for novel drug screens that target the later myelinating stages of oligodendrocyte development.

Results

Using a 3D microfibre system for *in vitro* myelin sheath formation (described by Bechler, Byrne and ffrench-Constant (2015)), I first asked whether compounds that had been

identified as increasing differentiation in conventional 2D culture systems enhanced myelination in the 3D cultures. While Benztropine and Clemastine showed an increase in the number of MBP+ (differentiated) oligodendrocytes in the 2D system, consistent with previous publications, no increase in myelin sheath formation was seen with any of the drugs in the 3D system, highlighting the potentially important differences between differentiation and myelin sheath formation for drug discovery.

Next I developed a multiwell plate based assay to allow 3D myelination assays to be used for drug screening. Using electrospinning to produce PLA microfibres, I was able to develop and optimise a technique to insert and suspend the fibres across the bottom of a 96-well plate that can be incorporated into an automated pipeline for high-throughput drug screening. The 3D myelin sheaths could be imaged using the Leica SP8 confocal system with the MatrixScreener extension and the Opera Phenix high-content screening system.

Finally, I addressed the problem of imaging myelin in such screens. CARS was shown to be able to preferentially detect myelin sheaths in fixed and live slices in regions and time-points of varying myelin densities. As the development of new myelin sheaths requires the formation of lipid and therefore the incorporation of hydrogen, the consumption of D_2O (heavy water) with a ^2H atom allowed the non-invasive labelling and detection of myelin sheaths using SRS. Future experiments will allow us to confirm whether this deuterium detection is preferential and/or specific to new myelin sheaths.

Significance

With only about 10% of drugs that enter Phase I trials successfully launching into clinics, there is an important need for more effective drug screens that better model disease-relevant processes and so reduce late-stage failures. The high-throughput-compatible 96-well plate with suspended PLA microfibres that combines the recent progresses in 3D cellular model systems with bioengineering and the recent advances in high content imaging systems may give us the opportunity to more accurately model these disease-relevant structures *in vitro*, and therefore improve drug discovery for regenerative therapies in multiple sclerosis and other myelin diseases.

The research on Raman-based label-free imaging of myelin sheaths is not only applicable for imaging myelin sheaths in the context of drug validation, but could be important for live

imaging of brain slices and detection of newly-formed myelin sheaths without the need for complex and expensive transgenic animals.

LAY ABSTRACT

Multiple Sclerosis is a disease that results from our own immune system attacking the protective myelin sheets surrounding the long nerve fibres (axons) of our neurons. The cells that make myelin sheets are oligodendrocytes, and they develop in our nervous system from a stem cell-like state and undergo a process called differentiation (in which cells become more specialised) to produce myelin sheets that wrap around axons in 3D tube-like structures called myelin sheaths. Myelin sheaths act like the plastic covering around electrical wires, and therefore the damage to these structures results in the malfunctioning and death of the neurons that transmit signals around our body. However, evidence suggests that there is a failure of the oligodendrocytes to recover the myelin sheaths in Multiple Sclerosis. Current treatments only dampen the immune system attack to prevent damage to the myelin sheaths, but no treatments are available to improve their replacement once the damage has already occurred.

One way to discover new treatments is by testing a wide range of potential drugs simultaneously in multi-well plates (plates to grow cells in with 96 individual wells or more) to identify ones that improve certain characteristics (phenotypes) of the cells affected in disease. Current drug discovery efforts to target the replacement of the lost myelin sheaths has been conducted by looking for drugs that increase the number of oligodendrocytes developing from the stem cell-like state to a 2D myelin sheet-producing differentiated oligodendrocytes by looking for proteins that detect this process has occurred. However, as the oligodendrocytes are not given axons to wrap around, it is not possible to detect whether these drugs will actually increase the formation of the 3D tube-like myelin sheaths.

In my thesis, I have therefore created a new multi-well plate that allows us to test multiple drugs simultaneously and identify oligodendrocytes that are forming myelin sheaths. To do this, I used a technique called electrospinning, which is akin to making candy floss out of sugar or Spider-Man making webs from his web shooters. Electrospinning allows us to make micrometre-thin fibres that are the same diameter as axons by applying a high voltage to a polymer and collecting the fibres that are produced in this process. I was able to produce and insert these electrospun fibres into a multi-well plate, so that when oligodendrocytes differentiate from their stem cell-like state to their differentiated state, they can also produce the 3D myelin sheaths around these artificial axons. In this way, we can detect drugs that

increase the formation of myelin sheaths to improve their replacement and decrease the damage to neurons in Multiple Sclerosis.

ABBREVIATIONS

^{14}C Carbon-14

2D Two dimensional

3D Three dimensional

AD Alzheimer's disease

ADME Absorption, distribution, metabolism and excretion

AEP Anterior entopeduncular area

AKT Protein kinase B

AMPAR α-amino-3-hydroxy-5-methyl-4-isoxazolepropionic acid receptor

BBB Blood-brain barrier

BCRP Breast cancer resistance protein

BDNF Brain-derived neurotrophic factor

BLA Biologic license application

BMP Bone morphogenetic protein

BSL-1 Unconjugated Griffonia (Banderiraea) Simplicifolia Lectin 1

CaF_2 Calcium fluoride

CARS Coherent anti-Stokes Raman Spectroscopy

CGE Caudal ganglionic eminence

CM_cytoplasm HCS CellMask™ Green Stain

CNP 2',3'-cyclic nucleotide phosphodiesterase

CNS Central nervous system

CNTF Cilliary neurotropic factor

COC Cyclic olefin copolymer

COX Cytochrome c oxidase

CSPG Chondroitin sulphate proteoglycans

CV Coefficient of variation

CXCL12 C-X-C Motif Chemokine 12

CXCR4 C-X-C Motif Chemokine Receptor 4

D_2O Deuterium oxide

DCC Deleted in colorectal cancer

DCM Dichloromethane

DMEM Dulbecco's Modified Eagle Medium

DMF Demethylformamide

DMSO Dimethyl sulfoxide

DRG Dorsal root ganglion cells

DTI Diffusion tensor imaging

EAE Experimental autoimmune encephalomyelitis

ECM Extracellular matrix

EGF Epidermal growth factor

EM Electron microscopy

ENPP6 Ectonucleotide pyrophosphatase/phosphodiesterase 6

ERK Extracellular signal-regulated kinase

ESC Embryonic stem cell

fAD Familial Alzheimer's disease

FDA US Food and Drug Administration

FGF Fibroblast growth factor

FGFR Fibroblast growth factor receptor

fMRI Functional magnetic resonance imaging

FOV Field-of-view

GalC Galactocerobroside

GluRs AMPA-preferring glutamate receptors

GFAP Glial fibrillary acidic protein

GGF Glial growth factor

GM Grey matter

GRO-α Growth-regulated-oncogene- α

HDAC Histone deacetylase

HFIP 1,1,1,3,3,3-Hexafluoro-2-propanol

HSPG Heparin sulphate proteoglycan

HyD Hybrid Detector

IGFs Insulin-like growth factor

iPSC Induced pluripotent stem cell

ITS Insulin-transferrin-sodium selenite

LGE Lateral ganglionic eminence

LFB Luxol Fast Blue

LIF Leukaemia inhibitory factor

LINGO-1 LRR and Ig domain-containing, Nogo receptor-interacting protein

LOA Likelihood of approval

LPC Lysophosphatidyl choline

MAG Myelin-associated glycoprotein

MAPK Mitogen-activated protein kinase

MBP Myelin basic protein

MCT1 Monocarboxylate transporter 1

MDCK Madin-Darby canine kidney

MDR1 Multidrug resistance protein 1

MEM Minimal Essential Medium

MFP Mean free path

MGE Medial ganglionic eminence

MOG Myelin/oligodendrocyte glycoprotein

MR Magnetic resonance

MS Multiple Sclerosis

mTOR Mammalian target of rapamycin

MRF Myelin gene regulatory factor

MYRF Myelin regulatory factor

$NaHCO_3$ Sodium bicarbonate

NCAM Neural cell adhesion molecule

NDA New drug application

NG2 NG2 chondroitin sulfate proteoglycan

NMDAR N-methyl-D-aspartate receptor

NRG1 Neuregulin 1

NRG3 Neuregulin 3

NsA Neurosphere-derived astrocytes

NT3 Neurotrophin 3

OCM Optical coherence microscopy

OCT Optical coherence tomography

OEC Olfactory ensheathing cells

OL Oligodendrocyte

OPC Oligodendrocyte precursor cell

PALM Photoactivation localisation microscopy

PDGFRA Platelet derived growth factor receptor A

P-gp P-glycoprotein

PET Positron emission tomography

PI3K Phosphoinositide 3-kinase

PIP3 Phosphatidylinositol 3,4,5-trisphosphate

PLA Poly-L-lactic acid

PLP Proteolipid protein

PMT Photomultiplier Tube

PPMS Primary progressive Multiple Sclerosis

PSA Polysialic acid

PSA-NCAM Polysialylated-neural cell adhesion molecule

PSF Point-spread function

PTEN Phosphatase and tensin homolog

PU Polyurethane

PV Predictive validity

R&D Research and development

RGC Retinal ganglion cells

ROCK Rho-A/Rho-associated kinase

RRMS Relapsing-remitting Multiple Sclerosis

RXRγ Retinoid X receptor gamma

SCoRe Spectral confocal reflectance microscopy

SCRM Scottish Centre for Regenerative Medicine

SD Standard deviation

SEM Scanning electron microscopy

SERS Surface enhanced Raman spectroscopy

SFK Src family kinase

SHH Sonic Hedgehog

SIM Structured illumination microscopy

SORS Spatially offset Raman spectroscopy

SPMS Secondary progressive Multiple Sclerosis

SRG Stimulated Raman gain

SRL Stimulated Raman loss

SRS Stimulated Raman Scattering

STED Stimulated emission depletion

STORM Stochastic optical reconstruction microscopy

TH Thyroid hormone

THF Tetrahydrofuran

THG Third-harmonic generation

TFEB Transcription factor EB

TMFP Transport mean free path

TN-C Tenascin-C

TTX Tetrodotoxin

VZ Ventricular germinal zone

WM White matter

Wnt-Cxcr4 Wnt-chemokine receptor 4

YY1 Yin Yang 1

TABLE OF CONTENTS

LIST OF FIGURES

LIST OF TABLES

CHAPTER I. LITERATURE REVIEW

As part of the broad strategy in Edinburgh and beyond to discover new treatments for progressive Multiple Sclerosis (MS), the aims for my PhD project were: (1) to address the lack of an *in vitro* phenotypic drug screening platform that is able to fully recapitulate myelin sheath formation, with the long-term goal being to enhance the discovery of pro-remyelination therapies in progressive MS, and target the poor drug discovery rates in brain disorders which is partially due to poor disease modelling, and (2) the exploration of non-linear optical imaging microscopy techniques that targets both the resolution and speed to study myelination.

To place this into context, in this introduction I will therefore review: (1.1) Multiple Sclerosis, and the evidence towards why remyelination is an important therapeutic target in the treatment of this disease, (1.2) the current immunomodulatory treatments available for the prevention of lesion formation but not regeneration once damage has already occurred, (1.3) oligodendrocyte functions and the role of myelin sheaths in the CNS, particularly their role in providing metabolic support to axons, (1.4) the distinct stages of oligodendrocyte development, starting from the birth of the precursor cells to the formation of myelin sheaths, (1.5) the causes of the remyelination failure that contributes to progressive MS, including the evidence towards a significant block in later stage myelin sheath formation in MS lesions and why this might be, (1.6) the reasons why drug discovery for remyelination has been so difficult, reviewing both the problems with CNS disease in general and specific issues around MS research, (1.7) the current phenotypic cell-based methods for assessing myelination, including their caveats in being able to model myelin sheath formation *in vitro* when used for drug discovery, and (1.8) how we can image these cells *in vitro*. Finally (1.9) I will bring these parts together and discuss current evidence suggesting that existing screening strategies are poor at addressing an important property of oligodendrocyte biology; that differentiation and myelin formation are regulated differently.

1.1 Multiple Sclerosis

1.1.1 Cause and classification

Multiple Sclerosis (MS) is a neurological disorder characterised by chronic inflammation of the CNS, and affects more than two million people globally (GBD 2015 Neurological Disorders Collaborator Group, 2017). In the 'outside-in' theory of the pathogenesis of MS, the disease can be characterised into two main phases (**Figure 1.1**): (1) an inflammatory phase where focal areas of demyelination occur, leaving underlying axons denuded, and (2) subsequent neurodegeneration (Bruck, 2005; Lublin *et al.*, 2014; Stefano *et al.*, 1998). An alternative 'inside-out' hypothesis suggests that autoreactivity against myelin precedes inflammation and demyelination (Traka *et al.*, 2015). In both theories, following the demyelination, the loss of myelin results in conduction velocity block or reduction, refractory period of transmission being extended, and impairment of high frequency axonal signal transmission (McDonald and Sears, 1970). With prolonged myelin loss, i.e. when remyelination fails, the vulnerability of the denuded axons to continued inflammatory attack along with loss of metabolic support result in axonal death, leading to progressive and permanent disability in patients (Bruck, 2005; Stefano *et al.*, 1998).

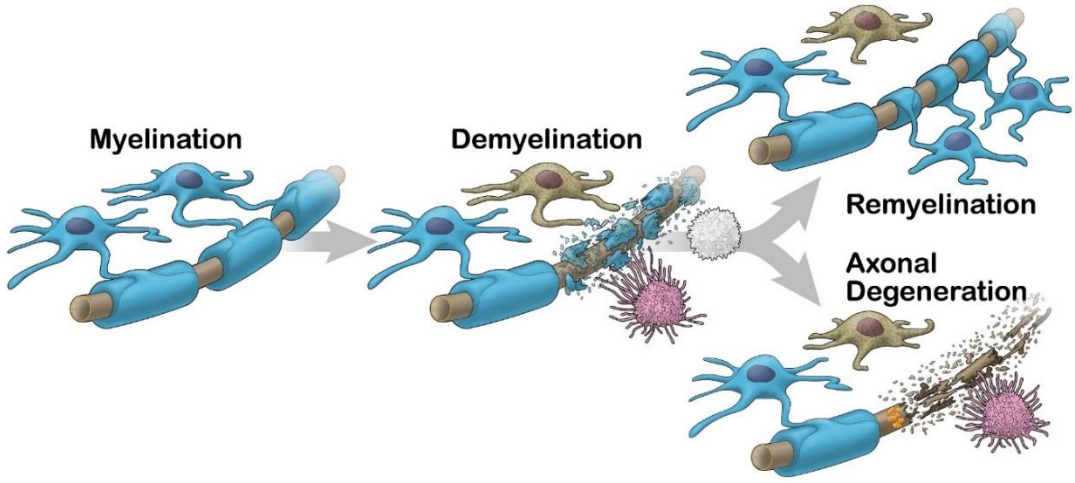

Figure 1.1 Summary of the main phases of Multiple Sclerosis

In MS, myelin sheaths and oligodendrocytes undergo an inflammatory attack ('outside-in' theory) or autoreactivity ('inside-out' theory), resulting in demyelination. In some cases, new oligodendrocytes are able to come into the lesion and remyelinate. However, when remyelination fails, the axons that have been left exposed undergo axonal degeneration.

(Figure by ScideLight)

Based on the progression of symptoms, MS can be categorised into 'relapsing-remitting' MS (RRMS), 'secondary progressive' MS (SPMS), or 'primary progressive' MS (PPMS). 80% of patients are first diagnosed with RRMS, where there are phases of MS-related symptoms ('relapse', where focal demyelinated lesions occur in different areas of the CNS) and phases of no symptoms ('remission', or resolution of the inflammatory attack, remyelination, and compensation by the brain), with this form of MS being characterised by acute inflammatory immune activity and therefore having the best response to immunomodulatory treatment (**Figure 1.2**). Two-thirds of RRMS patients progress onto SPMS, where the disease becomes a continuous progressive worsening of symptoms and increasing disability, after about 25 years (Weinshenker *et al.*, 1989), with more than 80% of RRMS patients eventually developing SPMS, which is due to neurodegeneration and more resistant to treatment. The remaining 20% of patients are diagnosed with PPMS, where there is progressive accumulation of disability from the disease onset, mostly due to

neuronal damage, with no major relapses and remissions (Bitsch and Brück, 2002; Compston and Coles, 2002; Lublin *et al.*, 2014; Reich, Lucchinetti and Calabresi, 2018a).

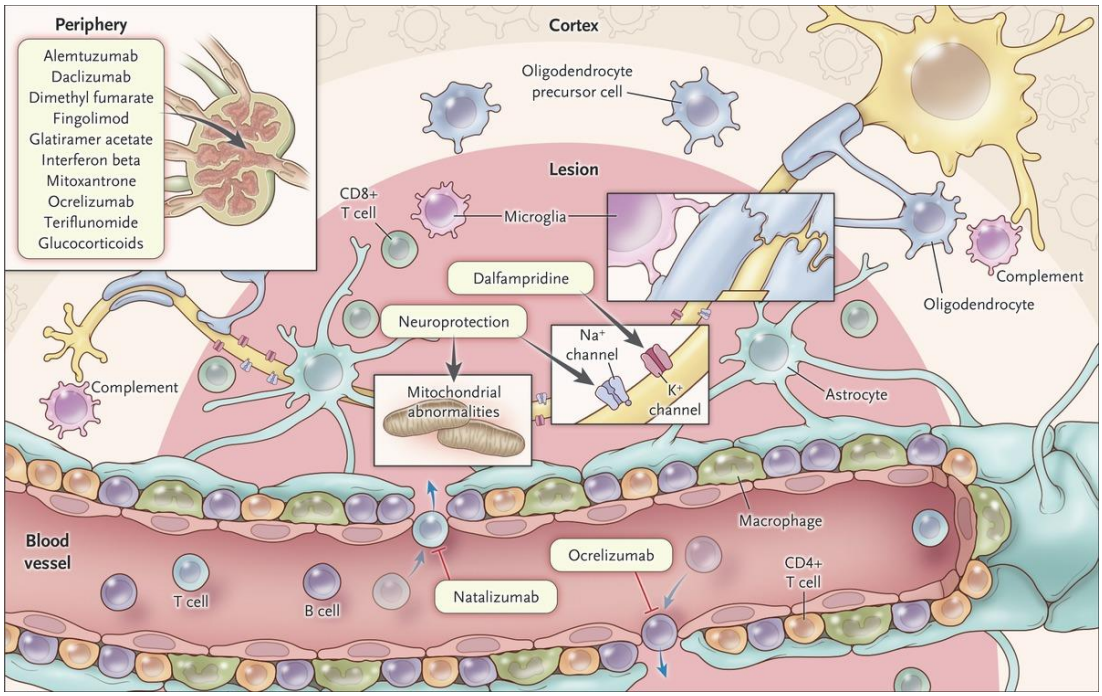

Figure 1.2 Schematic of major cell types and current treatments for MS

The diagram summarises some of the major cell types targeted for current non-inflammatory treatments for MS.

For example, Dimethyl fumarate, although the mechanism is not fully understood, works to decrease inflammation caused by the immune system in the peripheral lymph nodes. Fingolimod prevents T and B cells from leaving the lymph nodes, and interferon beta and glucocorticoids are interferons and hormones, respectively, which dampen inflammation.

In the CNS, Natalizumab is an antibody-based treatment that sticks to T cells to stop them reaching the CNS, and Ocrelizumab targets the CD20 on B cells to have its anti-inflammatory effect.

Figure from Reich, Lucchinetti and Calabresi (2018)

Based on epidemiological studies, the prevalence of MS is higher in females and with increasing latitude, with Scotland having the highest rate of MS diagnosis in the world (Pugliatti, Sotgiu and Rosati, 2002; Handel *et al.*, 2011; Mcdonald *et al.*, 2019). Compared to England with an estimated prevalence of 164 per 100,000, Scotland has a prevalence of 209 per 100,000, with the highest rate being 402 per 100,000 in Orkney (Multiple Sclerosis Trust, 2018). The increased risk of MS diagnosis in certain populations have been linked to risk factors such as certain genetic variations like HLA-*DRB1* risk alleles (IMSGC and WTCCC, 2011), levels of vitamin D intake (Mokry *et al.*, 2015; Munger *et al.*, 2004; Laursen *et al.*, 2016), and exposure to Epstein-Barr virus (Belbasis *et al.*, 2014; Guan *et al.*, 2019). Due to the disability associated with MS, resulting in patients not being able to work, there is also a high economic burden associated with the disease, with an estimated €27,000 per patient and €15 billion total in Europe in 2010 (Gustavsson *et al.*, 2011; Olesen *et al.*, 2012).

MS lesions can be classified into 4 distinct types: active demyelinating, chronic active, chronic inactive, and remyelination lesions. Active demyelinating lesions are the initial forms of MS lesions, and are therefore most often found in patients in the remitting phase of RRMS or early on in SPMS. These lesions are hypercellular, containing macrophages and microglia digesting myelin sheaths and astrocytes (Kutzelnigg *et al.*, 2005; Kuhlmann *et al.*, 2017). Chronic active lesions are characterised by a chronic demyelinated lesion surrounded by activated phagocytotic cells (Prineas *et al.*, 2001; Zrzavy *et al.*, 2017) containing breakdown products of myelin proteins (Kuhlmann *et al.*, 2017), representing an expanding lesion which sometimes show active or expanding premyelinating or early myelinating OLs (Fard *et al.*, 2017). Chronic inactive lesions represent an end-stage of lesion formation, with no active inflammation or remyelination, and are hallmarked by a significant reduction in OPCs, OLs, and inflammatory cells such as microglia (Wolswijk, 2000; Zrzavy *et al.*, 2017). Shadow plaques are lesions in which the active inflammation has subsided, and are characterised by thinner myelin sheaths. They also do not have the significant increase in macrophage infiltration as would be seen in an active demyelinating lesion that have not completely been demyelinated (Patrikios *et al.*, 2006). The appearance of these thin myelin sheaths have previously been thought to be due to

remyelination, but a more recent theory suggests that they may also be attributed to compromised myelin sheaths that survived demyelination (Yeung *et al.*, 2019).

1.1.2 Remyelination in MS

Remyelination is one of the major therapeutic interventions in treatment development for MS, particularly in progressive forms where remyelination and clinical remission fails. Remyelination can be detected extensively in the lesions of MS patients, and are characterised by thinner myelin sheaths (Blakemore, 1974). Prineas *et al.* (1993) observed ~20% of plaques in patients who died 18 months or longer after clinical onset showing remyelination in at least 10% of the plaque area (Prineas *et al.*, 1993), Patrikios *et al.* (2006) detected 60 to 96% of the global lesion area showing remyelination in a subset of 20% of the patients (Patrikios *et al.*, 2006), and Patani *et al.* (2007) identified that 22% of WM lesions were fully myelinated and 73% showed at least partial remyelination (Patani *et al.*, 2007). These quantifications show that remyelination does occur in a subset of lesions in a subset of MS patients as an endogenous regeneration process.

Remyelination is important because of the evidence that is neuroprotective and promotes functional recovery, In 1979, Smith *et al.* (1979) showed that once remyelination begins following an injection of lysophosphatidyl choline (LPC) into the spinal cord of a cat to form an acute lesion, impulse conduction, measured by pairs of platinum or stainless steel electrodes implanted into the spinal cord, begins to progressively return to normal, with efficient impulse conduction being restored in the demyelinated axons even though the myelin sheaths have the characteristic thinner and shorter properties of remyelination (Smith, Blakemore and McDonald, 1979). Although computational studies predict that that conduction will not completely return to normal due to the thinner myelin sheaths in remyelination (Smith and Koles, 1970), this suggests

that functional recovery of the saltatory conduction can be restored with remyelination.

Cuprizone to induce global demyelination followed by irradiation to prevent endogenous remyelination showed that with transplantation of embryo-derived neural progenitors to promptly restore remyelination capacities increased axon survival when compared to cuprizone and irradiation-treated mice without cell transplantation (Irvine and Blakemore, 2008). However, transplanted neural stem cells have been shown to have a neuroprotective and immunomodulatory effect that is distinct from the effects of remyelination (Pluchino *et al.*, 2005), and this effect therefore cannot be excluded when considering the decreased axonal damage seen in this study. Muscarinic acetylcholine receptor M1 is a potent negative regulator of OL differentiation and myelination. When M1 muscarinic receptor (Chrm1) was genetically ablated in OPCs in an EAE mouse model, the acceleration and enhancement of the remyelination process resulted in increased preservation of axons and functional recovery (Mei *et al.*, 2016), supporting that the remyelination by the transplanted cells did contribute to axonal protection, at least to a certain extent. In addition, endogenous remyelination in a dietary manipulated model of demyelination in cats showed restoration of function (Duncan *et al.*, 2009), and thin myelin sheaths, which are the hallmarks of remyelination, in canines with hypomyelinating genetic mutations persisted and preserved axonal function (Duncan *et al.*, 2017). These studies highlight the axon-protective benefits of remyelination as a potential therapeutic advantage of remyelination treatments.

1.2 Current Treatments for MS – Immunomodulatory, not regenerative

In acute relapses of MS, corticosteroids have been used as a potent anti-inflammatory and immunosuppressive treatment to shorten its duration and improve recovery rate. Its mode of action is through binding to cytosolic glucocorticoid receptors to mediate genomic effects in inducing anti-inflammatory cytokines and inhibiting pro-inflammatory ones, as well as non-genomic effects in activation of signal cascades that suppress the immune response (Sloka

and Stefanelli, 2005; Stahn *et al.*, 2007). Although corticosteroids reduced worsening or non-improvement of the relapse 5 weeks from symptom exacerbation (Citterio *et al.*, 2013; Deun and Pesch, 2017), they do not modify the disease, and are therefore do not have long-term benefits in its usage.

Several disease-modifying treatments for MS exist, mainly being immunosuppressants, immunomodulators, and monoclonal antibodies, and include azathioprine, cyclophosphamide, interferon β (IFNβ, glatiramer acetate, methotrexate, mitoxantrone, natalizumab, and most recently ocrelizumab (Filippini *et al.*, 2013; Mulero, Midaglia and Montalban, 2018). These drugs inhibit various immune cells and cytokines to suppress and prevent new inflammatory attacks, and therefore decrease the formation of new lesions and the occurrence of relapses, and are therefore most efficient in RRMS. A 2013 meta-analysis suggests that natalizumab, followed by IFNβ-1a and mitoxantrone, is the most effective at improving the disease course (Filippini *et al.*, 2013). Ocrelizumab, which was first approved for use in the UK in 2018, is the first and only current drug approved for treatment of PPMS (Mulero, Midaglia and Montalban, 2018).

Currently, no disease-modifying treatments are available that is able to target the non-inflammatory neurodegenerative phase of the disease, highlighting a significant clinical challenge. One intervention technique for targeting the neurodegenerative phase of the disease would be remyelination therapies. However, no therapies that effectively enhance remyelination is available, although several are in clinical trials including Opicinumab against LINGO-1, and clemastine, discussed in the next section.

1.3 Oligodendrocytes and the Role of their Myelin Sheaths in the CNS

Oligodendrocytes (OLs) were first identified by Scottish pathologist William Ford Robertson in 1899 when he noticed a unique subset of small branched cells that could be labelled with platinum, which he referred to as ‘mesoglia’. It was re-discovered and first described as the myelin-producing cells of the central nervous system (CNS) in 1922 by Spanish neurohistologist and pathologist Pío del Río-Hortega following his development of the silver carbonate method to distinguish OLs and microglia from Spanish neuroscientist and pathologist Santiago Ramón y Cajal’s “third element” of the CNS, the “first and second

elements" being neurons and astrocytes. The term *myelin* was first coined by the German pathologist Rudolf Ludwig in 1854, derived from the Greek word *myelos* after the colour and texture of bone marrow, and first described by Dutch scientist Antoni van Leeuwenhoek in 1717. (reviewed by Boullerne 2016; Pérez-Cerdá et al. 2015)

Myelination is a predominantly postnatal process, with oligodendrocyte precursor cells (OPCs) continuing to be maintained, proliferate, and produce myelinating OLs into adulthood (Hughes *et al.*, 2013; Young *et al.*, 2013a; Yeung *et al.*, 2014), with the ability to reinitiate the growth of mature myelin sheaths (Snaidero *et al.*, 2014). Changes in the white matter (WM) of related brain regions in learning sensory-motor (Bengtsson *et al.*, 2005), novel visuo-motor (Scholz *et al.*, 2009), and cognitive (Lee *et al.*, 2010) tasks have been identified by diffusion tensor imaging highlighting the relevance of white matter plasticity and myelination remodelling throughout life. The high degree of cellular and molecular conservation of myelination across various species, such as with an early OL progenitor stage transcription factor *olig2* in zebrafish (Park *et al.*, 2002), to mammals, such as chick (Zhou, Choi and Anderson, 2001) and mice (Zhou and Anderson, 2002), also highlights the evolutionary importance of the function of these structures in the CNS. Our current understanding on the role of OLs and their myelin sheaths support the idea that they have two key functions in supporting neuronal function: (i) speeding up axonal signalling via saltatory conduction, and (ii) providing metabolic support to neurons and their axons.

1.3.1 Saltatory Conduction

Myelination restricts the clustering of ion channels required for nerve conduction to unmyelinated segments, called nodes of Ranvier, which are flanked by myelin sheaths, to propagate axonal signalling via these nodes, in a process called saltatory conduction (**Figure 1.3**) (Rushton, 1951; Hodgkin and Huxley, 1952; Waxman, 1977). The presence of myelin sheaths dictates the pattern and localisation of ion channels, such as distinct sodium channel subunits in nodes of myelinated ($Na_v1.6$) versus unmyelinated ($Na_v1.2$) axons (Boiko *et al.*, 2001). Mechanisms of nodes of Ranvier construction involve OL-derived extracellular matrix components, axonal-myelin sheath adhesion molecules as barriers, and cytoskeletal scaffolds to stabilise the positioning of sodium

channels (Susuki *et al.*, 2013). Other non-myelin sheath-related mechanisms include clustering of sodium channels and other nodal proteins to node-forming regions (Kaplan *et al.*, 1997, 2001; Freeman *et al.*, 2015).

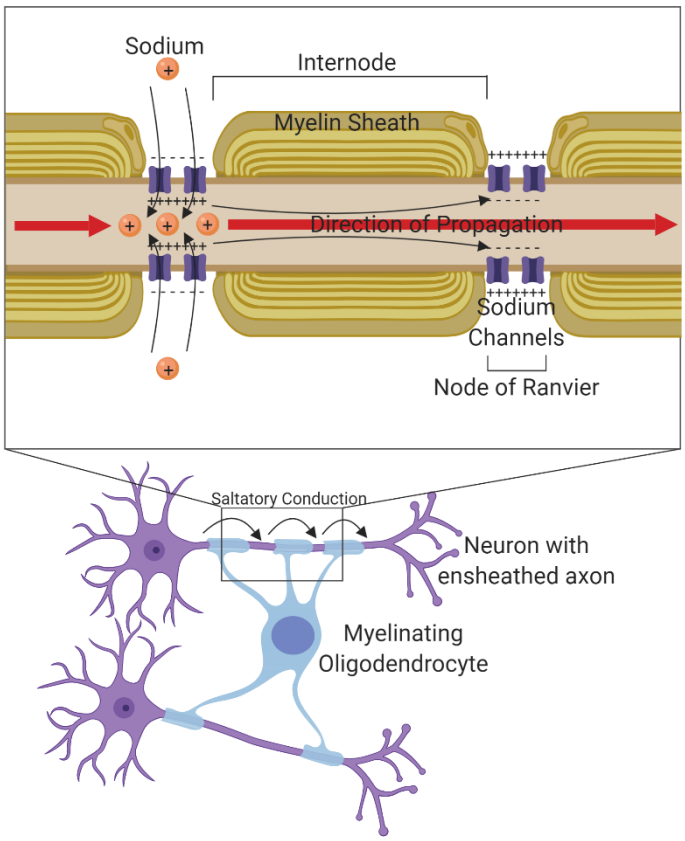

Figure 1.3 Node of Ranvier and Saltatory Conduction

Schematic diagram of a myelinating oligodendrocyte wrapping myelin sheaths around the axon of a neuron.

This clusters the voltage-gated sodium channels, restricting the active depolarising regions to these nodes, allowing signals to be transmitted along the axon quickly along the nodes of Ranvier.

Figure drawn on BioRender.

Changes to the internodal, the distance between nodes, structure and parameters contribute to variations in the conduction velocity of the axon (Moore *et al.*, 1978). Increasing the distance between internodes increases

conduction velocity, although only to a certain point, where it reaches a "flat maximum" (Huxley and Stampfli, 1949; Wu *et al.*, 2012). Even minor changes to the ratio between the thickness of the myelin sheath and axon unit compared to the axon calibre (*g* ratio), with a maximum value when the ratio is between 0.6 and 0.7 based on computer simulation (Smith and Koles, 1970), and diameter changes in myelinated axons, as shown along the optic nerve of the ferret (Baker and Stryker, 1990), can significantly affect conduction velocity. This allows not only for the speeding up of conduction velocity through the presence of myelin sheaths, but for the control of conduction times by internodal parameters variation, as exampled in the auditory brainstem of the chicken for precise temporal integration of the auditory information in order to achieve sound localisation (Seidl, Rubel and Harris, 2010; Seidl, Rubel and Barria, 2014).

1.3.2 Metabolic Support

In addition to its role in saltatory conduction, myelin sheaths are also thought to provide metabolic support to the underlying axon that it ensheaths. Proteolipid protein (PLP)-deficient mice and 2',3'-cyclic nucleotide phosphodiesterase (Cnp1)-inactivated mice, which are both major components of myelin sheaths, were able to form structurally normal myelin sheaths, but showed severe axonal pathology as a primary phenotype ahead of subsequent myelin abnormalities (Griffiths *et al.*, 1998; Lappe-Siefke *et al.*, 2003). This emphasises the role of myelin sheaths beyond physical ensheathment and demonstrates the requirement of specific myelin proteins in promoting neuronal health and survival, with importance in demyelinating conditions like MS, where the loss of these myelin sheaths results in several axonal damage (Trapp *et al.*, 1998), and leads to progressive neurodegeneration.

One mechanism by which OLs could be metabolically supporting axons is through the transfer of glucose and lactate. Cytochrome c oxidase (COX) is a component of the electron transport chain required for mitochondrial respiration. Fünfschilling *et al.* (2012) produced conditional *Cox10* mutant mice by crossing the $Cox10^{flox/flox}$ animals with $Cnp1^{Cre/+}$ or *Plp1-CreERT2* lines to knockout *Cox10*

expression in myelinating cells, with *Cox10* mutants being unable to form stable COX, and therefore its loss biasing ATP generation towards aerobic glycolysis and lactate production versus glucose metabolism. In these mutant animals, there were no detectable signs of OL pathology, changes in *g*-ratio, nor increases in apoptotic cells or inflammatory cells in the WM of adult animals despite confirmed absence of COX activity by histochemical measurements and the presence of severe peripheral neuropathy. This suggested that the survival and maintenance of OLs, their myelin sheaths, and associated axons are not affected by mitochondrial dysfunction once myelination had already occurred. In experiments exploring this, they noted that when brain lactate concentration was measured by localised proton magnetic resonance spectroscopy, there was a large increase in accumulated lactate levels in the cortex and white matter of mutant animals in the presence of volatile isoflurane anaesthesia, with levels decreasing rapidly following the withdrawal of the anaesthetic, suggesting its rapid use by local metabolisation (Fünfschilling *et al.*, 2012). This led to the discovery that lactate is transported exclusively by monocarboxylate transporters, with monocarboxylate transporter 1 (MCT1) being highly enriched in OLs, predominantly in myelin sheaths. Oligodendrocyte-specific loss of MCT1 was shown to lead to axonal dysfunction, and ultimately neuronal cell death (Lee *et al.*, 2012). Studying the mechanism of metabolic support in an exogenous glucose deprivation (aglycemic) paradigm, Meyer *et al.* (2018) showed that in the corpus callosum, the dialysis of lactate could only partially rescue action potential activity in mouse brain slices during aglycemic conditions compared to 70% by glucose addition, suggesting that glucose is the most efficient at providing axonal support in the corpus callosum. The simultaneous blocking of OL MCT1/2 and OL GLUT1 during aglycemic conditions in slices with OLs dialysed with glucose resulted in the complete loss of action potential activity, demonstrating that both glucose and lactate transporter activity may be required from OLs during aglycemic conditions to sustain axonal activity. Collectively, these provide evidence towards an important role of glucose and myelin-derived lactate, for axonal ATP production via the citric acid cycle, in axonal health, survival, and function (**Figure 1.4**).

Another mechanism through which OLs may provide metabolic support is through the activity-dependent release of exosomes, which carry various proteins and RNA, to axons (**Figure 1.4**). In culture, glutamate signalling from axons was able to evoke exosome release through OL N-methyl-D-aspartate receptor (NMDAR) and α-amino-3-hydroxy-5-methyl-4-isoxazolepropionic acid receptor (AMPAR) stimulation and subsequent Ca^{2+} signalling, with the exosomes then being taken up by the neurons. These exosomes were shown to improve neuronal viability in conditions simulating oxidative stress and nutrient deprivation (Frühbeis *et al.*, 2013). Although further research is required to test the *in vivo* role of OL-derived exosomes in axonal metabolic support, along with whether other biologically and disease-relevant mechanisms exist, it provides further evidence towards the neuroprotective role of OLs.

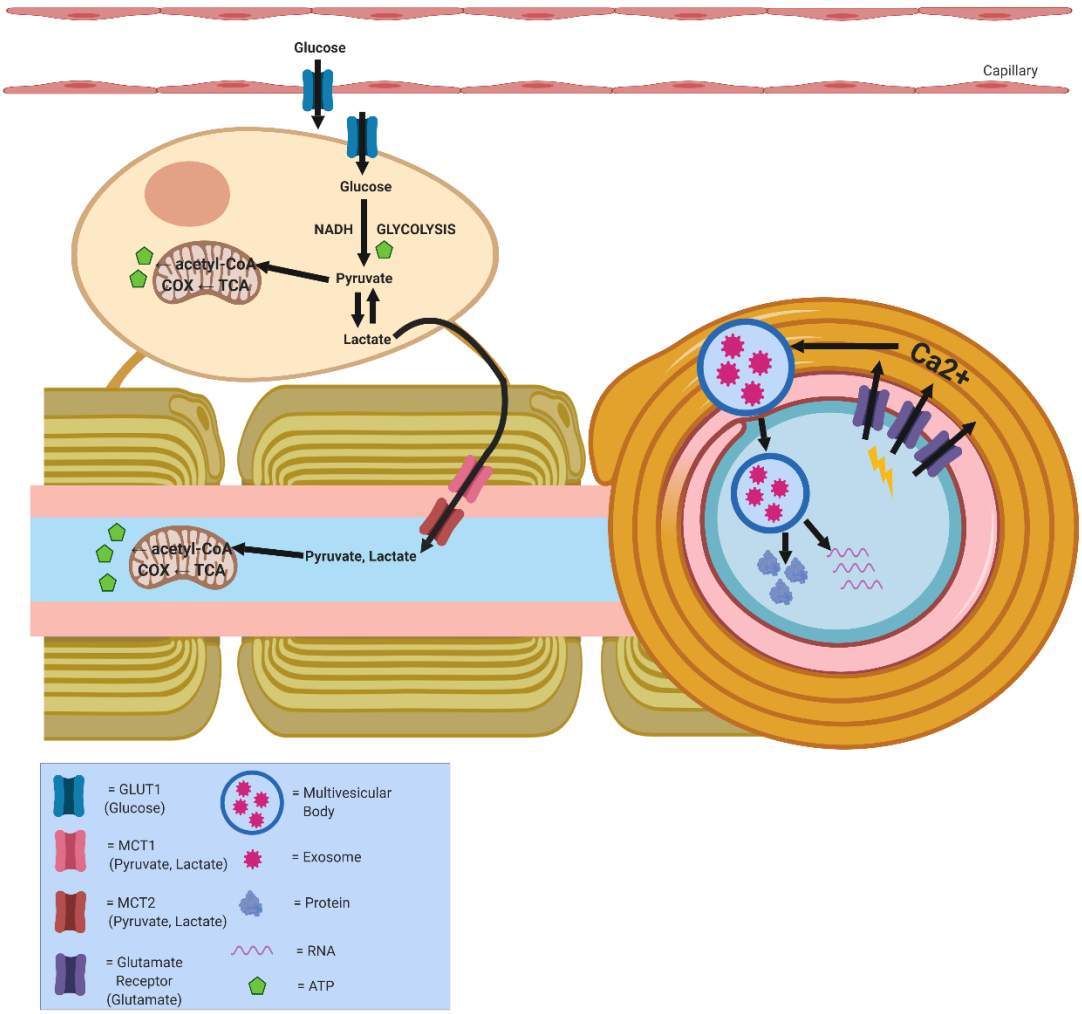

Figure 1.4 Schematic of the two proposed models of metabolic support between oligodendrocytes and axons

The two proposed models of metabolic support by which oligodendrocytes transfer glucose and lactate to the underlying axons are illustrated: (1) the transportation of glucose and myelin-derived lactate for axonal ATP production via the citric acid cycle, and (2) the activity-dependent release of exosomes carrying various proteins and RNA to the underlying axons.

Adapted from Fünfschilling *et al.*, 2012; Frühbeis *et al.*, 2013.

Figure drawn on BioRender

1.4 Oligodendrocyte development

In order for myelin sheath formation to be achieved, an OL needs to go through various stages of development (**Figure 1.5** A). The oligodendrocyte precursor cells (OPCs) from which they form were first characterised by Raff and colleagues in 1983 (Raff, Miller and Noble, 1983), and shown to proliferate within the CNS in the rat optic nerve in adults in 1986 (ffrench-Constant and Raff, 1986) and in newborn animals in 1987 (Dubois-Dalcq, 1987), and in the rat telencephalon in 1989 (Gard and Pfeiffer, 1989). Further experiments provided evidence for the presence of OPCs in the adult human CNS including a 1992 study in which Armstrong *et al.* (1992) were able to isolate O4+ (early oligodendrocyte lineage marker), galactocerebroside-negative (GalC-, oligodendrocyte marker), and glial fibrillary acidic protein-negative (GFAP-, astrocyte marker) OPCs from the adult human CNS of patients undergoing partial temporal lobe removal for epilepsy that differentiate into oligodendrocytes *in vitro*. They were also able to identify these O4+ GalC- GFAP- OPCs in "tissue prints", where they mildly digested the brain tissue enzymatically to adhere a thin layer of the cells onto a coverslip, to check for their presence *in vivo*.

OPCs follow a specific transcriptional and morphological trajectory, as originally described by del Río-Hortega, and characterised by Dubois-Dalcq *et al.* (1986) in the distinct expression pattern of myelin-associated glycoprotein (MAG), proteolipid protein (PLP), and myelin basic protein (MBP) in rodent-derived OLs independent of neuronal signals. More recent single-cell sequencing data in mouse (**Figure 1.5** B) (Marques *et al.*, 2016) and post-mortem human tissue (**Figure 1.5** C) (Jäkel *et al.*, 2019) confirm this trajectory from OPCs to immature/intermediate differentiated OLs, and finally into fully mature myelin sheath-forming OLs.

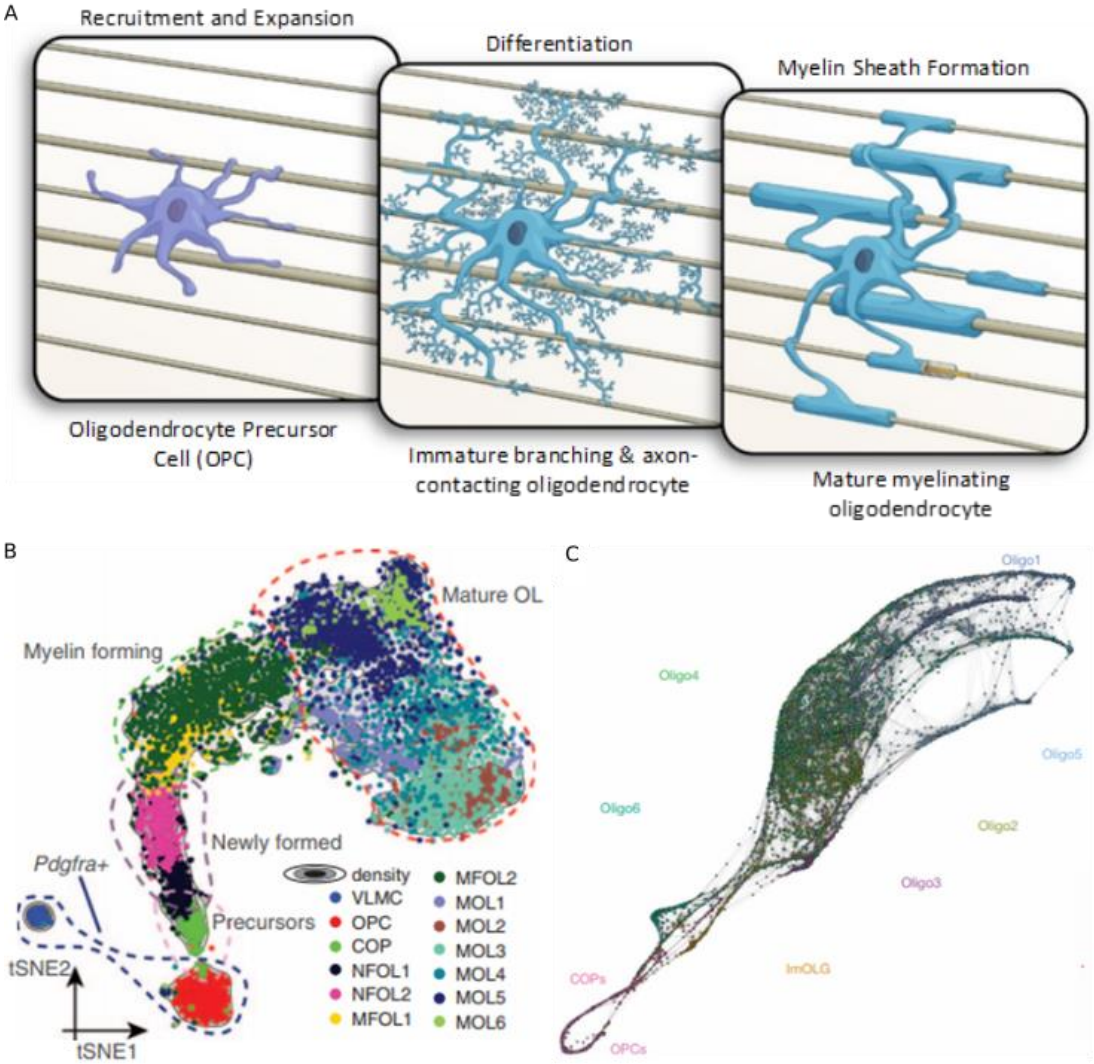

Figure 1.5 Morphological and Transcriptional Developmental Stages of Oligodendrocytes

A. Morphological developmental stages of an oligodendrocyte.
(Figure designed by ScideLight)

B. *t*-Distributed stochastic neighbour embedding projecting from single-cell RNA sequencing of juvenile and adult mouse CNS showing the transcriptional trajectory from OPCs to mature OLs.
VLMC = vascular and leptomeningeal cells; OPC = oligodendrocyte precursor cell; COP = differentiation-committed oligodendrocyte precursor cell; NFOL = newly formed oligodendrocyte; MFOL = myelin-forming oligodendrocyte; MOL = mature oligodendrocyte
(Figure from Marques et al. 2016)

C. SCN3E pseudotime analysis of single-nucleus RNA sequencing of human oligodendrocyte lineage cells from the WM of post-mortem human brains.
(Figure from Jäkel et al. 2019)

1.4.1 Oligodendrocyte Precursor Cells

OPCs have been shown to have various developmental origins and time-points, followed by migration throughout the CNS in response to intrinsic and extrinsic cues to diversify and become heterogeneous based on brain region and age (Kessaris *et al.*, 2006; Pringle and Richardson, 1993; Spitzer *et al.*, 2019; Sun *et al.*, 1998). Adult OPCs, which were first shown to exist in the adult CNS in 1986 (ffrench-Constant and Raff 1986), are abundant throughout and continue to increase and proliferate in the adult CNS (Clarke *et al.*, 2012; Young *et al.*, 2013b), being estimated to make up between 2 to 9% of the total cell population (Pringle *et al.*, 1992; Dawson *et al.*, 2003). They can be identified by the presence of NG2 chondroitin sulphate proteoglycan (Stallcup and Beasley, 1987), platelet derived growth factor receptor A (PDGFRA) (Pringle *et al.*, 1992), and ganglioside antibody A2B5 (Raff, Miller and Noble, 1983), although these are not exclusively expressed by OPCs, and are therefore combined with OL lineage markers Sox10 (Kuhlbrodt *et al.*, 1998) and Olig2 (Zhou and Anderson, 2002) to verify their presence. The transcription factors Sox10 and Olig2, along with Nkx2.2 are also essential for terminal differentiation of OPCs into oligodendrocytes (Claus Stolt *et al.*, 2002; Lu *et al.*, 2002; Takebayashi *et al.*, 2002; Zhou, Choi and Anderson, 2001). Adult OPCs may also respond and behave differently, at least to some degree, in comparison to neonatal OPCs, that are present during development, due to the evidence that they both respond to and modulate neuronal activity, with the neuronal network changing with age (Maldonado *et al.*, 2013; Sakry *et al.*, 2014).

1.4.1.1 The birth of OPCs in vivo

OPCs, identified by *in situ* hybridisation and immunohistochemistry, can first be detected in the ventral region of the ventricular germinal zones (VZs) near the floor plate, a region that also gives rise to motor neurons, at embryonic day 12.5 (E12.5) in mice (Timsit *et al.*, 1995), at E14 in rats (Pringle and Richardson, 1993), and 45 days post-conception in humans (Hajihosseini, Tham and Dubois-Dalcq,

1996) in the spinal cord. These OPCs arise under the influence of Sonic Hedgehog (SHH) (Alberta *et al.*, 2001) over the same range of concentration as with motor neuron induction, suggesting a potential theory in which a common precursor population generates both types of cells at different times during development (Richardson *et al.* 1997). They then proliferate rapidly and migrate widely, becoming dispersed throughout the grey and white matter of the ventral spinal cord by E16 and uniformly distributed in the cord by E18 in rats (Pringle and Richardson, 1993), with similar patterns of dispersion being observed in humans (Hajihosseini, Tham and Dubois-Dalcq, 1996). A SHH signalling pathway-independent, late, and transient second wave of OPC generation also occurs in the dorsal spinal cord, at E14.5 in mice (Cai *et al.*, 2005), that do not migrate widely and are produced through trans-differentiation of a subset of radial glial cells (Fogarty, Richardson and Kessaris, 2005). In the forebrain, the developmental origin of OPCs appear to occur in three waves in a temporal ventral-to-dorsal gradient, likewise with the SHH signalling pathway important for ventral OPC generation (Tekki-Kessaris *et al.*, 2001), as shown by Cre-*lox* fate mapping in transgenic mice. The first wave is in the medial ganglionic eminence (MGE) and anterior entopeduncular area (AEP) in the ventral forebrain at E11.5 which go on to populate the embryonic telencephalon, before the second wave from the lateral and caudal ganglionic eminences (LGE and CGE) at E15, followed by the final third wave within the postnatal cortex. These sequentially and spatially distinct populations of OPCs appear to be redundant as targeted destruction of any one population results in the remaining cells re-populating the region, and the MGE- and AEP-derived OPCs from the first wave being eliminated during postnatal life (Kessaris *et al.*, 2006). In postnatal mice, ventrally-derived OPCs make up 80% of the oligodendrocyte (OL) lineage cells in the spinal cord and 20% in the corpus callosum, and dorsally-derived OPCs outcompete ventrally-derived ones in the myelination of dorsal axons despite having similar electrical properties (Tripathi *et al.*, 2011). These OPCs start to express markers of differentiation into OLs from shortly before birth, and continue to generate new myelinating oligodendrocytes into adulthood, with myelinogenesis peaking at 2 to 4 weeks in postnatal mice but continuing until at least 8 months of age,

and heterogeneous OPC populations of cycling and quiescent or slowly dividing cells (Rivers *et al.*, 2008).

1.4.1.2 OPC migration

In order for myelination to occur, a series of developmental events must occur, starting with oligodendrocyte precursor cells migrating to the correct locations, proliferating to sufficient quantities, and then differentiating into mature oligodendrocytes. The patterning and regional specification of oligodendrocyte development occur due to an interaction between cell-intrinsic and regionally restricted extrinsic factors, with OPCs initially appearing in discrete locations in the embryonic CNS but becoming homogeneously distributed throughout in the adult with their origin and migration distance being well conserved between birds and mammals (Miller, 1996; Olivier *et al.*, 2001), and OPCs being shown to be extremely migratory with implants from the olfactory bulb of wild type mice into shiverer animals showing extensive dispersion of normal myelination beyond the point of the original graft (Lachapelle *et al.* 1983). Although the exact mechanism through which this dispersion occurs is not well understood, this process likely involves contact-mediated interactions with pre-formed axonal tracts. For example, OPCs were shown to migrate along the optic nerve axon in an axophilic manner in chick embryos, unaffected by the removal of neural cell adhesion molecule (N-CAM)-associated PSA (Ono *et al.*, 1997), and that axonal topography may guide the migration pattern of OPCs isolated from the rat optic nerve (Webb *et al.*, 1995), while, conversely, barriers to prevent OPC migration may exist such as in the junctional region of the rat optic nerve that prevents OPCs from entering the retina where myelination may impair vision by decreasing the ability of light to reach the photoreceptors (ffrench-Constant *et al.*, 1988). In the mouse embryonic optic nerve, semaphorin receptors, neuropilin-1 and -2, and netrin-1 receptors, deleted in colorectal cancer (DCC) and unc5H1, were shown to modulate OPC migration through a balance of their effects, with Sema 3A being repulsive and netrin-1 being attractive, and Sema 3F being both chemoattractive and mitogenic (Spassky *et al.*, 2002). Both

polysialylated-neural cell adhesion molecule (PSA-NCAM) and polysialic acid (PSA) also influence OPC migration in late embryonic and early postnatal stages. PSA-NCAM-positive neural precursors from the subventricular zone were detected in lysolecithin-induced demyelination in the corpus callosum, giving rise to oligodendrocytes that had a role in the myelin repair (Nait-Oumesmar *et al.*, 1999), and PSA was shown to be a requirement for OPC migration from *in vitro* explant cultures (Wang, Rougon and Kiss, 1994). Through the use of the Boyden microchemotaxis chamber and the Dunn direct viewing chamber, Zhang *et al.* (2004) showed the role of PSA and PSA-NCAM in establishing the directionality of the migratory behaviour of OPC along the PDGF concentration gradient. However, their removal does not eliminate the random migration of OPCs in a homogeneous PDGF concentration, suggesting that they are not required for the motility itself. More recently, Tsai *et al.* (2016) showed the role of the vasculature in the migration of OPCs in the developing nervous system, with the architecture of the vasculature being important for the migratory behaviour of OPCs *in vivo* in mice, and the Wnt-chemokine receptor 4 (Wnt-Cxcr4) signalling potentially being important for the regulation of this OPC-endothelial cell interaction. The migration of OPCs is therefore likely coordinated through several, potentially redundant, pathways, along axons and the vasculature to result in their dispersion throughout the CNS.

1.4.1.3 OPC proliferation

As discussed below, PDGF and FGF, along with other growth factors such as epidermal growth factor (EGF) (Yang *et al.*, 2017) and G protein-coupled receptor GPR56 (Giera *et al.*, 2015), are mitogenic for OPCs (**Figure 1.6**). In defined medium containing PDGF and lacking thyroid hormone (TH), OPCs proliferate for many passages without differentiating. There appears to be a cell-intrinsic clock that counts the number of divisions before undergoing differentiation into OLs (Temple and Raff, 1985; Barres, Lazar and Raff, 1994; Tang, Tokumoto and Raff, 2000), with OPCs isolated from younger tissue allowing for more divisions (Temple and Raff, 1986; Durand and Raff, 2000). This timer appears to be

composed of two components, with the first part driven by mitogens like PDGF activating cell-surface receptors to promote continued proliferation and measure elapsed time, and the second part being regulated by the presence of hydrophobic intracellular signals like THs, glucocorticoids, and retinoid acids, to stop cell division and trigger cell differentiation (Barres, Lazar and Raff, 1994; Durand and Raff, 2000). The cell-cycle inhibitor p27/Kip1 accumulation in OPCs appearing to be an important component of the timing mechanism, with p27 null animals going through one or two additional cycles of division compared to WT cells before differentiating (Durand *et al.*, 1998; Durand and Raff, 2000).

During embryogenesis, the rate of cell division declines from 24 hours in E12.5 mouse spinal cord to over 100 hours at E17 as the number of OPCs increase. The saturation of PDGF signalling accelerating this cell cycle seems to suggest its role as the rate limiting step *in vivo*, with the rate of cell cycle decline appearing to correlate with the decrease in PDGF signalling during development and the final cell number being proportional to the supply of PDGF available. The limiting factor in OPC proliferation in the embryo therefore appears to be due to environmental factors, the availability of PDGF, rather than a cell-intrinsic mechanism (Van Heyningen, Calver and Richardson, 2001). In the adult CNS, the density of OPCs appear to be controlled by a cell-intrinsic homeostatic mechanism, in which cortical OPCs constantly survey their local environment using motile filopodia and growth cones to continuously migrate at an average rate of 2µm per day to areas where they can maintain their unique territory through self-avoidance of other OPCs. At this later stage, the proliferation of OPCs therefore seem to be maintained through a balance of growth and repulsion to ensure that they are available to replace lost and damaged OPCs in repair and regeneration rather than populate the CNS as in development (Ethan G. Hughes *et al.*, 2013).

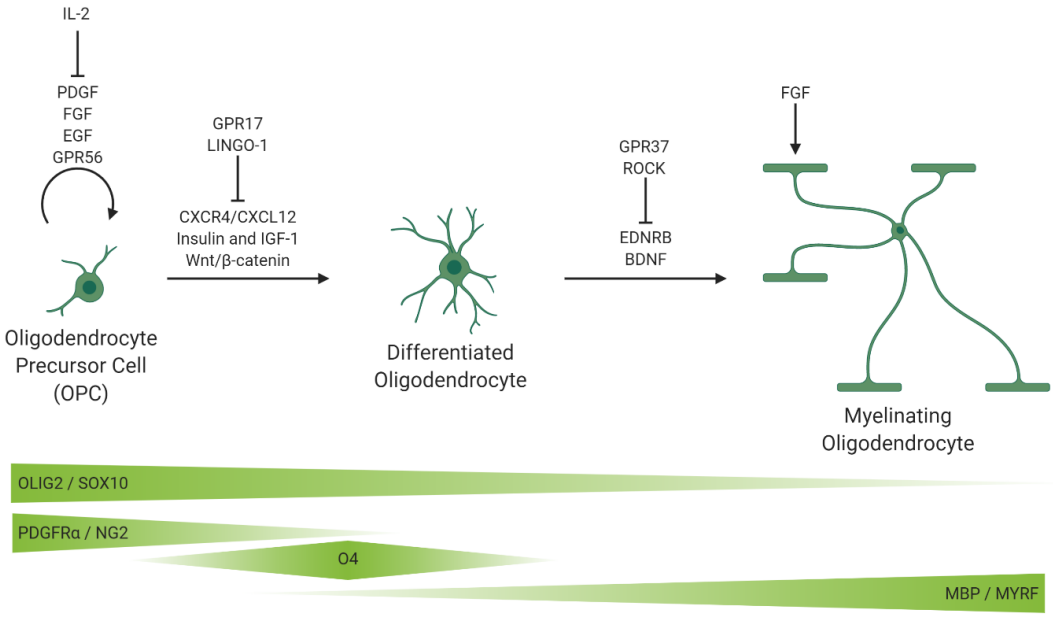

Figure 1.6 *Schematic of OPC development with known markers and factors influencing its development*

The diagram represents some of the key markers for the stages of oligodendrocyte development (below the figures) and the various factors that induce or inhibit their transitions (above).

Figure was drawn on BioRender.

1.4.1.4 OPC differentiation

Several mechanisms regulate the differentiation of oligodendrocytes and the myelination process. One potential mechanism would be the expression of extracellular ligands which, to date, have all been inhibitory in nature, including Jagged via the Notch pathway with Notch1 receptors being expressed on OPCs (Wang *et al.*, 1998), PSA-NCAM, with its expression on all fibres during development and its downregulation leading to myelination on PSA-NCAM-negative axons (P. Charles *et al.*, 2000), and LINGO-1, which is expressed in OLs and the attenuation of its function leading to increased differentiation and myelination through the activation of RhoA (Mi *et al.*, 2005). The Wnt/β-catenin pathway (**Figure 1.6**) may also play a complex role in OL development, with a genome-wide screen of transcription factor-encoding genes in remyelinating

rodent lesions and human MS lesions showing active and dynamic expression of the Wnt pathway mediator Tcf4/Tcf7l2, which was also identified as playing an important role for OPC maturation in an independent *in silico* screen (Fu *et al.*, 2009), in lesioned WM, the activation of β-catenin signalling during OL development and remyelination, their subsequent downregulation in mature OLs, and the disruption of the Wnt/β-catenin signalling delaying both developmental myelination and remyelination (Fancy *et al.*, 2009). The targeted disruption of Tcf4/Tcf7l2 in mice blocks OL differentiation (Ye *et al.*, 2009), suggesting that the role of the Wnt/β-catenin pathway is in the initial stages of differentiation, with its subsequent downregulation being required for continued differentiation to occur. The inhibition of Rho-A/Rho-associated kinase (ROCK) signalling pathway (**Figure 1.6**) appears to enhance myelinating OLs in rodent and human OPCs, in human neuron-OPC co-cultures, and in remyelination in rat brain tissue (Pedraza *et al.*, 2014). In addition, he G protein-coupled receptor GPR17 (Chen *et al.*, 2009) and ɣ-secretase (Watkins *et al.*, 2008) appear to have inhibitory effects on myelination through yet unknown ligands. As discussed further below, the electrical activity of axons appear to be important for OPC development and myelination. Neuronal activity may affect OL differentiation through influencing the expression of surface ligands and receptors, such as L1 and neural cell adhesion molecule (NCAM) (Itoh *et al.*, 1995), the activity of adenosine receptors on OPCs, which inhibit OPC proliferation and promote differentiation and myelination (Stevens *et al.*, 2002), or indirectly through stimulating leukaemia inhibitory factor (LIF) release from astrocytes which promote myelination (Ishibashi *et al.*, 2006). More recently, the G protein-coupled receptor endothelin receptor B (**Figure 1.6**) and PKC epsilon were shown to increase the number of myelin sheaths produced by individual OLs in mice and zebrafish in experience-dependent neuronal activity-associated myelination (Swire *et al.*, 2019).

Intrinsic factors may also play a role in the control of OL behaviour, such as transcriptional regulation, with factors such as Olig1, Nkx2.2, Sox10, Ascl1, YY1, and Tcf4 being required for the production of mature OLs, and the removal of "inhibitory" transcription factors like Id2, Id4, Sox6 and Hes5 that maintain undifferentiated OPCs allowing the progression of OPC development (Wegner,

2008). The myelin gene regulatory factor (MRF) is a transcriptional regulator that is specifically expressed in postmitotic terminally differentiated OLs, with its knockdown and overexpression preventing and promoting the expression of myelin genes, respectively. The absence of MRF from OL lineage cells results in severely neurologically abnormal mice with premyelinating OLs that fail to myelinate, highlighting their critical role for OL maturation and myelination (Emery *et al.*, 2009). Chromatin remodelling and epigenetics may be another intrinsic mechanism through which OL differentiation is regulated, with the inhibition of histone deacetylases (HDACs) resulting in hypomyelination, prolonged expression of OPC markers, and delayed expression of differentiation markers (Shen, Li and Casaccia-Bonnefil, 2005), with HDACs being required at multiple stages of OPC development to inhibit the Wnt/β-catenin pathway and being recruited by Yin Yang 1 (YY1) to repress inhibitors of myelin gene expression like Tcf4 and Id4 (He *et al.*, 2007; Ye *et al.*, 2009). MicroRNAs may also regulate OL differentiation and myelination, with targeted deletion of Dicer1 disrupting miRNA processing and normal CNS myelination, and miR-219 being shown to be necessary and sufficient for OL differentiation (Dugas *et al.*, 2010).

1.4.1.5 Death of newly differentiated oligodendrocytes

As first shown by Barres *et al.* (1992a, 1992b) in the developing rat optic nerve, about 50% of newly differentiated oligodendrocytes die in a process characteristic of programmed cell death within a few days after being generated. In *in vitro* conditions, this death is preventable through exposing the cells to conditioned medium from their *in vivo* neighbouring cells, or through exposure to PDGF and insulin-like growth factors (IGFs). Decrease in normal OL death by up to 90% is achievable by increasing exposure to PDGF in the developing optic nerve, resulting in the doubling of the number of OLs. In the developing rat brain, Trapp *et al.* (1997) subsequently showed that newly differentiated premyelinating OLs either myelinated axons or underwent cell death, with about 20% of these newly formed OLs degenerating in P7 to P21 cerebral cortex, and those that ensheathed and formed compact myelin being exempt from dying.

Cumulatively, this suggests that once OPCs have differentiated into OLs, there is competition for the limited availability of growth factors, which act via the extracellular matrix (ECM) as discussed further below, and the presence of axonal influences that promote their survival and maturation into myelinating OLs, with *in vivo* imaging showing most pre-myelinating OLs undergoing apoptosis prior to myelination (Hill, Li and Grutzendler, 2018; Hughes *et al.*, 2018). One of the key molecular mechanisms through which the regional and temporal specificity of myelination may be regulated is the transcription factor EB (TFEB), which is highly expressed in differentiating and premyelinating OLs. Mice with conditional knock out of this transcription factor exhibit precocious and ectopic myelination with thicker myelin sheath formation, suggesting its role in myelination specificity and control. Sun *et al.* (2018) showed that TFEB functions in a cell-autonomous manner to promote OL apoptosis and prevent their maturation via the pro-apoptotic factor PUMA, and regulates the spatial and temporal specificity of CNS myelination by activating the PUMA-Bax-Bak pathway, and therefore suggesting a molecular mechanism through which OPC proliferation is controlled to not cause hypermyelination.

1.4.1.6 Factors that regulate OPC development

1.4.1.6.1 Growth factors

OPCs express platelet-derived growth factor alpha-receptors, PDGFRα, with the mitogen PDGF-AA released by neighbouring astrocytes promoting DNA synthesis, increased proliferation and motility, and regulating their cell cycle and the timing of their differentiation into oligodendrocytes, with oligodendrocytes losing PDGFRs as they mature (**Figure 1.6**) (Noble *et al.*, 1988; Richardson *et al.*, 1988; Hart *et al.*, 1989; Pringle *et al.*, 1992; Calver *et al.*, 1998). PDGF therefore appears to be important for the normal development of the oligodendrocyte lineage, with *PDGF-A* null mice showing severe deficiencies in OPC development, with the hindbrain and midbrain showing 42% and 28% *PDGFRα+* cells, respectively, compared to wild-type control at E15, whereas the subunit *PDGF-B* null mice showed no difference to the wild-type. In postnatal mice, there is also a similar

reduction in *PDGFRα+* cells in *PDGF-A* null animals, although the extent is region-dependent, with almost 100% vs. an 80% reduction in the optic nerve compared to the cerebral cortex at birth, with a parallel decrease in the subsequent number of oligodendrocytes and the extent of myelin formation (Fruttiger *et al.*, 1999). PDGF interacts with other molecules and their receptors to achieve its mitogenic activity, such as the membrane protein NG2 chondroitin sulfate proteoglycan (NG2) and the ECM glycoprotein tenascin-C (TN-C). NG2 expression is strongly co-localised and regulated in parallel with and their co-expression important for the proliferative response of PDGF (Nishiyama *et al.*, 1996). The loss of TN-C from the matrix results in faster OPC migration *in vitro*, and shows reduced OPC proliferation from the loss of PDGF responsiveness, with TN-C acting via the αvβ3 integrin receptor, which is expressed during OPC differentiation (Milner *et al.*, 1997), to increase the mitogenic effects of PDGF on OPCs (Garcion, Faissner and ffrench-Constant, 2001).

Fibroblast growth factors (FGFs) highly influence OLs at various stages of their development (**Figure 1.6**), with the FGF receptors (FGFRs) expressed on OL lineage cells changing through the maturation process *in vitro* and FGF2 effecting OL development at all stages (Butt and Dinsdale, 2005; Fortin *et al.*, 2005; Furusho *et al.*, 2011, 2012; Murtie *et al.*, 2005). *In vitro*, the combination of PDGF and FGF2 promote continuous division of OPCs without differentiation for a prolonged period, with FGF2 maintaining PDGFα receptor expression on OPCs (Bögler *et al.*, 1990; McKinnon *et al.*, 1990). Terminal differentiation of OPCs seem to be blocked by the FGF8 and FGF17 ligands on FGFR3, process growth on differentiated OLs being triggered by FGF9 on the FGFR2 signalling pathway, and OPCs and OLs both being targeted by FGF18 acting on the FGFR2 and FGFR3, with FGFR expression changing from FGFR3 to FGFR2 as OPCs differentiate into OLs. Ligand availability and the changing expression of FGFRs appear to critically regulate normal OL development, with FGF2 activation of FGFR1 promoting OPC proliferation but having deleterious effects on OLs, leading to the loss and preventing new generation of myelin-forming OLs (Butt and Dinsdale, 2005; Fortin *et al.*, 2005). However, although *Fgfr1* and *Fgfr2* appear to be required for the initial OPC generation in the mouse ventral forebrain by cooperating with Shh signalling, their conditional deletion showed that, unlike what has previously

been shown in *in vitro* experiments, they did not appear to be required for the proliferation of OPCs *in vivo* (Furusho *et al.*, 2011). In *Fgf2* null mice, although its knockout out in the germline did not affect OPC proliferation in the developing spinal cord, there was an increase in the number of differentiated OLs, suggesting that *in vivo*, FGF2 and FGFR1 play an important role in the inhibition of differentiation in OL lineage cells (Murtie *et al.*, 2005). *Fgfr1* and *Fgfr2* deletion in differentiated OLs *in vivo* in mice showed reduced Erk1/2-MAPK signalling pathway activity, and showed hypomyelination with thinner myelin sheath formation, although OPC proliferation and differentiation, and axonal ensheathment and myelination initiation were unaffected (Furusho *et al.*, 2012). Cumulatively, these studies show the complexity of Fgf signalling in the normal CNS, with different members of the FGF family and their receptors affecting different stages of OL lineage cell development.

Neuregulins are a family of transmembrane and soluble protein isoforms that have been implicated in the survival, proliferation, migration, and differentiation of oligodendrocyte lineage cells in their normal development, with their absence in active MS lesions potentially contributing towards poor remyelination (Canoll *et al.*, 1996; Flores *et al.*, 2000; Viehover *et al.*, 2001). Heregulin binds to erbB2, erbB3, and erbB4 receptors from a family of tyrosine kinases which are all expressed on OL lineage cells, to induce a time- and dose-dependent phosphorylation of Akt. Dominant negative overexpression of Akt through adenoviral gene transfer activated the caspase cascade to induce apoptosis in both OPCs and OLs, and growth factor deprivation-induced apoptosis of OPCs could be prevented by heregulin. This suggests a role for the phosphatidylinositol (PI)-3 kinase/Akt pathway in the survival of OL lineage cells (Flores *et al.*, 2000), which was also shown to be the pathway through which Neuregulin 3 (NRG3) elicited its OL survival role in the embryonic CNS through the activation of the erbB4, an important receptor for brain development (Carteron, Ferrer-Montiel and Cabedo, 2006). Glial growth factor (GGF), specifically GGF2, is a soluble recombinant isoform of neuregulin which mediates its effect, likewise, via the erbB2, erbB3, and erbB4 receptors. GGF2 has been shown to be a potent mitogen of OPCs, promote their survival, and prevent their differentiation, with cortical neurons releasing a soluble mitogen whose effects can specifically be

blocked by antibodies against GGF (Canoll *et al.*, 1996). In the developing rat optic nerve, neuregulin was shown to support the survival of aged OPCs and OLs, and increase or decrease death induced by nerve transection by neutralising or delivering the growth factor, respectively (Fernandez *et al.*, 2000). Cumulatively, these suggest an axon-associated regulatory role in the survival and proliferation of OL lineage cells by neuregulins. In the migration of OPCs, neuregulin 1 (NRG1) acts on the erbB4 receptor in the developing embryo, with Nrg1 acting as a potent chemoattractant during the first wave of OPC migration but not during later postnatal stages, and a deficit in *erbB4* leading to impaired OPC migration during development, highlighting the role of NRG1/erbB4 signalling pathway in early development OPC migration (Ortega *et al.*, 2012). The NRG1/erbB pathway also has a role in regulating CNS myelination, although it is not essential for myelin sheath formation as in the PNS (Vartanian, Fischbach and Miller, 1999). Co-cultures of OPCs with NRG1 type III deficient dorsal root ganglions (DRGs) result in normal differentiation and myelinate, although to a lesser degree than with wild type DRGs. Transgenic NRG1 type I or type III overexpression lead to hypermyelination, although the expression of NRG1 type III is not sufficient to drive myelination in unmyelinated axons such as the sympathetic neurons. Haploinsufficient mice for NRG1 type III are hypomyelinated in the brain, but unaffected in the optic nerve and spinal cord. Cumulatively, this suggests a region-specific role for NRG1 in the extent of myelination, specifically in the brain (Brinkmann *et al.*, 2008; Taveggia *et al.*, 2008). Like the FGFs, the family of neuregulins have a pleiotropic effect on the OL lineage cells in a developmental stage, region-specific, and isoform-dependent manner.

Neurotrophins are another class of growth factors that regulate various stages of OL development. In particular, neurotrophin-3 (NT3) has been shown to be important for promoting the survival of OPCs, and, in conjunction with PDGF, to also be able to stimulate OPC proliferation. TrkC, the high-affinity receptor for NT3, is expressed throughout all stages of the OL lineage development, with NT3 inducing the phosphorylation of mitogen-activated protein kinase (MAPK) to elicit its effect (Barres *et al.*, 1993, 1994; Cohen *et al.*, 1996). Brain-derived neurotrophic factor (BDNF), which acts through the trkB receptor, increases DNA synthesis in OPCs, differentiation of postmitotic OLs, and has a role in regulating

myelination (**Figure 1.6**). Knockout animals for BDNF show reduced OPC numbers at embryonic day 17 (E17), postnatal day 1 (P1), P14, and in the adult animal, as well as decrease myelin basic protein (MBP), myelin associated glycoprotein (MAG), and proteolipid protein (PLP), suggesting its importance in OPC development and differentiation (Vondran *et al.*, 2010). Conditional knockout of the receptor TrkB on OLs also results in decreased myelin protein expression, as well as reduced myelination in the CNS during development despite normal numbers of OLs and myelinated axons, with myelin sheath thickness being significantly impacted, suggesting the role of BDNF in myelin ensheathment rather than axonal contact. Interestingly, these animals also showed increased OPC density and proliferation, suggestive of a modification of the proliferative potential of OPCs in conditional knockouts (Wong *et al.*, 2013). In contused adult rat spinal cord, 10 weeks post-injury, transplants containing grafts of fibroblasts producing the neurotrophic factors NT3 and BDNF contained more axons than other grafts, including ciliary neurotrophic factor and basic fibroblast growth factor, and, importantly, enhanced myelinogenesis, which BrdU labelling was able to associate with increased expansion of OL lineage cells (McTigue *et al.*, 1998). These highlight the role of neurotrophins, such as NT3 and BDNF, on the survival, differentiation, and myelination potential of OL lineage cells.

1.4.1.6.2 Chemokines

In addition to growth factors, such as those discussed above, several chemotactic cytokines, or chemokines, which are regulatory molecules that modulate the inflammatory responses, have a role in modulating OL lineage cells. For example, growth-regulated-oncogene-α (GRO-α), which is released in part by a subset of spinal cord astrocytes, is a potent promoter of OPC proliferation and has a synergistic and localised influence on the mitogenic effects of PDGF in a developmentally regulated manner from the ventral to dorsal spinal cord white matter (Robinson *et al.*, 1998). C-X-C Motif Chemokine Receptor 4 (CXCR4) and its chemokine ligand C-X-C Motif Chemokine 12 (CXCL12) also regulate OPC survival and migration (**Figure 1.6**). OPCs isolated from newborn mice

coexpressed CXCR4 and PDGFRα, and CXCR4 expression decreased with differentiation *in vitro*. Neonatal OPCs showed CXCR4- and CXCL12-dependent migratory behaviour in a concentration-dependent manner in chemotactic chambers, and CXCR4-defective mice showed decreased PDGFRα-expressing OPCs in the embryonic spinal cord with decreased indications of ventral to dorsal migration during development (Dziembowska *et al.*, 2005). In studying the effects of another CXCR, CXCR7, the use of an *in vivo* EAE model and *in vitro* primary OPCs showed that CXCR4 was downregulated and CXCR7 upregulated with OPC differentiation and maturation, with CXCR4 being undetectable in the CNS of the EAE model. CXCL12 was also shown to promote the maturation of *in vitro* OPCs in a CXCR7-depenent manner through pharmacological inhibition (Göttle *et al.*, 2010). Cumulatively, Dziembowska *et al.* (2005) and Göttle *et al.* (2010) highlight the role of various CXC receptors, specifically the CXCR4 and CXCR7, and their ligand CXCL12 on different stages of the OL lineage maturation.

1.4.1.6.3 Extracellular Matrix (ECM)

As discussed previously, ECM components such as TN-C and integrin play an important role in interacting with mitogens like PDGF to elicit their effect (Garcion, Faissner and ffrench-Constant, 2001; Milner *et al.*, 1997). The ECM, comprised of a complex system comprised primarily of collagens, glycoproteins, and glycosaminoglycans, provides signals for growth, differentiation, and migration of cells, and are critical for the developmental organisation of the CNS (Novak and Kaye, 2000). *In vitro*, the purified ECM protein fibronectin enhanced the survival, proliferation, migration, and process extension properties above the PDL control, and above the purified ECM laminin and secreted ECM protein mixture Matrigel (Hu *et al.*, 2009), showing the preference of OL lineage cells for certain ECM components. The integrins have also been shown to be important ECM components in OL development, particularly in the regulation of OL survival and death, with the absence of α_6 integrin receptor for laminins in null animals resulting in increased apoptosis of myelinating OLs. The $\alpha_6\beta_1$ integrins have been shown to activate a “switch” that is mediated via association with the Src family kinase (SFK) Fyn to change neuregulin signalling to increase dependence on the

more highly activated MAPK signalling pathway (differentiation) versus the PI3K pathway (proliferation) in survival signalling. Another SFK Lyn acts on the $\alpha_v\beta_3$ integrin earlier in the lineage to promote OPC proliferation (Colognato et al., 2002, 2004). The non-integrin ECM receptor, dystroglycan, which interacts with laminin, has also been shown to play an important role in regulating myelin formation. The absence of dystroglycan, either by antibody blocking or siRNA knockdown, lead to decreased differentiation and myelin-specific protein levels (MBP and CNP), and the loss of complex myelin membrane sheets production and nascent myelin sheath structure formation, suggesting its role in later stages of OL development (Colognato *et al.*, 2007).

In neuropathology, the CNS microenvironment has been shown to become perturbed and contain ECM components that are inhibitory to the regenerative process (Fitch and Silver, 2008). Of particular interest to MS, members of the chondroitin sulphate proteoglycans (CSPG) ECM family, which play a role in patterning cell migration and axonal growth guidance in development and in plasticity in adulthood (Laabs *et al.*, 2005), have been shown to be upregulated and present at the borders of chronic lesions (Sobel and Ahmed, 2001), and inhibit OPC process outgrowth and differentiation *in vitro* which is reversible with Rho kinase inhibitor treatment (Siebert and Osterhout, 2011a). In addition, basement membrane components, predominantly associated with the vasculature in the normal CNS, have been shown to be expressed in active lesions, including laminin, collagen type IV, and heparin sulphate proteoglycans (HSPGs) (van Horssen *et al.*, 2006; Van Horssen, Dijkstra and De Vries, 2007). In MS patient tissue samples and in the EAE mouse model, high molecular weight hyaluronan was shown to accumulate in chronic demyelinated lesions, with their presence inhibiting remyelination in lysolecithin-induced WM demyelination model, and shown *in vitro* to inhibit OPC maturation which degradation of this ECM component could improve (Back *et al.*, 2005). Together, the inhibitory effect of upregulated ECM components in MS suggest their role in providing a conducive environment for OL lineage development in the unperturbed CNS in health.

1.4.1.6.4 Electrical activity

OPCs have been shown to express a variety of neurotransmitter receptors, including those for glutamate (kainate, AMPA, and NMDA), GABA, and acetylcholine in serum-free cultures (Barres *et al.*, 1990), in mouse hippocampal brain slices (Jabs *et al.*, 1994; Steinhäser, Jabs and Kettenmann, 1994), and gene profiling (Patneau *et al.*, 1994; Cahoy *et al.*, 2008), and show brain region- and age-specific heterogeneous expression profiles of ion channels and neuronal activity sensitivity (Spitzer *et al.*, 2019), suggesting their responsiveness to the demands of surrounding neurons. OPCs appear to be the only glial cells to directly form synapses with neurons to receive postsynaptic inputs, forming synapses with glutamatergic neurons throughout the grey and white matter which become more robust throughout maturation (Bergles *et al.*, 2000; Káradóttir *et al.*, 2005; Müller *et al.*, 2009), and with GABAergic neurons in the grey matter which change to extrasynaptic signalling with age (Lin and Bergles, 2004; Velez-Fort *et al.*, 2010). Although the function of these synaptic inputs in OPCs are less clear than for neurons, AMPA and NMDA receptor expression has been shown to be rapidly down-regulated and the synapses removed with OPC differentiation (Biase, Nishiyama and Bergles, 2010; Kukley, Nishiyama and Dietrich, 2010), suggesting their role in communication with neurons at the precursor stage of migration and OL development (Gudz, Komuro and Macklin, 2006; Yuan *et al.*, 1998). Electrical activity has been shown to be important for OPC proliferation through influencing growth factor release (Barres and Raff, 1993), and in inducing myelination through tetrodotoxin (TTX) blocking of neuronal firing (Demerens *et al.*, 1996). More recently, stimulation of the neural circuit in adult animals have shown increases in OPC proliferation, OL myelination, and myelin sheath thickness (Wake, Philip R. Lee and Fields, 2011; Gibson, Purger, Mount, Goldstein, Lin, Wood, Inema, Miller, Bieri, Zuchero, B. A. Barres, Woo, Vogel and Monje, 2014; McKenzie *et al.*, 2014), with the frequency of the neuronal firing itself, and not just its presence, seeming to affect OPC behaviour. The different patterns of neuronal activity modulates the neurotransmitter and synaptic profile at axon-OPC synapses through changes in glutamate release. The implantation of an electrode array into the corpus callosum of adult mice showed that the degree of stimulation of axons changed

the density of OPCs and pre-myelinating OLs, with testing of OPC behaviour at three different stimulation paradigms showing that 5 Hz seemed to be more efficient at affecting differentiation behaviour, whereas 25 Hz and 300 Hz triggered proliferative ones (Nagy *et al.*, 2017). The ability to communicate with and detect neuronal signals, and the specific pattern of this signalling, therefore seems to play an important role in the ability for OPCs to develop and mature in the CNS.

1.4.2 Oligodendrocyte Formation and Heterogeneity

In order to form myelin sheaths, OPCs need to differentiate into OLs, with this transition being highly regulated by, for example, GABAergic signalling positively driving differentiation whilst negatively regulating proliferation, and its peak signalling being coordinated with onset of oligodendrogenesis (Orduz *et al.*, 2015; Velez-Fort *et al.*, 2010; Zonouzi *et al.*, 2015). Differentiating OLs can be identified by marker proteins CNP (Poduslo and Norton, 1972), O4 (Schachner and Sommer, 1981), and ectonucleotide pyrophosphatase/phosphodiesterase 6 (ENPP6) (Xiao *et al.*, 2016), whilst more mature OLs express a range of myelin-specific proteins and transcription factors such as MBP (Sternberger *et al.*, 1978), MAG (Sternberger *et al.*, 1979), myelin/oligodendrocyte glycoprotein (MOG) (Linnington, Webb and Woodhams, 1984), PLP (Sobel *et al.*, 1994), and myelin regulatory factor (MYRF, which is essential for differentiation of mature myelinating OLs and lack of expression leads to hypomyelination and OL apoptosis) (Emery *et al.*, 2009).

OLs are highly heterogeneous, including their morphological properties (Murtie, Macklin and Corfas, 2007; Vinet *et al.*, 2010). A transgenic mouse line expressing membrane-associated EGFP expression under the control of MBP, labelling <1% of the myelinating cells so that individual OLs could be imaged and quantified, showed diversity with the number of myelin internodes formed per OL, with a range of 10 to 60, and sheath length, between 20 to 200 microns (Chong *et al.*, 2012). OLs from distinct regions have also been shown to have different properties including myelinogenic capabilities and myelination preference. In

the grey matter (GM), a high-throughput electron microscopy (EM) reconstruction technique to visualise myelination in the mouse neocortex showed distinct and variable distribution of myelin, with superficial layers showing higher diversity (Tomassy *et al.*, 2014). Injection with attenuated rabies virus and adeno-associated virus to visualise individual OLs in WM, the corpus callosum, showed that 25% of OLs preferentially myelinated motor or sensory cortical axons, whereas 75% showed no preference (Osanai *et al.*, 2017). Collectively, these suggest that the myelination properties of individual OLs are highly diverse, which may be linked to functional and regional diversity.

Further evidence for diversity comes from homo- and heterotropic cell transplantation experiments of OLs from GM and WM of the adult mouse cortex that showed higher efficiency of WM-derived OLs in differentiating in either GM and WM environments in comparison to GM-derived OLs (Viganò *et al.*, 2013), and from single-cell sequencing experiments have shown six different transcriptional profiles of myelin-forming OLs (Marques *et al.*, 2016; Jäkel *et al.*, 2019). However the biological significance of this diversity remains unknown.

1.4.3 Myelin Sheath Formation

Once an oligodendrocyte is formed, the next step is myelin sheath formation. The exact mechanism by which a myelin sheath is constructed is not yet fully understood. One model, later called the “carpet crawler model” (Sobottka *et al.*, 2011), used electron microscopy data to suggest the outer myelin membrane is formed, followed by the inner layers migrating underneath in a “rolled up carpet” motion (Bunge, Bunge and Bates, 1989). More recently, the “liquid croissant model” was suggested, which addresses some of the limitations of previous models such as the high energy required to overcome the friction of pushing myelin layers underneath already formed ones in the “carpet crawler model”, or how the maximum thickness of the myelin at the middle of the internode is formed. In this study, high-resolution confocal microscopy was used to describe the process of myelin sheath formation as the creation of a triangular-shaped myelin sheet, with the “pouring out” of myelin proteins along the triangular

shaped OL process following initial axon contact in a bidirectional coiled manner, and sheath thickness and length increase occurring by subsequent layers "pouring" on top of previously formed inner layers and extending sideways in a "croissant" shape (Sobottka *et al.*, 2011). Snaidero *et al.* (2014) found with fluorescent signal intensity analysis from confocal images of zebrafish *in vivo* and high-resolution three-dimensional reconstructions of the mouse optic nerve from electron microscopy that myelin sheath growth appears to initially be nonuniform in the growing myelin sheath, with more layers at the centre compared to the lateral edges. The inner tongue appears to extend around the axon underneath the previous membrane layer, with *in vivo* virus labelling of glycoprotein and electron microscopy data showing selective targeting of new membrane material at this active growth zone facilitated by cytoplasmic channels. Simultaneous lateral extension in the growing myelin sheath seems to lead to a more uniform thickness along the mature sheath. Collectively, these data support Sobottka *et al.* (2011)'s "liquid croissant model" of myelin sheath formation, with further evidence showing that the phosphoinositide 3-kinase (PI3K)/protein kinase B (AKT)/mammalian target of rapamycin (mTOR) signalling pathway regulates the cytoplasmic channels in myelin growth regulation.

The role of the actin cytoskeleton has been implicated as important for myelin wrapping (**Figure 1.7**). In this process, F-actin is redistributed and polymerised at the leading edge as a mechanical force to push out the myelin membrane and then disassembled, which triggers the myelin sheet to spread and adhere. Actin assembly in myelin wrapping appears to be mediated by the Arp2/3 complex in driving OL process growth and branching, with deletion early on in myelin formation resulting in myelination defects, although it is not required for subsequent wrapping (Zuchero *et al.*, 2015). Subsequently, actin disassembly appears to be facilitated by ADF/cofilin1, with deletion resulting in an abnormal size of the inner tongue of the wrapping myelin sheet and impaired myelin growth and hypomyelination (Nawaz *et al.*, 2015), and indirectly via MBP by binding to membrane PI(4,5)P2 to induce the release of actin disassembly proteins, with MBP and actin filaments occupying non-overlapping domains in differentiating OLs and knockdown of MBP resulting in abnormal actin filament accumulation (Zuchero *et al.*, 2015).

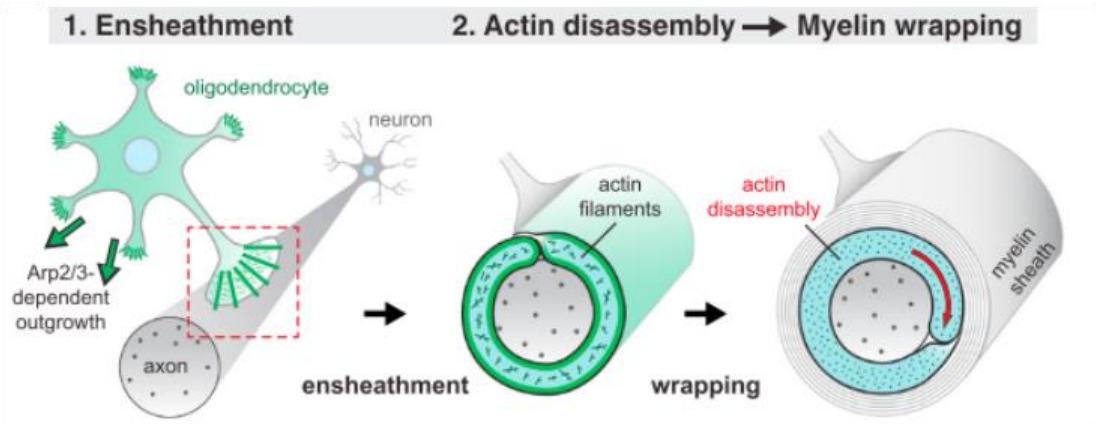

Figure 1.7 Potential mechanism for myelin wrapping

As described by Zuchero et al. (2015), myelin wrapping may occur in a two-step process by which ensheathment occurs due to an Arp2/3-dependent actin assembly, followed by its disassembly in the inner tongue for myelin wrapping to occur.

Figure from Zuchero et al. (2015).

Once wrapping has initiated, myelin sheaths elongate and compact in order to become mature myelin sheaths. Live *in vivo* studies in zebrafish show that in addition to its role in process retraction in axon selection, calcium plays an important role in sheath elongation. High frequency of intracellular [Ca^{2+}] transients appear to promote sheath lengthening, with elongation occurring about 1 hour after calcium concentration being increased, with calcium buffering being sufficient to result in shorter sheath lengths (Krasnow *et al.*, 2017; Baraban, Koudelka and Lyons, 2018). These changes in calcium may regulate the activity of proteins involved in the cytoskeleton or calcium-activated signalling pathways, such as the PI3K-AKT-mTOR pathway (Zonouzi *et al.*, 2011). The generation of myelin appears to have a variety of signalling pathways that play a role, such as phosphatidylinositol 3,4,5-trisphosphate (PIP3) and extracellular signal-regulated kinases (ERK)/mitogen-activated protein kinases (MAPK). Various mouse mutants to elevate the PIP3 signalling pathway, such as through the disruption of its antagonist phosphatase and tensin homolog (PTEN) (Goebbels *et al.*, 2010) and constitutive activation of its downstream target AKT kinase (Flores *et al.*, 2008), and transgenic mice with sustained ERK1/2 activation (Ishii,

Furusho and Bansal, 2013) showing increased myelin thickness, highlighting their roles in controlling myelination. The conditional mouse mutant of a highly evolutionarily conserved regulator of cell polarity, Scribble, showed decreased longitudinal myelin extension but increased myelin thickness (Jarjour *et al.*, 2015), suggesting that radial and longitudinal growth of myelin requires individual coordination of signals along both axis of growths to regulate cohesively. Myelin compaction is the final stage in the myelin sheath formation process by which the extracellular and cytoplasmic sides of adjacent myelin lamellae connect tightly, with compaction starting from the outside in (Snaidero *et al.*, 2014). Although the exact mechanism through which this process is initiated is not yet understood, MBP (Raasakka *et al.*, 2017) and CNPase (Yin *et al.*, 1997) appear to play important roles.

1.4.3.1 Regulation of Myelination - Intrinsic and Extrinsic Signals

The mechanisms described above suggest an intrinsic programme driving sheath formation, a conclusion supported by the finding that when OPCs are cultured in the absence of axonal signalling, such as on paraformaldehyde-fixed axons (Rosenberg *et al.*, 2008) and polystyrene microfibers (Lee *et al.*, 2013), these OPCs are able to differentiate and form compact myelin sheaths. Importantly, spinal cord-derived OLs produced longer sheaths than cortex-derived OLs when cultured on poly-L-lactic acid (PLA) microfibers (Bechler, Byrne and ffrench-Constant, 2015), with these lengths being comparable to their respective *in vivo* sheath lengths (Murtie, Macklin and Corfas, 2007; Bechler, Byrne and ffrench-Constant, 2015), highlighting the origin of OPCs as determining their intrinsic myelinogenic potential.

In addition to these intrinsic mechanisms, however, there is abundant evidence that myelination can be altered through extrinsic signalling, such as with experience and learning. A key signal here is thought to be axonal activity, as first suggested by experiments with mice reared in complete darkness showing decreased myelination (Gyllensten and Malmfors, 1963), the blocking of axonal potential with tetrodotoxin inhibiting myelination (Demerens *et al.*, 1996), and

more recently by optogenetic stimulation of the premotor cortex in mice promoting oligodendrogenesis and increasing myelination (Gibson *et al.*, 2014). In addition, socially isolated male rhesus monkey infants (Sánchez *et al.*, 1998) and socioemotionally deprived children raised in orphanages (Eluvathingal *et al.*, 2006), with decreased social, cognitive, and emotional stimulation during development, were shown to have decreased white matter volume and cognitive and behavioural deficits. In mice, two weeks of social isolation immediately after weaning led to hypomyelination of the prefrontal cortex, with oligodendrocytes having reduced branching, sheath number and thickness, and deficiencies in behavioural tests, such as social exploration, which was irreversible with reintroduction to a social environment and suggests a critical window for myelin plasticity. This phenotype could be replicated by the loss of ErbB3 receptors in OLs, highlighting the neuregulin-1 (NRG1)/ErbB3 signalling pathway as a potential molecular mechanism through which this stimulation-dependent myelination occurs (Makinodan *et al.*, 2012).

Linked to the role of activity in influencing myelination, Mckenzie *et al.* (2014) conducted a study in which mice learnt a new complex motor task of running on a "complex wheel" in which rungs on the running wheel were removed at random positions. These mice showed an increase in OL formation, suggesting the effect of increased neuronal activity specifically from learning a new motor task in increasing myelination. However, interestingly, when *Myrf* was conditionally knocked out to prevent new OL development, deficits in the learning could be seen. This suggests both that increased neuronal stimulation through learning increases myelin formation, and that myelination is also required for this learning to occur (Mckenzie *et al.*, 2014).

A key question is how activity signals to the oligodendrocyte, and synaptic vesicle release has been shown to be one of the mechanisms through which this occurs. Vesicular release of glutamate from axons stimulate the local translation of MBP in OLs through the Fyn kinase-dependent pathway (Wake, Philip R Lee and Fields, 2011), and tetanus toxin inhibition of axonal activity results in fewer myelinated axons, and vice versa with stimulated neuronal activity through the use of a GABA-A receptor antagonist (Mensch *et al.*, 2015). Fyn signalling appears to be

important in modulating myelination as the activation and disruption of Fyn increases and decreases sheath number per OL, respectively (Czopka, ffrench-Constant and Lyons, 2013), with its tyrosine kinase activity appearing to be important for myelination (Sperber *et al.*, 2001).

Activity-related signals might explain in part why the formation and degree of myelination progresses in a relatively fixed topographical and chronological sequence, which is generally hierarchical starting from regions controlling basic homeostasis to areas of increasing complexity, sensory systems usually before motor systems (Brody *et al.*, 1987; Kinney *et al.*, 1988), and axons being myelinated, partially myelinated, or unmyelinated (Tomassy *et al.*, 2014). However, the question as to whether other cues on the surface of CNS axons play a role remains unanswered.

Suggesting that such cues exist, OLs actively explore their surrounding environment using highly dynamic processes (Kirby *et al.*, 2006; Ethan G Hughes *et al.*, 2013), with cells determining whether to retract or stabilise and elongate the formation of myelin sheaths by mediation of intracellular calcium concentrations (Baraban, Koudelka and Lyons, 2017; Krasnow *et al.*, 2017) in a relatively restricted time window (Czopka, ffrench-Constant and Lyons, 2013). Inhibitory molecules of myelination have been discovered, such as polysialylated-neural cell adhesion molecule (PSA-NCAM) on immature neurons (P Charles *et al.*, 2000) and JAM2 on neuronal cell bodies (Redmond *et al.*, 2016) in developmental myelination, and semaphorin 3A, which is elevated in active MS lesions, as an inhibitor of OPC recruitment and remyelination in pathology (Piaton *et al.*, 2011; Syed *et al.*, 2011). However factors such as NRG1 (Brinkmann *et al.*, 2008; Taveggia *et al.*, 2008) and integrin β1 (Câmara *et al.*, 2009) that play a key role in PNS myelination have only been shown to play a role in modulating myelination in the CNS – they are not necessary for myelination. Thus, Brinkmann *et al.* (2008) created conditional mutant mice lacking NRG1 in almost all projection neurons in the forebrain. Surprisingly, these animals did not show abnormalities in myelination development or timing when knockout occurred in adults or in embryonic development. Double mutants for ErbB3 and ErbB4, the receptors for NRG signalling, also did not affect CNS myelination. The

overexpression of NRG1 type III isoform, conversely, led to hypermyelination and premature myelination, although "ectopic“ myelination of normally unmyelinated axons was not observed and it did not increase myelination in LPC lesions. However, Taveggia *et al.* (2008) found that haploinsufficient mice for NRG1 type III have myelination defects on DRG neurons and are hypomyelinated in the forebrain. Collectively, these studies suggest NRG1 acts as an axonal signal that promotes myelination, but is not sufficient or exclusive in driving its occurrence. Câmara *et al.* (2009), in addition, showed that dominant-negative β1 integrin transgenic mice transiently required a higher axonal calibre for developmental myelination to occur, with a lower percentage of myelination of axons below 0.6 microns in diameter, and that oligodendrocytes derived from dominant-negative β1 animals formed fewer internodes in co-culture, suggesting an intrinsic signalling abnormality. .

While the precise molecular cues that determine whether and where an axon will be myelinated has yet to be determined, the role for physical cues should also be considered. Oligodendrocytes ensheathing biologically inert polymer microfibers show a preference for larger diameter microfibres of above 0.4 micron on whether ensheathment occurs and the length of the myelin sheath formed (Bechler, Byrne and ffrench-Constant, 2015; Lee *et al.*, 2012), suggesting that physical cues such as axon calibre may play a role in this axon selection process.

1.4.3.2 Differentiation vs. Myelination

Whether differentiation and myelination occur in a one-step process, whereby the initiation of the signalling pathways that result in differentiation result in direct progression into myelination, or a two-step process, where the OL must receive two different signals for each step to occur, is highly debated. From a clinical perspective, the difference between these two theories are significant as the one-step theory suggests that a pro-differentiation drug is sufficient to result in myelination, whereas the two-step theory would mean that different pro-differentiation and pro-myelination drugs are required.

A key study that suggests the differential signalling required to initiate differentiation and myelination looked at the temporal and spatial progression of these two developmental stages in the rat optic nerve. As summarised in **Figure 1.8**, OPCs differentiate into OLs from the optic chiasm towards the eyes, with the OPCs near the optic chiasm expressing markers of differentiation, mRNAs of MBP and PLP, 3 days before those near the eyes. Conversely, however, MBP and PLP proteins, as markers of myelination, were detectable firstly near the eyes and subsequently towards the optic chiasm in a reverse gradient to differentiation (Colello *et al.*, 1995). Although OPC heterogeneity could be one possible explanation for the temporal difference between differentiation and myelination of the potential different sub-populations of OPCs along the optic nerve, the chronology of the two different events does, however, highlight that there appears to be two different signalling mechanisms to initiate differentiation, starting from the optic chiasm, and another one to initiate myelination, from the eyes, providing evidence towards the two-step theory.

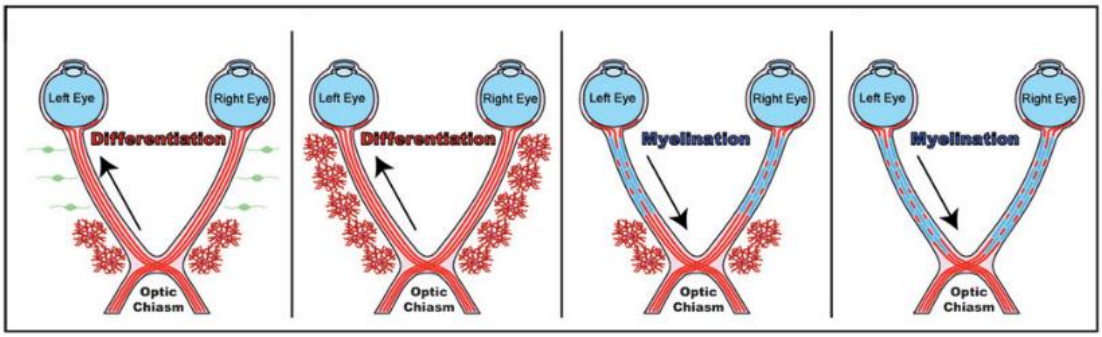

Figure 1.8 Uncoupling differentiation and myelination in the rat optic nerve

OPCs (shown in green) differentiating into OLs (shown in red) occurs from the optic chiasm to the eye in the rat optic nerve. Myelination (shown in blue) occurs in the opposite direction from the eye to optic chiasm.

(Figure from Rosenberg, Powell and Chan, 2007)

In addition, *in vivo* and *ex vivo* imaging, EdU pulse-chase experiments, and cell fate mapping showed that in postnatal mouse brains, P8 animals exhibited a

critical temporal window of 3 to 4 days for a plateau to be reached in OPCs differentiating into OLs after cell division, and P21 animals of 7 to 8 days, but that OL maturation and myelination appeared to occur more gradually over an extended period of time (Hill *et al.*, 2014). Live *in vivo* imaging in zebrafish has shown that there is a critical time window of 5 hours for new myelin sheaths to be generated and number of sheaths formed by the oligodendrocyte to be determined (Czopka, ffrench-Constant and Lyons, 2013), and co-cultures of rat retinal ganglion cells and OPCs showed a 12 hour critical window for OLs to form stable myelin segments after initiation after which continued interactions did not result in stable segment formation (Watkins *et al.*, 2008). Collectively, these suggest two potentially distinct critical periods for differentiation and myelin sheath initiation to occur, highlighting that there may be two different mechanisms modulating these two processes.

In supporting this idea, OPCs have been shown to be electrically excitable (Clarke *et al.*, 2012), with expression of voltage-gated sodium channels and ionotropic glutamate receptors, and the ability to form synapses with glutamatergic neurons (Biase, Nishiyama and Bergles, 2010). However, as these OPCs transitioned into myelinating OLs, there was a decrease in synaptic input, and downregulation of the sodium channels and glutamatergic receptors, with a shift towards non-synaptic inputs for promoting myelin sheath formation such as vesicular release (Biase, Nishiyama and Bergles, 2010; Wake *et al.*, 2015). Therefore, there is evidence to suggest that neuronal activity affects both transitional phases in the OL development independently, with synaptic mechanisms modulating differentiation, and non-synaptic mechanisms for myelination, and consequently that different pharmacological modulators of these two independent processes may be required to enhance myelination in the treatment of MS, with G protein-coupled receptor endothelin receptor B having been shown to have opposing responses in inhibiting and enhancing differentiation and myelination, respectively (Swire *et al.*, 2019).

1.5 Reversing Remyelination Failure

1.5.1 Ageing and remyelination

Chronic demyelination and decreased remyelination is a defining characteristic of progressive MS, and potential causes of remyelination failure include extrinsic, such as increased inhibitory or insufficient pro-regenerative, and intrinsic factors, such as the impaired capacity of the OL. As a key intrinsic factor, ageing is an important consideration for both remyelination and MS. MS patients are often diagnosed in their 30s or 40s, and have a life expectancy of at least 25 years (Compston and Coles, 2002), making ageing a component of disease progression. The rate of remyelination slows throughout adult life, progressively impairing OPC recruitment and differentiation (Sim *et al.*, 2002), with this decline being more rapid in the more efficiently remyelinating WM (Hampton *et al.*, 2012; Pfeifenbring *et al.*, 2015; Shields *et al.*, 1999). There is also evidence for an accumulation of axonal damage resulting in permanent clinical deterioration, which may explain the transition from RRMS to SPMS (Irvine and Blakemore, 2006). In fact, regardless of the initial age and pattern of MS at onset of disease, patients reached specific and similar levels of disability at the same age, suggesting there was an age-associated decline (Confavreux and Vukusic, 2006), with cellular senescence impairing remyelination (Nicaise *et al.*, 2019) and MS patients potentially undergoing accelerated ageing (Confavreux and Vukusic, 2006). This age-related decline in remyelination has been shown to be reversible through exposure to a “youthful systemic milieu” of blood-derived monocytes from young animals in a heterochronic parabiosis experiment (Ruckh *et al.*, 2011).

1.5.2 Extrinsic factors that inhibit remyelination

Our now quite detailed understanding of oligodendrocyte biology and myelination has led to many studies examining the possible causes of poor remyelination seen in patients with MS. Myelin debris represents an important

extrinsic factor, as myelin contains inhibitors of OPC differentiation and maturation (Trapp *et al.*, 1997; Robinson and Miller, 1999; Plemel *et al.*, 2012). In the intact CNS, with disrupted BBB aiding efficient myelin debris removal (Pohl *et al.*, 2011), this mechanism prevents OPCs from undergoing differentiation and myelination in areas already containing myelin, or in areas where there are no exposed axons as this would result in apoptosis. However, in MS lesions, where myelin debris from the inflammatory attack on oligodendrocytes and myelin sheaths are present, this could prevent remyelination due to the presence of the inhibitory signals (Baer *et al.*, 2009; Kotter *et al.*, 2006; Lampron *et al.*, 2015; Skripuletz *et al.*, 2013). Therefore, activation of the immune system to promote myelin debris clearance from extracellular space by microglia (Baer *et al.*, 2009; Kotter *et al.*, 2006; Lampron *et al.*, 2015; Skripuletz *et al.*, 2013), as well as modulation by T cells to promote spontaneous remyelination (Bieber, Kerr and Rodriguez, 2003; Nielsen *et al.*, 2011; Dombrowski *et al.*, 2015), is required to achieve remyelination.

Most studies, however, have focussed on the signalling pathways that regulate OPC and oligodendrocyte behaviour. From these, a number of additional inhibitors of remyelination have been identified (**Figure 1.9**). These have in turn led to candidate-led research programmes to develop therapies to enhance remyelination. One important inhibitor of remyelination is LRR and Ig domain-containing, Nogo receptor-interacting protein (LINGO-1), a CNS-expressed transmembrane protein in the NgR1/p75 and NgR1/Taj(Troy) signalling complexes in regulating axon growth which is also expressed in OLs. LINGO-1 antagonists, through lentivirus RNA interference and exogenous antagonist addition, resulted in increased OL differentiation and axonal myelination, including in demyelination/remyelination models (Lee *et al.*, 2007; Mi *et al.*, 2005; Mi *et al.* 2009). This resulted in the development of a potential remyelination enhancement therapy, Opicinumab, a human monoclonal antibody against LINGO-1 (Cadavid *et al.*, 2019), that is currently in clinical trials (NIH U.S. National Library of Medicine, 2019). Other inhibitors in the extracellular matrix, such as chondroitin sulphate proteoglycans (Siebert and Osterhout, 2011b) and hyaluronan (Back *et al.*, 2005), and fibrinogen (Petersen *et al.*, 2017) have also

been shown to have inhibitory effects on OLs and remyelination and represent a promising approach to further experimental medicine programmes.

An alternative approach to the discovery of pathways that reverse remyelination failure is the discovery of new molecules implicated in normal remyelination. One such molecule, Retinoid X receptor gamma (RXR-ɣ), was detected in OL lineage cells in remyelination in a rat focal demyelination model from a transcription-profiling screen and has been shown to be an accelerator of remyelination. Administration of an agonist, 9-*cis*-retinoic acid, and antagonism, through siRNAs, antagonists, and null mice, of this receptor in *in vitro* and *in vivo* studies were able to show increased remyelination and delayed differentiation, respectively (Huang *et al.*, 2010). Subsequently, the vitamin D receptor was found to be one of the nuclear receptor binding partner of RXR-ɣ, which is of clinical interest as vitamin D is thought to be linked with MS prevalence (Mokry *et al.*, 2015), and therefore may provide a therapeutic target of increasing remyelination through this signalling pathway. Other possible molecules will come from ongoing research – so, for example, with demyelinated axons being shown to be electrically active and form new synapses with OPCs, targeting of neuronal activity through the glutamate signalling pathway (Gautier *et al.*, 2015) could also enhance remyelination using an indirect cellular target.

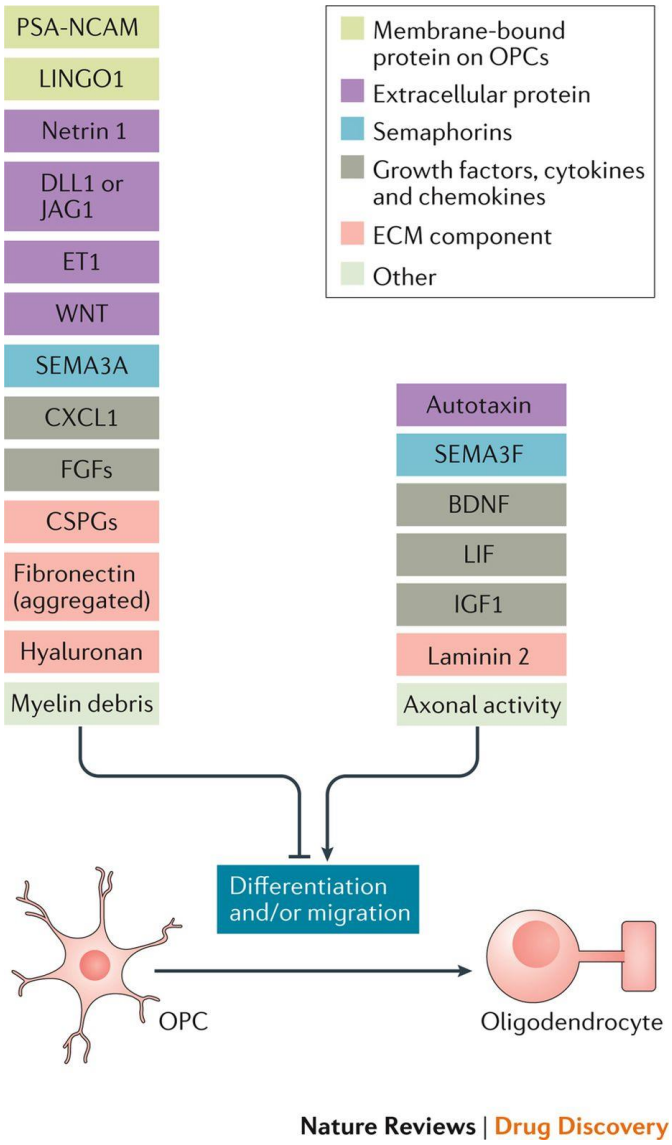

Figure 1.9 Positive and negative factors that regulate OLs

Figure from Plemel, Liu and Yong (2017)

1.5.3 At what stage does remyelination fail

In about 30% of MS lesions, a failure of remyelination occurs due to lack of OPC recruitment, whereas in the remaining 70%, the block occurs at a later stage in OL development (Boyd, Zhang and Williams, 2013; Chang *et al.*, 2000; Jäkel *et al.*, 2019; Lucchinetti *et al.*, 1999; Wolswijk, 1998). However the exact stage at which

this block occurs in the 70% of lesions with OPCs and OLs within them remains undetermined. A block in OPC maturation in the majority of MS lesions has been supported by various studies, including Wolswijk (1998), who characterised post-mortem MS tissue of patients at chronic stages of the disease, and found variable densities of O4+, GalC- OPCs (2.3 to 34 cells/mm^2) in all 22 lesions investigated, with 15 of these lesions (~68%) showing almost complete absence of GalC+ oligodendrocytes and myelin at their centres. Using double-labelling with O4 (OPC) and Ki-67 (active proliferating cells) antibodies, none of the ~7000 O4+ cells in the 15 lesions were positive for Ki-67, suggesting the presence of quiescent OPCs in these chronic MS lesions with little to no myelination. Lucchinetti *et al.* (1999) examined brain biopsy and autopsy specimens from 113 early MS cases for a total of 395 lesions at various stages of demyelination, which was narrowed down to 56 cases with lesions extending from the periplaque WM to the active demyelinating edge and inactive plaque centre, and OLs were identified using PLP mRNA for immature and mature OLs synthesising and maintaining myelin, and MOG protein for terminally differentiated mature OLs. In their study, however, they found 39 of the 56 cases (~70%) showed increased OL numbers, suggesting their recruitment, in demyelinated and/or remyelinated areas compared to active lesions. They also found increased PLP+ MOG- cells in 29 out of 43 cases (~67%) with inactive demyelinated or remyelinated areas, suggesting increased immature OLs in these lesions in early MS cases. Chang *et al.* (2002) obtained autopsy samples from 10 MS patients for a total of 48 chronic lesions, and used confocal microscopy images to quantify premyelinating OLs, determined as PLP+ cells with multiple processes that were not in contact with myelin internodes. They were able to identify premyelinating OLs in 34 out of the 48 lesions (~71%) (**Figure 1.10** A).

Together these studies showing lesions lacking myelin but containing either OPcs or OLs suggest there may be blocks at different stages in differentiation and remyelination in MS. More recently, single-cell transcriptomic analysis of OL lineage cells from a mouse model of MS, the experimental autoimmune encephalomyelitis (EAE) model (Falcão *et al.*, 2018), and post-mortem human tissue (Jäkel *et al.*, 2019) support this conclusion by showing a change in the transcriptional profile of OLs in disease. In post-mortem human tissue, single-

nucleus transcriptional analysis from the WM of control and MS brains showed a skewing of the heterogeneous subclusters of OLs, with a preference for immature and intermediate OL populations in MS (**Figure 1.5** C and **Figure 1.10** B) (Jäkel *et al.*, 2019). Collectively, these studies suggest that in 70% of lesions, the lack of sufficient OPCs is not the limiting factor for why there is a failure for effective remyelination, that there is a change in the developmental and transcriptional profile of the OLs present, and that this skew may be towards pre-myelinating and immature OLs suggesting a maturation block in MS.

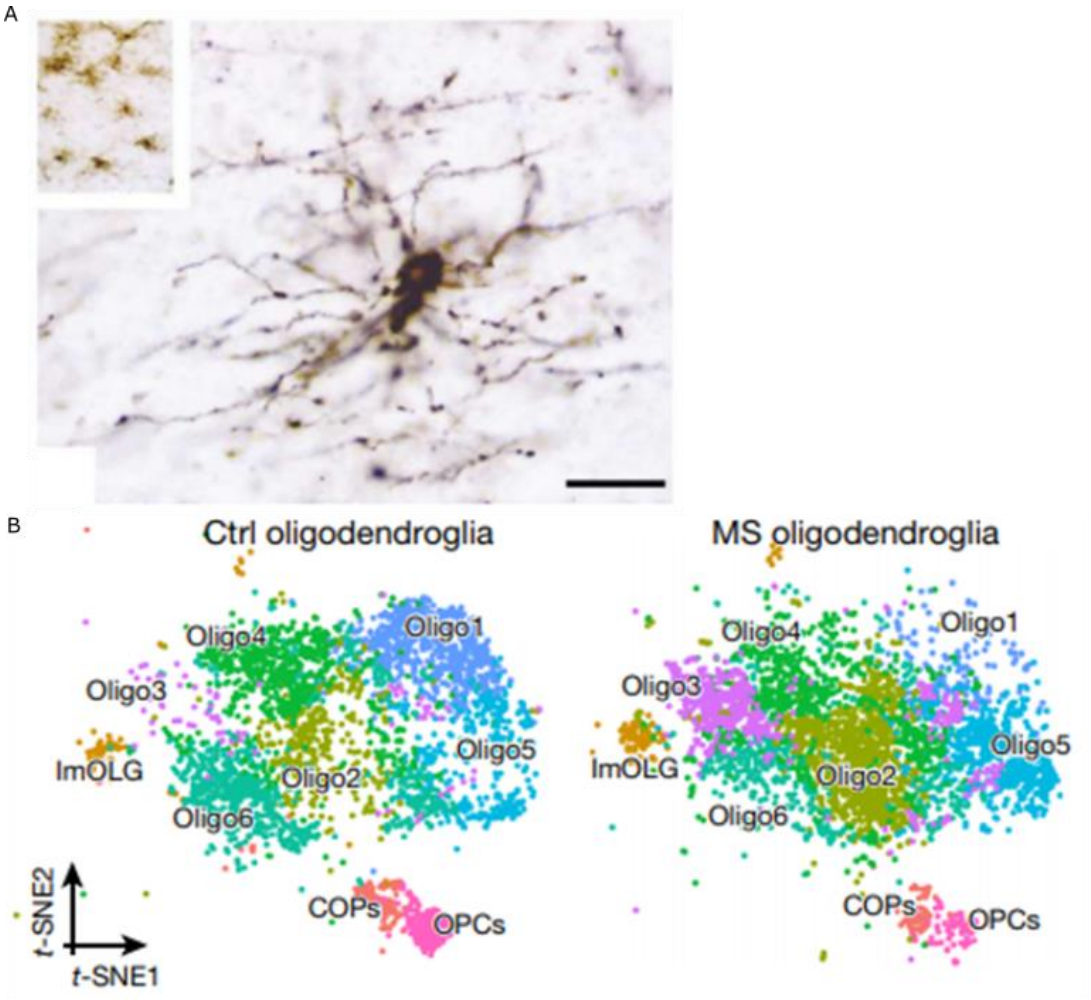

Figure 1.10 Oligodendrocytes in MS

A. Clusters of pre-myelinating OLs can be detected within MS lesions extending multiple processes parallel to the demyelinated axon. Stained with PLP antibodies. Scale bar = 30 µm

(Figure from Chang *et al.*, 2002)

B. *t*-SNE projections of OL subclasses in control and MS post-mortem human brain tissue.

Single-nuclear sequencing data on post-mortem human brain tissue show reduction in OPCs and intermediate Oligo6 populations, and a skewing of the OLs with a depletion in Oligo1 and enrichment in Oligo2, Oligo3, Oligo5, and ImOLG.

(Figure from Jäkel *et al.*, 2019)

1.6 Why has drug discovery for remyelination in MS been so difficult?

In this section I will review two principle causes as to why drugs for remyelination have not yet reached the clinic. These are, (1.6.1) the difficulties of drug discovery in the CNS in general, and (1.6.2) the challenges of extrapolating from the predominately animal-based studies above to human disease, as a result of which we still do not know which cell type drives remyelination in humans. A third possible reason, that the screens thus far have not considered the differences in the regulation of oligodendrocyte differentiation and myelination, will be discussed at the end of this chapter.

1.6.1 Brain Disorders across the piece have defied Drug Discovery

Brain disorders have largely defied drug discovery efforts, with few to no drugs being available for a large number of the major conditions. In order to consider as to why this may be the case, I will (1.6.1.1) first compare brain disorders with other organs and tissues to establish comparative rates of failure and where in the pipeline these failures occur. Following this, I will then describe the major challenges for drug discovery in the brain that causes these low success rates: (1.6.1.2) the lack of biomarkers, (1.6.1.3) pharmacokinetics and drug metabolism, (1.6.1.4) access to brain tissue, and lastly (1.6.1.5) disease modelling.

1.6.1.1 Drug discovery across organs and diseases

Success rates in drug discovery vary widely between different disease areas and organs, with cardiovascular diseases having approximately 20% rate of success versus 5% and 8% for oncology and CNS disorders, respectively (**Figure 1.11** A). When divided by the phase of development, the majority of attrition occurs later on in clinical development, around Phases IIb and III. The average failure rate for compounds for all disease areas is 23% at the registration stage, where the full time and cost burden of the drug discovery pipeline has already been incurred. CNS has the second highest failure rate after women's health at above 30% (**Figure 1.11** B) (Kola and Landis, 2004), and that it falls behind cancer and cardiovascular success rates in clinical trials (**Figure 1.11** C) with CNS drugs taking longer to reach the market at 12 to 16 years compared to the 10 to 12 years of non-CNS drugs (Alavijeh *et al.*, 2005; Srinivas, Maffuid and Kashuba, 2018). More recent data paints a similar landscape, with the likelihood of approval (LOA) for non-pain and non-psychiatric neurological drugs, of mainly neurodegenerative diseases, being 9.8% from phase I to II. For comparison, infectious diseases and autoimmune-immunology drugs, which had the two highest LOAs from the disease categories with sufficient sample size, had approval rates of 16.7% and 12.7%, respectively, and the lowest being oncology at 6.7%, for the same clinical phase (**Figure 1.11** D) (Hay *et al.*, 2014). Across the drugs which went through FDA approval for new drug application (NDA) and biologic license application (BLA) across various disease areas between 2005 to 2011, drugs for all neurological diseases, including neurodegenerative, pain, and psychiatric disorders, had the lowest approval rate for the first review at 36% compared to highest for oncology at 71%. The cumulative NDA/BLA success rate for neurology was 78%, second from the bottom with cardiovascular diseases also being 78% and endocrine being lower at 71%, and the highest being infectious diseases at 90% (Hay *et al.*, 2014). Cumulatively, these two studies show that the rate of drug approval for CNS/neurological disorders is low compared to other disease areas, and that this has remained consistent across the decade difference between the publications of these two papers, with oncology being the only other disease area to perform more poorly.

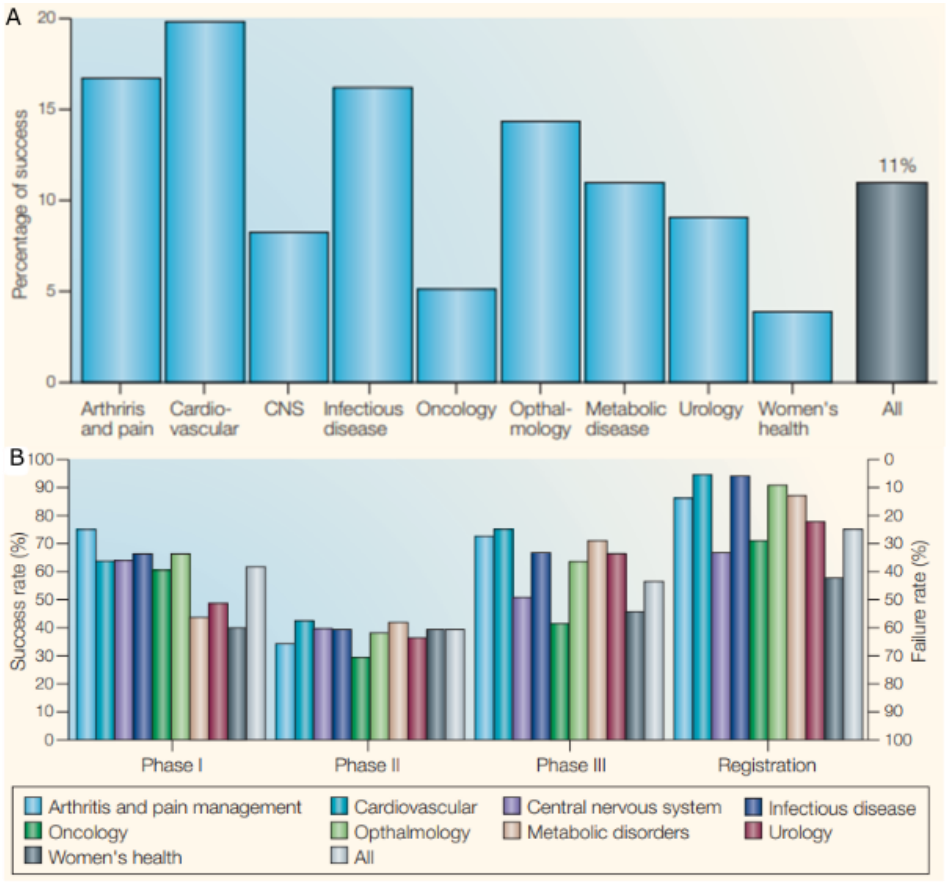

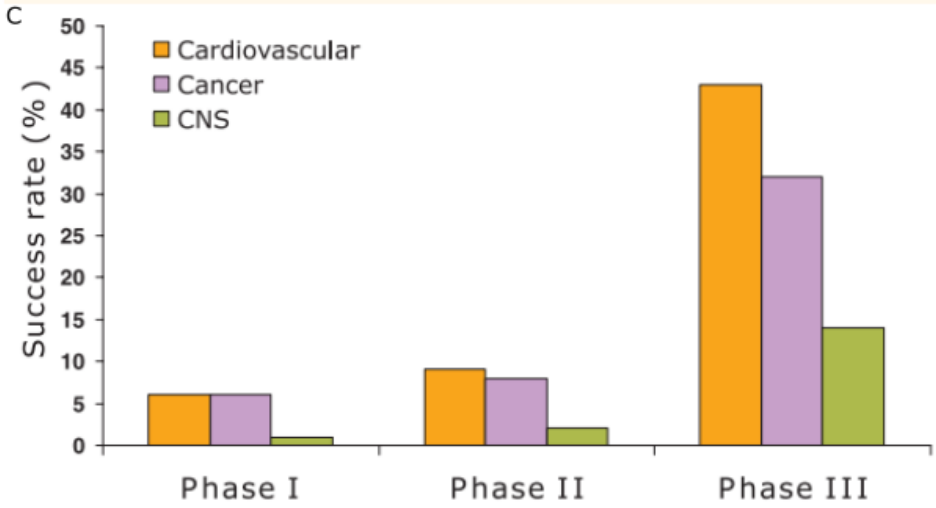

D

	Phase 1 to phase 2				Phase 2 to phase 3				Phase 3 to NDA/BLA				NDA/BLA to approval			
	Total in phase[b]	Advanced or suspended[c]	Phase success[d]	Phase LOA[e]	Total in phase[b]	Advanced or suspended[c]	Phase success[d]	Phase LOA[e]	Total in phase[b]	Advanced or suspended[c]	Phase success[c]	Phase LOA[e]	Total in phase[b]	Advanced or suspended[c]	Phase success[d]	Phase LOA[e]
Other[f]	254	198	72.2%	18.2%	419	251	44.2%	25.3%	252	159	71.1%	57.1%	169	112	80.4%	80.4%
Infectious disease	247	196	65.8%	16.7%	288	157	45.9%	25.4%	159	98	65.3%	55.4%	115	86	84.9%	84.9%
Autoimmune	241	178	68.0%	12.7%	350	215	34.0%	18.7%	149	95	68.4%	55.0%	88	61	80.3%	80.3%
Endocrine	223	180	58.3%	11.6%	293	198	33.8%	19.8%	147	95	67.4%	58.5%	91	61	86.9%	86.9%
Respiratory	110	90	66.7%	11.1%	193	120	27.5%	16.7%	58	30	63.3%	60.8%	33	25	96.0%	96.0%
Neurology	389	298	62.4%	9.4%	520	348	30.2%	15.0%	285	188	60.6%	49.9%	192	152	82.2%	82.2%
Cardiovascular	158	127	60.6%	7.1%	229	152	26.3%	11.7%	121	89	52.8%	44.6%	78	58	84.5%	84.5%
Oncology	919	651	63.9%	6.7%	1,451	827	28.3%	10.5%	383	221	45.2%	37.0%	142	104	81.7%	81.7%
Total	2,541	1,918	64.5%	10.4%	3,743	2,268	32.4%	16.2%	1,554	975	60.1%	50.0%	908	659	83.2%	83.2%

Figure 1.11 Clinical success rates by disease area

A. Clinical success rates from first-in-man to registration between 1991-2000 for ten big pharmaceutical companies in the United States and Europe divided by disease areas, with the overall rate being 11%.

   10 companies: AstraZeneca, Bistol-Myers Squibb, Eli Lilly, F. Hoffman-La Roche, GlaxoWellcome, Johnson & Johnson, Novartis, Pfizer, Pharmacia, Schering-Plough, and SmithKline Beecham.

   Figure from Kola and Landis (2004)

B. Clinical success (left y-axis) and failure (right y-axis) rates divided by phase of development, with significant attrition rates occurring later on in the pipeline.

   Figure from Kola and Landis (2004)

C. Cumulative success rate by phase of clinical development by disease area.

   Figure from Alavijeh *et al.* (2005)

D. Success rate and LOA by clinical phase per disease area. Neurological disorders, including pain, psychiatric, and neurodegenerative diseases, consistently performed at or below the total average.

   Comparing only non-psychiatric non-pain neurological diseases, the phase success was 9.8%, 36.6%, 55.9%, and 81.4%, and the phase LOA as 9.8%, 16.7%, 45.5%, and 81.4%. The percentages were therefore higher than for the total for both at the phase 2 to phase 3 stage only.

   Figure from Hay *et al.* (2014)

1.6.1.2 Lack of disease biomarkers

Contributing towards the difficulty in drug discovery in brain disorders is the lack of clinical biomarkers for neurodegenerative diseases. Biochemical, genetic, and neuropathological biomarkers are important tools for assessing and monitoring the changes in neurobiological and neuropathological processes that are associated with disease onset and progression and after administration of potential therapeutic agents in clinical trials to monitor the response, and should ideally be specific to the disease and reliable. A small number of biomarkers for

neurodegenerative conditions are available from neuroimaging, such as diffusion tensor imaging (DTI)-detected changes in WM and GM integrity in MS and indirectly through [18F]FDG measurements for glucose metabolism from PET scans for various neurodegenerative diseases, biochemical approaches like phosphorylated tau levels in Alzheimer's disease (AD), and genetic biomarkers for common familial and sporadic genetic mutations to predict disease onset, like amyloid precursor protein gene mutation in AD and the number of CAG repeats on the *IT15* gene on chromosome 4 for Huntington's disease. However, the available biomarkers are either non-specific for the disease being studied, do not have the resolution required to accurately follow disease progression and detect small changes, or are predictive for diagnosis due to specific genetic mutations, and the current gold standard for neuropathological diagnosis is with an autopsy on post-mortem tissue, when it is too late to understand disease progression or treatment effects (Rachakonda, Pan and Le, 2004; Risacher and Saykin, 2013; Shi, Caudle and Zhang, 2009). In contrast, oncology has made further strides in the discovery of stratification or predictive biomarkers for subpopulations of the heterogeneous disease patient population, many of which are direct drug targets for their respective treatment, including the kinase biomarkers EGFT, HER2/neu, PDGFR, and estrogen receptor, as well as immune cell surface receptors such as CD20 and CD25, and range from genetic, transcriptomic, protein, microRNA, and metabolic biomarkers (Deyati *et al.*, 2013). Therefore, despite the similarly low rates of clinical trial success for oncology as for brain disorders (Kola and Landis, 2004; Hay *et al.*, 2014), there have been more activity and overall number of successes in the drug discovery for oncology due to the ability to detect whether a drug has worked in clinical trials, whereas treatments that only have small effects are missed in neurodegenerative diseases due to our inability to detect them with the lack of accurate and reliable biomarkers.

1.6.1.3 Pharmacokinetics and drug metabolism (PKDM)

One of the barriers to drug discovery in brain disorders is in the pharmacokinetics of getting the drug delivered to the brain. The brain, as part of the CNS, is a sanctuary site with protective barriers, specifically the blood-brain barrier (BBB), which is highly neuroprotective, and is constituted by endothelial cells in the capillaries with three levels of barrier formation for physical, transport, and metabolic (Alavijeh *et al.*, 2005; de Boer and Gaillard, 2007; Gaillard *et al.*, 2012). The poor BBB penetration for drugs prevents 98% of small molecules and almost 100% of large molecules not making it across to the brain, especially if they are hydrophilic, and compounds may still be targeted for degradation by endosomal/lysosomal or ubiquitin/proteasomal systems once across the BBB (de Boer and Gaillard, 2007). Alternative strategies to increase drug delivery to the brain include highly invasive direct injection of the drugs into the CSF, potentially permanently damaging non-specific and non-selective transient disruption and increased permeability of the BBB, the modification of the compound with a homing device for the specific and selective targeting of endogenous transport mechanisms, and other mechanisms to improve the absorption, distribution, metabolism and excretion (ADME) properties of the compound such as lipophilicity and hydrogen bonding (de Boer and Gaillard, 2007; Gaillard *et al.*, 2012). In addition, the difference in the BBB permeability, and the drug metabolising enzymes and transporters between animal models, where *in vivo* assessment of brain penetration by ventricular CSF sampling and tissue microdialysis can be routinely performed over time (Alavijeh *et al.*, 2005; Srinivas, Maffuid and Kashuba, 2018), compared to human patients mean that pharmacokinetic predictors of the degree of drug penetrance in the CNS are not necessarily predictive of human drug exposure. Measurements of drug concentration and exposure in the CNS in human patients can be performed by techniques such as (1) positron emission tomography (PET), which is restricted by the cost, use of radioactivity, and inability to distinguish between the drug and its metabolites, (2) microdialysis, which is only available during intraoperative procedures, or (3) lumbar punctures, with medical risks, not performed routinely, as well as the measurement being location and time

dependent, and therefore the data not always available or predictive even when taken in human patients (Deo, Theil and Nicolas, 2013; Markou *et al.*, 2009; Srinivas, Maffuid and Kashuba, 2018). Although the BBB functions to maintain the brain's homeostasis, this also sometimes prevents potential drugs for treatment from reaching the area in sufficient quantities for the length of time required for its therapeutic function (Alavijeh *et al.*, 2005), and therefore adds complexity to the pharmacokinetic properties of the drugs that are appropriate for the treatment of brain disorders even if they were efficient in pre-clinical studies of *in vitro* and *ex vivo* models.

A commentary by Aronson (2007) highlighted the lack of pharmacodynamics reports in drug development, with concentration-effect relationships being quantified in animal models with limited ability to predict the human disease and efficacy (Markou *et al.*, 2009). Pharmacodynamics for the CNS is measured using various endpoints, including (1) receptor occupancy/binding affinity as *in vitro* and *in vivo* measurements of the ligand-receptor complex formation, respectively, but is limited by species translatability despite its benefit as a direct measure of drug efficacy, as well as discrepancies between *in vitro* and *in vivo* data in complicating interpretations, (2) behavioural symptom changes and clinical ratings scales, which is clinically easy to understand and perform longitudinal studies tracking, but is rarely translatable between animal models and humans, and can create difficulties with translation, and (3) neuroimaging markers, such as PET scans and functional magnetic resonance imaging (fMRI), but are generally expensive, and lead to exposure to radioactivity or high-intensity magnetic fields, respectively (Srinivas, Maffuid and Kashuba, 2018). The location of and the heightened immune protection provided to the brain therefore restricts our ability in being able to take direct samples and measurements routinely over a long period of time, and limits the applicability of animal models to human patients, making understanding the pharmacodynamics properties of compounds in drug discovery for brain disorders more complex than organs that are more easily accessible.

In addressing some of these issues, the development of an *in vitro* Madin-Darby canine kidney (MDCK) cell line assay that express multidrug resistance protein 1

(MDR1), MDR1-MDCK, or breast cancer resistance protein (BCRP), BCRP-MDCK, which are 2 major efflux transporters of the BBB that actively eliminate compounds from the brain, were validated to be able to better predict brain penetration of compounds *in vivo*. This highlighted the role of *in vitro* models of brain penetrance as physiologically based pharmacokinetic models in simplifying complex organisms to quantitative systems (Feng *et al.*, 2019). Trapa *et al.* (2019) were also able to compare the efflux activity of two key transporters *in vitro*, BCRP and P-glycoprotein (P-gp), to *in vivo* unbound brain-to-plasma concentration ratio using approaches that took into account the scaling differences between *in vitro* models to *in vivo* organisms. They were able to validate that *in vitro* efflux data is able to accurately predict the degree of brain penetration across three preclinical species within their physiologically based pharmacokinetic framework, and therefore support that extrapolating the degree to which a compound could cross the BBB *in vivo* from *in vitro* models could improve pharmacokinetic predictions of brain drug discovery.

In silico simulations and predictions may further allow us to screen for compounds with the correct physiochemical features that allow them to be used in treating CNS conditions by crossing the BBB and having an effect on the relevant biological systems. Pajouhesh and Lenz (2005) described a classification system where they listed the attributes of a successful CNS drug as follows:

- Potent activity: low to subnanomolar
- Highly selective
- Molecular weight < 450
- Minimal hydrophobicity (clogp < 5)
- Number of H-bond donor < 3
- Number of H-bond acceptor < 7
- Number of rotatable bonds < 8
- H-bonds < 8
- Pka, neutral or basic with pK_a 7.5–10.5 (avoid acids)
- Polar surface area < 60–70 Å^2
- >30-Fold margin between hERG IC_{50} and effective unbound plasma concentration.
- Metabolic stability with >80% remaining after 1 h.
- P450 enzyme CYP inhibition $< 50\%$ at 30 μM.
- No significant CYP2D6 metabolism.
- Not a potent CYP3A4 inducer.
- Not an efficient P-glycoprotein substrate (*in vivo*).
- Not a high-affinity serum albumin ligand ($K_d < 10$ μM).
- Aqueous solubility > 60 μg/ml.
- Effective permeability $>1 \times 10^{-6}$cm/sec

Table 1.1 Characteristics of a successful CNS drug

Table from Pajouhesh and Lenz (2005)

Overall, molecules for brain disorders tend to be more lipophilic for BBB penetration, be less polar and less flexible, and have lower molecular weights and be smaller than compounds used for other therapeutic areas. As adjusting for one attribute affects others, medicinal chemistry to design compounds of the right physical chemistry properties will require a balance of the structure and activity, with guides such as the Pajouhesh and Lenz (2005) system aiding in the design of CNS therapeutics.

Improvements in *in vivo* imaging techniques may aid in understanding the pharmacokinetics in the distribution of drugs in a whole organism or even in human patients. Magnetic resonance (MR) spectroscopy and spectroscopic imaging are non-invasive techniques, therefore allowing repeat measurements and long-term follow-up in healthy subjects and patients, for evaluating the body's metabolism using predominantly the proton in ^{1}H-MR spectroscopy for the brain and has been used in the research of psychiatric brain conditions (Mason and Krystal, 2006; Zhu and Barker, 2010). As it is relatively low sensitivity, it can only detect millimolar quantities of small, mobile molecules *in vivo*, with

commonly used field strengths and long echo times only being able to pick up signals from choline, creatine, and *N*-acetylaspartate in normal conditions, and potentially lactate, alanine, and other compounds in elevated concentrations in pathological conditions. Short echo times allow the detection of other structures including glutamate, glutamine, *myo*-inositol, lipids, and macromolecules. The signal is localised to the voxel by using the intersection of three orthogonal slice-selective selections, with voxel sizes for the human brain being 4 to 8 cm^3. MR spectroscopic imaging especially, despite its longer time compared to MR spectroscopy, can be used to measure multiple locations simultaneously for increased spatial variation information on the distribution of metabolites, with multiple approaches being implemented to improve its speed, each with its own benefits and caveats (Zhu and Barker, 2010). Despite its current limitations, MR spectroscopic imaging provides a promising *in vivo* imaging technique to detect in animal models and in humans the localisation of the drug metabolites in studying the pharmacokinetics of the drug distribution. However, its low resolution does mean that it is currently difficult to distinguish between the various brain regions, and between the brain region and perivascular space, which may be remedied by the development of novel variations of this imaging technique in the future.

1.6.1.4 Access to brain samples

The limited access to human brain samples, especially during active disease progression (Denic *et al.*, 2011), also limits our current understanding of brain disorders. As discussed in detail later, Brain Banks have given us access to post-mortem human brain tissue from generous donors and their families (Ravid, 2008). However, these samples, due to the nature of the tissue collection being post-mortem, are all end-stage disease, containing mostly chronic lesions in MS brain tissue (Wolswijk, 1998; A Chang *et al.*, 2002), and therefore limits our ability to study disease progression. Although brain biopsies have been used to study MS lesions previously (Lucchinetti *et al.*, 1999), such tissue are rare to access unless the patient is already undergoing surgery for another brain-related

medical condition. Due to this lack of access for direct histological analysis, studies and clinical trials for MS have relied upon various proxy outcome measurements for tissue repair by, for example, measuring the shortening of P100 latency delay on full-field, pattern-reversal, visual-evoked potentials, or through imaging techniques such as MRI, which allows detection in gross changes to lesion size and location but doesn't have the resolution to allow these to be studied at a cellular level (Ari J. Green *et al.*, 2017). Conversely, other organs such as the liver allow for regular biopsies, permitting long-term follow-up studies to be performed, such as one on non-alcoholic fatty liver disease (NAFLD) where they correlated biopsy-proven NAFLD with BMI to conduct a follow-up study ranging up to 40 years in length (Hagström *et al.*, 2018). We are therefore limited in our ability to follow the progression of the active disease in patients, and therefore rely on *in vitro* human or animal-derived cells, *ex vivo* animal model brain slices, or *in vivo* animal models to predict the clinical development.

1.6.1.5 Disease modelling

Another important factor hindering drug discovery in this therapeutic area is the lack of predictive animal models, making preclinical studies for efficacy less translatable at the clinical trial stage (Kola and Landis, 2004; Markou *et al.*, 2009). Unlike fields such as haematopoiesis which has benefited from humanised mouse models as a powerful tool to more accurately study diseases like leukaemia (Lysenko *et al.*, 2017), animal models in MS research, whilst they have been extremely valuable in contributing to our understanding of the disease, have been restricted to the ability to model only specific aspects of this complex disease. Multiple models of the demyelinating phase of MS are available, including the experimental autoimmune encephalomyelitis (EAE), virus-induced demyelination, and toxic models such as dietary administration of the copper chelator cuprizone for global demyelination and lysophosphatidylcholine (LPC) injection for focal lesion formation. However, EAE, the oldest animal model of MS, only recapitulates the autoimmune phase of the disease while being a poor

predictor of the remyelination phase in drug efficacy studies. The virus-induced model best represents demyelination following viral infection, such as encephalitis, but its pathogenesis does not accurately represent that of MS. Whilst the toxic models allow remyelination to be modelled, and allows the timing of both demyelination and remyelination to be controlled more precisely, the complexity of the cuprizone model makes interpretation of the responses of the various cell types involved more difficult, and is limited in applicability to certain breeds and genders of mice with female mice in certain strains being resistant. The LPC injection model, whilst having been valuable in examining cellular and molecular determinants of remyelination and allows precise control of the location of focal demyelination, does not recapitulate the ongoing immune activity seen in MS with its single dose of injection for lesion formation (Denic *et al.*, 2011; Plemel, Liu and Yong, 2017; Ransohoff, 2012). There is therefore no "magic bullet" animal model that can fully recapitulate all aspects of complex and heterogeneous diseases as described here for MS but are common patterns in other brain disorders. Each of the currently available animal models for brain disorders must therefore be selected for their value in studying the aspect of the disease that they are able to represent, and the compound of interest studied in this model within the perspective of the purported therapeutic use (Markou *et al.*, 2009), whilst needing to acknowledge their limitations in clinical translation in making successful drug discovery for brain disorders more difficult.

One of the methods to overcome the limitations in the availability of clinically representative models of the brain in drug discovery is the development of physiologically-relevant *in vitro* models. For example, as also discussed later, the advancements in stem cell technology has allowed human OPCs to be modelled *in vitro* using human ESCs (Wilson, Onischke and Raine, 2003; Biswas *et al.*, 2019) and human iPSCs (Livesey *et al.*, 2016; Ehrlich, Mozafari, Glatza, Starost, Velychko, A.-L. Hallmann, *et al.*, 2017; Rodrigues *et al.*, 2017a; Biswas *et al.*, 2019), with patient-derived iPSCs allowing patient-specific disease mutations to be studied *in vitro* (Livesey *et al.*, 2016). However, the two-dimensional nature of these cell cultures limit their applicability in understanding the three-dimensional interactions between the various cell types present in the CNS. Brain

organoids, which are three-dimensional aggregates that resemble the cell type population and cytoarchitecture of human embryonic brains, have added a valuable layer of *in vitro* complexity to our ability to mimic brain structures *in vitro* whilst overcoming the species differences of using animal models (Qian, Song and Ming, 2019). For example, Choi *et al.* (2014) were able to form human neural stem cell-derived three-dimensional cultures with familial Alzheimer's disease (fAD) mutations in β-amyloid precursor protein and presenilin 1 that recapitulated both the extracellular amyloid β plaque formation and phosphorylated tau aggregates and filaments, the two key pathological features of AD. In previous models of fAD, the amyloid β plaques and neurofibrillary tangles were not seen in 2D AD patient-derived neurons despite the presence of toxic amyloid β and phosphorylated tau (Choi and Tanzi, 2012; Israel *et al.*, 2012), and mouse models represented the amyloid β pathology and behavioural memory deficits, whilst lacking the neurofibrillary tangle pathology (Chin *et al.* 2010). Accumulatively, the developments in stem cell technology and *in vitro* 3D modelling will advance our ability to model brains "in a dish" to study them in physiologically- and disease-relevant cellular models.

Despite their advantages over non-human cell models, neither 2D nor 3D *in vitro* human cell models are able to fully recapitulate the complexity of the whole organism as with *in vivo* animal models, whilst many of these models only represent aspects of the complex human brain disorders, such as MS rodent models primarily inducing an inflammatory response to cause demyelination as described above. However, this only represents one aspect of the neuropathology of MS and assumes the "outside-in" hypothesis as the cause of demyelination, with the absence of remyelination being another important aspect to be able to model *in vivo*. Shiverer mice have an autosomal recessive mutation that results in the lack of MBP, and therefore the inability to form compact myelin in the CNS, with a shivering phenotype being visible in the mutant animals (Molineaux *et al.*, 1986; Readhead and Hood, 1990). Differentiated human cells, such as neural stem cells derived from iPSCs differentiated into OLs (Biswas *et al.*, 2019), are able to be transplanted into these shiverer mice to study whether they are able to form compact myelin sheaths *in vivo* when no endogenous myelination should be present. The

transplantation of human neural stem cells into shiverer-immunodeficient mice have shown preferential differentiation into OLs, which formed functional compact myelin with normal nodal organisation and physiological properties (Uchida *et al.*, 2012). The combination of the human-derived OLs and the *in vivo* animal model provide an approach that both combines being able to study and model myelin sheath formation by human OLs prior to the end-stage of the disease as seen in post-mortem human tissue and the lack of an *in vivo* system to be able to study the role of OLs in a hypomyelinating environment.

Just how significant the problem of poor models of disease-relevant cells may be in contributing towards the poor drug discovery rates in discovering treatments for the remyelination phase of MS is clear from the work of Scannell and Bosley (2016). These authors constructed a quantitative classifier model (**Figure 1.12**) that represents the predictive validity (PV) of a model in decision-making. The decision threshold, y_t, is a measure of the throughput, attrition rate, and rigor of the decision-making, and molecules that exceed the decision threshold classified as a positive hit for further investigation, with the higher the threshold value, the more compounds need to be screened (i.e. increased throughput) for each hit. A hit is only a true positive if it also surpasses the reference threshold r_t on the reference variable R. As represented in these models, a good model will yield a better ratio of true positives, with fewer false positive hits costing more R&D costs, and fewer losses as false negatives, whereas worse models have lower predictive validity and therefore detect fewer true positives, with more false positives and false negatives. The positive predictive value, PPV, is a measure of decision quality in R&D, calculated as PPV = $\frac{\#TP}{\#TP+\#FP}$ = 1 – FDR, where # represents number of, and FDR stands for false discovery rate. Thus maximising of PPV reduces the cost of the R&D process per each therapeutic candidate, with better models with higher PV and/or the application of high y_t thresholds to increase throughput resulting in higher PPVs.

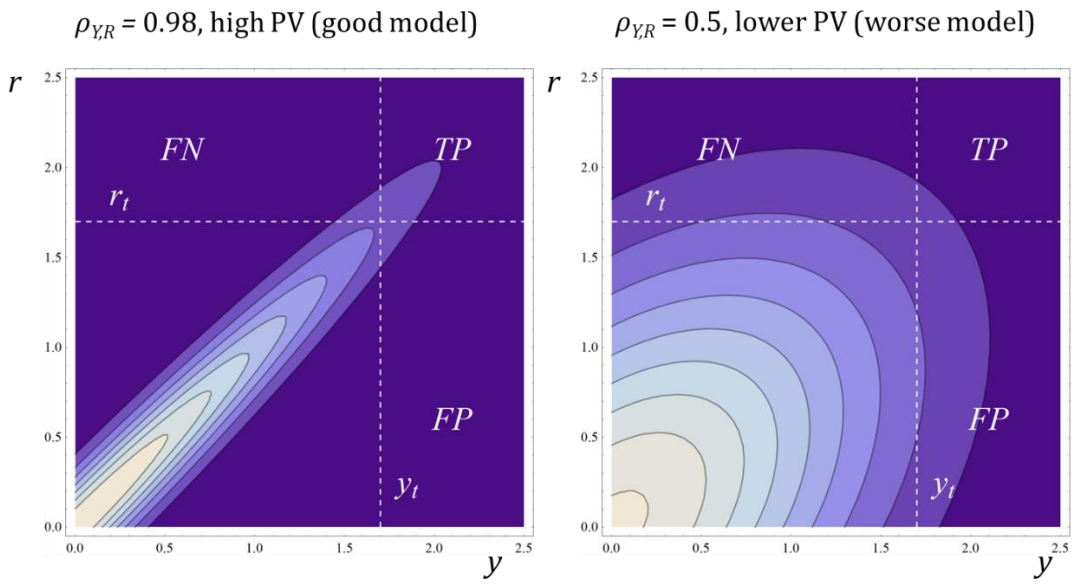

Figure 1.12 The quantitative classifier model

Probability density function diagrams based on the correlation, $\rho_{Y,R}$, between the decision variable Y, the measure on which the classification decision is based, and reference variable R, the test of the performance of the decision process. The colours indicate probability density of candidate molecules, with light being high and dark being low. The axis units are one standard deviation, and the y_t and r_t are decision and reference thresholds, respectively. PV is the predictive validity, calculated as the Pearson correlation coefficient between Y and R in this model.

TP = true positives, FP = false positives, and FN = false negatives

(Figure from Scannell and Bosley (2016))

Scannell and Bosley (2016) and Horvath *et al.* (2016) also predict the continued presence of poor disease models with low PVs in diseases that represent major global health problems and urgent areas of unmet medical need, and the interest in such reductionist models for simplicity, ease of use, "tradition", and 'brute-force' efficiency. The validation of good reductionist models requires time, effort, innovation, and "guess-work" to verify they fit within "domains of validity", a term used in physics to refer to the parameter in which a model is valid, resulting in the reluctance in their adoption despite the potential for improved clinical relevance and success. The development, verification, and use of 3D cell-based models of disease provides additional challenges to overcome in comparison to

the relatively simpler 2D models (Horvath *et al.*, 2016; Carragher *et al.*, 2018), including increased cost, sample processing, imaging, data generation and storage, and analysis. However, with the continuing development of better high-throughput liquid-handling machines, more 3D-compatible high content imaging platforms and analysis software, and the decreasing cost and improved capacity for larger datasets, along with the continued poor success at discovery of pro-remyelination treatments for progressive MS, there is a need to overcome the 'basic research-brute force' bias and improve the *in vitro* cell model for MS.

1.6.2 The challenges of extrapolating from animal-based studies to human disease

1.6.2.1 Limitations of cell culture approaches

Stem cell technology has allowed us to model human OPCs *in vitro* using human embryonic stem cells (ESCs) (Biswas *et al.*, 2019; Wilson, Onischke and Raine, 2003) and human induced pluripotent stem cells (iPSCs) (Biswas *et al.*, 2019; Ehrlich *et al.*, 2017; Livesey *et al.*, 2016; Rodrigues *et al.*, 2017), and therefore overcome the constraints of limited access to human OLs in research. These human cell-derived OPCs have been shown to have similar properties to rodent-derived ones, such as the markers expressed (Livesey *et al.*, 2016; Wilson, Onischke and Raine, 2003), the growth factors that promote maturation (Wilson, Onischke and Raine, 2003), and their physiological characteristics such as the expression and activity of electrophysiological channels and receptors (Livesey *et al.*, 2016). Patient-derived iPSCs can also be cultured, allowing disease-relevant mutations to be studied *in vitro* (Livesey *et al.*, 2016), human OPCs genetically manipulated using techniques such as CRISPR/Cas9 (Rodrigues *et al.*, 2017b) and retroviral vectors (Biswas *et al.*, 2019), and the ability to produce these human iPSC-derived OPCs in a defined, efficient, and scalable manner means that they may be suitable for high-throughput screens for drug discovery (Ehrlich *et al.*, 2017; Rodrigues *et al.*, 2017b). These human cell-derived stem cells are therefore highly valuable in studying and understanding the role of OLs in biology and disease in a controlled and defined environment *in vitro*. However,

despite these invaluable benefits as technical and biological tools in studying diseases such as MS, they are poor models for studying the complexity of the disease *in vivo*, limited by the nature of their development in a strictly defined and artificial environment in cell culture. It is therefore important to not over-estimate the conclusions drawn from cell culture studies, and put them in the wider context of the disease using methods such as those described below.

1.6.2.2 Limitations of post-mortem human brain tissue pathology

Access to post-mortem human brain tissue has allowed us to develop an understanding of the pathology of MS in the context of human disease rather than within the scope and limitations of animal models, with findings such as the quantification of the heterogeneity of MS lesions (Lucchinetti *et al.*, 1999), and the presence of quiescent OPC populations (Wolswijk, 1998) and differentiated but non-myelinating oligodendrocytes (Ansi Chang *et al.*, 2002) in chronic lesions. Brain Banks have been instrumental to the collection, classification, preservation, and distribution of post-mortem human brain tissue samples for researching diseases of the nervous system in an ethically and legally regulated manner (Ravid, 2008).

The histological classification system for MS lesions in post-mortem human brain tissue have been described initially by Lucchinetti *et al.* (2000), and more recently in an updated version by (Kuhlmann *et al.*, 2017). (Lucchinetti *et al.*, 2000), following on from observations of distinct patterns and heterogeneity in MS pathology (Lucchinetti *et al.*, 1996), defined 4 distinct patterns of demyelination based on myelin protein loss, the size and shape of the plaque, the pattern of demyelination, and the immunological response. They described Patterns I and II of suggesting T-cell and T-cell and antibody-mediated autoimmune pathology, and Patterns III and IV of being primary OL damage (**Figure 1.13** A). The more recent (Kuhlmann *et al.*, 2017) classification combines the inflammatory activity based on macrophages/microglia (**Figure 1.13** B) with the demyelinating activity present in lesions to propose a more unifying classification system, as summarised in **Figure 1.13** C. In short, active lesions

contain macrophages/microglia throughout the lesion, whereas mixed active/inactive lesions compose of a hypocellular centre and border of macrophages/microglia, with inactive lesions lacking these inflammatory cells. Active and mixed active/inactive lesions are further classified based on the degree of demyelination. These classifications highlight the lack of consensus within the field when studying neuropathology using post-mortem human brain tissue in determining the lesion types being analysed. Further complications arise due to: (1) post-mortem tissue sample preparation, (2) their strong bias as end-stage disease tissue, and (3) limitations due to the lack of markers to study MS pathology.

A

Feature	Pattern I	Pattern II	Pattern III	Pattern IV
Inflammation				
Composition of Infiltrates				
CD3 T cells	197 ± 68	133 ± 18	145 ± 23	134 ± 71
Plasma cells	5.9 ± 1.9	9.3 ± 2.1	5.4 ± 1.6	3.8
Macrophages	1,158 ± 105	931 ± 71	842 ± 91	1,650 ± 30
C9neo	–	++	–	–
Demyelination				
Perivenous pattern	+	+	–	±
Lesion edge	Sharp	Sharp	Ill-defined	Sharp
Concentric pattern	0/10	0/45	8/25	0/3
Oligodendrocytes				
#OG in DM	295 ± 73	249 ± 30	51 ± 24	55 ± 55
DNA frag in OG	±	±	++APO	++PPWM
OG apoptosis	–	–	14–37%	–
Myelin protein loss	Even	Even	MAG ≫ Others	Even
Remyelination				
Shadow plaques	++	++	–	–

B

	Macrophages/microglia throughout lesion	Only macrophages/microglia at lesion border	LFB+ or MBP+ or PLP+ degradation products within macrophages/microglia	CNP+ or MAG+ or MOG+ degradation products within macrophages/microglia
Active	+	–	±	±
Active and early demyelinating	+	–	+	+
Active and late demyelinating	+	–	+	–
Active and post-demyelinating	+	–	–	–
Mixed active/inactive	–	+	±	±
Mixed active/inactive and demyelinating	–	+	+	±
Mixed active/inactive and post-demyelinating	–	+	–	–
Inactive	–	–	–	–

C

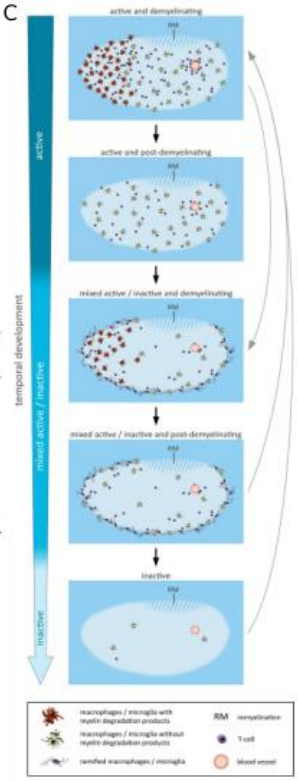

Figure 1.13 Tables of MS lesion classifications

A. Features of different patterns of active MS lesions, with values given as cells/mm^2.

#OG = density of OLs in inactive demyelinated plaque centre, DNA frag in OG = OLs showing nuclear DNA fragmentation, OG apoptosis = OL apoptosis in active lesion, MAG = myelin-associated proteins, PPWM = DNA fragmentation in OLs in periplaque WM

Table from Lucchinetti *et al.* (2000)

B. Histological characteristics of various MS lesion types.

LFB = luxol fast blue, MBP = myelin basic protein, PLP = proteolipid protein, CNP = 2',3'-cyclic-nucleotide 3'-phosphodiesterase, MOG = myelin oligodendrocyte glycoprotein

Table from Kuhlmann *et al.* (2017)

C. Schematic diagram of the temporal development of MS lesions starting from active demyelinating to inactive. The re-introduction of subsequent waves of macrophages/microglia may result in a mixed active/inactive or inactive lesion to become active again.

Figure from Kuhlmann *et al.* (2017)

1.6.2.2.1 Post-mortem tissue sample preparation

Due to the nature of the tissue sample collection happening after death, there are numerous factors that contribute to the quality, or lack thereof, of the samples. For example, pre-mortem events that prolong damage to the brain during the process of death, like an inflammatory response, hypoxia, or fever, may result in non-neurodegenerative disease-related injury to the sample collected. Post-mortem delays between death and sample collection, which varied as widely as just under 4 hours to close to 10 hours in Wolswijk (1998)'s paper, the temperature of storage of the cadaver and the removed brain samples, and the methodological framework and solutions used in the preservation of the sample, like the fixative used or variability in the process of freezing, may contribute towards post-mortem degradation of the brain samples. Unpredictable case-to-case and brain region-to-region variability despite otherwise similar parameters of preservation further complicate and limit the accurate analysis of post-mortem human brain tissue (Ferrer *et al.*, 2008).

1.6.2.2.2 End-stage disease

In addition to the variability in tissue quality, due to the nature of the timing of the sample collection being post-mortem, the samples that can be studied are end-stage tissue of predominantly chronic lesions (Wolswijk, 1998; Ansi Chang *et al.*, 2002). Furthermore, these tissue samples, although extremely valuable in our ability to study and understand the disease in human patients, only provide a single time snapshot of the disease at the moment of death of the patient donor, making it difficult to infer the processes involved in disease progression. For example, 8 out of the 10 patients and lesions studied in Chang *et al.* (2002)'s paper were of secondary progressive patients with the duration of disease ranging from 9 to 44 years, and only 1 patient having relapsing-remitting MS with less than 1 year since disease diagnosis, and therefore the study being representative of mostly late-stage MS. As the proportion of lesions with pre-myelinating oligodendrocytes appeared to decrease with an increase in the duration of disease in this small sample of MS patients, the limitations in being able to focus on only one time-point of the disease progression is highlighted as it is not possible to study whether there are changes as the disease progresses that makes chronic lesions less favourable to the presence of pre-myelinating oligodendrocytes, or whether this difference is due to patient heterogeneity. Although it is possible to obtain brain biopsies at earlier stages of the disease progression, such as in Lucchinetti *et al.* (1999)'s paper, the highly invasive nature of obtaining biopsies from the brain compared to other organs, such as the liver or kidneys, means that it is rare to be able to obtain samples in this manner, almost impossible to repeat at different time-points of the disease due to practical and ethical reasons, and the influence of the medical condition that led to requiring a biopsy cannot be excluded in whether a sample is appropriate to include in the analysis.

1.6.2.2.3 Lack of markers

A significant contributor to the difficulty in understanding and classifying post-mortem human brain tissue is the limited number of markers available. These are broadly limited to histological dyes with low resolution and non-specific for markers, such as Luxol Fast Blue (LFB) to stain for myelin (Lucchinetti *et al.*, 1999), or *in situ* hybridisation and immunohistochemistry with antibodies that are specific for markers that distinguish between OPCs, such as NG2 (Wolswijk, 1998; Ansi Chang *et al.*, 2002) and, more commonly, Olig2+ (marker for all OL lineage cell bodies) NogoA- (more mature OL cell bodies) cells (Kuhlmann *et al.*, 2017), and differentiated OLs that are both non-myelinating and myelinating, like PLP and MBP (Wolswijk, 1998; Lucchinetti *et al.*, 1999), with MOG, MAG, and CNP being helpful in determining early or late lesion formation (Kuhlmann *et al.*, 2017), which limit the ability to distinguish between the various stages of OL development. Recent advances in RNA sequencing techniques have expanded our ability to study the heterogeneity of the oligodendrocytes present within human MS brain tissue while overcoming the limitations of restricted markers available, as discussed below.

The difficulty in analysing post-mortem human brain tissue is highlighted by the ^{14}C-dating research, published by the Frisén Lab in *Nature* in 2019 (Maggie S. Y. Yeung *et al.*, 2019). In their paper, they measured the integration of ^{14}C into DNA, as correlated to the changes in atmospheric levels due to historic nuclear testing, to assess oligodendrocytes in post-mortem multiple sclerosis patient brain samples. They concluded that in “shadow plaques”, regions where thin myelin sheaths from remyelination have formed following demyelination, the ^{14}C levels indicate that the oligodendrocytes present were not newly formed, suggesting that remyelination occurs due to pre-existing oligodendrocytes forming new myelin sheaths in MS lesions. This understanding of the dynamics of oligodendrocyte generation may have had significant consequences for remyelination therapies in drug discovery, as this would suggest that pro-remyelination drugs would have to predominantly, if not solely, promote myelin sheath formation to be of therapeutic value in MS, rather than a combination of enhancing differentiation and myelination. However, more recent views in the field suggest that the “shadow plaques” studied in the post-mortem brain

samples in this paper may potentially have been sites of cerebral oedema, and therefore not be sites of demyelination and subsequent remyelination, which may explain why no newly formed oligodendrocytes were present. This emphasises the difficulty in assessing post-mortem brain tissue, even by researchers with experience and expertise, in classifying the types of lesions present accurately.

1.6.2.2.4 Caveats of single-nucleus RNA sequencing of post-mortem human brain tissue

As mentioned previously, recently, Jäkel *et al.* (2019) were able to perform single-nucleus RNA sequencing (snRNA-seq) on the WM of post-mortem human brain tissue of both control and progressive MS patients using the Chromium 10x Genomics and Illumina next-generation sequencing pipeline. They were able to isolate nuclei from NAWM, active, chronic active, chronic inactive, and remyelinated lesions within the WM of the same MS patient, and identify several clusters and subclusters of cells types, including seven subclusters of OLs and clusters of OPCs and committed oligodendrocyte precursors (COPs). Using this method, they were able to compare the proportion of the various OL lineage cell populations and subclusters in MS compared to control brains, including a reduction in the intermediate Oligo6 cells and the skewing in the subclusters of mature OLs. Although the same limitations in tissue preservation and quality as when analysing neuropathology still apply, with additional variables in the preservation of the integrity of RNA (Ferrer *et al.*, 2008), as well as the samples representing a single time-point end-stage disease state, snRNA-seq avoids the need for existing markers to identify the different populations of the OL lineage cells and therefore allows the exploration of the wider scope of the heterogeneity of the various stages and subclusters of OL development. In addition, the use of sequencing technology has allowed differential gene expression analysis to be performed in the context of disease, and opens up the potential to be used to classify lesion types through the detection of unique biological markers, which may also improve clinical accuracy in diagnosing patients beyond research purposes. Although immunohistochemistry and *in situ* hybridisation is still the gold standard in confirming the results obtained in this

novel application of snRNA-seq for the neuropathological analysis of MS, this technology provides great promise in enhancing our ability to understand the human disease without being restricted to available markers. Through this identification of new markers and increasing our understanding of the transcriptional profile differences of the various subclusters of OLs, snRNA-seq also has the capability to improve the relevance of neuropathological analysis of post-mortem human brain tissue and the application of human stem cell cultures in human MS research.

1.6.3 Which cell type drives remyelination - OPCs or OLs?

The clearest evidence as to the difficulties of extrapolating from animal models to human disease comes from the ongoing debate as to whether myelin sheaths in human remyelination are formed by differentiating OPCs or differentiated OLs. There is conflicting evidence, with the traditional view based on animal work being that once myelin sheaths have formed, these OLs becomes structurally fixed. In supporting this, gene expression profiling of neonatal and adult mice OPCs suggest that following demyelination, the activated OPCs revert to an immature neonatal-like state (Moyon *et al.*, 2015), suggesting priming to enhance their contribution to the regenerative process of remyelination. In addition, fate map tracing of OPCs in transgenic mice (Zawadzka *et al.*, 2008) and tamoxifen-induced YFP expression in OPCs in the EAE model (Tripathi *et al.*, 2010) suggest that it is the OPCs that populate lesions and differentiate to form the new myelin sheaths in remyelination. Membrane-bound GFP labelled mature OLs in a focal demyelinating mouse model also showed no evidence of the mature OLs contributing to remyelination (Crawford *et al.*, 2016).

However, in both complementary models of a food-induced demyelination in cats and the spinal cord of B_{12}-deficient rhesus monkey with extensive demyelination but OL survival, evidence of adult OLs ensheathing axons and remyelinating were observed (Duncan *et al.*, 2018). Also, constitutive activation of Akt in the PI3K-AKT-mTOR pathway (Flores *et al.*, 2008), sustained activation of ERK1/2 in pre-existing OLs (Jeffries *et al.*, 2016), optogenetic stimulation of

axonal activity (Gibson *et al.*, 2014), and social re-integration and enrichment following social isolation (Liu *et al.*, 2012) all show increase in myelin formation, mainly in increased myelin thickness. This adaptive myelination in differentiated OLs suggest that these myelinating OLs are not as fixed as conventionally thought, and therefore potentially may be able to show plasticity in remyelination. Recently, the changes in atmospheric carbon-14 (^{14}C) integration into genomic DNA due to nuclear bomb testing during the Cold War was used to assess the dynamics of OL generation in shadow plaques of MS. The ^{14}C levels in the OLs of these remyelinated lesions suggested that the OLs present were pre-existing OLs, rather than new ones (Yeung *et al.*, 2019). Although caution must be taken in interpreting such data, especially due to questions about ^{14}C incorporation and stability of their levels over time, as well being able to interpret their levels with such precision across relatively short time scales, this data suggests that there is potential for remyelination to occur from pre-existing OLs, rather than direct differentiation and myelination by new OLs.

1.7 Current phenotypic cell-based drug screens for regenerative and remyelination therapies.

The studies reviewed thus far have informed us that in order to increase myelin sheath formation as a therapeutic strategy for progressive multiple sclerosis, we need to target increasing myelination directly rather than relying on increasing differentiation. In order to be able to study myelin sheath formation directly, two main challenges need to be addressed: (1.7) creating a system that enables myelination to be studied *in vitro*, and (1.8) imaging the myelin sheath formation. The strategies to tackle these two issues will be addressed in the next two sections.

1.7.1 Two-dimensional cultures

1.7.1.1. Single oligodendrocyte cultures

Oligodendrocytes can be purified and cultured in isolation, allowing for well-defined cell populations to be studied *in vitro*. For example, from the rat cerebral cortex, oligodendrocytes can be isolated using an orbital shaker for mechanical purification from mixed glial cultures prepared from animals of or less than postnatal 2 days (P2) of age with >95% purity (**Figure 1.14** A) (McCarthy and de Vellis, 1980), or by immunopanning using a series of negative selections against contaminating cells and positive selection using O4 for OPCs using P7 animals for a purer population (**Figure 1.14** B) (Barres *et al.*, 1992a; Foo *et al.*, 2011), among other techniques such as fluorescence-activated cell sorting (McMorris *et al.*, 1986; Behar *et al.*, 1988). These isolated OPCs, in the absence of axons, extend flat 2D membranes, and express markers of differentiated OLs, such as MBP, allowing them to be valuable in the study of compounds that increase the rate of differentiation, like using rat optic-nerve-derived progenitor cells by Deshmukh *et al.* (2013), mouse epiblast stem cell (EpiSC)-derived OPCs by Najm *et al.* (2015), and using O4 immunopanned OPCs by Lariosa-Willingham *et al.* (2016). Although the simplicity of this model is of great value to the field, with differentiation drug screens culturing OPCs being able to be performed in under 7 days (Deshmukh *et al.*, 2013; Lariosa-Willingham *et al.*, 2016; Najm *et al.*, 2015), the lack of myelin sheath formation limits their physiological representation and their applicability to look beyond OPC proliferation, migration, survival, and differentiation in OPC development.

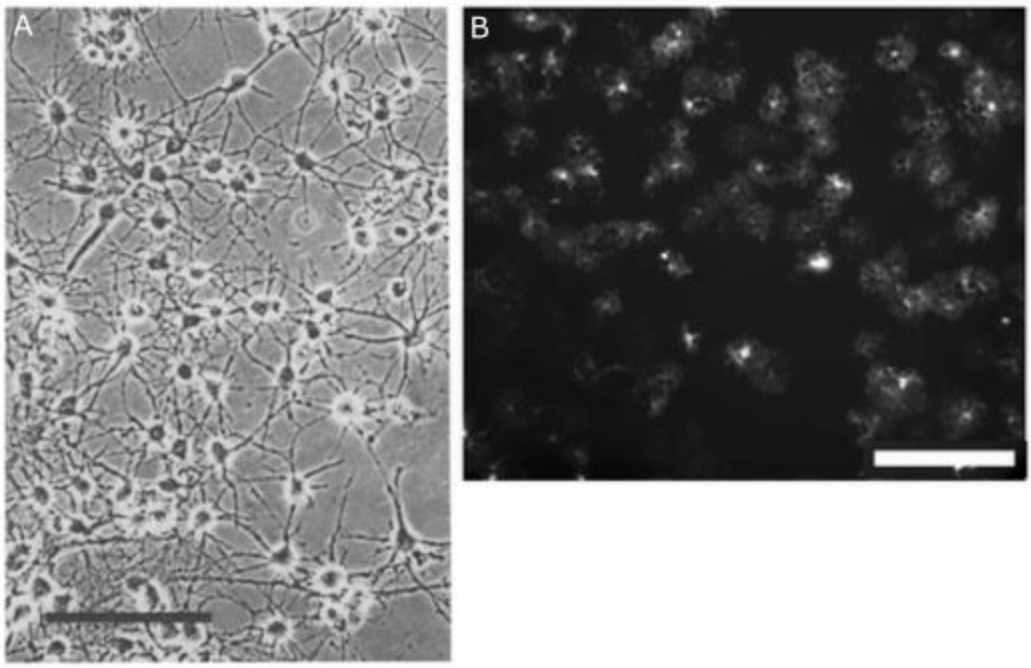

Figure 1.14 Isolated two-dimensional oligodendrocyte cultures

A. Phase contrast image of oligodendrocyte culture isolated using the mechanical shaking method.

   Scale bar = 50µm

   Figure from McCarthy and de Vellis (1980)

B. Immunofluorescence image of oligodendrocyte culture isolated using the O4 immunopanning method and cultured in the presence of T3 for 4 days.

   Scale bar = 200µm

   Figure from Lariosa-Willingham *et al.* (2016)

1.7.1.2 Myelinating cultures

Neurons, such as dorsal root ganglion cells (DRGs) (Svenningsen *et al.*, 2003; Wood, Okada and Bunge, 1980) and retinal ganglion cells (RGCs) (Goldberg *et al.*, 2004), can be isolated from embryonic or postnatal rodents and cultured with separately isolated OPCs in myelinating co-cultures (**Figure 1.15**). The use of neuron-oligodendrocyte co-cultures have been instrumental to studying myelin

sheath formation, like the signals involved, i.e. the role of integrin and contactin in controlling Fyn activity in regulating myelination (Laursen, Chan and ffrench-Constant, 2009), the role of neuronal activity, such as glutamate released through synaptic vesicles on axons increasing myelination also through a Fyn kinase-dependent signal (Wake, Philip R. Lee and Fields, 2011), and mechanical stimulation by the axon influencing the fate of the OLs (Rosenberg *et al.*, 2008). Although valuable in allowing us to study myelin sheath formation *in vitro*, the technical challenges from the low yield of neurons in the co-cultures (Lariosa-Willingham *et al.*, 2016b), as well as the inability to separate the effect of compounds on axons and OLs limit their applicability for our purposes.

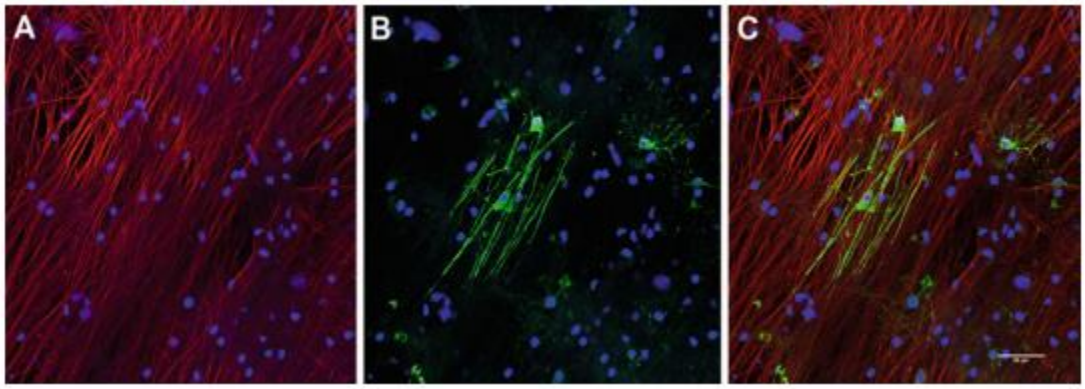

Figure 1.15 DRG-oligodendrocyte myelinating co-cultures

A. DRG neurons (red)
B. MBP-expressing oligodendrocytes (green)
C. Overlay of OLs myelinating DRG neurons.

Scale bar = 50µm

Figure from Swire and ffrench-Constant (2019)

More complex myelinating cultures have also had significant contributions to our ability to study the interactions of OLs with neuronal and other non-neuronal cells *in vitro.* For example, primary embryonic (E18) rat cortical cells have been shown to be compatible in a 96-well plate format for high-throughput screening for the detection of promoters of myelination (Lariosa-Willingham *et al.*, 2016b),

and E13 mouse spinal cords shown to recapitulate *in vivo* electrical and microglia phagocytosis activity as well as being compatible with adaption into a 96-well plate format for screens (Bijland *et al.*, 2019). Despite the value of these heterogenous myelinating cultures in more accurately depicting the interactions between the various cell types *in vivo*, the difficulty, as with the neuron-OL co-cultures, in extricating the cell types through which pro-myelination effect may be occurring, and the risk of variability in the proportion of the various cell types present in each isolation, may restrict our ability to understand the mechanism through which potential pro-remyelination compounds are having their effect, and their applicability in high-throughput formats to screen for compounds.

1.7.2 Three-dimensional cultures

1.7.2.1 Single oligodendrocyte cultures

Three-dimensional cultures may allow us to study the oligodendrocyte-specific effects of compounds in the absence of neuronal influences whilst also studying beyond differentiation into their effects on myelination. One such assay developed for screening is the 'binary indicant for myelination using micropillar arrays', or BIMA (Mei *et al.*, 2014a). In this system, cones, or micropillars (**Figure 1.16** A), made out of silica were compressed into a 96-well plate format. These micropillars are representative of freestanding fibres, which are described below, around which immunopanned O4+ rodent OPCs could wrap their concentric membranes as a "binary indicator" for myelin sheath formation (**Figure 1.16** B) in a method that is high content-compatible for imaging (**Figure 1.16** C) and analysis. Although they described that the MBP+ membrane were thicker than the PDGFRα+ membrane, suggesting increased wrapping with differentiation, as can be seen on **Figure 1.16** C, both OPCs and OLs form rings around the micropillar, and therefore making their expression of PDGFRα versus MBP the main output to detect pro-differentiation compounds. Although the BIMA platform has increased our ability to study compounds that increase OPC differentiation in a more 3D nature in an OPC-specific manner, due to it still

quantifying the extension of membrane across a surface rather than the formation of multiple complex myelin sheaths by a single OL, there is a limit to its applicability as a myelination assay rather than a differentiation one.

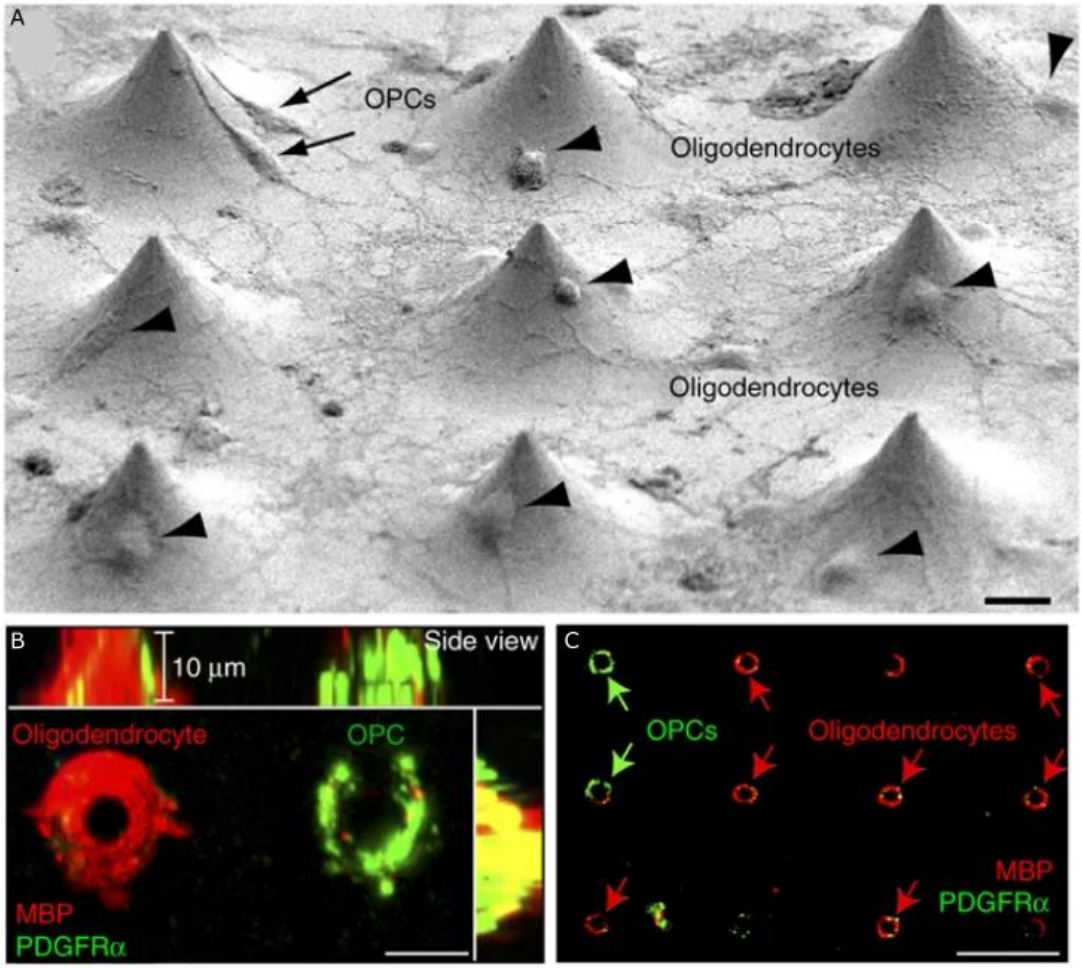

Figure 1.16 The Binary Indicant for myelination using Micropillar Arrays (BIMA)

A. SEM image of OPCs and OLs interacting with and wrapping the micropillars. Arrows indicate multiple OPCs interacting with a single micropillar, and arrowheads indicate OLs interacting with a single micropillar.

   Scale bar = 10µm

B. Compressed z-stack image and orthogonal views of an MBP+ OL and PDGFRα+ OPC obtained using the Zeiss LSM-700 confocal microscope.

   Scale bar = 10µm

C. PDGFRα-positive green OPCs and MBP-positive red OLs interacting with micropillars, imaged using the Zeiss microscope, and visualised in 2D from a compressed z-stack image to view the rings from the membrane wrapping.

Scale bar = 25µm

Figures from Mei *et al.* (2014)

1.7.2.2 Organoids

Organoids or spheroids allow the 3D environment, including spatial complexity, between CNS cell types to be replicated *in vitro*. These 3D structures are formed from the aggregation of dissociated neuronal cells under constant rotation, and have been shown to recapitulate some of the patterns of biochemical differentiation as *in vivo* such as with acetylcholine activity in embryonic mouse reaggregates (Seeds, 1971), and be used to study demyelination and remyelination *in vitro* using anti-MOG, IFNɣ, or LPC-induced demyelination in rat-derived spheroid cultures (Diemel *et al.*, 2004; Loughlin *et al.*, 1994; Vereyken *et al.*, 2009) including the influence of macrophages on the remyelination process (Diemel *et al.*, 2004; Loughlin *et al.*, 1994). More recently, human organoids with myelinating oligodendrocytes, including oligocortical spheroids (**Figure 1.17** A and B) (Madhavan *et al.*, 2018), human oligodendrocyte spheroids also containing neurons and astrocytes (Marton *et al.*, 2019), forebrain organoids with OLIG2/GFP reporter lines (Kim *et al.*, 2019), have been described that have been derived from human pluripotent stem cells. Oligocortical spheroids especially addressed the lack of OPCs and oligodendrocytes in the previously established neurocortical spheroids by treating the spheroids with PDGF-AA, IGF-1, and T3 at various stages of the spheroid development (**Figure 1.17** C), and could recapitulate the disease phenotype of the subject from whom the spheroid was generated (Madhavan *et al.*, 2018).

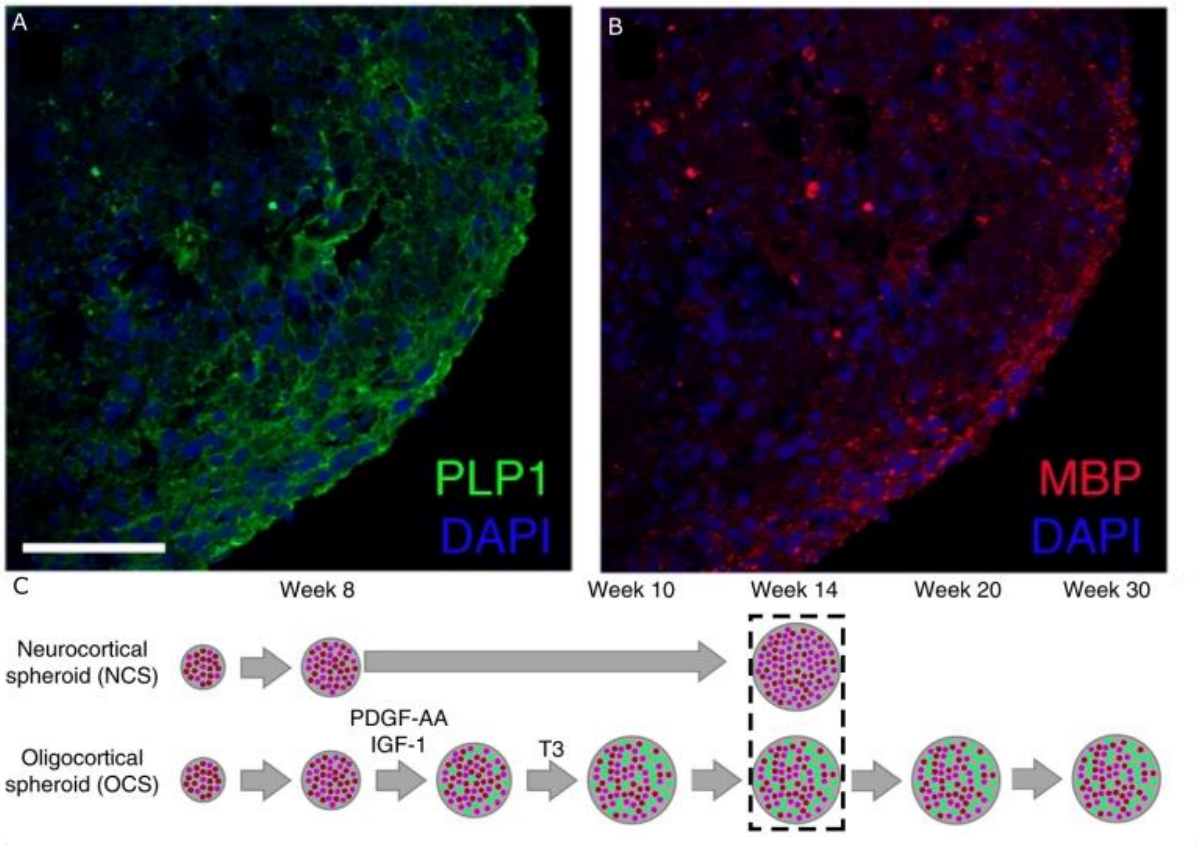

Figure 1.17 Generation of human oligocortical spheroids

A. and B. Fluorescent images of Week 20 oligocortical spheroids expressing mature OL markers.

Scale bar = 50µm

C. Schematic of neurocortical and oligocortical spheroid generation, including the adaption to the culture media required to increase the OPC/OL generation. PDGF-AA and IGF-1 treatment were from days 50 to 60, and T3 from days 60 to 70.

Magenta = neurons, red = astrocytes, green = OPCs/OLs

Figures from Madhavan *et al.* (2018)

These organoids provide a platform for investigating cellular interactions and organisation of oligodendrocytes in a more physiologically-relevant 3D structure *in vitro*, which are accessible to exposure to experimental conditions due to their spherical shape and small diameter, without the need for *in vivo* animal models which limit the number of conditions that can be tested to one per animal

(Vereyken *et al.*, 2009). However, despite their ability to recapitulate the complexity of the physiologically-relevant *in vivo* system, the cellular composition of the spheroids can be varied (Diemel *et al.*, 2004), the influence of the other cell types, especially the neuronal cells required for myelin sheath formation, cannot be separated in understanding the mechanism of action of potential pro-remyelination therapies, and the complexity of miniaturising them makes them less compatible for high content purposes.

1.7.2.3 Neuron-free microfibre system

A method for studying myelin sheath formation in 3D without the need for neurons was described by (Lee *et al.*, 2012). In their paper, they substituted axons for biologically inert electrospun fibres made out of polystyrene and poly-L-lactic acid (PLA), to uncouple the effects of fibre diameter from axonal signals, with glass and vinyl fibres having previously been shown to also be permissive to myelination (Bullock and Rome, 1990; Howe, 2006). They showed that myelination occurs in the absence of axonal signalling, the diameter of the fibres influence oligodendrocyte behaviour (**Figure 1.18** A and B), and that these artificial axons can be used to study myelination with concentric wraps being formed around the fibres (**Figure 1.18** C and D). Bechler, Byrne and ffrench-Constant (2015) further showed evidence of complete ensheathment of electrospun PLA microfibres by the myelin membrane by confocal microscopy (**Figure 1.18** E) and electron microscopy, with distinct, multiple compact membranes clearly being evident after 14 days (**Figure 1.18** F). More importantly, they showed that: 1) the sheath lengths formed on these fibres were comparable to *in vivo* cortex distribution (Murtie, Macklin and Corfas, 2007), and 2) that differences in myelin sheath formation could be detected and quantified, such as between cortical vs. spinal cord, smaller vs. larger diameter, and PDL vs. laminin-coating of the fibres. The electrospun microfibre platform therefore provides a 3D *in vitro* system that is capable of distinguishing oligodendrocyte-specific mechanisms of myelin sheath formation in drug discovery without indirect axonal influences.

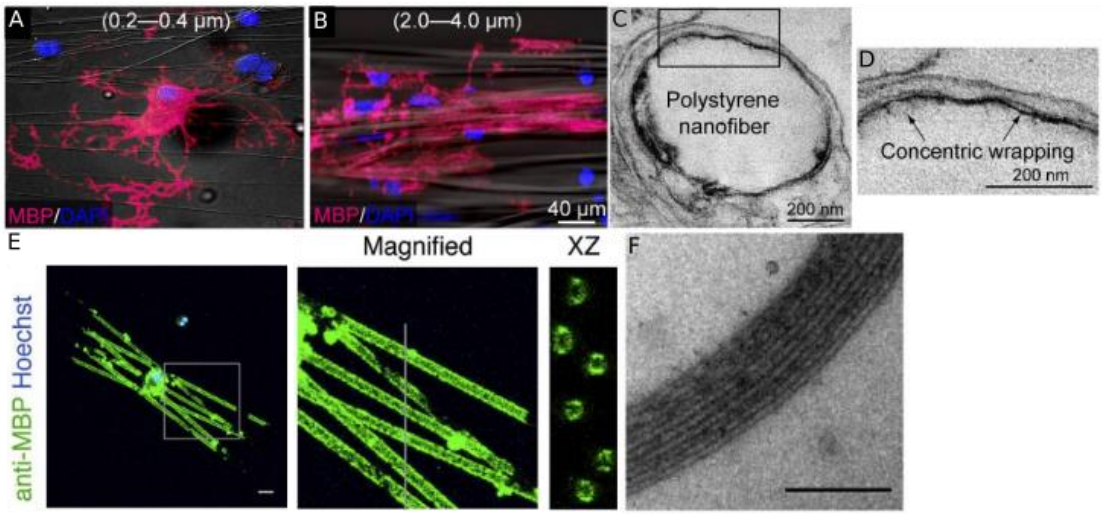

Figure 1.18 Myelin sheath formation on biologically inert electrospun microfibres

A. 0.2-0.4µm diameter fibres with differentiated but unmyelinating oligodendrocyte.

   Scale bar as shown on B.

B. 2-4µm diameter fibres with differentiated and myelinating oligodendrocyte.

   Scale bar as shown on figure.

C. Electron micrograph of an oligodendrocyte wrapping a polystyrene fibre.

   Scale bar as shown on figure.

   Figures A-C from Lee *et al.* (2012)

D. Higher magnificent image of the inset box from C) with concentric wrapping highlighted with arrows.

   Scale bar as shown on figure.

E. 1-2µm diameter fibre with a myelin sheath-forming oligodendrocyte. The magnified and cross-section (XZ) images show the wrapping of the myelin sheaths completely around the fibres.

   Scale bar = 10µm

F. Electron micrograph of multi-layered membranes formed by an oligodendrocyte around a microfibre after 14 days.

   Scale bar = 200nm

   Figures E-F from Bechler, Byrne and ffrench-Constant (2015)

However, neurons are not the only potential cell types that may have indirect effects on myelination, and contaminating astrocytes are present in oligodendrocyte microfibre cultures. As reviewed by Barnett and Linington (2013), astrocytes play a significant role in oligodendrocyte myelination and in MS. Bhat and Pfeiffer (1986), Noble *et al.* (1988), and Raff *et al.* (1988), and others have shown that astrocytes release mitogens and other factors that influence OPC self-renewal and differentiation, including PDGF. In fact, Sorensen *et al.* (2008) showed that myelin sheath formation, including the formation of nodes of Ranvier, from embryonic rat spinal cord-derived OL-CNS axon cultures were best when plated on a monolayer of neurosphere-derived astrocytes (NsAs) compared to a layer of olfactory ensheathing cells (OECs) or Schwann cells, and that conditioned medium from NsAs promoted myelination when the OL-axons were cultured on OEC monolayers. Although contaminating astrocytes are present in the neuron-free electrospun microfibre platform, and therefore indirect effects via mechanisms acting through these non-OL cell types cannot be completely excluded, the evidence seems to suggest that a low level of "contaminating" astrocytes may actually improve baseline myelin sheath formation. Although not completely free of contaminating cells, the electrospun microfibre platform provides an alternative *in vitro* 3D system to be able to study myelination in the absence of confounding axonal effects.

1.8 How we can image these different ways of examining myelination *in vitro*?

In order to conduct any screen for remyelination strategies, a microscopy technique with the capability to image and confirm the multi-layered wrapping and compaction of myelin sheaths is required. As described below, conventional optical imaging and electron microscopy techniques, for different reasons, are not suitable for these purposes, and therefore novel imaging strategies are required. I will now illustrate the strengths and weaknesses of the traditional methods of myelin imaging, including electron microscopy, histological dyes, confocal and super-resolution microscopy, and then go on to propose the nonlinear optical imaging technique of Coherent anti-Stokes Raman Scattering (CARS)

microscopy as the solution I tested, along with how an alternative technique, Spectral confocal reflectance microscopy (SCoRe), may also be appropriate.

1.8.1 Electron Microscopy

Electron microscopy (EM), which generates high resolution images by using electrons with very short wavelengths as the source of illumination, has been used to study the axonal components from as early as the 1940's with Richards, Steinbach, and Anderson looking at the axoplasm of the giant fibre of the squid in 1943 and de Robertis and Schmitt studying nerve types of various crustaceans, squid, amphibians, and mammals in 1948 (de Robertis and Schmitt, 1948), with Fernández-Morán first visualising the organisation of the myelin sheath layers using osmium tetroxide-fixed, freeze-sectioned tissue in 1950 followed by Sjöstrand using methacrylate-embedded thin sections for more detailed visualisation in 1953 (Mcalpine and Finean, 1961). EM still remains to this day the gold standard for myelin imaging for the acquisition of ultrastructural data, such as myelin thickness in detecting sites of remyelination in MS and relevant animal models, and confirm compact myelin sheath formation. As such, this technique has been used to study myelin-related mutations, such as in the transgenic shiverer mice where compact myelin is absent (Readhead and Hood, 1990), as well as the confirmation of myelin sheath formation in novel *in vitro* systems, such as for the micropillar array in showing myelin membrane extension and wrapping (Mei *et al.*, 2014b) and electrospun PLA microfibres in the confirmation of compact multi-layered myelin membrane formation around the polymer fibres (Bechler, Byrne and ffrench-Constant, 2015), and to study the maturation of oligodendrocytes in human cell-derived organoids (Madhavan *et al.*, 2018). Immunoelectron microscopy, an adaptation of the conventional EM technique, uses markers such as gold-conjugated antibodies to gain additional information about the abundance and localisation of the protein of interest (Weil *et al.*, 2019). Although the gold standard, the conventional sample preparation relies on chemical fixation, which results in artefacts that may be difficult to discriminate from the effects of the animal model mutation in the myelin

architecture being studied. The application of high-pressure freezing improves tissue preservation and decreases fixation artefacts, particularly due to the sensitivity of the lipid-rich myelin structure to chemical fixation, by freezing the tissue in milliseconds at 2000 bar pressure (Möbius, Nave and Werner, 2016; Weil *et al.*, 2019). Due to the highly intensive sample preparation (Weil *et al.*, 2019), as well as the low-throughput of the image acquisition speed, this technique is most suitable for detailed ultrastructural imaging of myelin.

1.8.2 Histological dyes

Another method of visualising myelin is through the use of histological dyes. Toluidine blue, or tolonium chloride, is an acidophilic (basic) thiazine metachromatic dye that was discovered in 1856 by William Henry Perkin. It selectively stains acidic tissue components, such as sulphates, carboxylates, and phosphate radicals, and therefore has a high affinity for nucleic acids. Its metachromatic property means that it is highly selective in the tissue structures that it stains, and absorbs light at different wavelengths depending on its surroundings and concentration due to the stacking of cations from the dye at the tissue where there are a high density of anionic groups. Toluidine blue staining allows the visualisation of individual myelinated nerve fibres in resin embedded semi-thin sections, with osmium tetroxide post-fixation improving the resolution of the image (Feirabend, Choufoer and Ploeger, 1998; Ghnenis *et al.*, 2018; Sridharan and Shankar, 2012). Luxol Fast Blue (LFB) is one of the most commonly used myelin histological dye discovered by Kluver and Barrera in 1953. It is a copper phthalocyanine dye that is attracted to the bases found in lipoproteins, and therefore stains myelin and myelinated axons on fixed and paraffin-embedded or frozen tissue sections in blue, although not to a single axon resolution (Scholtz, 1977; Ineichen *et al.*, 2017). Another example of a histological dye used to visualise myelin is sudan black, an oil-soluble dye that stains the lipid phase of myelin. It has been shown to distinguish myelin morphology and detect demyelinated versus remyelinated axons with comparable results to the gold standard histological dye toluidine blue but is less

labour intensive and less toxic (Ineichen *et al.*, 2017; Schmued, 1990). Although these dyes have been and are instrumental for detecting demyelinated and remyelinated lesions in tissue sections, their lack of specific markers means that they are non-specific for myelin, data collection is hindered by inefficient diffusion of the dye, and the images are relatively low resolution in our ability to visualise individual myelin sheaths.

1.8.3 Immunofluorescence

Immunofluorescence microscopy is the use of fluorescently tagged molecules to allow for the visualisation of the localisation and expression levels of proteins of interest. An antibody targeted against the protein is fluorescently labelled, allowing for the location of the antibody, and hence the protein it is bound to, to be determined by fluorescence microscopy (Asai 2015; Shakes, Miller and Nonet, 2012). Antibodies against proteins in oligodendrocytes and myelin sheaths have long been used to study their development and function, including antibodies against cell surface markers O1 and O4 or intracellular MBP and CNP to study their expression patterns and role in OL differentiation (Bansal, Gard and Pfeiffer, 1988; Bansal *et al.*, 1990; Schachner and Sommer, 1981), to more recent markers against MYRF to examine their role in myelination (Bujalka *et al.*, 2013). These fluorescence microscopes encompass more simple systems such as epifluorescence microscopes, to more complicated designs that allow more detailed structures to be examined, such as through the use of confocal microscopy as discussed next.

1.8.4 Confocal microscopy

Confocal microscopy is an optical imaging technique pioneered by Marvin Minsky in 1955 at Harvard University. It uses a spatial pinhole at the image plane to increase the optical resolution and contrast of the signal generated by blocking out-of-focus light from reaching the detector and creating a focused

region of light. This focused spot of illumination is then scanned across the specimen using a set of two mirrors moving in the x- and y-axis, and paired with a motorised z-axis, in order to build up a precise 3D image. Combined with the development of spectral detection systems that allow precise separation of the growing library of available fluorescence signals with overlapping emission spectra through the use of multi-element photomultiplier tubes (PMTs) and Hybrid Detectors (HyDs), and the exploitation of antibody binding specificity to target specific antigens and proteins in cells or tissue through immunohistochemistry like PLP and MBP for differentiated oligodendrocytes and myelin imaging (Agrawal *et al.*, 1977; Hartman *et al.*, 1982), confocal microscopy can be used to detect and separate even closely matched fluorophores in increased spectral resolution with increased sensitivity and specificity. The use of the spinning disk, which incorporates a pattern of pinholes or slits onto a disk, paired with cameras for detectors, results in decreased resolution but increased speed of data acquisition for improved temporal resolution and decreased photobleaching and phototoxicity to the sample (Semwogerere and Weeks, 2005; St Croix, Shand and Watkins, 2005). Immunohistochemistry-based high content microscopy techniques will be explored in order to achieve the high-throughput screening aspect of this thesis.

Advances in super-resolution microscopy has advanced our ability to directly visualise how cells function and are morphologically structured, as well as how molecules interact, by changing the optical resolution previously visible from 250nm in the x- and y-axis and 450 to 700nm in the z-axis of conventional light microscopy to as small as 10nm. The conventional limit of resolution is determined by the point-spread function (PSF), which is the fixed size of a single point of light that is diffracted through the microscope. Any object smaller than the PSF appears to be the same size as the PSF, and any collection of objects that are less than the PSF apart in distance cannot be distinguished. In super-resolution microscopy, the excitation or activation of light is temporally or spatially modulated in order to overcome this diffraction limit. Two commonly used techniques include the saturation of the fluorophore emission to a transient dark state that either bleaches it, such as with stimulated emission depletion (STED) microscopy (Hell and Wichmann, 1994), or leads to the emission of light

on a microsecond or millisecond time scale rather than nanosecond, or induce photochemical reactions to stochastically switch between on and off states or change colours in a subset of photoswitchable or photoactivatable fluorophores, respectively, that are spatially separated by the distance of the PSF, like photoactivation localisation microscopy (PALM) and fluorescent PALM (fPALM) (Hess, Girirajan and Mason, 2006), or stochastic optical reconstruction microscopy (STORM) (Rust, Bates and Zhuang, 2006) and direct STORM (dSTORM) (Heilemann *et al.*, 2008) (Galbraith and Galbraith, 2011; Sydor *et al.*, 2015; Thompson, Larson and Webb, 2002).

Super-resolution microscopy has been used to better understand oligodendrocyte biology and myelin sheath formation such as through the use of the super-resolution microscopy technique structured illumination microscopy (SIM), which overcomes the limitations of lateral resolution by illuminating the sample with spatially structured excitation light in a series of images that are reconstructed to extract the additional lateral information (Gustafsson, 2000), to understand the interaction of MBP and actin filament formation and disassembly during differentiation and membrane extension (Zuchero *et al.*, 2015). STED microscopy, which reduces the diameter of the PSF by surrounding the focal excitation point with longer wavelengths of light at a high intensity to saturate the surrounding fluorophores (Hell and Wichmann, 1994), has also been used to pick apart the ultrastructural anatomy of the nodes of Ranvier in teased sciatic nerve fibres to a nanoscale resolution, such as the cytoskeletal proteins and sodium and potassium channels organisation, with implications for the mechanism through which paranodal junctions and nodal gaps function and have roles in health and disease (D'Este *et al.*, 2017). The degree of detail and resolution obtainable through these super-resolution techniques come at the cost of the speed of image acquisition as they use conventional microscope optics and hardware to achieve these higher resolution images (Galbraith and Galbraith, 2011), with a 2.5 by 1.8µm field-of-view at a 2D resolution of 62nm taking a reported 35 seconds to image (Westphal *et al.*, 2008), with the length of image acquisition accumulating with larger fields-of-view and the trade-off between resolution and speed becoming even larger in single-resolution super-resolution microscopy techniques due to the need for stochastic excitation to

overcome the PSF limitations. Therefore, current applications of super-resolution microscopy is limited to low temporal and high spatial resolution microscopy requirements rather than the types of high content imaging required for screening in drug discovery or hit validation. In the next section, I will discuss a technique which could balance the ability to detect myelin sheaths with a similar acquisition speed to the conventional confocal microscopy to give the required spatial and temporal resolution, and act as a non-fluorescent-based label-free imaging technique for the orthogonal screen of the drug screening cascade in hit validation.

1.8.5 Non-linear optical imaging

Optical imaging is the use of light to investigate cellular and molecular functions in a non-destructive manner, with images being generated using photons of light in the ultraviolet to near infrared wavelength range. Conventional linear microscopy techniques are limited by the mean free path (MFP) of a photon, which describes the average distance that a photon is able to move between two consecutive scattering events, with scattering being particularly strong in the near-infrared and especially visible and ultraviolet spectral regions, and limiting the depth of penetration of light to allow imaging. The improvement of optical imaging and advanced microscopy has increased the depth of imaging from 10 to 20μm to up to several hundreds of micrometres due to the physical parameter set by the transport mean free path (TMFP), which combines MFP with the average angle of photons being scattered in a single scattering event to indicate the distance that a photon can travel into a tissue before it loses its initial propagation direction, with this value typically being 10 times larger than MFP (Farrar *et al.*, 2011; Ntziachristos, 2010).

Coherent anti-Stokes Raman Scattering (CARS) microscopy, as discussed in more detail in Chapter 7, is an optical imaging technique that uses a four-wave mixing process of combining a tuned pump field E_p (ω_p) and Stokes field E_s (ω_s) to generate an anti-Stokes field E_{as} that matches the intrinsic vibration of a molecular bond to create a 3D image that coincides with the spatial location of

the molecular bond of interest in the sample in a label-free manner. Due to the nonlinear nature of this imaging technique, the signal is only produced from a small focal volume which increases the resolution of the image generated (Fu *et al.*, 2008; Wang *et al.*, 2005). By using the CH_2 bond that is abundant in lipid, CARS has been shown to be able to produce images of myelin in *ex vivo* whole brain slices and *in vivo* in the subcortex white matter in mice (Fu *et al.*, 2008), and in the live spinal cord tissue of guinea pigs (Wang *et al.*, 2005). CARS increases our ability to visualise myelin sheaths without the need for endogenous transgenic or exogenous labelling of myelin to simplify sample preparation, while also avoiding the effects of photobleaching and non-specific binding, and is able to provide images with sharp contrast for subcellular resolution imaging that allows quantitative analysis to be performed upon, such as volume, density, and orientation of myelin. However, despite its advantages and value in advancing myelin imaging, as shown in Chapter 7, CARS microscopy, like other optical imaging techniques, is limited by two main constraints. Firstly, despite the subcellular resolution provided, the thickness of myelin is still below the threshold of the resolution. Wang *et al.* (2005) quantified the value of *g* ratio in his publication as 0.68 and 0.63 based on whether forward- or epi-detected CARS measurements were used, which differs from the gold standard EM technique of 0.81. Although they argued that this was due to the intense sample preparation and dehydration involved in EM, this difference is likely due to the resolution limitations of the technique. The other limitation in optical imaging and CARS microscopy is the difficulty of live *in vivo* imaging due to the thickness of the skull and the size of the animal and its brain, although longitudinal *in vivo* imaging of the spinal cord has been shown due to its easier access (Shi *et al.*, 2011). On the other hand, while Wang *et al.* (2005) demonstrated *in vivo* brain imaging of a live mouse, they removed the grey matter to be able to access the white matter, which is less than ideal for *in vivo* imaging. However, the combination of labelling-independent myelin sheath detection with the speed of image acquisition were attractive characteristics in the exploration of this technique.

Although not discussed further as part of this thesis, other optical imaging methods include third-harmonic generation (THG), which is a nonlinear optical

process in which the frequency of the light source is tripled as it passes through a non-linear medium as three photons of the same frequency are upconverted to a photon at the third harmonic (Farrar *et al.*, 2011), and optical coherence microscopy (OCM), a label-free imaging technique based on optical coherence tomography (OCT) that is based on the intrinsic contrasting of back-scattered coherent light to provide 3D reconstructions in the absence of fluorescent labelling (Ben Arous, 2011). THG has been shown to predominantly image myelin in fixed mouse CNS tissue, as well as *in vivo* mouse spinal cord, and an adaptation of OCM, called deep-OCM, was used to quantify the density of myelinated fibres in the rat cortical grey matter and sciatic nerve. The signal produced in THG is only in a focal volume, providing advantages in imaging in scattering tissue, and has increased depth of penetration to CARS, and OCM shows promise as an alternative non-invasive method for imaging individual myelin sheaths with increased depth of penetration of up to 300 microns. Although both optical imaging techniques are of value in imaging myelin and provide benefits compared to other microscopy techniques in being label-free, and therefore requiring less sample processing, and potentially non-invasive, similar to the limitations of CARS microscopy, they are still restricted by the depth that light can penetrate to restrict live imaging, with OCM still requiring a craniotomy to thin the skull and the dura mater removed in some cases to visualise the underlying somato-sensory cortex, and have limited resolution, with individual myelin sheaths being visible but their thickness and sub-micron structures still being below their threshold (Ben Arous, 2011; Farrar *et al.*, 2011). A more novel imaging technique, although not explored as part of this thesis, Spectral confocal reflectance microscopy (SCoRe), may also provide a method of label-free imaging of myelin sheaths with similar temporal resolution to conventional confocal microscopy and similar potential for *in vivo* imaging with surgical adaptations.

1.8.6 SCoRe

Spectral confocal reflectance microscopy, or SCoRe, is a high-resolution *in vivo* imaging technique described by Schain, Hill and Grutzendler (2014) for visualising myelinated axons. SCoRe relies on the use of a conventional laser-scanning confocal system with tunable wavelength detection capabilities without the need for fluorescent labelling by using the high refractive index of lipid-rich myelin to create a composite image of individually generated discontinuous segments from multiple confocal lasers (488, 561, 633 nm) to visualise continuous myelin sheaths. By labelling myelin with fluoromyelin dye through a craniotomy for *in vivo* imaging of Thy1-YFP mice with a subset of layer V cortical pyramidal neurons labelled with YFP, they were able to confirm that only fluoromyelin-labelled myelinated fibres were reflective, whereas YFP-labelled dendrites, unmyelinated axons, astrocytes, and microglia were not, and this reflective signal was reduced in shiverer mice with an absence of compact myelination. Due to the highly reflective nature of the lipid in myelin, they were able to reach a depth of 400µm even with low laser intensities, a depth of penetration not easily reached by other optical imaging techniques. With this system, longitudinal imaging of the same region was feasible, could be used to detect myelin pathologies *in vivo*, and even showed potential in human tissue myelin imaging. This technique was recently independently applied to quantify compact myelin on fixed frozen brain sections in a cuprizone model of demyelination by Gonsalvez *et al.* (2019) to quantitatively and qualitatively assess compact myelin integrity in control and injury mouse model of demyelination. Although still limited in its use thus far, SCoRe represents a promising *in vivo* label-free optical imaging technique to study compact myelin formation in preclinical animal models and potentially in human brain tissue.

1.9 Project Rationale – the need for new screening assays.

The work above emphasizes the need for new drugs to enhance remyelination. Traditional drug discovery has relied on molecular target-based screens (Zheng, Thorne and McKew, 2013). However, there are limitations to the application of this type of drug screen for MS due to our incomplete understanding and the complexity of the biology of the myelination and remyelination process. For example, both NRG1 (Brinkmann *et al.*, 2008) and integrin β1 (Câmara *et al.*, 2009) have been shown to be axonal signals that modulate myelination, but are not sufficient to "force" myelination to occur, and therefore their target biology may be more complicated to develop treatments against. In addition, there are limitations to the disease-relevant and predictive preclinical models available to validate these targets, as summarised in reviews such as Lassmann and Bradl (2017), with many being able to only recapitulate one aspect of the multi-faceted pathophysiology of MS, usually the inflammatory phase. The complex nature of the disease also means it is unlikely that a single drug against a single target would be effective, with drug combinations being much more likely to be effective. Therefore, a "target-agnostic" phenotypic drug discovery approach (Zheng, Thorne and McKew, 2013) has been taken, representing an alternative to the conventional target hypothesis-driven drug discovery to allow for empirical discovery of novel targets and drug combinations if physiological- and disease-relevant screening assays can be developed.

In performing these disease-relevant screening assays, the majority of current published high-throughput phenotypic drug screens (where high-throughput is the adoption of various automation techniques to increase the accuracy and efficiency of the screen (Clemons, Tolliday and Wagner, 2009)) to discover remyelination therapies in MS use a two-dimensional flat culture system to screen libraries of small molecules or US Food and Drug Administration (FDA)-approved drugs. The goal of these screens is to detect compounds that increase the number of differentiated but non-myelinating OLs from OPCs (**Figure 1.19**). Deshmukh *et al.* (2013) used primary rat optic-nerve-derived progenitor cells and identified Benztropine, an antagonist of muscarinic receptors, as the most effective compound (Deshmukh *et al.*, 2013b). Najm *et al.* (2015) used mouse epiblast-derived OPCs to identify Miconazole and Clobetasol. Although there are no obvious signalling pathways responsible, Miconazole activates mitogen-activated protein kinase, and Clobetasol activated the

glucocorticoid receptor and is also a potent immunosuppressant (Najm *et al.*, 2015). Lariosa-Willingham *et al.* (2016a, 2016c) conducted two different two-dimensional drug screens using acutely dissociated and immunopanned purified rat OPCs in "normal" media and in media containing tumour necrosis factor α and IFNɣ to mimic the inflammatory condition of MS lesions to detect differentiation and cytokine protection hits, respectively, including Benztropine and Clemastine identified in other drug screens (Lariosa-Willingham *et al.*, 2016a, 2016c). Eleuteri *et al.* (2017) performed a systematic and staged screening of compounds on mouse OPCs, starting from stimulation of cellular metabolic activity followed by proliferation and differentiation effects (Eleuteri *et al.*, 2017).

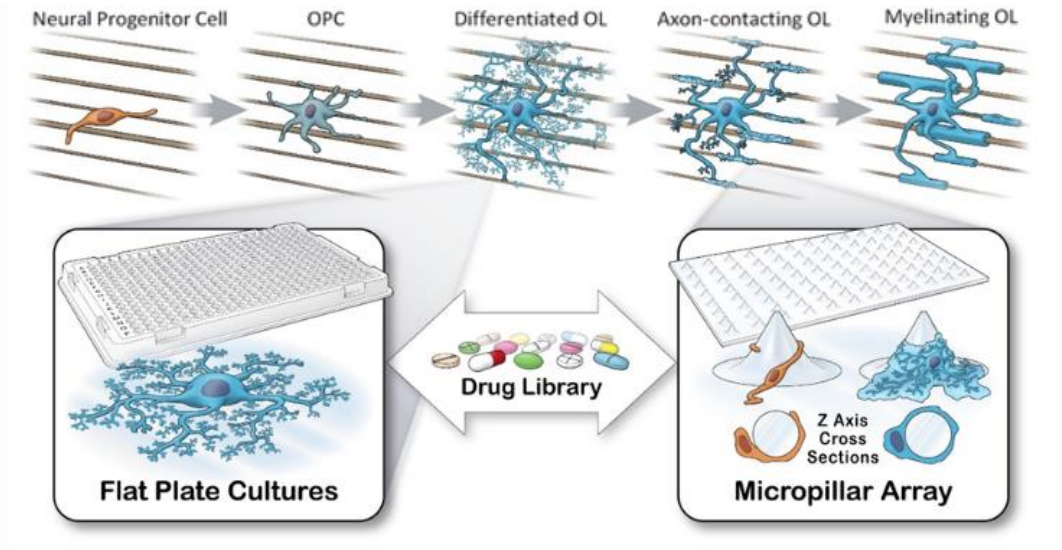

Figure 1.19 A summary of the current high-throughput drug screens for discovery of a remyelination therapy

The majority of current drug screens use a two-dimensional flat culture platform that is able to detect differentiation from OPC to a differentiated but non-myelinating OL.

The BIMA screen is able to detect one stage further along the OL development by being able to detect those extending axon-contacting processes through the use of micropillars.

(Figure from ScideLight)

1.9.1 Need for shift in focus in drug discovery from differentiation to myelination

These current efforts in drug discovery are screens developed based on the assumption that simply increasing differentiation will result in increased remyelination. The biological evidence as reviewed throughout this chapter, however, provides strong support towards myelination failure likely being a major block in MS, and that its regulation is controlled independently of differentiation. There is therefore a clinical need for remyelinating compounds in progressive MS that directly enhance myelination, and the current screens available poorly model this stage in oligodendrocyte development. Hence, we need methods that are able to measure myelination directly. Although Lariosa-Willingham *et al.* (2016b) developed a co-culture system of embryonic rat cortical cells and rat OPCs, axonal myelination systems are difficult to scale up due to these systems being difficult to culture, being impacted by axonal survival and density in addition to the OPCs. One screen was able to take screening for remyelination compounds one step further towards myelination beyond simply detecting markers of differentiation, and allow the process of membrane wrapping to be recapitulated and quantified in a high-throughput-compatible format. Mei *et al.* (2014) developed a 'binary indicant for myelination using micropillar arrays' (BIMA) screen in which cones, or pillars, of micrometre dimensions were inserted into the bottom of a 96-well plate. Differentiation could then be detected through the expression of OL markers, and myelination through the wrapping of the OL membrane around the base of the micropillar (**Figure 1.19**) (Mei *et al.*, 2014b). The drug detected using the BIMA screen, Clemastine, was able to meet its primary efficacy endpoint in reducing the latency of visual evoked responses and improving the conduction velocities in the optic pathway (Green *et al.*, 2017). The screen has subsequently been used to detect the kappa-opioid receptor (Mei *et al.*, 2016) and selective estrogen receptor modulators (Rankin *et al.*, 2019) in enhancing remyelination. Although the screen is ingenious in its simplicity, the extension of membrane around the base of a cone does not quite recapitulate the complexity of the myelin sheath formation, therefore leaving room for further development of more

physiologically- and disease-relevant cell-based high-throughput drug screen that detects myelin sheath formation as its endpoint.

The overall aim of my project (**Figure 1.20**) is to develop a high-throughput drug screening platform for oligodendrocyte myelination using the PLA microfibre culture system developed by Bechler *et al.* (2015) as a system to recapitulate the complexity and 3D nature of the myelin sheaths *in vitro.* In order to achieve this, I have investigated whether there was a difference in response to the published pro-differentiation drugs in the 2D flat culture systems and the 3D microfibre system. Next, I used bioengineering to scale up the poly-L-lactic (PLA) microfibre system into a 96-well plate, which I then verified as compatible for high-throughput drug screening purposes using the latest advances in liquid-handling robots and image-based high content screening. Last, I explored Coherent anti-Stokes Raman Spectroscopy (CARS) and Stimulated Raman Scattering (SRS) microscopy as label-free techniques of imaging myelin in *ex vivo* slices as a potential method of validating the hits from the drug screen in the future.

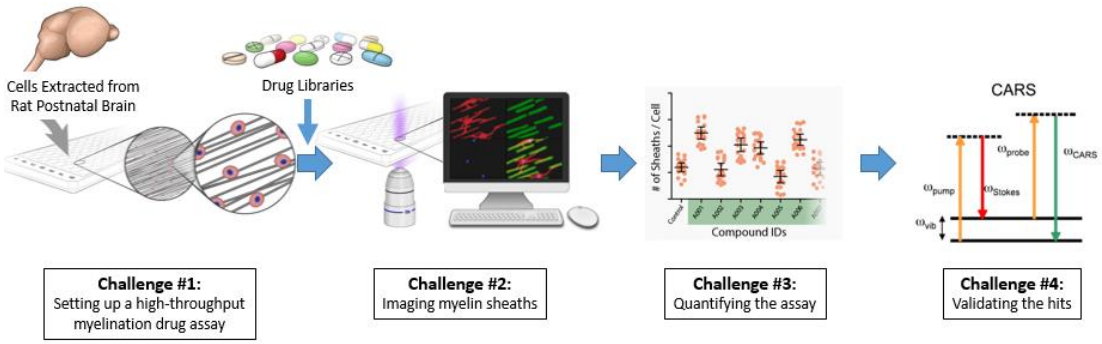

Figure 1.20 Project Overview of the High-Content Screening for Remyelination Treatment in MS

The main high-throughput drug screening phase of my thesis can be divided into 4 main challenges:

Challenge #1: The development of a high-throughput myelination drug assay using bioengineering

Challenge #2: Imaging of the three-dimensional myelin sheaths on the microfibres in a high content-compatible manner

Challenge #3: The quantification of the myelin sheath formation per compound in an automated fashion (done by Dr. Marie E. Bechler, in collaboration with Dr. Beth A Cimini and Professor Anne E. Carpenter of the Broad Institute)

Challenge #4: Exploration of label-free imaging techniques as potential methods of validating the hits from the high-throughput assay

(Figure adapted from ScideLight and Potma and Xie, 2004)

CHAPTER II. MATERIALS AND METHODS

2.1 Media

2.1.1 Mixed Glial Culture Dissection Media

The mixed glial culture dissection media was prepared by adding 1% Penicillin/Streptomycin (Pen/Strep; Invitrogen 15140-122) to Minimal Essential Medium (MEM), HEPES, no glutamine (Life Technologies 32360-026) at a final concentration of 100U/ml of Penicillin and 100µg/ml of Streptomycin.

2.1.2 Mixed Glial Culture Media

The mixed glial culture media was prepared by adding 1% Pen/Strep, and 10% Foetal Calf Serum (FCS; Life Technologies 10270106, Batch 42G4850K) to Dulbecco's Modified Eagle Medium (DMEM; Life Technologies 41966-029).

2.1.3 Immunopanned O4+ OPCs Proliferation Media

The proliferation media for immunopanned O4+ OPCs was prepared by adding 1% 100x SATO stock, 1% GlutaMAX supplement (Life Technologies 35050061), 1% Sodium Pyruvate (Gibco 11360-039), 1% Pen/Strep, 1% insulin-transferrin-sodium selenite (ITS; Sigma-Aldrich I3146), 0.1% NAC stock, 0.1% Trace Elements B (Corning 25-022-Cl), and 0.1% d-Biotin stock. Forskolin (final concentration at 4.2µg/ml; Sigma-Aldrich F6886), CNTF (final concentration 10ng/ml; PeproTech 450-13-20), PDGF (final concentration 10ng/ml; Peprotech 100-13A), and NT-3 (final concentration 1ng/ml; Peprotech 450-03) were added to the media just before use.

100x SATO stock was prepared by adding 1.61mg/ml Putrescine (Sigma-Aldrich P5780), 6µg/ml Progesterone (Sigma-Aldrich P8783), and 10mg/ml Bovine Serum Albumin fraction V (Sigma-Aldrich A-4919) to DMEM.

NAC stock was prepared by dissolving N-acetyl L-cysteine (Sigma-Aldrich A8199 and A9165) in Neurobasal® medium (Life Technologies 21103-049) at 5mg/ml.

D-biotin stock was prepared by dissolving d-Biotin (Sigma B4639) in water at 10µg/ml.

2.1.4 Myelination Media

Myelination media was prepared by mixing 1:1 ratio of Neurobasal® medium and DMEM, and the addition of 0.5% GlutaMAX supplement, 1% Pen/Strep, 1% ITS, 1% myelination media SATO stock, 2% B27 (Gibco 17504-044) or B19 stock, 0.1% NAC, and 0.1% d-Biotin.

The 100x SATO stock for myelination media was modified to contain 40µg/ml of L-Thyroxine (T4; Sigma T-1775) and 40µg/ml Tri-iodothyroxine (T3) (Sigma T-6397).

B19 stock (based on NS21 (Chen *et al.*, 2008)) was prepared by adding to Neurobasal media containing 2.5mg/ml Bovine Serum Albumin (BSA; Sigma-Aldrich A4161): L-Carnitine (final concentration 2µg/ml; Sigma-Aldrich C7518), Ethanolamine (final concentration 1µg/ml; Sigma-Aldrich E9508), D(+)-galactose (final concentration 15µg/ml; Sigma-Aldrich G5388 and G0625), Putrescine (final concentration 16.1µg/ml), Sodium Selenite (0.01435µg/ml; Sigma-Aldrich S9133), Corticosterone (0.02µg/ml; Sigma-Aldrich C2505), Linoleic Acid (1µg/ml; Sigma-Aldrich L1012), Linolenic Acid (1µg/ml; Sigma-Aldrich L2376), Lipoic Acid (0.047µg/ml; Sigma-Aldrich T1395), Progesterone (0.0063µg/ml), Retinol Acetate (0.1µg/ml; Sigma-Aldrich R7882), Retinol, all trans (vit. A) (0.1µg/ml; Sigma-Aldrich 95144), D,L-alpha-Tocopherol (vit. E) (1µg/ml; Sigma-Aldrich 95240), D,L-alpha-Tocopherol acetate (1µg/ml; Sigma-Aldrich T3001), Catalase (2.5µg/ml; Sigma-Aldrich C40), Glutathione (reduced) (1µg/ml; Sigma-Aldrich G6013), Insulin (4µg/ml; Sigma-Aldrich I6634), Superoxide Dismutase (2.5µg/ml; Sigma-Aldrich S5395), and Transferrin (5µg/ml; Sigma-Aldrich T5391).

2.1.5 Live Adult Slices Dissection Media

The dissection media to slice live adult mouse brains on the vibratome was prepared by adding 2% B27 (Life Technologies 17504001), 2mM L-glutamine (Invitrogen 25030-024), and 1% Pen/Strep to Hibernate-A medium (Thermo Fisher A12475-01).

2.1.6 Live Adult Slices Serum-Free Culture Media

Live adult slices were cultured in Neurobasal-A medium containing 2% B27, 2mM L-glutamine, 1% Pen/Strep, and 80µM Indomethacin (Sigma-Aldrich I0200000).

2.2 Rat Oligodendrocytes Precursor Cell Isolations

2.2.1 Mixed Glial Culture

OPCs were purified from mixed glial cultures as previously described (Bechler, Byrne and ffrench-Constant, 2015; McCarthy and de Vellis, 1980). Briefly, the brains of postnatal day 0 to 2 (P0-2) Sprague Dawley rats were dissected, and their cortices with the meninges removed collected in mixed glial culture dissection media. The cortices were minced with fine scissors and digested in filter sterilised mixed glial culture dissection media with 1.2U/ml papain (Lorne Laboratories LS003127), 0.1mg/ml L-cysteine (Sigma-Aldrich C7477), and 0.40mg/ml DNase 1 type IV (Sigma D5025) for 1 hour at 37°C. Digestion was halted by the addition of mixed glial culture media, and centrifugation at 1000rpm for 5 minutes. The pellet was re-suspended in mixed glial culture media and triturated gently with a 21G needle before being added at a density of 1.5 brain per T75 flask (Scientific Laboratory Supplies Ltd. 353110), pre-coated in 2.5µg/ml of poly-D-Lysine (PDL; Sigma P6407) overnight at 37°C. Cells were cultured at 37°C in 7.5% CO_2, with media changes (mixed glial culture media) every 2 to 3 days.

After 10 to 12 days, OPCs were purified using mechanical separation on an orbital shaker at 250rpm and 37°C. The flasks were initially agitated for 1 hour to remove microglia, and then shaken for a further 16 to 18 hours in fresh mixed glial culture media to collect OPCs, while leaving the astrocytes still attached. The OPC-containing media were added to 10cm untreated plastic petri dishes for 30 minutes at 7.5% CO_2 and 37°C to remove additional microglia. The remaining cells were collected, centrifuged at 1000rpm for 5 minutes, re-suspended in myelination media, gently triturated with a 21G needle, and counted with a haemocytometer to dilute at the appropriate density for the experiment.

2.2.2 Purification of OPCs by Immunopanning

OPCs were isolated by immunopanning and collecting the O4+ cells in the protocol previously described for collecting ITGB5+ astrocytes (Foo *et al.*, 2011; Foo, 2013). The brains of P7 rat pups were dissected, and their cortices with the meninges removed collected in dPBS with calcium, magnesium, glucose, and pyruvate (dPBS; Thermo Fisher 14287072). The brains

were manually diced with a scalpel, and then enzymatically digested in enzyme solution (10% Earle's Balanced Salt Solution (EBSS) 10x (Sigma-Aldrich E7510), 0.46% D(+)-Glucose (Sigma-Aldrich G8644), 26mM $NaHCO_3$, 0.5mM EDTA dissolved in sterile Milli-Q water, with 4.55U/ml papain and 0.2mg/ml L-cysteine) with 31.25U/ml of 0.4% DNase (Worthington LS002007, dissolved in EBSS (Sigma-Aldrich E6267)) on a 37°C heat block with 5% CO_2/95% O_2 bubbled over the top of the brains to prevent hypoxia for 40 minutes. After the digestion, the digested cortices were washed four times in inhibitor solution (10% EBSS 10x, 0.46% D(+)-Glucose, and 26mM $NAHCO_3$ dissolved in sterile Milli-Q water) containing 6.7% v/v of 10x low ovomucoid stock (low ovo; 15mg/ml Bovine Serum Albumin (BSA; Sigma A4161) and 15mg/ml Trypsin inhibitor (Worthington LS003086) at pH 7.4) and 55.6U/ml 0.4% DNase, dissociated in further low ovo-containing inhibitor solution and the single cell solution collected in low ovo-containing inhibitor solution. Inhibitor solution containing 16.7% v/v of 10x high ovomucoid stock (high ovo; 30mg/ml BSA and 30mg/ml Trypsin inhibitor at pH 7.4) and 20.8U/ml 0.4% DNase was layered under the single cell suspension, and the solution spun down for 5 minutes at 1350rpm (with acceleration and deceleration set to 6) to completely inhibit the papain digestion. The collected pellet was re-suspended in 0.02% BSA/DNase (10% 0.2% BSA/DNase (10% v/v of 4% BSA stock (40mg/ml BSA in dPBS), and 5U/ml DNase in dPBS) in dPBS, with an additional 12.5U/ml DNase), filtered through a 20µM cell strainer (Pluriselect 43-50020-03), and allowed to recover at 37°C and 7.5% CO_2 for 45 minutes.

The immunopanning dishes were prepared by coating with secondary antibodies in 50mM Tris-HCl (pH 9.5) overnight at 4°C, and coating with primary antibody in 0.2% BSA/Dnase for at least two hours at room temperature on polystyrene petri dishes (Greiner Bio-One 633181). The single cell solution was transferred onto the "secondary only" dish (secondary antibody goat anti-mouse IgG + IgM (H+L) (Jackson Immuno 115-005-044), no primary) for 10 minutes, "BSL-1" dish (no secondary, Unconjugated Griffonia (Banderiraea) Simplicifolia Lectin 1 (GSL 1, BSL 1) (Vector Laboratories L1100) dissolved in dPBS, overnight) for 10 minutes, and "CD45" dish (secondary antibody goat anti-rat igG (H+L) (Jackson Immuno 112-005-167), and primary antibody rat anti-mouse CD45 (BD biosciences 550539) for 10 minutes to remove microglia, macrophages, and endothelial cells. The cells were then transferred onto the "O1" dish (goat anti-mouse IgG + IgM, O1 (R&D systems MAB1327)) for 30 minutes, and then "O4" dish (goat anti-mouse IgM µ-chain specific (Jackson Immuno 115-005-020), O4 (R&D systems MAB1326) for 30 minutes for OPCs.

The adhered cells were collected from the "O4" dish with 25U/ml trypsin (Sigma-Aldrich T9935, stock prepared in EBSS (Sigma-Aldrich E6267)) in EBSS equilibrated at 7.5% CO_2 for 3 minutes, the reaction stopped with 30% FCS (Life Technologies 10270106, Batch 42G2083RK) in dPBS equilibrated at 7.5% CO_2, and the dislodged cells collected. The O4 positive cells were spun down with 125U/ml DNase at 1350rpm for 12 minutes, re-suspended and plated in immunopanned O4+ OPCs proliferation media onto TC-treated dishes for 2-3 days to rest, before being lifted using 10% trypsin-EDTA (0.5%) (Thermo Fisher 15400054) in EBSS and 30% FCS. The collected cells were centrifuged at 1350rpm for 12 minutes with 125U/ml DNase, re-suspended in myelination media, gently triturated with a P200 tip, and counted with a haemocytometer to dilute at the appropriate density for the experiment.

2.3 Optimised 96-well Microfibre Plate Construction

These protocols were optimised as described in 'CHAPTER IV. CONSTRUCTION OF A HIGH-THROUGHPUT-COMPATIBLE 96-WELL MICROFIBRE PLATE'.

2.3.1 Electrospinning

The electrospinning set-up (IME device) is shown in **Figure 2.1**. 10% PLA (Corbion Purac Purasorb® PL 18) in 1,1,1,3,3,3-Hexafluoro-2-propanol (HFIP) (Manchester Organics G26383) (w/w) was mixed thoroughly on a rolling mixer overnight and loaded into a syringe. The syringe was attached to a solution tubing, with an 18G tip connected to the other end. The 18G tip was inserted and secured into the moving needle, and set 18cm away from the rotating collector (working distance). The rotating collector was covered in a sheet of aluminium foil with 2 sheets of 10cm by 14cm release paper (Stix2) attached for the collection of the microfibre. The control panel was used to set the pump (flow rate) to 1.3ml/hr, the rotating collector to spin at 2000rpm for fibre alignment, the movement of the needle to cover 160mm at 50mm/s, and the voltage of the positive end (needle) to 19-24kV (usually 20-22kV) and negative end (rotating mandrel) to -1kV in order to achieve a stable Taylor cone. Microfibres were collected for 20 minutes (density).

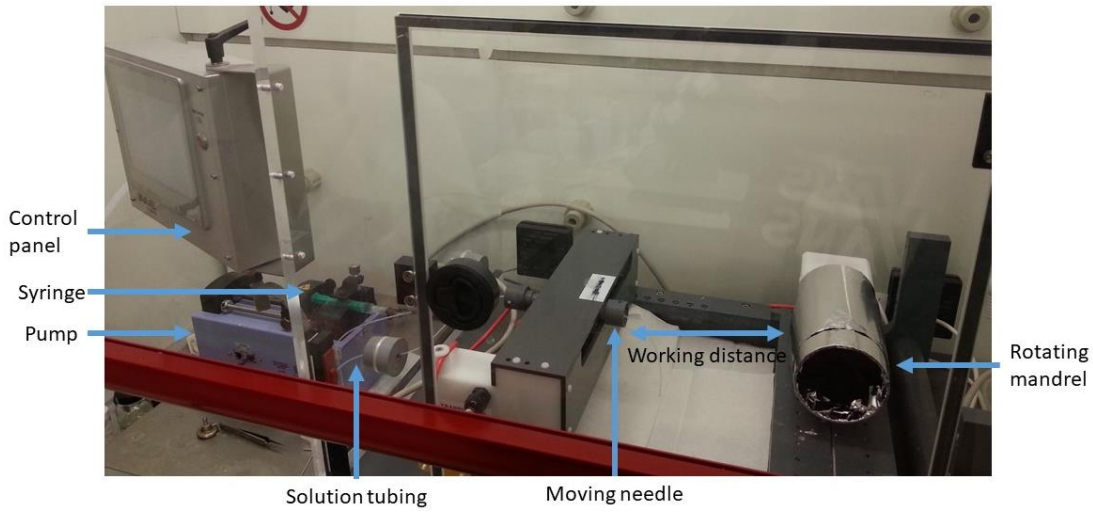

Figure 2.1 Electrospinning set-up

The photograph is of the electrospinner used for the final optimised electrospinning protocol. Note the rotating mandrel allowing for aligned fibre collection and the moving needle to allow for even distribution of fibres.

Scanning electron microscopy (SEM) to verify the diameter of the electrospun microfibres was performed by mounting the microfibres onto SEM aluminium stubs with carbon adhesive, sputter coating them with 20 nm gold/palladium by Dr. Stephen Mitchell (EM Facility Manager), and imaging on the Hitachi S-4700 Scanning Electron Microscope. The images were quantified manually on ImageJ, and plotted using GraphPad Prism. The density of the fibres was measured by taking brightfield images on the Leica SP8 confocal microscope with the MatrixScreener (section '2.5.3 96-well Microfibre Culture Plates') of the transferred fibres onto the base of the 96-well plates (as described below in section '2.3.2 Plate Construction'), drawing a straight line perpendicular to the alignment of the parallel fibres and measuring the distance between individual microfibres on ImageJ. The graph was plotted using GraphPad Prism.

2.3.2 Plate Construction

The final plate construction has been summarised in **Figure 2.2**. A bottomless 96-well plate was prepared by laser cutting holes at the base of the individual 96-wells on a PerkinElmer CellCarrier-96 Black plates (CellCarrier, PerkinElmer 6005558) or PerkinElmer CellCarrier-96

Ultra microplates (CellCarrier-Ultra, PerkinElmer 6055302) and then sandpapered to smooth the surface, or using a bottomless ViewPlate-96 Black (ViewPlate, PerkinElmer 6005430). A sheet of electrospun microfibres was lifted from the release paper onto the laser cut double-sided tape (Stix2), laser cut PCR plate seal (Life Technologies AB0558), and cyclic olefin copolymer (COC), and attached to the base of the bottomless 96-well plate with a sheet of laser cut double-sided tape. The layers were then compressed together with a metal block. Laser cutting was performed by Dr. Anthony Buchoux (Stokes Lab, Scottish Microelectronics Centre).

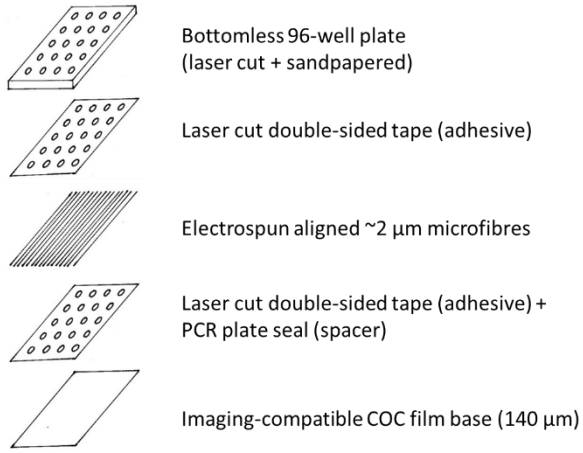

Figure 2.2 Optimised plate construction set-up

The figure shows the optimised layers for the construction of the 96-well microfibre plate that is cell- and imaging-compatible and water-tight.

2.4 Rat OPCs Cultures and Immunostaining

2.4.1 96-well Flat Culture Plates

CellCarrier plates were prepared by coating in 2.5µg/ml PDL in Milli-Q water overnight. The OPCs isolated from mixed glia culture were diluted to 160,000 cells/ml and plated at 50µl per well (for a final density of 8,000 OPCs/well) onto pre-dispensed 45µl myelination media per well using the Multidrop™ Combi Reagent Dispenser (Thermo Fisher 5840300) with the Multidrop™ 'small tube plastic tip dispensing cassette' (Thermo Fisher 24073290) or Steinle 'standard tube dispensing cassette' (Steinle ST-0010).

The ‘compound plate’ was prepared by adding the drug at its stock concentration, and doing 1 in 3 serial dilutions into the solvent (Dimethyl sulfoxide (DMSO, Sigma-Aldrich D8418) or 0.03M sodium bicarbonate ($NaHCO_3$)). The ‘media plate’ was prepared by doing 1 in 50 dilutions of the ‘compound plate’ into myelination media. The compounds were then added to the ‘cell plate’ (i.e. the CellCarrier plates containing the plated OPCs) 4 hours post-plating (to prevent interference with cell adherence) by adding 5µl of the ‘media plate’ per well for a final volume of 100µl per well and 1 in 1000 dilution from the ‘compound plate’ at a final concentration of 0.1% DMSO per well. Vehicle control (0.1% DMSO) was added to control wells. If the cells were cultured for more than 3 days, the ‘media plate’ was prepared again from the ‘compound plate’ stored at 4°C, and media change with drug addition performed by removing 50µl, adding 45µl myelination media, and 5µl of the ‘media plate’ added. This was all performed using the Thermo Fisher E1-ClipTip electronic multichannel pipette and compatible 125µl ClipTip pipette tips (Thermo Electron LED GmbH PIP0362).

The cells were fixed at the appropriate time-point by adding 100µl 8% formaldehyde (prepared from 37% formaldehyde solution (Sigma-Aldrich 252549) in PBS) with the Multidrop™, for a final concentration of 4% formaldehyde per well, for 10 minutes. The BioTek LS 405 microplate washer was used to aspirate (height: 3.811mm to leave approximately 50µl of solution per well) and dispense PBS (dispense rate: 2, volume: 100µl/well, x-axis offset to dispense onto the side of the wells, dispensing height: 14.610mm) for 3 cycles to remove the formaldehyde and leave 50µl, 50µl of 0.2% tritonX-100 (0.1% final concentration) dispensed with the Multidrop™ for cell permeabilisation, washed for 1 cycle with the BioTek LS 405, and primary antibody rat anti-MBP antibody, clone 12 (MBP, AbD Serotec MCA4095) added with the Multidrop™ for a final concentration of 1 in 250 in PBS for incubation at 4°C overnight. The plates were washed for 1 cycle with the BioTek LS 405, and incubated for 1 hour at room temperature in Alexa Fluor 488 Goat Anti-Rat IgG (H+L) antibody (anti-rat488, Life Technologies A-11006) added with the Multidrop™ at a final concentration of 1 in 1000. After 1 cycle of the BioTek LS 405, the cells were incubated in a final concentration of 5µg/ml Hoechst (Thermo Fisher 62249) added with the Multidrop™ for 10 minutes, remaining antibodies and dyes removed with 3 cycles of the BioTek LS 405, and sealed with adhesive PCR plate seals (Life Technologies AB0558) for imaging. The number of BioTek LS 405 cycles tolerated by the cells without being damaged was optimised by testing the “optimal” number of washes (i.e. 3 cycles in between each step) and “minimum”

number of washes (i.e. 1 cycle except after the formaldehyde fixing and at the end of the protocol).

Cell viability assays were performed using the Caspase-Glo 3/7 Assay (Caspase Assay, Promega G8091) and CellTiter-Glo Luminiescent Cell Viability Assay (ATP Assay, Promega G7571). The cultured cells were removed from the incubator and equilibrated at room temperature for 30 minutes. As per standard protocol, 50µl of media/well was removed and 50µl of the respective assay solution added using the Multidrop™. The Caspase Assay plate was shaken at 300rpm for 30 seconds and incubated at room temperature for 30 minutes. The ATP Assay plate was shaken at 300rpm for 2 minutes and incubated at room temperature for 10 minutes. 25µl per well was transferred into a white 96-well microplate (Greiner 655075) in triplicates, and luminescence recorded on the Promega GloMax Explorer. The luminescence measurement of no cells was subtracted from each measurement as background signal, and each measurement normalised to the DMSO control using Microsoft Excel. The resulting data was plotted using GraphPad Prism.

2.4.2 12-well Microfibre Scaffolds

12-well scaffolds with aligned 2µm PLA microfibres were purchased from the Electrospinning Company (TECL006). The fibres were used as previously described by Bechler, Byrne and ffrench-Constant (2015). Briefly, the scaffolds were soaked in 70% ethanol for 15 minutes to sterilise and increase the hydrophilicity of the hydrophobic microfibres. They were then rinsed in sterile Milli-Q water and coated in 2.5µg/ml PDL in Milli-Q water overnight. Before plating, the scaffolds were rinsed with sterile Milli-Q water, and soaked in myelination media for at least 10 minutes to remove any remaining water before changing to 2ml of fresh myelination media per scaffold. The OPCs isolated from the mixed glia culture were diluted at 150,000 cells/ml and plated at 34,500 cells per scaffold in a dropwise fashion to prevent clumping.

The drugs were diluted at 1µM and 0.1µM from the 10mM stock concentration into myelination media, including the DMSO control, and the concentration at which the cells looked healthier visually after staining used for future repeats. The media changes with drug addition were performed every 2 to 3 days, with the first drug addition being 3 days post-plating to target myelination rather than differentiation.

At day 14, the scaffolds were rinsed in PBS, fixed for 15 minutes in 4% formaldehyde, and permeabilised in 0.1% triton-100 for 15 minutes. The scaffolds were incubated in 1 in 250 MBP in PBS overnight at 4°C, 1 in 1000 anti-rat488 in PBS for 1 hour at room temperature, and 5µg/ml Hoechst in PBS for 5 minutes. The scaffolds were mounted by placing a drop of Fluoromount-G® (Fluoromount, SouthernBiotech 0100-01) onto a cut colour frosted blue microscope slide (VWR 631-1555), removing excess PBS carefully from the sides of the scaffold, placing the scaffold on the Fluoromount drop with additional Fluoromount on top of the fibres, sandwiching the fibres onto the microscope slide with a 13mm borosilicate glass coverslip (VWR 631-0149), and leaving to dry for at least 24 hours at room temperature. Once set, the scaffold was carefully removed, leaving the fibres sandwiched between the microscope slide and coverslip for imaging.

2.4.3 96-well Microfibre Culture Plates

Similar to the 12-well scaffolds, the constructed 96-well microfibre plates were prepared by sterilising and increasing the hydrophilicity of the PLA microfibres in 70% ethanol for at least 15 minutes, being careful of bubbles forming under the fibres, rinsed in Milli-Q sterile water, and coated in 2.5µg/ml PDL in Milli-Q water overnight. The fibres were rinsed, soaked in myelination media for at least 10 minutes, 100µl of fresh myelination media placed in each well, and the plate placed at 7.5% CO_2 until ready for plating. The O4+ immunopanned OPCs collected from immunopanning were diluted to the appropriate density, i.e. 50,000 cells/ml for 100µl plating for 5,000 cells/well.

The experiments with added growth factors (performed at Roche) in the myelination media were prepared by adding 10ng/ml Cilliary neurotropic factor (CNTF, Peprotech 450-13) and 1ng/ml Neurotrophin 3 (NT3, Peprotech 450-03).

An additional fibrin-coated PLA microfibres experiment was performed at Roche (Basel, Switzerland) using the protocol from Bacakova *et al.*, (2016). After PDL-coating, the fibres were coated in 10µg/ml fibrinogen (EMD Millipore 341576, Lot 3105287) for 1 hour, followed by 2.5U/ml thrombin (EMD Millipore 605195) for 15 minutes, 200µg/ml fibrinogen and 0.5U/ml antithrombin III (Sigma A2221) for 1 hour, all dissolved in and rinsed with 50mM Tris-HCl buffer, before soaking in myelination media for plating.

The drugs were added 3 days after plating, and media changes made every 2 to 3 days afterwards, by diluting the drugs to 2 times the final concentration in myelination media, and doing half media changes. The cells were fixed 14 days after plating at the Scottish Centre for Regenerative Medicine (SCRM), and 17 days after plating at Roche. Fixation was performed by removing 100µl and adding 100µl of 8% PFA for 10 to 15 minutes, rinsing in PBS, permeabilising in final concentration of 0.1% triton-100 for 10 to 15 minutes, and incubating in MBP at 1 in 250 dilution final concentration overnight at 4°C. The cells were then incubated in anti-rat488 or goat anti-rat IgG (H+L) Secondary Antibody, Alexa Fluor® 647 conjugate (anti-rat647, Invitrogen A21247) for 1 hour at room temperature, and, when appropriate, stained with HCS CellMask™ Green Stain (CellMask_cytoplasm, Life Technologies H32714) at 1 in 20,000 final concentration for 30 minutes at room temperature. The cells were incubated in 5µg/ml Hoechst in PBS for 10 to 30 minutes, and sealed for imaging.

The plates prepared at Roche were filled with PBS, sealed with a PCR plate adhesive seal and parafilm, covered in aluminium foil, and shipped back to Edinburgh in an ice box. This resulted in the loss of cells due to the movement of the fibres as the PBS could not be filled all the way to the top without losing the ability to adhere the seals.

2.4.4 Compounds

The compounds used were as follows:

Drug	Company	Catalogue #	Dissolved in	Comments
Benztropine	Stratech Scientific Ltd.	S3163-SEL	DMSO	Identified in differentiation drug screen (Deshmukh *et al.*, 2013; Mei *et al.*, 2014)
Clemastine	Stratech Scientific Ltd.	S1847-SEL	DMSO	Identified in differentiation drug screen (Mei *et al.*, 2014)

Clobetasol	Stratech Scientific Ltd.	S3163-SEL	DMSO	Identified in differentiation drug screen (Najm *et al.*, 2015)
DAPT	Stratech Scientific Ltd.	S2215-SEL	DMSO	Used as positive control in myelination co-culture drug screen (Lariosa-Willingham *et al.*, 2016)
Miconazole	Stratech Scientific Ltd.	S2536-SEL	DMSO	Identified in differentiation drug screen (Najm *et al.*, 2015)
FR 236924	Tocris Biotechne	3091	DMSO	Identified to increase myelin sheath number by Dr. Matthew Swire (unpublished), selective PKCε activator
BQ-3020	Tocris Biotechne	1189	0.03M $NaHCO_3$	Identified to increase myelin sheath number by Dr. Matthew Swire (Swire *et al.*, 2019), selective ET_B agonist

AG 1478 Hydrochloride	Tocris Biotechne	1276	DMSO	Decreased myelin sheath length by Dr. Matthew Swire (unpublished), selective EGFR kinase inhibitor
U0126	Tocris Biotechne	1144	DMSO	Decreased myelin sheath number by Dr. Matthew Swire (unpublished), selective MAP kinase inhibitor
Compound R	Roche		DMSO	

2.5 Rat OPCs Cultures Imaging and Analysis

2.5.1 96-well Flat Culture Plates

The 96-well flat culture plates were imaged on the PerkinElmer Operetta High-Content Imaging System (Operetta) and Harmony software using the 20x long WD (NA 0.45) lens. The MBP was detected using the Alexa 488 settings at 200ms exposure, and the Hoechst detected using the DAPI settings at 20ms exposure. 31 non-overlapping fields were selected for imaging per well, and imaged at 1 time-point and 1 plane. The imaging of only 1 plane was determined based on optimal imaging quality and speed, as the minimum recommended distance between planes of the objective used was 3.6µm, with no additional imaging details being obtained by increasing the number of planes imaged.

Image analysis was performed using the PerkinElmer Columbus platform. All images were adjusted using the automatic flatfield correction generated to compensate for unequal illumination across the fields-of-view. Quantification was conducted by segmenting and

selecting the nuclei filtered by morphology (area and roundness) and intensity, and then the MBP+ cytoplasm of the selected nuclei filtered by morphology (area) and intensity (**Supplementary Data 2.1**: Columbus 96-well Flat Culture Analysis Pipeline Example). Wells containing cells that were only incubated in secondary antibody were used to determine background noise of the secondary antibody, and therefore used to determine the minimum intensity for a true signal per plate.

The analysed data was exported into Microsoft Excel, each condition at each concentration normalised to the DMSO control, and plotted using the GraphPad Prism software.

2.5.2 12-well Microfibre Scaffolds

The 12-well microfibre coverslips were imaged by randomly selecting 4 to 24 fields of view per condition, depending on the quality of the cells - with all coverslips except 1 having at least 8 fields of view, on the Leica TCS SP8 confocal microscope with 5 detectors system using the 40x oil (NA 1.25) lens, with a z-step of 0.37µm. The same settings (laser power, gain, etc.) were used between coverslips in a single repeat of the experiment.

The images were blinded and analysed using ImageJ (Schindelin *et al.*, 2012), with a complete myelin sheath being defined as a complete and continuous MBP+ signal surrounding the microfibre as assessed through the 0.37µm z-series (**Figure 2.3**). The length and number of these complete tubes were measured and recorded.

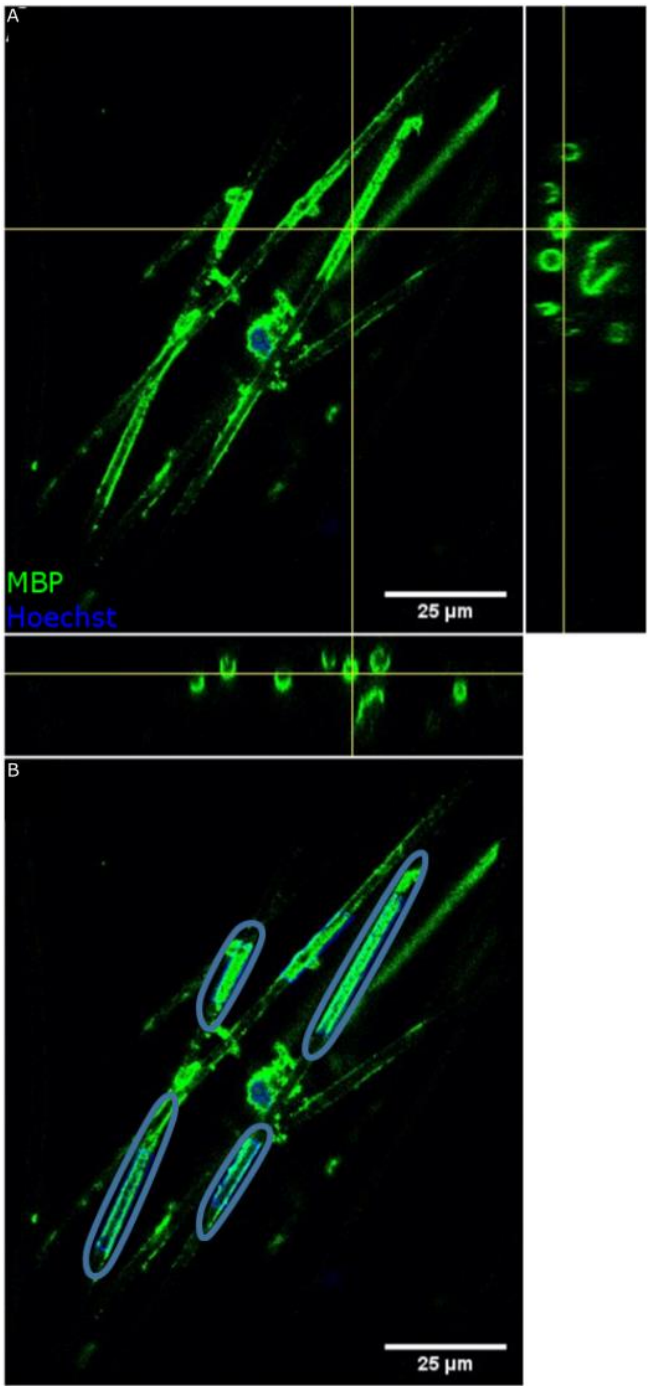

Figure 2.3 Quantification of myelination on the microfibre cultures

A. An example of a MBP+ rat OL cell cultured *in vitro* on the 12-well microfibre scaffold for 14 days. The orthogonal views demonstrate myelin sheath formation by complete MBP signal detected around the individual microfibre.
B. Lengths of the myelin sheaths (highlighted with blue outlines overlaying the green MBP) were quantified by tracing and measuring complete tube formation through the 0.37µm z-series.

The measurements were recorded and unblinded in Microsoft Excel, and plotted and analysed in GraphPad Prism. Statistical tests were performed by determining the mean per condition per biological replicate, and performing the 1way ANOVA with Kruskal-Wallis and Dunn's Multiple Comparison Tests for statistical significance.

2.5.3 96-well Microfibre Culture Plates

The 96-well microfibre plates were imaged on the Leica SP8 confocal using the MatrixScreener extension and the 25x water (NA0.95) lens at 1.6x zoom. The images were obtained by imaging the central 8 by 4 wells, with the outer wells being inaccessible due to the skirt of the plate, at 290µm FOV with a 10µm overlap, and capture range of 500µm with a 0.5µm z-step size, with the settings (image format and resolution, gain, laser power, etc.) kept consistent across all plates. The transmission was used to detect the focal plane of the microfibres per each plate, and the focus map used to optimise the optimal z-galvo plane to set all the microfibres within the capture range (**Figure 2.4**).

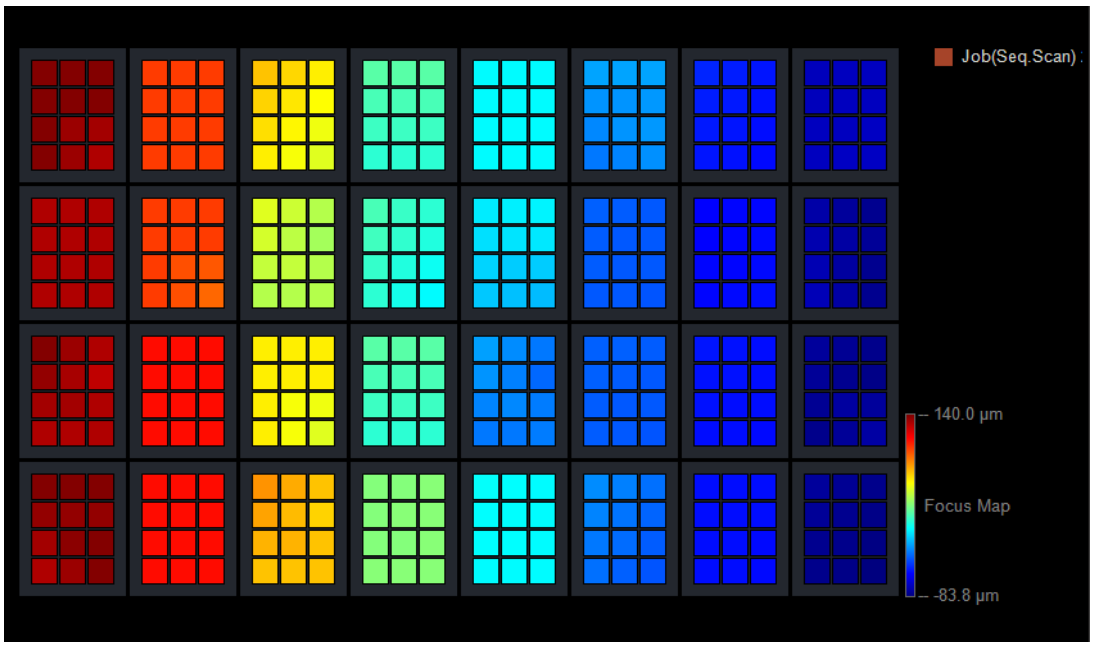

Figure 2.4 An example of a focus map of the range of focal plane of the microfibres in a 96-well microfibre plate as detected by the SP8 MatrixScreener

The figure shows an example focus map generated by the SP8 MatrixScreener to detect the range of focal planes at which it has detected the microfibres. This is used to aid the autofocusing of the subsequent imaging in locating the z-plane of the microfibre in each well to capture the cells. The colours represent the position of the fibres either above (red) or below (blue) the manually set approximate mid-point, showing the range of the position of the fibres in this plate to be about 225µm, which was fairly consistent across all plates imaged by the MatrixScreener.

The images, saved as individual .tiff files, were stitched and stacked together per well using a script written by Dr. Bertrand Vernay (former Head of Imaging at SCRM) (Supplementary Data 2.2: Leica SP8 MatrixScreener Imaging Stitching Script), and the myelin sheath formation analysed as per 12-well microfibre scaffold images on ImageJ (Schindelin *et al.*, 2012), recorded in Microsoft Excel, and plotted and analysed on GraphPad Prism.

2.6 Mouse Brain Slices for CARS/SRS

2.6.1 Animals

The organs from wild-type control animals (C57BL/6NCrl) were obtained at the appropriate ages by either increasing CO_2 concentration and removal of brain into live adult slices dissection media or 4% PFA, or by overdosing on Domitor/Vetalar followed by perfusion fixation and removal of the brain into 4% PFA. The culls were carried out by Dr. Steffen Mayerl, Dr. Lida Zoupi, and Dr. Marie Bechler.

The LPC injection was performed by Amanda Boyd and Dr. Sarah Jaekel by injecting 2µl of lysophosphatidyl choline (LPC) into the corpus callosum of C57BL/6NCrl adult male mice, and collecting their brains after 8 days when the lesion should still be clearly visible. The D_2O animals were obtained by giving 30% deuterium oxide (D_2O, Sigma-Aldrich 1518882) in normal drinking water once they had been weaned, after P21, for 2 weeks before organ harvesting by perfusion fixation by Dr. Steffen Mayerl.

2.6.2 Vibratome

The slices were obtained on the Leica VT1000M vibratome. The brains were set in 2 to 4% agarose, attached to the vibratome stage and placed in either live adult slices dissection media or PBS. The slices were obtained at the required thickness (mostly 300µm, 500µm for the live slices imaged in 3D printed ring, and 50µm for the D_2O experiments), with the blade moving at speed 1 to 2 at frequency 7 to 8. Fixed slices were immediately transferred into PBS for storage until imaging, and live slices were transferred onto Millicell Insert 30mm Organotypic PTFE 0.4µm (MERK Millipore PICM0RG50) in a 6-well plate with 1ml of live adult slices serum-free culture media underneath and placed at 5% CO_2.

2.6.3 Immunostaining

The slices were stained by fixing in 4% PFA for 1 hour, placing in block (3% heat inactivated horse serum (Life Technologies 26050-088), 2% BSA, 0.5% saponin (vs. tritonX-100 - to preserve lipid integrity, Sigma-Aldrich 84510) at room temperature on a rocker for 1 to 2 hours, and placing in primary antibody (MBP, Caspr (Abcam ab34151), Olig2 (Millipore

AB9610)) in block on a rocker at 4°C for two overnights. After washing with block, the slices were placed in secondary antibody (anti-rat488 for MBP, and Alexa Fluor 568 Goat Anti-Rabbit IgG (H+L) Antibody (anti-rabbit568, Life Technologies A11011) for Caspr and Olig2) in block on a rocker at 4°C overnight. The slices were stored in PBS until imaging.

2.6.4 Imaging

Coherent anti-Stokes Raman Scattering (CARS) and Stimulated Raman Scattering (SRS) microscopy was performed under the technical support of Dr. Martin Lee (Brunton Lab, IGMM) as described in Lee *et al.* (2015) and Tipping *et al.* (2017), respectively. Images were taken using a custom-built multi-modal microscope setup with an Olympus FV1000MPE microscope as the foundation, which is also capable of two-photon fluorescence and Second Harmonic Generation (SHG) imaging. Briefly, the tunable pump laser (720-990nm, 7ps, 80 MHz repetition rate) and a temporally and spatially overlapped Stokes laser (1064nm, 5-6ps, 80 MHz repetition rate) was created using a picoEmerald (APE, Berlin, Gemany) laser, fed into the FV1000 MPE using a series of mirrors and lens based beam expanders. A 25x Olympus XLPL25XWMP (NA 1.05) objective lens focused the light onto the sample for imaging. The backscattered emission signal was detected using a short-pass 690nm dichroic mirror and IR cut filter (Olympus). The various emissions were demodulated onto one of four available PMTs in the following fashion: SHG signals were filtered using the following series of filters: FF552-Di02, FF483/639-Di01 and FF01-400/40. GFP two-photon fluorescence signals were filtered using filters: FF552-Di02, FF483/639-Di01 and FF510/84. RFP two-photon fluorescence signals were filtered using: FF552-Di02, and FF440/520-Di01 and HQ610/75m (Chroma). CARS signals were filtered using: FF552-Di02, and FF440/520-Di01 and ET687/95m (Chroma). All filters from Semrock unless noted separately. For SRS Imaging the Stokes beam was modulated with a 20MHz Electro-optical Modulator (EoM) built into the picoEmerald. Forward scattered light was collected with a 20× Olympus XLUMPLFLN objective (NA 1.00) and focused onto a photodiode connected to a lock-in amplifier (APE, Berlin). Stokes light was removed by filtering with an ET890/220m filter (Chroma). The signal from the lock-in amplifier was passed to the analogue unit of the FV1000MPE system. CARS signals were generated at 2845cm^{-1} and 2915cm^{-1} by tuning the pump beam to 816.8nm and 812.2nm, respectively. SRS signals were generated at 2855cm^{-1} and 2940cm^{-1} by tuning the pump beam to 816nm and 810.5nm, respectively. SHG and fluorescence images were

collected simultaneously with CARS/SRS images using the same laser frequencies. Deuterium bonds were detected with the pump tuned to 866.6 or 863.0nm (2141cm^{-1} or 2189cm^{-1}) and off resonance images taken at 870nm or 860nm (2096cm^{-1} and 2229cm^{-1}), or using the sweep function to collect multiple frequencies sequentially. All images were taken at 512 x 512, 1024 x 1024, or 2048 x 2048 pixels by the Olympus FV10-ASW software. CARS images were taken with a pixel dwell of between 4-10µs, and SRS images with a 20µs pixel dwell and 20µs time constant on the lock-in amplifier. Laser power on the sample varied from 20mW-50mW for the pump laser and 30-70mW for the Stokes laser.

Image processing was performed in ImageJ (Schindelin *et al.*, 2012) to subtract off resonant signals from the deuterium images using the subtract operation on the image calculator function. Flat-field correction done on tilescan images using a script written by Dr. Bertrand Vernay (Supplementary Data 2.3: CARS Flat-Field Correction Script for Tile Scan Images). Image analysis to measure myelin sheath length was performed using the 'Simple Neurite Tracer' plugin on ImageJ (Longair, Baker and Armstrong, 2011).

Live slices were transported sealed with parafilm and placed in a Styrofoam box with "ice" packs warmed to 37°C, and imaged in warmed live adult slices serum-free culture media or Hibernate-A media in a WPI FluoroDish Cell Culture Dish (imaging dish, WPI FD35-100) with an 18mm coverslip (Marienfeld 0117580) balanced on top to prevent the slice from floating, or inside a 3D-printed 500µm-thick ring (printed as per requested design by Dr. Anthony Buchoux) to balance the coverslip without compressing the slice. Fixed slices were transported sealed with parafilm and placed in a Styrofoam box with ice packs, and imaged in PBS in the imaging dish with a glass coverslip and small weight on top to reduce tissue movement while imaging.

2.6.5 Raman

Raman spectrum for the D_2O samples were obtained by placing the brain slice onto a calcium fluoride (CaF_2) slide (Crystran Limited CAFP76-26-1U) with a drop of PBS, and sandwiching with a CaF_2 0.2mm coverslip (Crystran Limited CAFP13-0.2R). The slice was placed into the inVia™ confocal Raman microscope (Renishaw), and the accompanying WiRE software used to take the Raman measurements with the 532nm laser and 2400 lines/mm grating. Measurements were taken between 2500cm^{-1} to 3300cm^{-1} to detect the CH_2 bond at 2845cm^{-1}, and 1700cm^{-1} to 2600cm^{-1} to detect the DH_2 bond at 2141cm^{-1}, with an exposure time of 1

second, laser power set to 100%, step size of 10µm for the map, and with a 20x objective. The collected Raman spectra were corrected for white light cosmic rays and baseline, and PCA performed on the WiRE software.

CHAPTER III. 2-DIMENSIONAL VS. 3-DIMENSIONAL CULTURES OF OLIGODENDROCYTES – DIFFERENTIATION VS. MYELINATION

3.1 Introduction

As discussed in the 'CHAPTER I. LITERATURE REVIEW', no disease-modifying treatments are currently available to target the non-inflammatory neurodegenerative phase of MS. Several lines of evidence suggest that promoting remyelination is neuroprotective and promotes functional recovery. Key exemplar experiments are: i) Smith *et al.* (1979) who recorded the restoration of impulse conduction in LPC-induced demyelinated axons of cats once remyelination initiated, ii) Irvine and Blakemore (2008) who reported improved axonal survival following cuprizone-induced global demyelination and irradiation to prevent endogenous remyelination when embryo-derived neural progenitors were transplanted to restore remyelination, and iii) Duncan *et al.* (2009) who showed restoration of function in cats with a dietary manipulated model of demyelination following endogenous remyelination.

As I also reviewed in the Introduction, quantification of OPCs and OLs in MS brain samples suggest that there is a failure of remyelination due to a block in OL development, rather than a lack of OPC recruitment, in the majority of lesions (Chang *et al.*, 2000; Lucchinetti *et al.*, 1999; Wolswijk, 1998). Based on these findings, several studies have been published where OPCs from various sources have been screened using libraries of FDA-approved drugs to detect the increase in MBP+ differentiated cells as their primary output in order to discover new treatments that promote remyelination in treating MS (Deshmukh *et al.*, 2013; Lariosa-Willingham *et al.*, 2016a, 2016c; Mei *et al.*, 2014; Najm *et al.*, 2015).

However, there is evidence suggesting that the OLs present in these 70% of MS lesions are premyelinating immature OLs (Chang *et al.*, 2000; Jäkel *et al.*, 2019; Lucchinetti *et al.*, 1999) rather than OPCs. In addition, studies on oligodendrocyte biology show that differentiation and myelination may occur as two independent processes in OPC differentiation and OL maturation (Colello *et al.*, 1995) with separate critical windows (Czopka, ffrench-Constant and Lyons, 2013; Hill *et al.*, 2014; Watkins *et al.*, 2008) and different neuronal signalling (Biase, Nishiyama and Bergles, 2010; Wake *et al.*, 2015). Collectively, these different studies show

that differentiation and myelination occurs as a two-step process, which indicates pro-differentiation compounds may not necessarily also enhance remyelination.

In order to validate this argument, in this chapter, I: (1) conducted a dose-response experiment using compounds identified as pro-differentiation in previously published screens or pro-myelination in our lab (Yuen *et al.*, 2013; Swire *et al.*, 2019) to verify that an increase in differentiation could be detected with the former in a 2D flat culture system, and also to determine whether the latter compounds would have been identified as hits in a 2D differentiation assay, and (2) screened the pro-differentiation compounds in a 3D microfibre culture system to investigate whether they also increase myelin sheath formation.

3.2 Results

3.2.1 Concentration-response curves for oligodendrocyte differentiation, cell death, and cell activity using published compounds in the 2D flat culture system

In order to test whether compounds that have previously been published in the differentiation (Deshmukh *et al.*, 2013; Lariosa-Willingham *et al.*, 2016a, 2016c; Najm *et al.*, 2015), ensheathment (micropillar assay (Mei *et al.*, 2014)), and axonal myelination screens (Lariosa-Willingham *et al.*, 2016b) also increase differentiation on our OPCs isolated from mixed glia cultures, I first performed a concentration-response drug screen on 2D flat cultures (as reviewed in the Introduction) using a 96-well plate system. I also included 2 molecules that have been identified to increase the number of myelin sheaths produced per oligodendrocyte by Dr. Matthew Swire in our lab (Swire *et al.*, 2019), the small molecule PKCε activator, FR236924, and the endothelin receptor agonist peptide, BQ-3020 (Yuen *et al.*, 2013), to test whether compounds identified in a 3D myelination assay would be identified as positive hits in a 2D differentiation assay. The three responses recorded were: (1) the changes in differentiation through the number of MBP+ cells, and the effect on cell viability through (2) a caspase activity reporter (cell death), and (3) ATP (cell activity) assays.

In order to be able to carry out the 2D concentration-response differentiation assay, two main challenges had to be overcome: (1) the consistency of the plating density, and (2) the

accuracy and timing of the compound addition. For the first challenge of achieving consistent cell density throughout the 60 wells of the 96-well plate, with the outer wells filled with PBS to prevent the edge effect from evaporation, the use of a single channel manual pipette created a large time delay between when the cells were added to the first well to when the final well was plated. This created issues on two levels. Firstly, this allowed time for the cells to settle during the plating process, especially if more than one plate was being used, leading to decreasing cell density over the course of the cells being plated. The consistent re-suspension of the cells in the media during the plating resolved this issue to a certain degree, but also increased the time required for the cell plating overall. Secondly, the time in which the cells were outside of the incubator (i.e. at room temperature and CO_2 level) was lengthy using this plating technique, and increased with more plates required for the drug screen. This additionally created inconsistencies in the timing of the drug addition, mentioned again below, with the time difference between when the cells were plated and when the compounds were added to each well due to the maximum pipetting efficiency with such a set-up. The use of the manual or automated multi-channel pipette improved these aspects, but still was limited by the maximum speed at which pipetting could be performed, especially when two to three plates to test all the compounds at the required drug concentrations with three replicates for a minimum of six to nine 96-well plates were required for the full concentration-response screen. Therefore, I optimised a protocol in which these cells were plated using the automated multi-well plate liquid handling ThermoScientific Multidrop™ instrument, with media pre-dispensed onto the plates and the plating speed set to low to decrease hydraulic stress on the cells, which decreased the time required to plate a single 96-well plate from over a minute to a couple of seconds each, and also eliminated the settling of the cells in the conical tube during the plating, therefore increasing the intra- and inter-plate consistency of cell density and the throughput of the plating. I was also able to optimise the staining and assay solution dispensing protocol by performing these steps using the Multidrop™ and BioTek LS 405 multiplate washer rather than by manual pipetting, thereby increasing the intra- and inter-plate consistency and the throughput of the assay screening pipeline, from hours to minutes, at later stages of the protocol as well.

The compounds were added 4 hours after plating, to allow the cells to adhere without potential influence from the compound upon cell adhesion yet still early enough to affect differentiation, and fixed 3 days later, when the percentage of MBP+ cells from total nuclei were high enough to be able to detect differences from control (assay window range) but

without reaching saturation (**Supplementary Figure 3.1** A). The second challenge, the accuracy and timing of compound addition, was addressed by optimising the protocol in compound preparation and addition. The manual preparation of individual compounds and their respective multiple concentrations increased the chances of human error and pipetting inaccuracies, including in the final volume of the compound and solvent present within each well (i.e. 0.1% DMSO standard within the field). Other sources of technical inaccuracies could also be identified, including the time required to add the compounds from the first to final well of each experiment, which, combined with the length of time required for cell plating as previously discussed, could vary the length of time cells were exposed to the compound drastically across the experiment. I therefore optimised the final compound addition protocol, involving a discussion with screening experts in the Edinburgh Phenotypic Screening Centre for advice on the industry standard technique. In this protocol, a 'compound plate' of the various compounds dissolved and diluted in their respective solvents (i.e. 100% DMSO and 1000x final compound concentration) was prepared first using a standard 96-well plate arranged in a plate map that allowed the use of an automated handheld multichannel pipette to perform the serial dilution systematically across the plate. This 'compound plate' could be prepared up to a week in advance, but was usually prepared fresh on the day. Towards the end of the four hours between cell plating and compound addition, a 'media plate' was prepared, in which the 'compound plate' was dissolved in the myelination media at 1 in 50 dilution (i.e. 2% DMSO and 20x concentration). This 'compound plate' was then added to the 'cell plate', i.e. the plates in which the cells had been plated four hours previously, with 5µl being added to a final 100µl volume per well for the final 1x compound concentration (0.1% DMSO). This streamlined protocol therefore addressed the technical and timing challenges of compound addition in a multi-compound concentration-response screen, and was used as the standard protocol in the results discussed below.

Using the optimised Multidrop™ protocol discussed, the intra-plate reliability of plating across a 96-well plate was first calculated by plating 9,000 cells per well across a 96-well plate using the Multidrop™ under control media-only conditions (**Figure 3.1** A-C). The segmentation and selection criteria for counting Hoechst+ cells is summarised in **Figure 3.1** D. The coefficient of variation (CV), the measurement of variability frequently used in assay development (Reed, Lynn and Meade, 2002; Clemons, Tolliday and Wagner, 2009), with an intra-plate CV value of <20% being the acceptable threshold. For the number of nuclei in this test plate, the CV was calculated to be 8.25% by Columbus, showing good consistency in cell

plating density across the plate using the Multidrop™. The CV values for the DMSO and $NaHCO_3$ controls were also calculated for 6 of the experimental plates (3 different biological replicates) from **Figure 3.2** for both Hoechst (plating density) and MBP (differentiation; segmentation and selection criteria summarised in **Figure 3.1** E). As summarised in **Figure 3.1** F, the intra-plate and inter-plate CV were consistently under 10% for both control conditions, and for both Hoechst and MBP measurements, showing good reproducibility within and between different plates for plating and differentiation under control conditions using this experimental method.

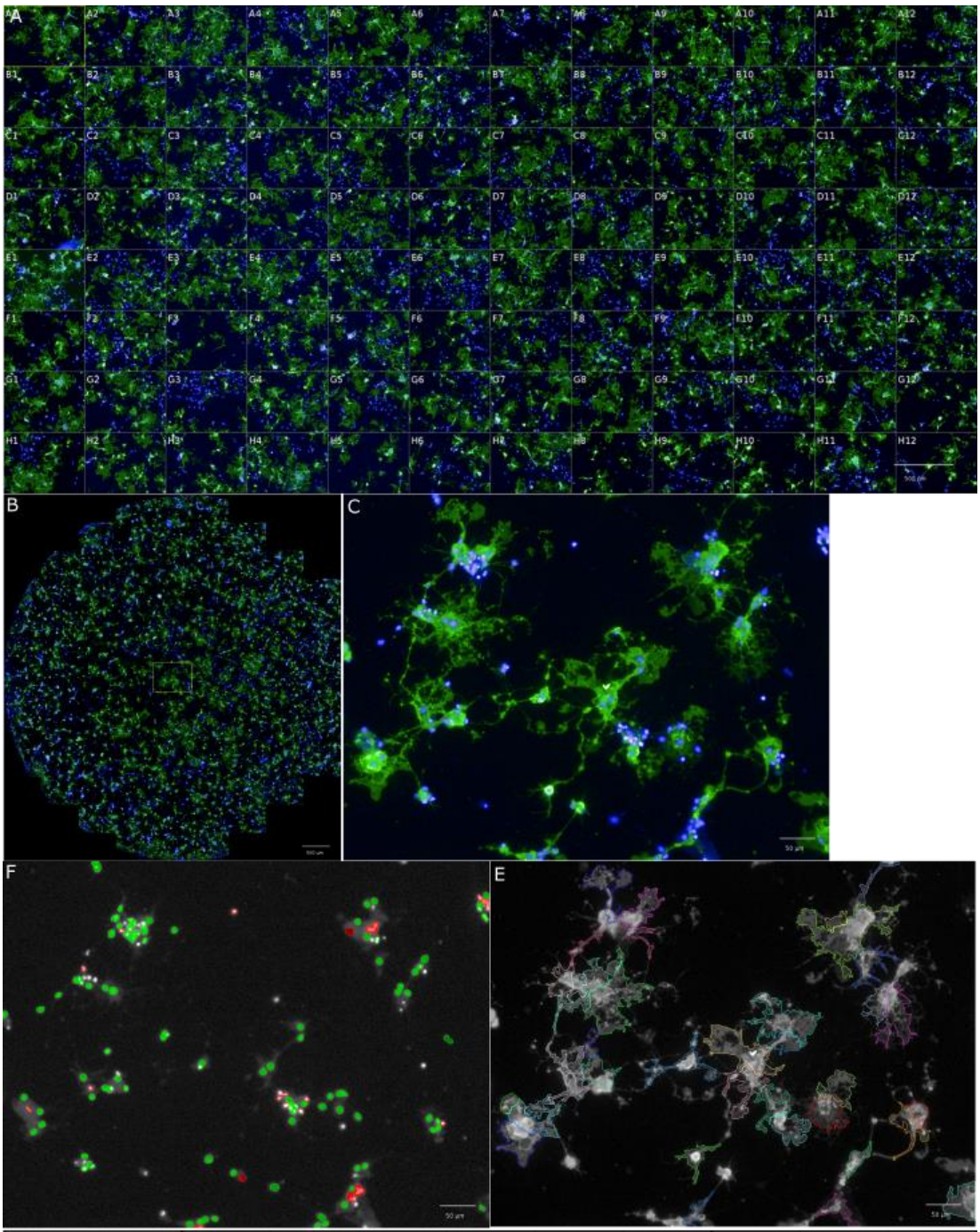

E	DMSO						$NaHCO_3$		
CV (%)	Plate 1	Plate 2	Plate 3	Plate 4	Plate 5	Plate 6	Plate 2	Plate 4	Plate 6
Intra-plate Hoechst	3.12	3.85	2.64	4.36	2.13	2.55	3.72	6.34	3.26
Inter-plate Hoechst	3.11						4.44		
Intra-plate MBP	1.84	5.10	4.51	6.48	6.53	5.60	2.76	8.12	6.08
Inter-plate MBP	5.01						5.65		

Figure 3.1 Test plate using the Multidrop™ to plate 9,000 cells/well shows consistent plating density and oligodendrocyte differentiation

A. Representative composite image from 1 out of the 93 fields-of-view imaged and analysed per well across the 96-well plate taken with the 20x objective on the Operetta system.
B. Representative composite image of a single well (E4) from the 96-well plate in A.
C. Representative single FOV from a single well (H6) taken on the Operetta using the 20x objective.
D. Segmentation and selection of Hoechst+ nuclei by Columbus from B.
   The selection criteria was: roundness > 0.8, 35 < area < 150, and mean intensity < 3000.
E. Segmentation and selection of MBP+ Hoechst+ cytoplasm by Columbus from B.
   The selection criteria was: morphology > 350, 295 < mean intensity < 1600.
F. The table summarises the coefficient of variation (CV) values for the DMSO and $NaHCO_3$ controls for 6 of the plates in the experiment in **Figure 3.2** for the Hoechst and MBP counts, segmented and selected on Columbus as per C. and D. n = 6
   The CV for both variables were consistently below 10% within and between plates, showing consistency for both plating density and oligodendrocyte differentiation using the Multidrop™ plating and Operetta imaging set-up in order to be able to determine changes based on compound addition.

Once CV calculations confirmed that differences in differentiation were due to changes in compounds and conditions rather than technical variability under the current experimental paradigm, concentration-response curves were performed for each of the compounds. Statistically significant increases in differentiation were detected at 0.37µM for Benztropine and Clemastine (**Figure 3.2** A and B). Interestingly, there was also a decrease in caspase level at the corresponding concentration (**Figure 3.3** A), from 0.12µM to 1.11µM. A preliminary experiment (n = 1) to count the number of caspase-positive Hoechst-positive cells in a live cell culture assay, which needs to be further optimised to improve staining quality, did not detect this decrease (**Supplementary Figure 3.1** B). No statistically significant increases were detected for ATP levels in any of the conditions tested (**Figure 3.3** B). However, adjacent 3D PLA microfibre culture system experiments and observations from the lab noticed a significant batch-to-batch variability in the cell viability and quality based on the batch of B21 prepared at the time of these experiments. As these assays were performed with media from 2 different batches of B21, I re-plotted and re-analysed the data to check whether any differences could be observed based on the batch of B21 used in the myelination media.

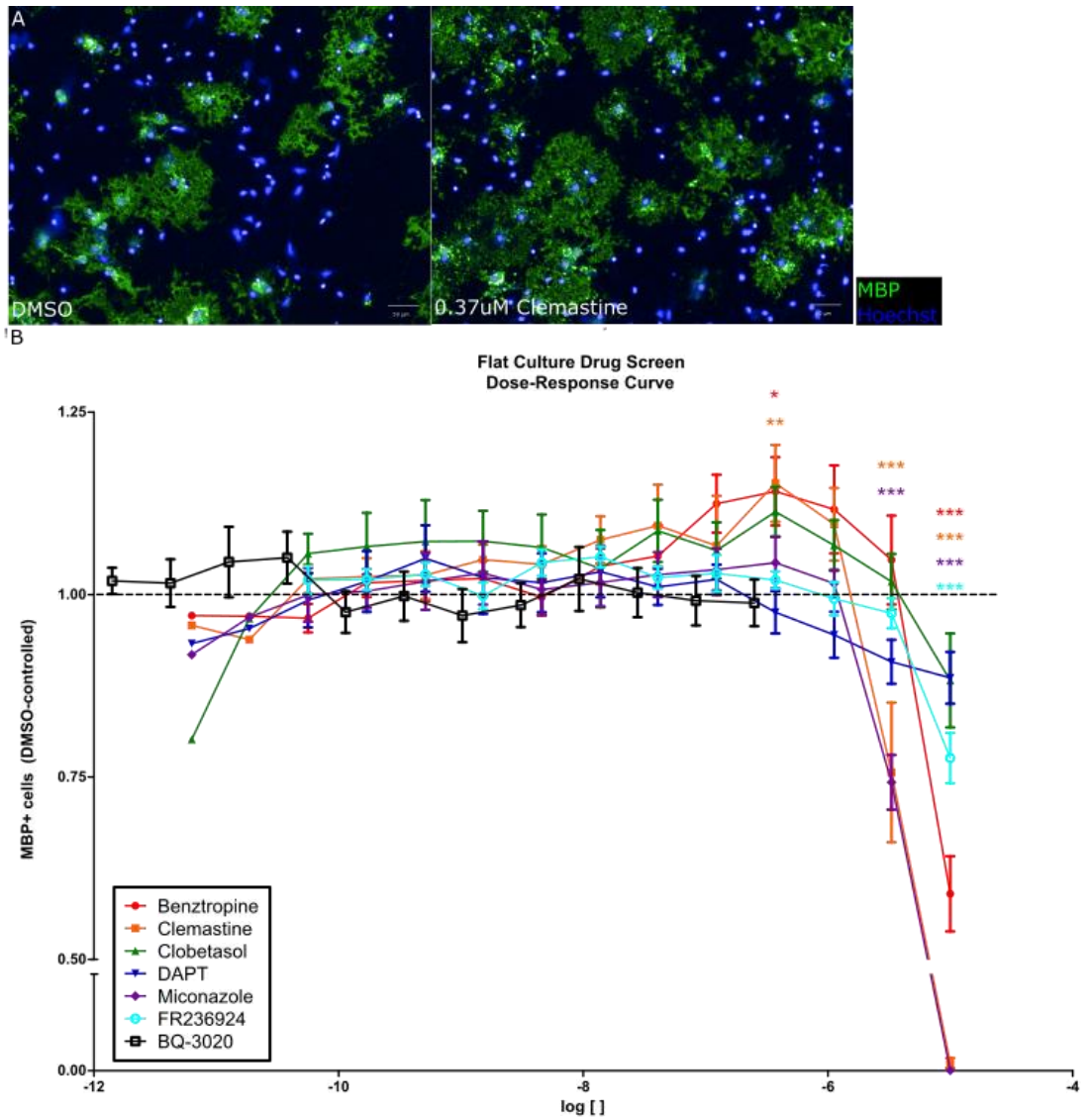

Figure 3.2 Differentiation quantification for a concentration-response curve on the 2D flat culture system shows increased oligodendrocyte differentiation with Benztropine and Clemastine at 0.37µM

A. Representative images taken on the Operetta of the DMSO control (left) and 0.37µM Clemastine (right). A statistically significant increase in MBP+ cells was detected in the 0.37µM Clemastine condition when compared to the DMSO control, as represented by the increased number of MBP+ cells in the images.

B. Differentiation response quantified by the number of MBP+ Hoechst+ cells as a ratio to the DMSO or sodium bicarbonate (BQ-3020 only) control shows significantly increased differentiated oligodendrocytes at 0.37µM for Benztropine and Clemastine.

   Each biological replicate was performed in duplicates or triplicates, and their average taken for statistical analysis. The 96-well flat culture plates were imaged on the Operetta, analysed

using a pipeline on Columbus, and plotted and analysed on GraphPad Prism. The dashed line depicts the DMSO and sodium bicarbonate control. n = 4-8

All statistics was performed on GraphPad Prism using the two-way ANOVA with post-hoc Bonferroni test in comparison to the appropriate control. * = $p < 0.05$, ** = $p < 0.01$, *** = $p < 0.001$

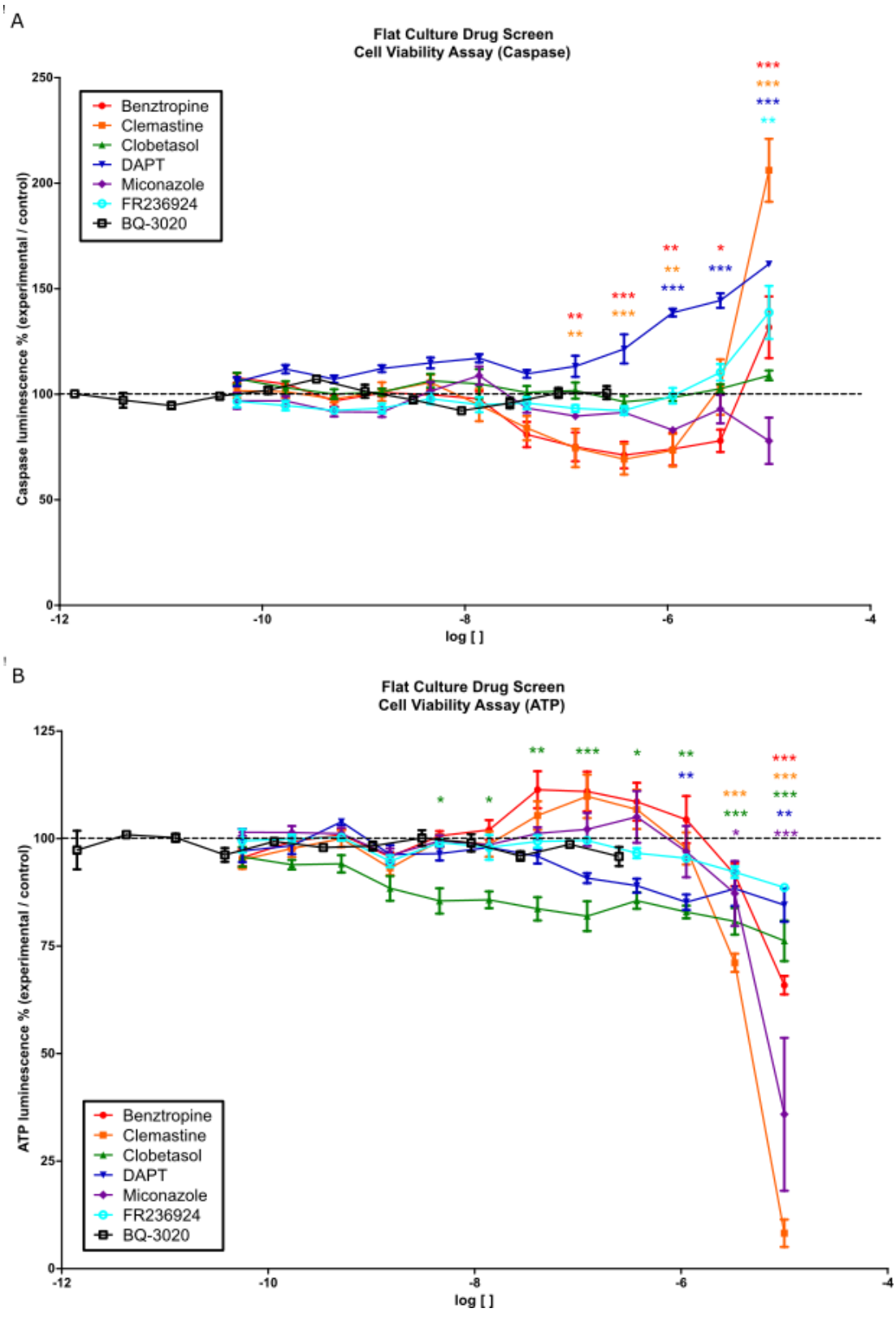

Figure 3.3 Cell viability quantification for a concentration-response curve on the 2D flat culture system shows decreased caspase levels at certain concentrations with Benztropine and Clemastine

A. Decreased caspase levels were detected at 0.12µM to 1.11µM for Benztropine and Clemastine.

   Cell viability response for caspase was quantified using the Promega Caspase-Glo® 3/7 Assay and luminescence measured on the Promega GloMax Explorer using the standard programme. The measured luminescent signal was divided by the average DMSO or sodium bicarbonate (BQ-3020 only) control measurements for the plate and recorded as a percentage. The data was plotted and analysed on GraphPad Prism. The dashed line depicts the DMSO and sodium bicarbonate control. n = 3-5

B. ATP levels were not significantly different for any of the compounds at all concentrations tested.

   Cell viability response for ATP was quantified using the Promega CellTiter-Glo® Luminescent Assay and luminescence measured on the Promega GloMax Explorer using the standard programme for the assay. The measured luminescent value was divided by the average DMSO or sodium bicarbonate (BQ-3020 only) control measurements for the plate and recorded as a percentage. The data was plotted and analysed on GraphPad Prism. The dashed line depicts the DMSO and sodium bicarbonate control. n = 3-7

   All statistics was performed on GraphPad Prism using the two-way ANOVA with post-hoc Bonferroni test in comparison to the appropriate control. * = $p < 0.05$, ** = $p < 0.01$, *** = $p < 0.001$

As can be seen in the re-plotted and re-analysed data (**Figure 3.4**), there was a clear difference in the readout for all 3 responses between the two different B21 batches, with 'Media Batch #2' seeming to eliminate the statistically significant increase in the differentiation effect for both Benztropine and Clemastine (**Figure 3.4**), and increase caspase levels (**Figure 3.5**) and decrease ATP levels (**Figure 3.6**) in comparison to 'Media Batch #1'. In adjacent experiments, 'Media Batch #1' produced oligodendrocytes with better myelin sheath formation on the 3D PLA microfibre culture system (**Figure 3.7** A), with a higher percentage of cells cultured in 'Media Batch #2' not producing myelin sheaths and appearing blebby (**Figure 3.7** B). It may therefore be possible to conclude that the results from 'Media Batch #1' better reflect the effect of the compounds, and that 'Media Batch #2' may not have been conducive to supporting the development and survival of the oligodendrocytes *in vitro*. The preliminary live caspase count (**Supplementary Figure 3.1** B) was performed in 'Media Batch #2'. Based on this assumption, Benztropine showed statistically significant increases in differentiation at 1.11µM ($p < 0.05$) and 0.37µM ($p < 0.01$) and Clemastine at 1.11µM ($p <$

0.01) (**Figure 3.4**), with significant decrease in caspase levels at 1.11µM and 0.37µM for both compounds ($p < 0.05$) (**Figure 3.5**). Statistically significant increase for ATP was not observed at the corresponding concentrations, but was observed at 0.12µM and 0.04µM for Benztropine ($p < 0.05$) and at 0.12µM for Clemastine ($p < 0.05$) (**Figure 3.6**). Collectively, it could be concluded that out of the published compounds tested on the 2D flat culture system using our mixed glia-purified OPCs, Benztropine and Clemastine showed a statistically significant effect in increasing differentiation and decreasing cell death (caspase) at certain concentrations. Importantly, the pro-myelination molecules FR236924 identified in a 3D myelination assay (Swire *et al.*, 2019) did not show any statistically significant effects in any of the responses measured on the 2D flat culture system in 'Media Batch #1'.

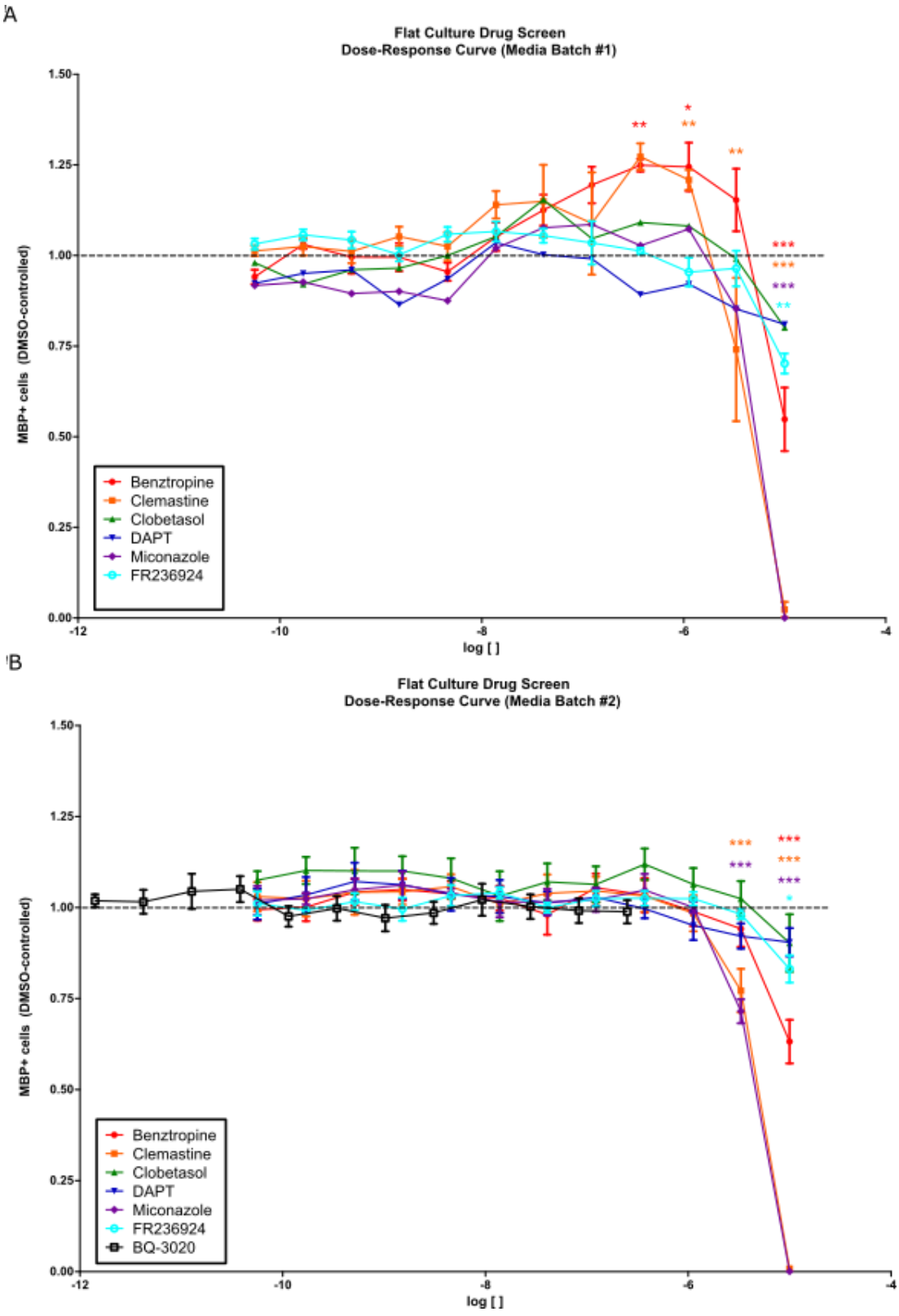

Figure 3.4 Differentiation concentration-response curve from **Figure 3.2** divided by the batch of B21 used in the myelination media show a loss of increased differentiation response in 'Media Batch #2'

The data from **Figure 3.2** was re-plotted to divide the biological replicates conducted in the myelination media prepared with the two different B21 batches due to the batch-to-batch variability in the cell culture quality between different B21 preparations.

The (A) first batch of B21 (n = 4) and the (B) second batch (n = 4) for the differentiation response show a loss of the significantly increased differentiation response for Benztropine and Clemastine at multiple concentrations in 'Media Batch #2' compared to 'Media Batch #1'.

All statistics was performed on GraphPad Prism using the two-way ANOVA with post-hoc Bonferroni test in comparison to the appropriate control. * = $p < 0.05$, ** = $p < 0.01$, *** = $p < 0.001$.

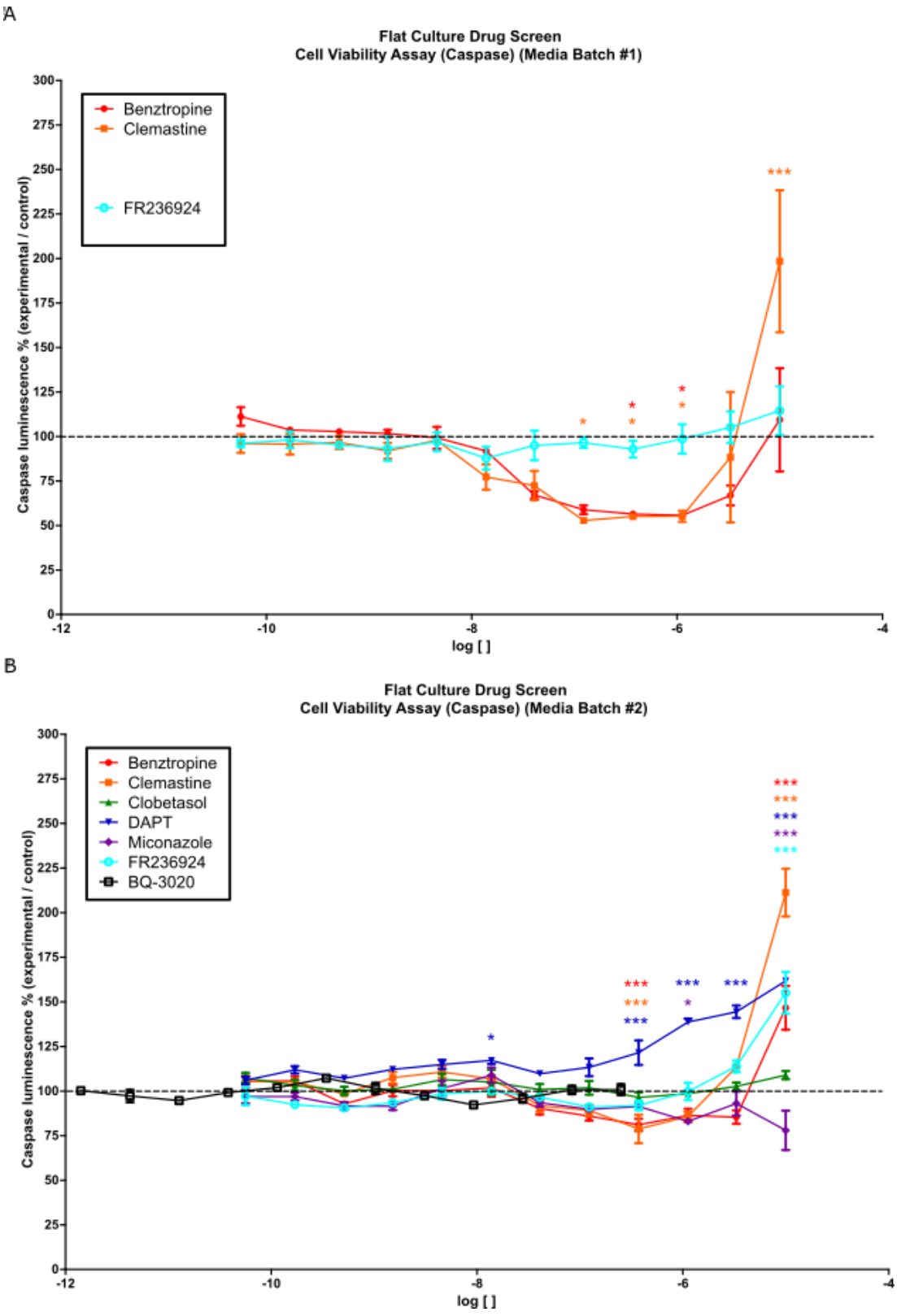

Figure 3.5 Cell death concentration-response curve from **Figure 3.3** divided by the batch of B21 used in the myelination media show increased caspase levels in 'Media Batch #2'

The data from **Figure 3.3** was re-plotted to divide the biological replicates conducted in the myelination media prepared with the two different B21 batches due to the batch-to-batch variability in the cell culture quality between different B21 preparations.

The (A) first batch of B21 (n = 2) and the (B) second batch (n = 3) for the caspase levels show the absence of the significantly decreased caspase levels with Benztropine and Clemastine in 'Media Batch #2' compared to 'Media Batch #1'.

All statistics was performed on GraphPad Prism using the two-way ANOVA with post-hoc Bonferroni test in comparison to the appropriate control. * = $p < 0.05$, ** = $p < 0.01$, *** = $p < 0.001$.

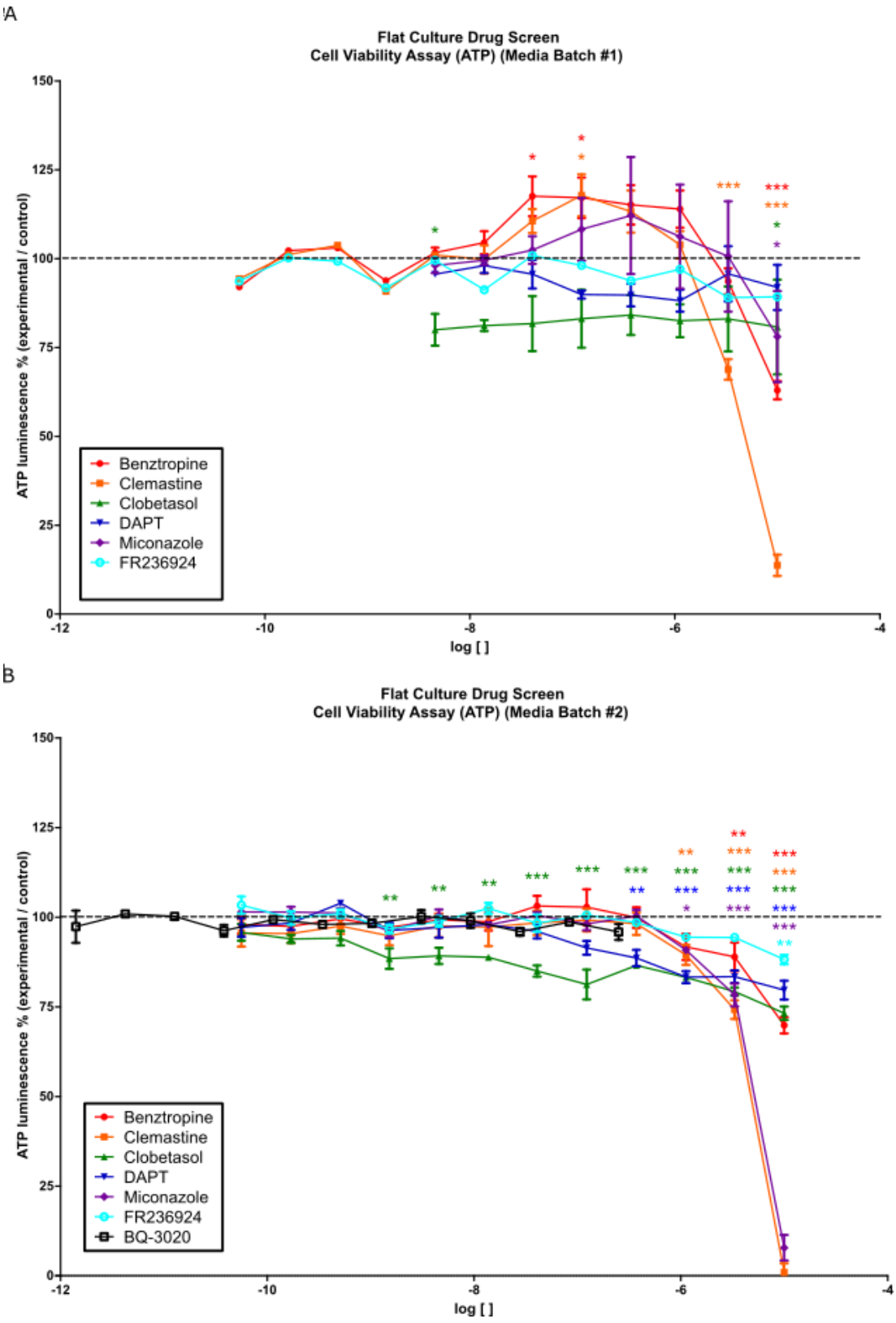

Figure 3.6 Cell activity concentration-response curve from **Figure 3.3** divided by the batch of B21 used in the myelination media show decreased ATP levels in 'Media Batch #2'

The data from **Figure 3.3** was re-plotted to divide the biological replicates conducted in the myelination media prepared with the two different B21 batches due to the batch-to-batch variability in the cell culture quality between different B21 preparations.

The (A) first batch of B21 (n = 4) and the (B) second batch (n = 3) for ATP levels show the absence of the significantly increased ATP levels with Benztropine and Clemastine in 'Media Batch #2' compared to 'Media Batch #1'.

All statistics was performed on GraphPad Prism using the two-way ANOVA with post-hoc Bonferroni test in comparison to the appropriate control. * = $p < 0.05$, ** = $p < 0.01$, *** = $p < 0.001$.

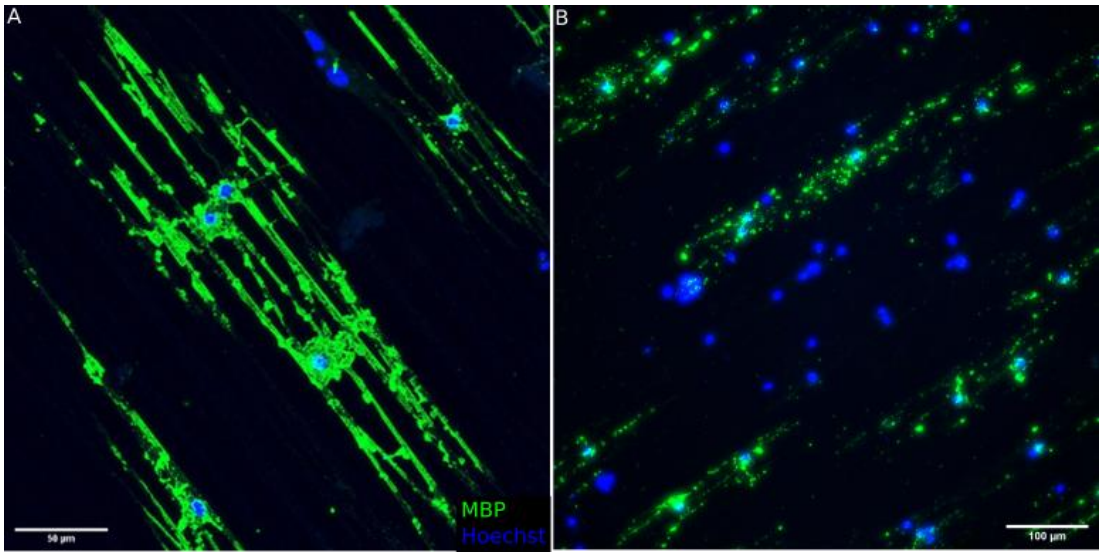

Figure 3.7 Comparison images of oligodendrocytes cultured on microfibres in 12-well scaffolds in 'Media Batch #1' versus 'Media Batch #2' show poor cell quality in 'Media Batch #2'

A. Representative image of oligodendrocytes cultured on microfibres in the DMSO control condition in 'Media Batch #1' imaged on the Leica SP8 (40x objective) show MBP+ oligodendrocytes producing myelin sheaths, as confirmed by z-stack imaging.
B. Representative image of oligodendrocytes cultured on microfibres in 'Media Batch #2' show MBP+ oligodendrocytes that are not producing myelin sheaths and appear to be producing blebs of broken up MBP+ membranes, highlighting poor cell quality in this batch of B21. Image provided courtesy of Dr. Peggy Assinck (Nikon, 20x objective).

3.2.2 Testing of the compounds identified in published drug screens on their effect on myelin sheath formation on 3D PLA microfibre culture system

In order to test whether these published drugs increased myelin sheath length and number, they were tested on OPCs purified from mixed glia cultures plated on 12-well PLA microfibre scaffolds. The drugs were first added 3 days after plating onto the fibres to test their effect on myelin sheath formation rather than differentiation with fresh drugs being added every 2 to 3 days until fixation on day 14. In the initial cultures, each of the drugs were tested at two different concentration, 1µM, as 1.11µM increased differentiation for Benztropine and Clemastine in the 2D flat culture system ('Media Batch #1'), and 0.1µM, a ten-fold lower concentration. The concentration at which the cells looked more viable when checked by confocal microscopy was used for all further repeats of the experiment (**Figure 3.8** A). During this period, our lab experienced significant issues with myelination on the microfibre culture system to which we narrowed down the issue to the B27 in the myelination media. Although I was able to obtain myelin sheath formation to a certain degree for this experiment, it was to a much lower quality and quantity than previously described (Bechler, Byrne and ffrench-Constant, 2015), and especially impacted the number of myelin sheaths that each oligodendrocyte was able to produce from an average of 6 sheaths per cell, and up to 15, to an average of 3 sheaths per cell in the impacted myelination media.

Figure 3.8 B represents the range of myelin sheath lengths observed across all quantified myelin sheaths in the control and compound treated conditions. The average per biological replicate was plotted, as shown in **Figure 3.8** C, and a one-way ANOVA with the post-hoc Dunn's Multiple Comparison test performed to check for significant changes in myelin sheath length compared to the DMSO control. None of the compounds at the tested concentrations appeared to significantly increase or decrease myelin sheath length on our PLA microfibre culture system. Potentially more physiologically and pharmacologically relevant for MS treatment, due to myelin sheath length being a key factor in saltatory conduction and nerve signalling coordination and therefore significant pharmacological changes in this property potentially hindering its physiological function, the number of myelin sheaths produced per MBP+ cell was also quantified. **Figure 3.9** A represents the range of myelin sheath numbers observed across all quantified cells in the control and compound treated conditions. The average per biological replicate, as shown in Figure 3.8 B, was used to perform a one-way

ANOVA with the Dunn's Multiple Comparison test. This detected no significant changes in myelin sheath number in any of the drug conditions as compared to the DMSO control. As mentioned, due to the number of myelin sheaths produced per cell being impacted by the poor quality of the B27 in the myelination media, especially highlighted by the average number of myelin sheath in the media control in **Figure 3.8** C, the data was re-calculated to control for the average number of myelin sheaths produced by the DMSO control in the same biological batch of cells to test whether the low inter-experimental consistency was masking any effect. However, even when taking into account the differences in the average number of myelin sheaths produced between different replicates, there was no significant changes to the number of myelin sheaths produced with any of the published drugs tested.

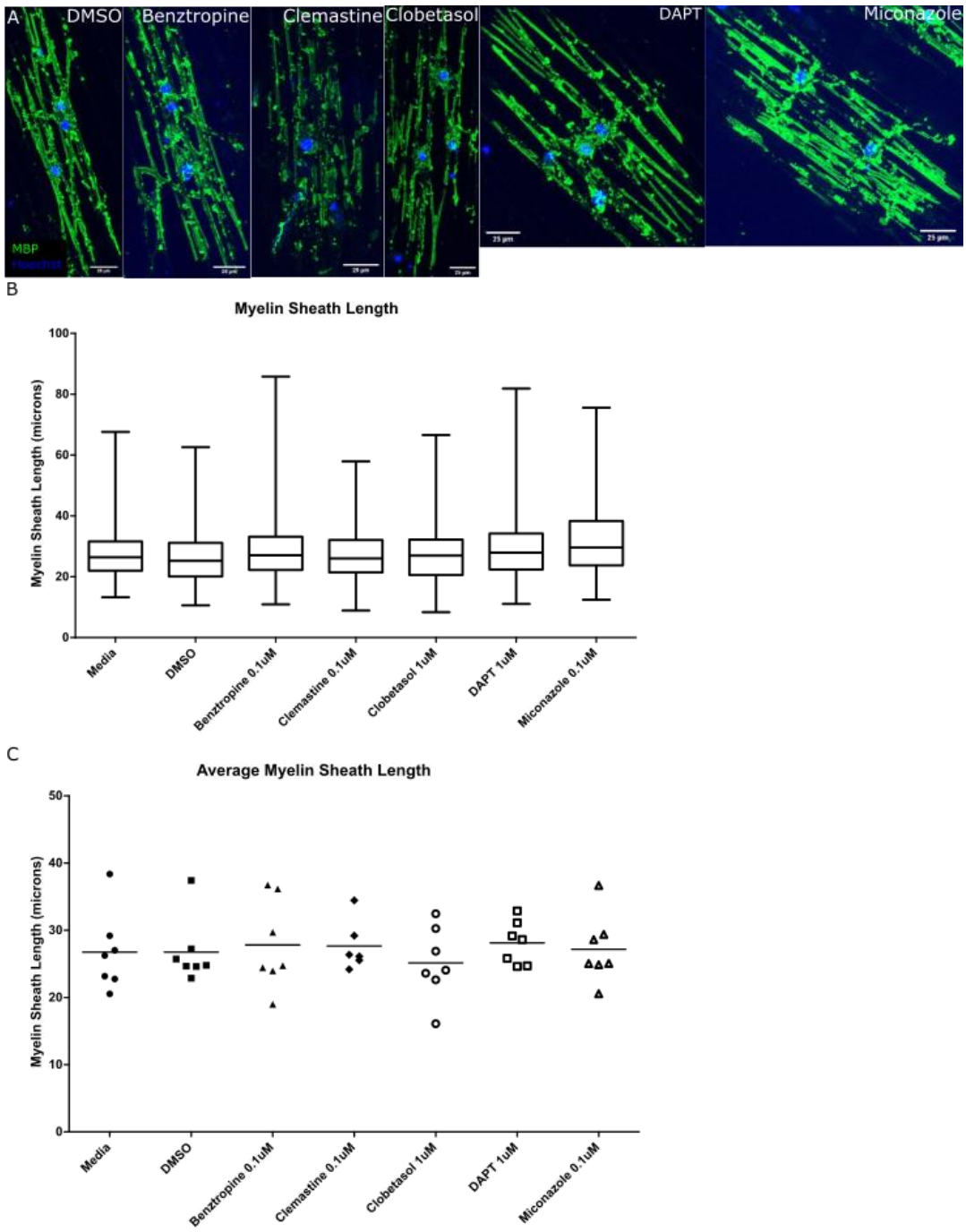

Figure 3.8 Myelin sheath length quantification on the 3D PLA microfibre culture system show no significant changes in any of the compounds identified from published screens

A. Representative images of myelin sheath-forming oligodendrocytes from each of the drug conditions taken with the 40x objective on the Leica SP8 confocal for quantification. Each of the compounds at the concentration tested show robust myelin sheath formation as determined by visualising an overview of each coverslip, and taking z-stack images of at least 15 cells per condition per biological replicate.

B. Myelin sheath length measurements was quantified by manual measurements on Fiji using simultaneous z-stack and maximum projected images, recorded on Excel, and plotted and analysed on GraphPad Prism 5. The box-and-whisker plot show the range of measurements obtained as represented by the maximum and minimum at the 'whiskers', and the 75th, 50th, and 25th quartiles with the lines on the 'box' from top to bottom. n =7

C. The average myelin sheath length per biological replicate was calculated from the data in A to test for statistical significance. No significant changes in any of the tested conditions were shown compared to media and DMSO controls.

   The statistical test performed was the one-way ANOVA with post-hoc Dunn's Multiple Comparison test for analysis.

A

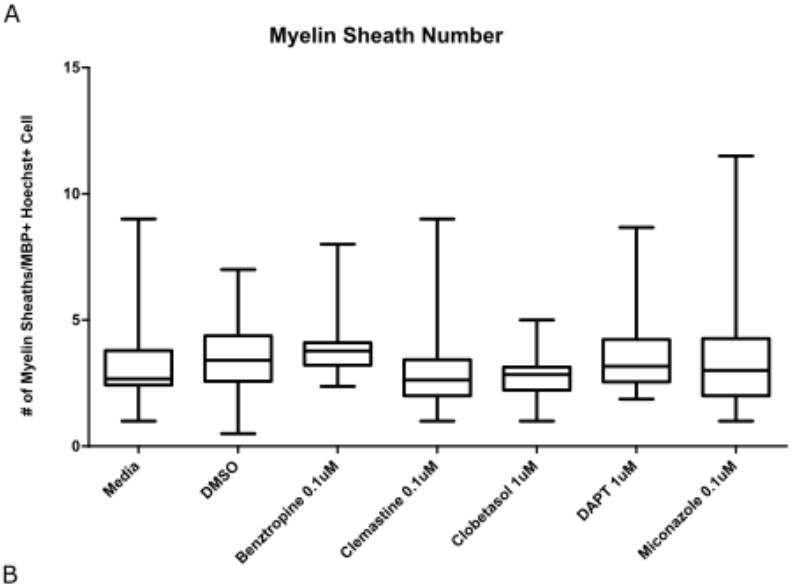
Myelin Sheath Number
# of Myelin Sheaths/MBP+ Hoechst+ Cell
15
10
5
0
Media
DMSO
Benztropine 0.1uM
Clemastine 0.1uM
Clobetasol 1uM
DAPT 1uM
Miconazole 0.1uM

B

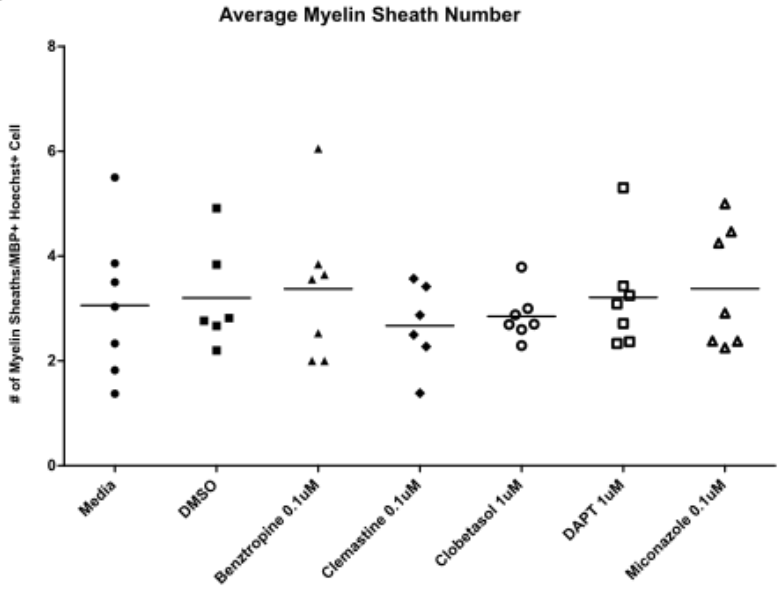
Average Myelin Sheath Number
# of Myelin Sheaths/MBP+ Hoechst+ Cell
8
6
4
2
0
Media
DMSO
Benztropine 0.1uM
Clemastine 0.1uM
Clobetasol 1uM
DAPT 1uM
Miconazole 0.1uM

C

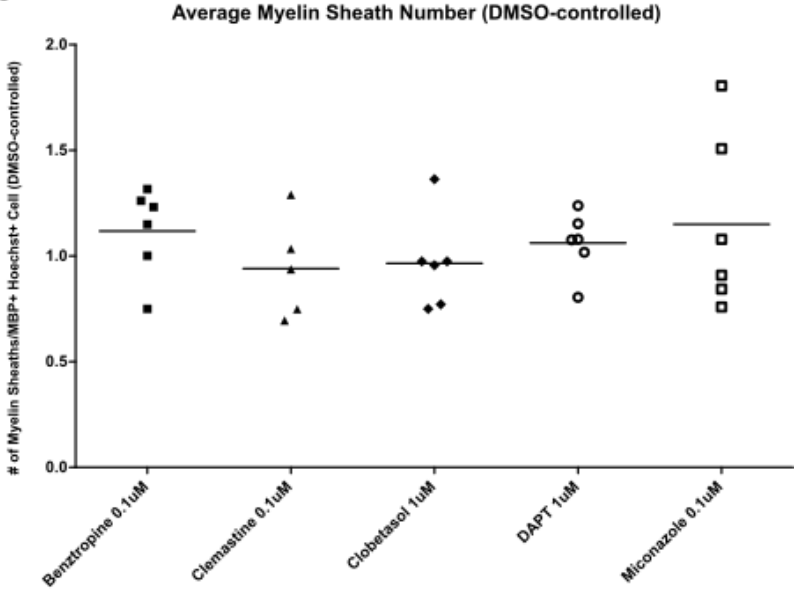
Average Myelin Sheath Number (DMSO-controlled)
# of Myelin Sheaths/MBP+ Hoechst+ Cell (DMSO-controlled)
2.0
1.5
1.0
0.5
0.0
Benztropine 0.1uM
Clemastine 0.1uM
Clobetasol 1uM
DAPT 1uM
Miconazole 0.1uM

Figure 3.9 Myelin sheath number quantification on the 3D PLA microfibre culture system show no significant changes in any of the compounds identified from published screens

A. The number of myelin sheath per MBP+ cell as shown on a box-and-whisker plot. Sheaths were only counted when MBP+ cells were distinctly separate, and excluded when the cell bodies were clumped in close proximity, making it difficult to distinguish the cell body from which the sheath originated. n = 7
B. The average number of myelin sheath per biological replicate as calculated from the data in A to test for statistical significance. None of the compounds tested showed statistically significant changes in the number of myelin sheaths produced compared to media and DMSO controls.

   Statistical analysis was performed using the one-way ANOVA with post-hoc Dunn's Multiple Comparison test for analysis.
C. The average number of myelin sheath was normalised for the DMSO control per biological replicate from data in C. Even after taking the potential variability between replicates into account, no significant changes were shown in the number of myelin sheaths in all of the conditions tested.

   Statistical analysis on this data was performed using the one-way ANOVA with post-hoc Dunn's Multiple Comparison test.

3.3 Discussion

In this chapter I asked the question whether, given that differentiation and myelination occurs as a two-step process, pro-differentiation compounds may not necessarily also enhance remyelination. To do this, I utilised compounds and peptides that have been previously published in differentiation (Deshmukh *et al.*, 2013; Lariosa-Willingham *et al.*, 2016a, 2016c; Najm *et al.*, 2015), ensheathment using wrapping around the base of micropillars (BIMA) (Mei *et al.*, 2014), and axonal myelination (Lariosa-Willingham *et al.*, 2016b) screens, as well as compounds identified to increase myelin sheath number by Swire *et al.* (2019) and Yuen *et al.* (2013), and tested these in a 2D versus 3D culture system using OPCs isolated from mixed glia cultures. My results provide preliminary support for the conclusion that pro-differentiation compounds do not promote myelination directly, and vice versa.

This conclusion is based on three results. First, accounting for the difference in results based on the batch of B21 used, and assuming 'Media Batch #1' to better reflect the OPC differentiation and the effects of the drugs in a more supportive environment based on the caspase and ATP assays and parallel 3D myelination experiments, and taking into consideration that the number of biological repeats for experiments solely performed on 'Media Batch #1' is quite low, especially for the caspase levels (n = 2), early results show a statistically significant increase in differentiation could be detected at 1.11µM and 0.37µM for Benztropine and at 1.11µM for Clemastine, with decreased caspase levels at 1.11µM and 0.37µM for both compounds and increased ATP levels at 0.12µM and 0.04µM for Benztropine and 0.12µM for Clemastine. The Clemastine was of particular interest as its positive Phase I clinical trial results have been published (Green *et al.*, 2017), and is currently in Phase II clinical trials.

Second, FR236924, one of the compounds identified to increase myelin sheath number by Dr. Matthew Swire, did not show pro-differentiation and cell survival results in the three metrics examined based on results of its testing in 'Media Batch #1'. It would therefore potentially not have been picked up in a pro-differentiation-based screen despite its pro-myelination property. Another myelination-promoting compound, the EDNRB agonist BQ-3020, was only included in the experiments using 'Media Batch #2' so, although it didn't show any positive effects, it would need to be re-tested in a different batch of media to confirm whether it was a pro-myelination but not a pro-differentiation compound, or whether it was potentially both but had its effect masked by the problematic media. Previous experiments conducted in our lab by Tracy Yuen using BQ-3020, however, showed that this compound does not increase the number of differentiated OPCs, and therefore suggests that it is likely a pro-myelination but not a pro-differentiation compound. Although this compound would ideally need to be re-tested in my experimental paradigm for direct comparison, this suggests that both these pro-myelination compounds would not likely have been identified in pro-differentiation assays.

Third, when tested on the 3D microfibre culture system, none of the published pro-differentiation compounds increased either myelin sheath length or number. Interestingly, γ-secretase inhibitor DAPT, a compound used as the positive control in an axonal myelination assay (Lariosa-Willingham *et al.*, 2016b), did not show increased myelin sheath formation in our microfibre oligodendrocyte myelination assay. This compound had previously been

reported to enhance differentiation and ensheathment in a myelinating CNS co-culture system of retinal ganglion cells (RGCs) from the optic nerve and OPCs, with the inhibition of the γ-secretase-activated Notch1 signalling enhancing differentiation, and the inhibition of γ-secretase enhancing ensheathment through a Notch1-independent mechanism (Watkins *et al.*, 2008). This highlights one of the limitations of a single cell type-specific assay, in which a compound may potentially work through a mechanism that requires the interaction between multiple cell types, and therefore not increase differentiation in 2D OL flat culture or increase myelination in 3D OL microfibre culture. Another reason as to why DAPT may not have increased myelination in the microfibre culture system was that it increased the number of OLs that were able to differentiate and ensheath axons in a system with poor OPC differentiation or high degree of trans-differentiation into astrocytes by the OPCs (Watkins *et al.*, 2008). Therefore, the increase in myelination through γ-secretase inhibition by DAPT may have been a characteristic of the co-culture system to improve its application in studying axonal myelination *in vitro*.

Collectively, although further biological replicates performed in media with a more supportive B21 batch would strengthen the evidence, these data support the conclusion that pro-differentiation screens do not necessarily pick up pro-myelination compounds, and that pro-differentiation compounds may not also be pro-myelination. This highlights the biological validity of developing a drug screening platform aimed at detecting myelination as its primary output. The low yield of RGCs, the difficulties of culturing neuronal-OPC co-cultures *in vitro*, and the reproducibility of the assay limits the current method of assessing myelination *in vitro* using co-cultures in its potential application for high-throughput screens.

How can one solve these problems with existing assays in detecting pro-myelinogenic drugs? Lariosa-Willingham *et al.* (2016b) targeted some of the limitations of low neuronal cells yield by using embryonic rat cortical brain cells in developing their co-culture based myelination assay, which resulted in cultures with approximately 23% neurons, 47% astrocytes, 22% OPCs/OLs, and 9% other unidentified cell types, with no exogenous OPCs added. However, the batch-to-batch variability of the cell composition may pose an issue in the reproducibility and consistency of the assay. A different approach, the 3D OL microfibre system has been shown to be able to detect increases in myelin sheath formation through OL mechanisms, such as endothelin receptor type B in OL lineage cells through the endothelin receptor agonist peptide BQ-3020 (Yuen *et al.*, 2013), and small molecule PKCε activator FR236924,

which were both verified to increase the number of myelin sheath number per OL on the microfibre system (Swire *et al.*, 2019). Therefore, the development of a high-throughput-compatible 96-well microfibre plate in screening for pro-myelination compounds in a neuron-free myelination assay takes a step forward in addressing: (1) the difference between pro-differentiation and pro-myelination compounds as tested through the 2D versus 3D culture systems in this chapter, (2) being able to detect compounds that are pro-myelination through OL mechanisms, and (3) the ability to increase the throughput of a myelination assay in a controlled reproducible system.

CHAPTER IV. CONSTRUCTION OF A HIGH-THROUGHPUT-COMPATIBLE 96-WELL MICROFIBRE PLATE

4.1 Introduction

To create a phenotypic screening platform suitable for the assessment of myelin sheath formation, the challenges are: i) to manufacture a material that can provide an artificial axon for the OL to form myelin sheaths around, and ii) to insert it into a multi-well plate as a floor suspended above an optically-transparent base so creating a format that is suitable for screening. As previously discussed, OLs cultured in the presence of artificial axons will wrap membranes around them, with materials used successfully including glass (Bullock and Rome, 1990) although coating is required for ensheathment (Howe, 2006), paraformaldehyde-fixed axons (Rosenberg *et al.*, 2008), and electrospun polystyrene and PLA fibres (Bechler, Byrne and ffrench-Constant, 2015; Lee *et al.*, 2012, 2013). The ability of myelin sheath formation on electrospun fibres is of particular interest due to, as described in the next section, the ability to use electrospinning to produce customised electrospun fibres of consistent diameter (of approximately 2µm) and density by controlling various parameters, that can then potentially be incorporated into a multiwell plate format suitable for high-throughput drug screening applications. As discussed in this chapter, I therefore started by developing this technology working with the guidance and expertise of colleagues at the Schools of Chemistry and Engineering, with the goals being: (1) to manufacture fibres permissive for myelination, and (2) to incorporate these into a custom-built 96-well plate.

4.1.1.Electrospinning

In 1887, C. V. Boys described “the old, but now apparently little-known experiment of electrical spinning”, whereby he observed that if a small insulated dish filled with a viscous material, including melted rosin, beeswax, and shellac, was connected to an electrical source, the material would be shot out as threads at the edge of the dish along “lines of force” (Boys, 1887). Patents for slightly different variations of the technique have been filed since 1934,

and the term “electrospinning” was introduced in literature more recently in 1994 (Huang *et al.*, 2003).

In the electrospinning process, a strong electrostatic field, ranging in the several tens of kV, is applied to a capillary tube/spinneret (i.e. a needle tip) that is connected to a syringe containing a viscous solution of a polymer dissolved in a solvent (**Figure 4.1** A). The electrostatic force causes the polymer solution at the end of the needle tip to deform into a Taylor cone (**Figure 4.1** B). As the voltage is increased, the electrostatic force overcomes the surface tension, resulting in a charged jet of polymer solution being ejected from the tip of the Taylor cone, at which point the solvent begins to evaporate to leave behind a deposition of thin polymer fibres that travels in an unstable and whipping manner. As the jet is charged, a counter electrode is used to control its trajectory and act as the grounded collecting plate, typically in the form of a metal screen, plate, or rotating mandrel. The rotating collector is particularly useful for the collection of aligned, mostly parallel electrospun fibres (**Figure 4.1** C) (Bhardwaj and Kundu, 2010; Bognitzki *et al.*, 2001; Doshi and Reneker, 1995; Huang *et al.*, 2003).

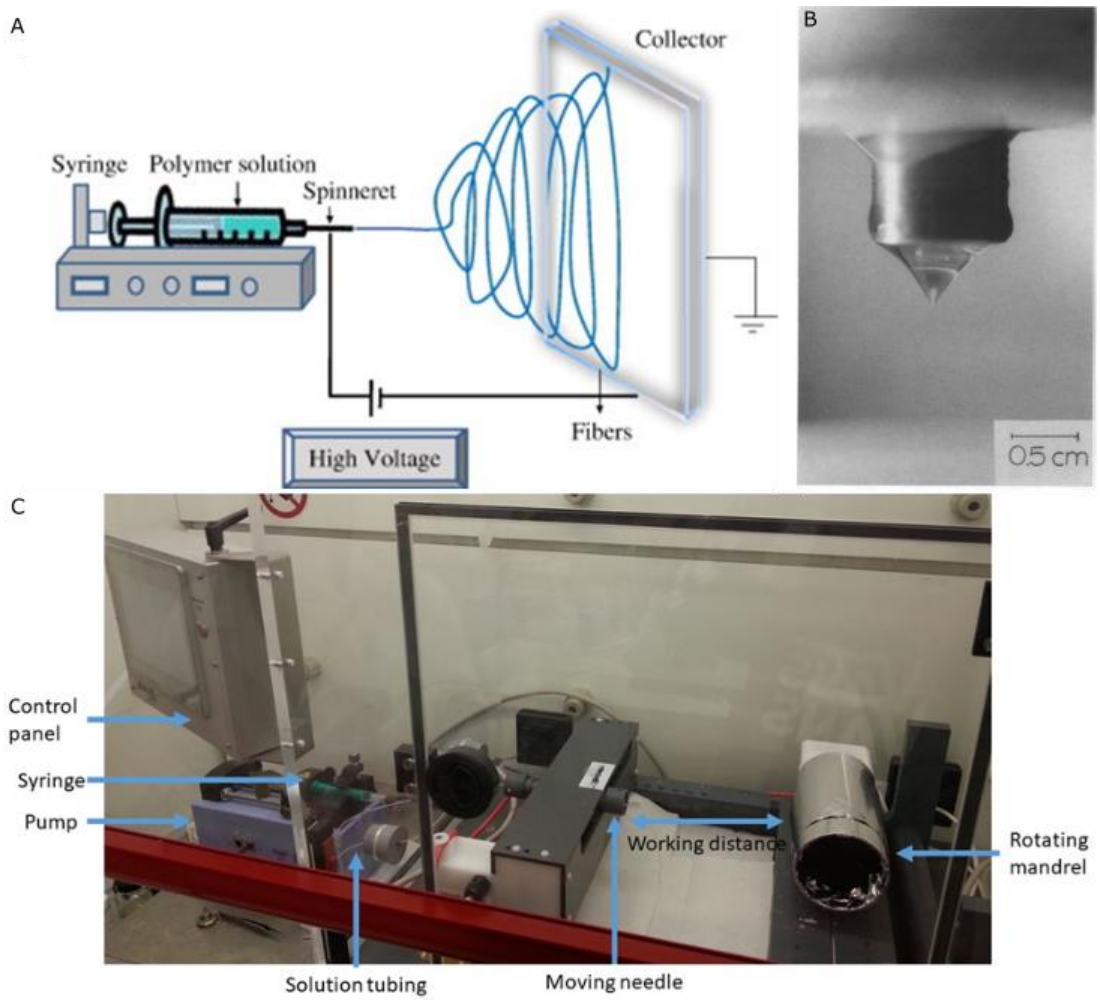

Figure 4.1 The electrospinning set-up

A. Schematic diagram of the set-up of a horizontal electrospinning apparatus: the polymer solution is contained within the syringe and extruded through the spinneret, where the high voltage is applied, for the fibres to be accumulated at the collector.
(Figure from Bhardwaj and Kundu, 2010)

B. Photograph of the conical shaped solution at the tip of the needle/capillary tube called the Taylor cone. The formation of the Taylor cone indicates that a stable flow of the polymer solution has been achieved at the tip of the needle, which is obtained by balancing the concentration of the polymer solution with the diameter of the spinneret, the voltage applied, the working distance to the collector, and the charge at the collector.
(Figure from Meesters *et al.*, 1992)

C. Photograph of the horizontal electrospinning set-up at the School of Engineering, The University of Edinburgh. The syringe contains the polymer solution, which is placed in the pump to control the flow rate. The solution travels through the solution tubing to the needle, which is placed in a moving head to allow even distribution of the fibres across a wider surface

area, and allows the high voltage to be applied. The solution travels across the working distance to the collector, which in this set-up is a rotating mandrel which allows the fibres to be collected in a parallel alignment by pulling the fibres across it as it spins. The control panel allows the speed of the pump, the voltage at the needle and the mandrel, the rate and distance travelled of the moving needle, and the rotation speed of the mandrel to be adjusted.

The properties of the electrospun fibres are dictated by several factors including: (1) solution parameters, (2) processing parameters, and (3) ambient parameters. A few key solution parameters include the molecular weight of the polymer, which influences electrical and rheological properties, and concentration, important for viscosity and surface tension of the solution and therefore having a strong influence on the shape and thickness of the fibres. The optimisation of a suitable solvent to be used in the complete dissolving of the polymer into solution in the preparation of the polymer solution is the essential first step in the optimisation of the electrospinning process as it not only dissolves the polymer, but also carries the polymer molecules towards the collector. Important solvent properties include: (a) its volatility in the formation of the polymer structures due to its influence on the phase separation process, (b) boiling point due to the use of high voltages, and (c) vapour pressure in determining the rate of its evaporation. Processing parameters include: (a) the voltage in overcoming the threshold to initiate electrospinning, (b) flow rate of the polymer from the syringe into the needle tip to control the material transfer rate and jet velocity while allowing the solvent to evaporate in controlling fibre diameter, (c) working distance from the tip to collector in regulating fibre diameter and morphology, and (d) the type of collector in the alignment and transfer of the collected fibres. In addition, ambient parameters including humidity and temperature could be of importance in manipulating fibre morphology due to their effect on polymer solution viscosity and solvent evaporation (Huang *et al.*, 2003; Bhardwaj and Kundu, 2010).

4.2 Results

4.2.1 Optimisation of the polymer solution for electrospinning and myelination

The first step in the construction of 96-well plate suitable for screening applications is the generation of microfibres of appropriate diameter (2µm). As described above, solvent and polymer choices (together creating the polymer solution) are the key variables, and so I started by optimising these.

Based on the expertise of the early electrospinning collaborators (Dr. Hua Dong, Bradley Lab at the School of Chemistry), initial experiments used 8% polyurethane (PU, Sigma-Aldrich 81367) as the polymer dissolved in 1 demethylformamide (DMF, Rathburn PTS6020): 1 tetrahydrofuran (THF, Thermo Fisher T/0701/17) (w/w/w) ratio or 8% PU in 1 DMF: 1 dichloromethane (DCM, Thermo Fisher D/1852/17) (w/w/w). Both ratios were initially tested as the polymer for electrospinning at the School of Chemistry, the University of Edinburgh. A vertical electrospinner set-up (Spraybase) with a stationary syringe and needle tip over a metal plate was used, with a 18G needle tip as the spinneret, voltage was set to between 6.43 and 6.76kV, and the working distance set to between 16 and 19cm. Temperature and humidity was also monitored. As shown in **Figure 4.2** A, the fibres were of uneven diameter and morphology, with differences in diameter of 1µm to over 5µm. Additionally, OPCs cultured on these PU fibres differentiated, as they expressed the marker MBP, but did not seem to ensheath the fibres even after 10 days (**Figure 4.2** B), in contrast to the myelin sheath formation being seen in commercially obtained electrospun microfibre cultures by at least 7 days by Bechler, Byrne and ffrench-Constant (2015). The OLs that had differentiated on these PU fibres seemed to more closely resemble OPCs cultured on flat coverslips rather than on fibres.

As OL myelin ensheathment had previously been shown on commercially obtained fibres made of PLA fibres by Bechler, Byrne and ffrench-Constant (2015), I next tested PLA as the polymer in this electrospinning device. 10% PLA (Sigma-Aldrich 81273) was dissolved in 3 DMF to 7 DCM (w/w/w) ratio, with an 18G needle tip, working distance set to 15cm, voltage to 9.09kV, and a pump to control the flow rate of the jet added, set to 0.6ml/hr. DCM was used due to its property as a good solvent, but due to its low boiling point, DMF was added to increase the boiling point of the solution and keep the polymer in solution when not being

warmed. The SEM image (**Figure 4.2** C) showed smoother, more tube-like fibres in morphology, and OLs cultured on these fibres for 10 days showed structures that looked like myelin sheath formation (**Figure 4.2** D). However, when the diameter of the fibres was measured across two different batches, the diameter was too low (based on previous work published by Bechler, Byrne and ffrench-Constant (2015) using fibres of 2µm diameter) with the majority of the fibres being between 1 to 1.5µm, and slight variations in diameter between the two batches (**Figure 4.2** E). To increase the diameter of the fibres, different concentrations of the PLA (10% vs. 12% vs. 15%) and in different ratios of DMF to DCM (w/w) (2:8, 4:6, 6:4). However, in all these tested concentrations and ratios, the solution turned too viscous to electrospin with (15% PLA), only produced a small amount of solution compared to the amount of material (10% and 12% PLA, 2 DCM: 8 DMF), or turned white and solid as the polymer crashed out of the solution and solidified (remaining conditions).

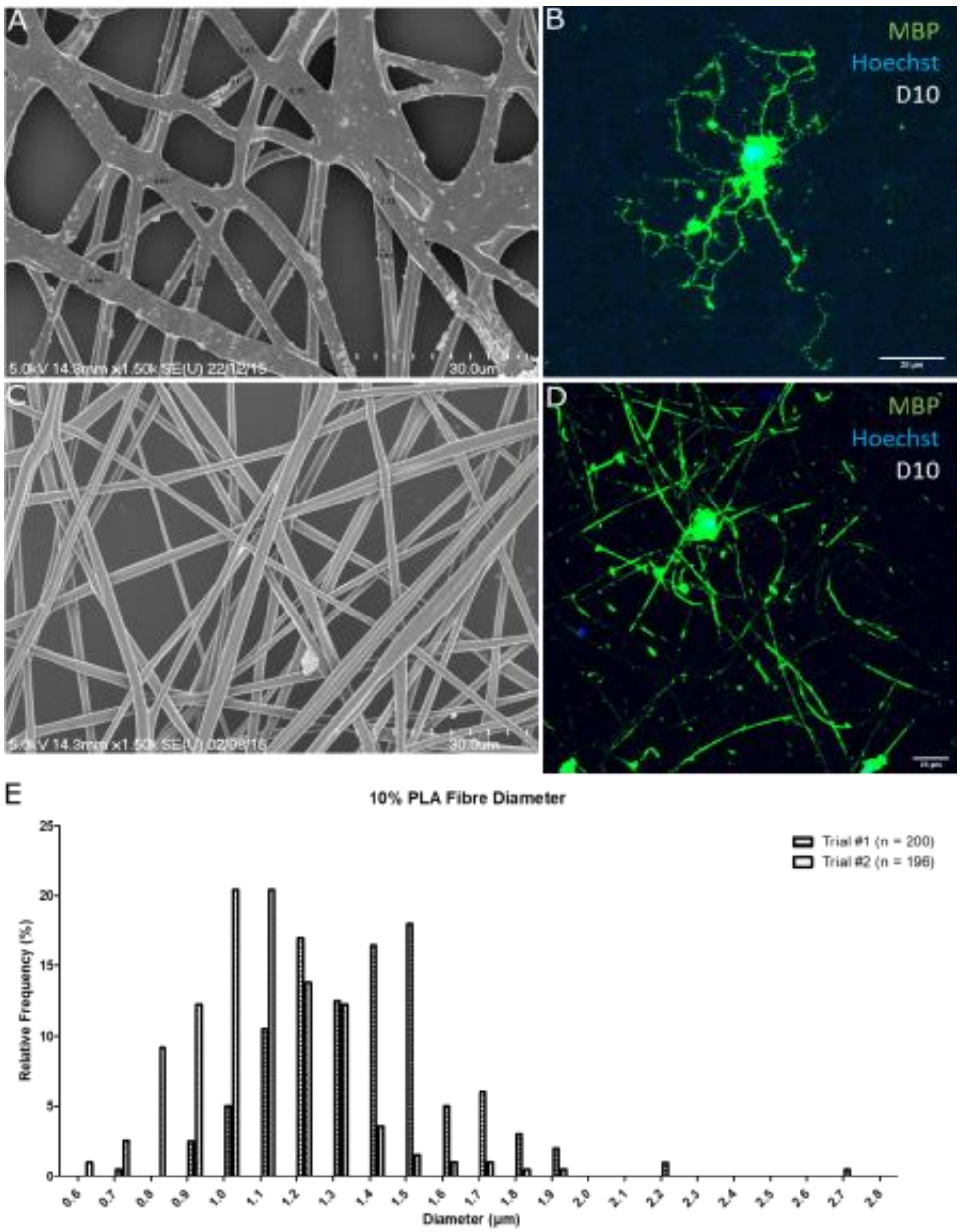

Figure 4.2 Polyurethane and poly-L-lactic acid dissolved in DCM and DMF does not produce microfibres of even appearance and equal diameter

a) Representative SEM image of electrospun 8% PU microfibres. The values of the individual fibres are labelled on the image, and range from just above 1µm to over 5µm, with the appearance of clumping and uneven morphology.

b) Representative confocal image of an OL cultured on the 8% PU fibres for 10 days, showing differentiation but not sheath formation.

c) Representative SEM image of electrospun 10% PLA microfibres dissolved in DCM and DMF, showing variable appearance between and within each microfibre, and not showing

consistently smooth and round tubular topography. The 'n' number represents the number of individual fibres measured for each batch.

d) Representative confocal image (Leica SP8, 40x objective) of an OL cultured on the 10% PLA (DCM:DMF) microfibre for 10 days, showing both differentiation and myelin sheath formation as determined by MBP staining and z-stack imaging. The myelin sheaths are randomly orientated using electrospun fibres produced using this set-up.

e) Histogram of the fibre diameter measured for the 10% PLA in DCM: DMF fibres across two independent batches. Variation in the distribution of the fibre diameter between the two batches can be seen, as well as uneven distribution within a batch.

In order to overcome the difficulty of producing a solution at a high enough polymer concentration to achieve the desired diameter, the speciality organic solvent 1,1,1,3,3,3-hexafluoro-2-propanol (HFIP, Sigma-Aldrich 105228) was used as the solvent in further experiments. HFIP, although costly, is reported to be able to dissolve a wide range of polymers, including those difficult to dissolve in ordinary organic solvents (Zhang *et al.*, 2007). On the Spraybase electrospinner, (1) 10% PLA in HFIP (w/w) at 15cm working distance, 18G needle tip, 6.14kV voltage, and 0.5ml/hr pump rate showed thin fibres of between 0.5 to 1.1µm, (2) 12% PLA in HFIP (w/w) at 20cm working distance, 18G needle tip, 8.49kV, and 0.6ml/hr pump rate only increased the diameter to slightly higher at around 1.5µm, and (3) 13% PLA (w/w) with otherwise same parameters increasing it to around 1.7µm. Given this modest increase, and the additional difficulties in collecting wide areas of evenly distributed fibres with a stationary needle, discussed further in the next section, along with the strong influence of the temperature and humidity fluctuations (due to the location of the machine in the School of Chemistry building in a room with large windows) on the ability to form a stable Taylor cone for electrospinning, I decided at this point to switch electrospinning machines. The IME electrospinner with a moving head and rotating mandrel collector (**Figure 4.1** C, located in a non-windowed room at the School of Engineering), was chosen as the most appropriate electrospinning machine for our purposes.

10% PLA (Corbion Purac Purasorb® PL 18) in HFIP (Manchester Organics G26383) (w/w) solution was loaded into a pump set to speed 1.3ml/hr (optimised from an initial trial of 1.2ml/hr), with an 18G needle tip inserted into the moving head set 18cm from the rotating mandrel. The moving head was set to move 16cm, slightly larger than the length of a standard 96-well plate, and travel at 50mm/s, as previously used on this machine (as advised by Dr.

Maaria Ginai, Callanan Lab at the School of Engineering). The rotating mandrel was covered in aluminium foil to allow the fibres to be removed, with 2 sheets of 10 by 14cm release sheets later added (as discussed in the next section), and set to 2000rpm to collect aligned fibres. The voltage to form a stable Taylor cone was between 19 to 23kV, and the counter electrode (i.e. the rotating collector) set to -1kV. Each batch of electrospinning was performed for 20 minutes to keep a consistent density. As shown in **Figure 4.3** A, the electrospun fibres using these conditions produced mostly aligned, smooth, tube-like microfibres, which OLs would ensheath to myelinate (**Figure 4.3** B). In addition, across 10 different batches, the fibres electrospun using this set-up and these parameters consistently produced microfibres with an average of around 2.1µm (**Figure 4.3** C), with a coefficient of variation (CV) ranging from 11.1 to 15.25 (average of 13). I was therefore able to optimise the electrospinning parameters required to produce consistent sheets of electrospun microfibres that oligodendrocytes would ensheath for my drug screening platform.

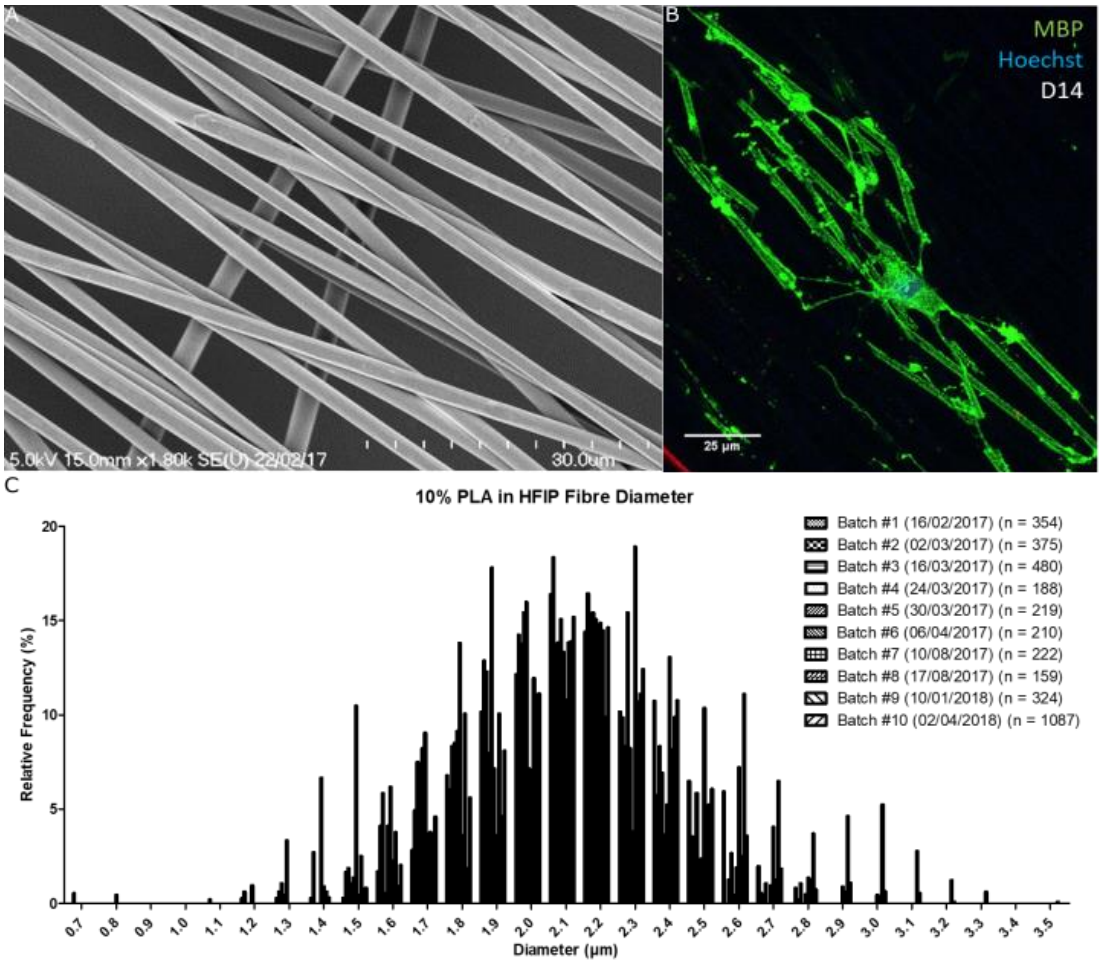

Figure 4.3 Poly-L-lactic acid dissolved in hexafluoroisopropanol is required to form a uniformly dissolved polymer solution for electrospinning, and to produce microfibres consistently of 2µm in diameter which the OLs will ensheath

a) Representative SEM image of electrospun 10% PLA microfibres dissolved in HFIP, showing smooth and round topography with consistent appearance between and within each microfibre.
b) Representative confocal image (Leica SP8, 40x objective) of an OL cultured on the 10% PLA in HFIP microfibres for 14 days. As shown by the MBP staining, the oligodendrocyte is able to extend multiple processes and form myelin sheaths around the electrospun PLA microfibres.
c) Histogram of the fibre diameter for the 10% PLA in HFIP fibres across 10 different batches showing peak microfibre diameter of approximately 2.1µm consistently across all 10 batches. The 'n' number represents the number of individual fibres measured for the batch.

4.2.2 Electrospun microfibres collection and transfer optimisation

Having established the protocol required to electrospin fibres suitable for myelination, I next addressed the question of transferring aligned electrospun fibres to form the base of each well in the final 96-well plate platform. This required that the method of collection was also optimised. Initially, electrospun fibres were collected on coverslips laid on the metal plate of the Spraybase electrospinner. However, due to the diversion of electrical charge from the glass, the fibres were electrically repelled from landing on the coverslips. To address this, the use of glue (3M Vetbond™), 1% agarose, and acid treating the coverslips in 1M HCl at 50°C for 4 hours was further explored. However, the glue and agarose was difficult to apply along the edge of the coverslips in a controlled manner, with the glue running along the fibres even when it visually appeared to have dried, and neither of them helping noticeably with the fibre collection due to not aiding with the electrical charge of the coverslips. Pre-treating the coverslips with acid to increase their charge also did not seem to make a significant difference to the collection of the fibres.

As an alternative strategy to increase the quantity and alignment of fibres collected, two other methods were explored next. In one method, a metal rod was bent in half, with the electrospun fibres being collected in between the two ends. In the second, pieces of aluminium foil were cut in a zig-zag manner and wrapped around a 12-well plate, with

scaffolds placed upside down to collect the fibres onto (**Figure 4.4** A). In both methods, the goal was to re-direct the electrical charge in between the pieces of metal, and therefore control the direction in which the fibres were collected. Both were able to align the fibres in a mostly parallel manner, with an example being shown from the second method in **Figure 4.4** A (inset figure), and the latter method producing better results in terms of fibre alignment and distribution. However, these methods were only able to align fibres in a fairly narrow area, i.e. approximately the width of one column of a 12-well plate, and therefore not appropriate for collecting aligned fibres across the bottom of an entire 96-well plate.

To increase the area of aligned fibres that could be collected, I therefore next designed and constructed a rotating plate collector (**Figure 4.4** B) in collaboration with Dr. Hua Dong and the School of Chemistry Workshop. The collector consisted of a metal holder for a bottomless 96-well plate, connected to a rod that would rotate the plate through an attached motor, so that the fibres were stretched across the plate in the direction of the rotation as they were produced and landed on the plate. As shown in **Figure 4.4** C, although the fibres were mostly collected in one direction, they were unevenly distributed, observable even by eye, with a higher density directly below the stationary needle tip and towards the edges close to the metal plate holder. This highlighted that for a wide area of evenly distributed fibres to be collected, a stationary needle set-up was not ideal.

To overcome this limitation imposed by a stationary needle, I therefore explored the use of an IME Electrospinner with a rotating mandrel, to collect aligned fibres, and a moving needle, for even distribution (set-up shown in **Figure 4.1** C). The rotating mandrel was covered in a piece of aluminium foil to allow easy removal of the fibres, with the fibres being attracted to the foil to keep them in place until their use. The rotating mandrel and moving needle was able to collect fibres of even distribution and aligned orientation (**Figure 4.3** A, **Figure 4.4** D - F).

Having solved the problem of creating fibre sheets of appropriate alignment and diameter, the final step required for their use is releasing them from the surface onto which they were sprayed. In initial attempts to transfer the sheet of electrospun fibres to the base of a 96-well plate, transfer of fibres directly spun onto the aluminium foil by sheets of adhesives (i.e. double-sided tape and/or PCR plate adhesive, as optimised in the next section) was problematic due to the tight adhesion of the tape onto the foil, which proved difficult to remove without disturbing the fibres. When the aluminium foil was soaked in water to lift

the fibres off, the orientation and distribution of the fibres was also disturbed. Therefore, I cut sheets of release paper to 10 by 14cm, slightly larger than the standard 96-well plate size of approximately 12.8 by 8.5 cm, to attach to the aluminium foil on the rotating mandrel (**Figure 4.4** D). The release paper was chosen as it is extremely thin and therefore did not seem to disturb the electrical charge significantly (**Figure 4.4** E), and also had a slightly waxy side to allow easy transfer of the fibres with the tape. When fibres were collected and transferred using this release paper method onto the base of bottomless 96-well plates, and their density quantified across 6 different constructed plates, the distribution of fibres stayed fairly consistent as controlled by both the length of the electrospinning and the transfer method, with the average distance between fibres across the 6 plates being at around 4.85μm (**Figure 4.4** F). By making use of a combination of a moving needle and rotating collector set-up and release paper, I was therefore able to optimise the collection and transfer of the sheets of electrospun fibres to produce the platform with aligned and evenly distributed fibres.

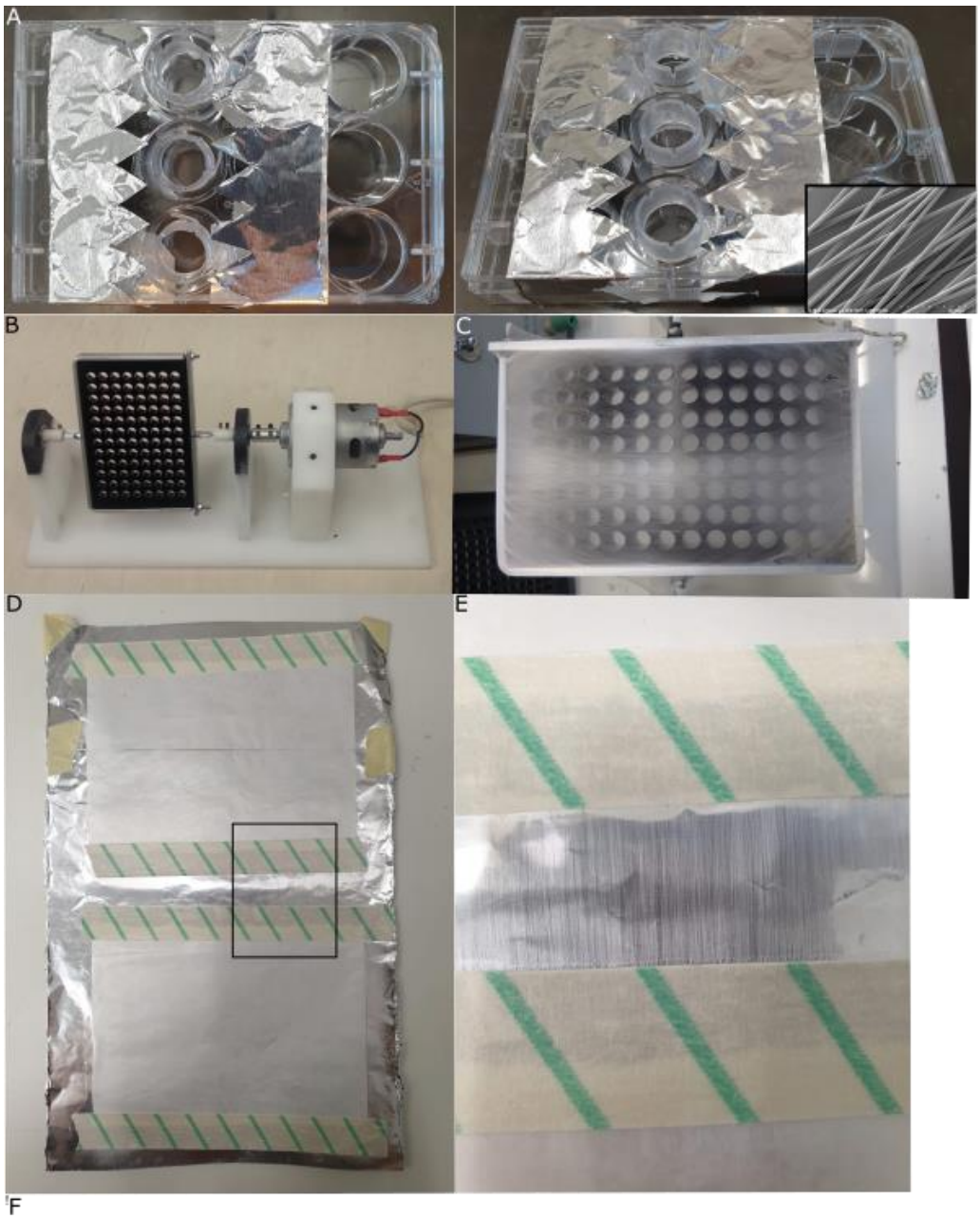
A
B
C
D
E
F
96-well Microfibre Plate Electrospun Fibre Density
Plate #1 (n = 114)
Plate #2 (n = 169)
Plate #3 (n = 193)
Plate #4 (n = 186)
Plate #5 (n = 193)
Plate #6 (n = 187)
Relative Frequency (%)
Density (µm)
0
20
40
60
0
2
4
6
8
10
12
14
16
18
20
22
24
26
28
30
32
34

Figure 4.4 A moving needle and rotating collector is required to form sheets of evenly distributed electrospun microfibres, with release paper to allow the sheets to be lifted

A. Top (left) and side (right) view of the aluminium foil wrapped around a 12-well plate with scaffolds for "aligned" fibre collection. The inset image in B. is a representative SEM image of the PLA microfibres dissolved in HFIP solvent collected using this method, showing smooth and even topography in the fibre appearance.
B. Photograph of the rotating plate collector with a metal holder for the 96-well plate, which is attached to a motor to spin the plate as the fibres are produced.
C. Photograph of the electrospun fibres collected using the rotating plate collector. A higher density of fibres can be seen at the centre of the plate, which is located just below the needle in this vertical electrospinner set-up, and towards the edges, due to the charge of the metal plate holder.
D. Photograph of the electrospun fibres collected on a rotating mandrel with 2 sheets of release paper attached (with autoclave tape) for easy transfer of the sheets of fibres.
E. Close-up photograph of the aligned fibres collected on the rotating mandrel from the area highlighted with the black box in C. The white vertically aligned PLA fibres can be seen against the silver aluminium foil in the region in between the release paper attached with autoclave tape.
F. Histogram of the density of fibres after being transferred from the sheet (as shown in D.) into a 96-well plate format to show consistent fibre density between independently constructed plates. The distance in between the fibres in a well was measured by taking brightfield images on the Leica Confocal SP8 MatrixScreener, stitching and stacking the images, drawing a line perpendicular to the direction of the fibres randomly across a well, and measuring the distance between fibres along the line using ImageJ. The measurements were taken from 2 wells from different parts of the plate, and the 'n' denotes the number of measurements taken per plate.

4.2.3 Optimisation of the bottomless 96-well plate and adhesive

In order to construct the plate, I needed to find a consistent source of bottomless 96-well plates over which I could lay the fibres before adding an imaging-compatible lower surface to the plate to act as a base to each well within which the fibres form a suspended floor. The suspended floor is created by the use of a spacer, ensuring the fibres were elevated from the base of the plate and therefore would be accessible for myelin sheaths to form around them.

The basic design is shown in **Figure 4.5** A; the sheet of fibres is stuck to the base of a bottomless 96-well plate, with the optically transparent floor then glued on with a spacer (into which holes have been cut to align with those in the plate) separating fibre sheet and base so as to create the suspended floor of fibres.

Contacts with various companies did not reveal any suitable suppliers of the bottomless 96-well plates, with only one company, Greiner, having some left-over stock from a discontinued product. Therefore, several alternative options were explored. Firstly, using the AutoCAD software and with the help of the Bradley Lab, I attempted to 3D print a portion of a 96-well plate (2 x 4 wells) as an initial test. However, the machine struggled to print this design without the layers of the 3D-printed material lifting off from the collecting surface, and therefore was excluded as a viable option. Next, I purchased sheets of acrylic (Sheet Plastics) and polypropylene (Cut Plastic Sheeting), the former material for cost and the latter as it is commonly used in the production of lab equipment including plates, for laser cutting. In collaboration with Dr. Anthony Buchoux (Stokes Lab at the Scottish Microelectronics Centre), I was able to successfully laser cut 96-well plates out of these materials (**Figure 4.5** B). However, due to the thickness of the plastics required to construct plates with enough height, the length of time it took for each plate to be cut and the distortion of the material due to the laser needing to re-trace each cut multiple times was problematic. In addition, due to the settings only allowing cuts to be made all the way through the material, these plates could not be cut with the standard skirt that is present around the base of all commercial 96-well plates, making them less compatible with components of the high-throughput pipeline such as liquid-handling machines and robotic arms for placing the plates into high content imaging systems. Therefore, the final design of the bottomless 96-well plates was created around commercial 96-well plates (PerkinElmer CellCarrier) with the base of each well cut out using the laser cutter, and then the base smoothed out by manual sandpapering to get rid of the slight ridges left behind by the high heat of the laser cutter. The PerkinElmer CellCarrier-Ultra plates also offer an alternative as the skirt of the plate is shorter, and therefore give the option of more wells being accessible for imaging on various imaging systems.

In order to create a 96-well plate with the layer of electrospun microfibres inserted under the plate and separated from the base by a spacer layer, I needed to ensure that I had a method of adhering the layers together that would be watertight to allow different drugs at different concentrations to be tested in each well. I therefore tested multiple alternative

medical adhesives for compatibility with cell culturing, including 3M's VetBond™, a medical adhesive paste (Factor II, Inc. A-100), a spreadable secure silicone adhesive (Factor II, Inc. B-460), and a medical adhesive spray (Factor II, Inc. 7730) (**Figure 4.5** C). However, none were suitable. The VetBond™, medical adhesive paste and silicone adhesive were difficult to apply as a thin even layer, and the medical adhesive spray was difficult to control. In addition, the VetBond™, silicone adhesive, and the medical adhesive spray, due to the consistency of the adhesive, would run along the fibre even if the microfibre layer was applied after giving plenty of time to allow the adhesive to dry and become tacky.

In order to overcome this issue of consistent adhesive application, I next tested double-sided tape, along with PCR plate adhesives, to act as both a spacer and the glue to hold the plate together. I first cultured OPCs isolated from the mixed glia culture method on 18-mm glass coverslips (VWR 631-1580) with or without a piece of double-sided tape and PCR plate adhesive adhered to the side of the well in a 12-well plate. By widefield microscope, I was able to check that the OPCs did not appear to be growing away from the adhesives nor were there any obvious differences in the cell density in the well with the tapes. This seemed to suggest that these adhesives were safe for use in close proximity with our OPCs. Next, I needed to be able to cut the tape to fit on the base of a bottomless 96-well plate without making the wells inaccessible. By layering a sheet of double-sided tape and a PCR plate adhesive, which would be the thicker sheet of adhesive required for the plate construction, I tested a biopsy punch, a single hole-punch, and a 96-well punch created by the School of Engineering Workshop. The biopsy punch and 96-well punch (**Figure 4.5** D (left) and E) proved difficult to punch holes through the adhesive layers, with the edges of the holes being rough and uneven, and the sheets of adhesive getting stuck on the 96-well punch and tearing while being removed. The single hole-punch (**Figure 4.5** D (right)) efficiently punched holes. To confirm that this provided a means of creating a watertight seal onto the bottomless plate, I used different food colouring dyes in adjacent wells. When the tape was cut into pieces (as shown in **Figure 4.5** D), there was leaking of the food colouring horizontally along the cuts made in the tape (**Figure 4.5** F) but not in the rest of the plate, confirming the adhesive was able to seal the plate with the microfibres in a watertight manner.

Although this proved the adhesive worked, it also showed the hole punch method was not satisfactory as the glue would easily clog up the hole-punch. Moreover, due to the design of single hole-punches, only the very outer-most two rows and columns were accessible. In the

final construction method, therefore, the adhesive layers were laser cut (**Figure 4.5** G), which provided consistent sheets of tape cut to shape in one piece.

Figure 4.5 Laser cut sheets of adhesives produce the most controlled and evenly distributed adhesives to attach the microfibres to the base of a (laser cut) bottomless 96-well plate

A. A schematic of the basic layers required for the construction of a 96-well microfibre plate. The sheet of electrospun microfibres need to be layered under a bottomless 96-well plate so that the oligodendrocytes can be plated and the compounds added through the individual wells of the plate onto the fibres. The fibre also needs to be suspended by a spacer above a base compatible with imaging so that the oligodendrocytes are able to access all sides of the fibres to form complete myelin sheaths, and be imaged through an inverted microscope.
B. Laser-cut 96-well plate from a sheet of polypropylene. The large sheet of polypropylene took several times of laser cutting over the same lines to cut all the way through the material, and the high heat from the laser left the surface uneven that required a lot of time in sandpapering to smooth out.
C. 4 types of medical adhesives tested for the adhesion of the fibres to the base of a bottomless 96-well plate, as labelled in the photograph. All the adhesives were difficult to apply evenly and precisely. The glue from the VetBond, silicone adhesive, and medical adhesive spray additionally ran along the fibres even when they had been given time to dry and become tacky before the fibres were added.
D. Double-sided tape and PCR plate adhesive (spacer) layers with holes punched with either a single hole-punch or with a biopsy punch (left), or just with a single hole-punch. The adhesive layers were cut into pieces due to the design of the single hole-punch only allowing the outer two rows or columns of holes to be accessed. The biopsy punch could not easily penetrate both layers of adhesives, even when placed on a firm surface with a slight give to allow for the punch to cut through to the other side whilst the adhesives layers stayed flat. Both the hole-punch and biopsy punch had to be cleaned regularly to remove the adhesives from the tape and plate adhesive sticking to the metal cutter.
E. Hole-punched double-sided tape and PCR plate adhesive layers with a 96-well hole-punch constructed by the School of Engineering Workshop. Due to the thickness of both layers of the adhesives combined, it was difficult for the 96-well hole-punch to cut through consistently and evenly, and the tape was easily ripped when being removed from the hole-punch.
F. Photograph of a laser-cut 96-well polypropylene plate with double-sided tape, sheet of microfibres, double-sided tape and PCR plate adhesive, and COC film layers. The white lines dividing the plate are the locations of the cuts along the adhesive layers for hole-punching using the single hole-punch. Leaking of the food colouring horizontally along the left dividing line and complete leaking of the liquid out of the plate after 1 night along the right dividing line could be observed, although the rest of the plate appeared to be watertight. This

confirmed that it was not the adhesive that was the issue but rather the cuts required for the hole-punch to access the inner areas of the tape.

G. Laser-cut double-sided tape and PCR plate adhesive layers, produced with the help of Dr. Anthony Buchoux. As shown, the cuts are even, smooth, and consistent along the holes corresponding to each well of a 96-well plate, and the flexibility offered by the laser cutter means that the sheet of adhesives can easily be cut to size to fit the base of a bottomless 96-well plate.

4.2.3 Final construction of the high content-compatible 96-well microfibre plate with suspended PLA microfibres

Thus far, I was able to find a consistent source of bottomless 96-well plates, optimise the production of the electrospun microfibres, and test for the current best option in adhering the layers together (summarised in **Figure 4.6** A). Lastly, I needed to be able to seal the base of the plate with a thin sheet of material that would be compatible with imaging. Cyclic olefin copolymer (COC) was tested due to its transparency, high heat-deflection temperature (for culturing in 37°C incubators for long periods), and low moisture absorption and strong water-vapour barrier qualities (Lamonte and McNally, 2001). TekniFilms CSF1416 and TOPAS 8007X4 COC films were initially tested by preparing them as PDL-coated “coverslips” and culturing OPCs isolated by the mixed glia culture method, and staining for MBP and Hoechst for confocal microscopy. As shown in **Figure 4.6** A, OPCs could be cultured and would differentiate in close proximity with COC, and it was possible to take confocal images through this material. Therefore, TOPAS COC 8007 X-04, which is approximately 140µm in thickness and was the closest to the standard 170µm commercial 96-well plate bases, and was the only readily available product in the quantity and format required for consistent plate construction, was used for further testing.

96-well microfibre plates were constructed fully as shown in **Figure 4.6** B, including the COC film base. In order to ensure that the layers were firmly adhered, metal blocks were placed on the base of the plate to compress the layers together for at least 2 days. The metal blocks were found to be the best weights due to their similar shape and size to the base of the plate. By contrast, irregular non-rectangular shapes compressed the layers unequally as confirmed by the Leica SP8 MatrixScreener, even when placed on lighter rectangular shapes to

distribute their weight. 96-well microfibre plates constructed using this optimised technique had food colouring placed in alternate wells for testing for cross-well contamination of individual wells to ensure they were watertight. No obvious leaking could be observed immediately. In order to verify whether changes in temperature would affect this, the plates were placed in the 37°C incubator for 2 weeks, the length of time required for the OL myelination culture, and placed for several days at room temperature and in the 4°C fridge, as required for staining and storage. The plate did not show any signs of leakage following these tests, as shown in **Figure 4.6** C, and therefore it was concluded that they could be used for drug screening, where distinct drugs or drug combinations added to the individual wells will not leak into adjacent ones for the duration of the experiment following this construction method.

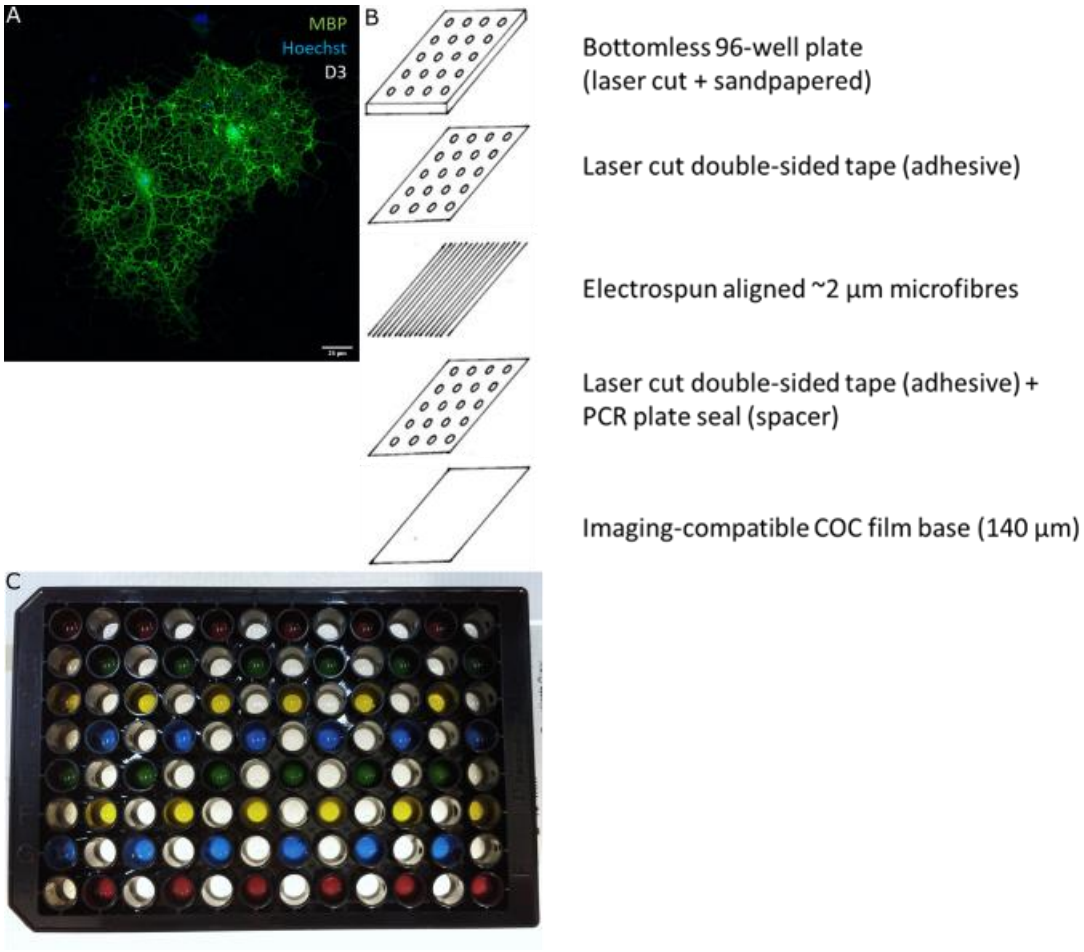

Figure 4.6 Final high-throughput-compatible 96-well microfibre plate design optimisation

A. Confocal image of OPCs isolated by the mixed glia culture method, cultured on COC film, and stained and imaged as per the 12-well scaffold method to confirm that the COC film is imaging-compatible.
B. Schematic of the final 96-well microfibre plate construction components. The bottomless 96-well plate was produced by laser cutting the bases of each of the individual 96-well plates and the edges smoothed using sandpaper. A single layer of double-sided tape was used to adhere the sheet of electrospun microfibres underneath. A laser cut PCR plate seal was used to suspend the fibres, and another layer of double-sided tape used to make both sides of the spacer layer adherent. The plate was finally sealed with COC film which, as shown in A, is imaging-compatible. The COC film used was 140µm in thickness, which was the most similar in thickness to the 170µm thickness of standard 96-well plates out of the commercially available films that could be obtained.
C. Water-tight test performed with food colouring mixed into alternative wells using the construction method in B. As shown in the photograph, there is no mixing and leaking of the food colouring into adjacent wells, highlighting that this construction method allows the construction of a 96-well plate with a suspended layer of electrospun microfibres that is water-tight and will let different compounds at varying concentrations to be tested in each well.

4.3 Discussion

The key technological and bioengineering advancement of my PhD project is the production of the 96-well microfibre plates with suspended electrospun microfibres (**Figure 1.20** Challenge and Solution #1). To achieve this, I designed and optimised: i) the concentration of poly-L-lactic acid (PLA) dissolved in hexafluoroisopropanol (HFIP) for fibre diameter; ii) electrospinning using a moving needle with a rotating collector for equal distribution, with release paper enabling easy transfer; iii) bottomless 96-well plates produced by laser cutting and sandpapering; iv) the adhesives to attach the sheet of electrospun fibres made compatible with the plate by laser cutting; and v) an optically-compatible cyclic olefin copolymer (COC) film providing the imaging-compatible base.

The basis of electrospinning fibres and inserting them into a 96-well plate format in itself is not novel – for example, the Electrospinning Company, from which I acquired the 12-well scaffolds for my experiments, also produce a product called ’96-well plate fixed scaffolds

(TECL-005)'. However in their product, the electrospun fibres are in close contact with the base of the plate. Although the production of plates without a spacer to suspend the fibres completely from the base of the plate may be technically easier and less expensive to produce due to fewer components being required in making watertight plates, for the study of myelin sheath formation, work from our own lab and others has found that such plates are unsuitable for quantitative myelination assays for two reasons. First, as observed by Dr. Marie Bechler in using the Electrospinning Company product, and by Ong *et al.* (2018) in their set-up of electrospun PCL fibres suspended by PCL films on glass coverslips (**Figure 4.7**), oligodendrocytes cultured on electrospun fibres that are in close proximity to flat surfaces will detect both the 3D fibres to ensheath and the 2D surfaces to extend membranes across, or a combination of both by the same cell. When developing a myelination assay where the measurement of complete myelin sheath is the quantifiable output, the degree to which the electrospun fibre is in contact with the fibres versus the underlying surface, and therefore the likeliness of membrane extension versus sheath formation, introduces an uncontrollable factor that reduces the precision and reproducibility of the assay.

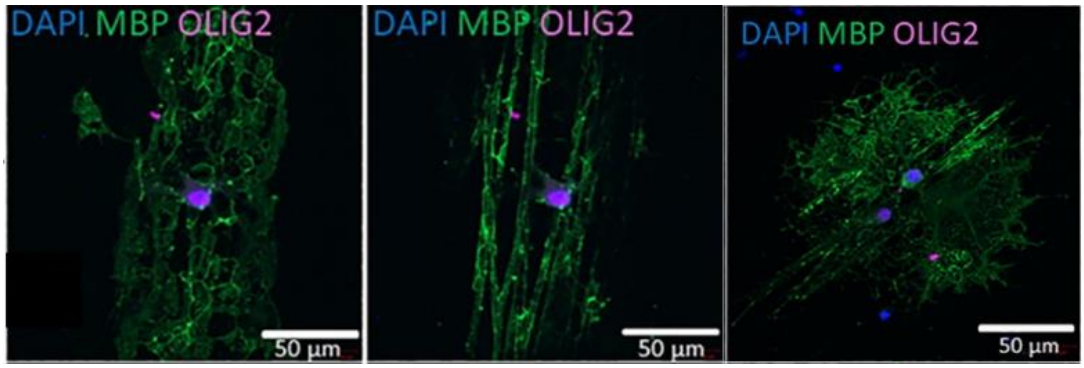

Figure 4.7 Confocal images from oligodendrocytes cultured on PCL fibres suspended by PCL films on glass coverslips

When oligodendrocytes are cultured on fibres that are in contact with a flat surface, they produce cells that form flat membranes (left), complete myelin sheaths (middle), and a combination of both flat membranes and myelin sheaths (right) as they detect both the 3D fibres and the 2D coverslip.

(Figures from Ong *et al.* (2018))

Second, the inter-plate consistency of the plate construction technique is very poor with the commercially available plates. As shown in **Figure 4.8** A and B, the consistency of the working distance required to image the myelin sheaths on the microfibres on the purchased plates varied vastly between and within plates, with certain wells not being within the available working distance (as shown in **Figure 4.8** B) or needing to divide up the plate into multiple sections to scan individually to be able to capture all the wells. On the other hand, the fibres and myelin sheaths in all the plates that I constructed using the final described construction method (**Figure 4.6** B) were well within the 500µm imaging range provided by the Leica SP8 MatrixScreener (**Figure 4.8** C and D), showing improved intra- and inter-plate variability, even when the number of fields-of-view being imaged was increased (**Figure 4.8** D). The significance of this reduced variability is its importance in high content imaging compatibility, with an increase in the range of z-steps that the microscope has to image to capture the cells reducing the potential for image automation and increasing the time required to scan a single experiment, if the microscope can image the plate at all. As also mentioned in the next chapter, this was highlighted when a plate from The Electrospinning Company and a plate that I constructed were prepared by Dr. Marie Bechler and myself, respectively, and imaged on the Yokogawa CV7000 at the Phenotypic Screening Centre in Dundee. The plate from The Electrospinning Company could not be registered on the microscope, and therefore no images could be obtained, whereas the 20x long working distance objective could be used to register and image the plate that I had prepared, with the potential for the use of higher objectives with further exploration and technical assistance from the engineers. The increased reproducibility and decreased variability of the construction technique for 96-well plates with suspended microfibres that I developed therefore shows more promise for its application for high content purposes, such as phenotypic drug screening.

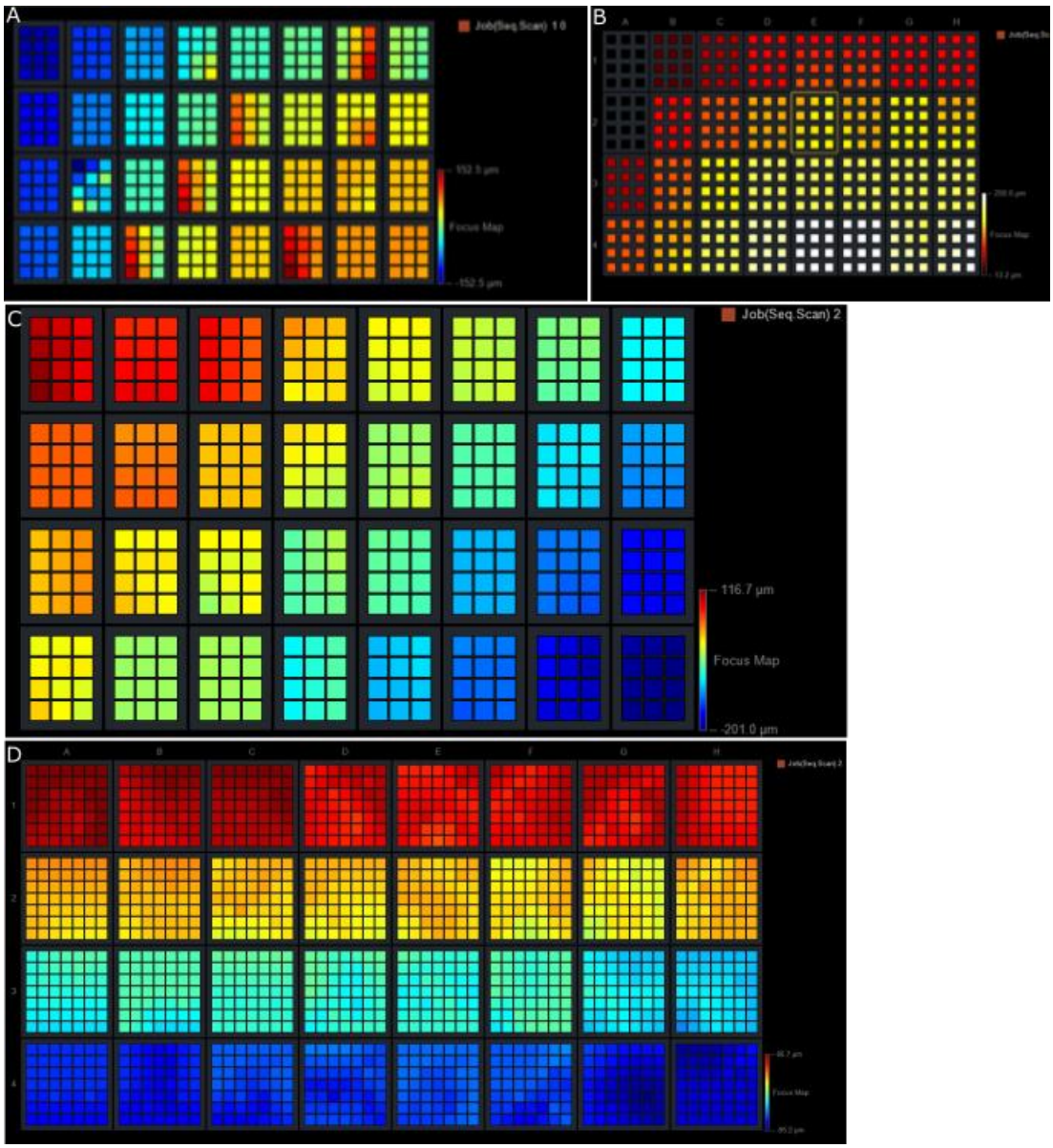

Figure 4.8 Autofocus maps obtained using the Leica SP8 MatrixScreener show better consistency between plates in the variation of the height of the fibres from the base of the plate using my construction method

The figure shows representative autofocus maps obtained using the Leica SP8 MatrixScreener from two plates prepared by The Electrospinning Company (A and B, images provided by Dr. Marie Bechler) and by myself using the construction technique as described in this chapter (C and D).

The autofocus maps were taken by setting an arbitrary mid-point for the range at which the microfibres are distanced from the base of the plate, and the MatrixScreener image-based autofocusing function used to detect how far the fibres at each set autofocus point were located above or below this mid-point. The colours represent the distance (±, in µm) at which the fibres were

detected to be most in focus from the arbitrary mid-point as shown in the calibration bar. The calibration bar in each image therefore indicates the total distance range for the fibres within the plate that could be imaged.

The small squares indicate each field-of-view included in the MatrixScreener scan, and the larger squares these make up represent each well. The blank squares in B (top left corner) are wells which were outside of the 500µm range for the autofocus map and subsequent imaging, and therefore could not be included in the scan.

These results showing the difficulties of working with commercially available products emphasize the importance of the technique described in this chapter of my PhD to reliably produce 96-well microfibre plates in which the electrospun microfibres are suspended from the base of the plate but are also within working distance range of imaging by high content imaging platforms. Such a plate also offers much greater future potential in increasing the flexibility of the experiments by adjusting the electrospinning and fibre preparation method (i.e. different diameters, materials, or coating). It will therefore provide a useful advance in allowing for the execution of high-throughput experiments for studying oligodendrocytes in a more physiologically-relevant model than simple 2D differentiation platforms.

CHAPTER V. VERIFICATION OF THE HIGH-THROUGHPUT 96-WELL MICROFIBRE PLATE PLATFORM

5.1 Introduction

The goal of the plate I have designed and constructed (described in the previous chapter) is to enable phenotype-based screens that identify compounds that directly promote myelination. This chapter describes initial work towards that aim in which I have: (5.2.1) tested whether the 96-well microfibre plate that I constructed was compatible for use in a high-throughput pipeline and with high content imaging platforms, (5.2.2) optimised the OPC isolation method and cell density required for individual oligodendrocytes and their respective myelin sheaths to be identifiable in the high-throughput format, (5.2.3) calculated the reproducibility of the assay using the coefficient of variation values, and (5.2.4) quantified the sheath length and number in the 96-well microfibre plates using compounds previously identified in the differentiation assays in Chapter 3 and a compound currently under investigation at Roche. Preliminary results of an experiment to increase the sensitivity of the assay using fibrin-coating of the fibres is also discussed at the end (5.2.5). To introduce this work I will review three relevant aspects of phenotype base screens: (5.1.1) the logic behind them, (5.1.2) aspects of assay design, and (5.1.3) the challenges introduced by 3-D screens such as the one I have designed.

5.1.1 Phenotypic-based screens

Although phenotypic-based screening strategies laid the groundwork for modern drug discovery in the 20th century, the past 30 years has seen the molecular target-based screening strategies becoming the traditional method due to the advances in pharmacology, molecular biology, synthetic and medicinal chemistry, laboratory screening automation, and understanding of disease at the genetic level. As summarised in **Figure 5.1**, the molecular target-based screening approach identifies a disease-relevant target, and then the development of an assay that searches for hits against the target in order to conduct a high-

throughput screen. On the other hand, phenotypic screening approach focuses on the cell- or organism-based characteristic of the disease to identify compounds that ameliorate the disease phenotype, without prior knowledge of the drug target (Clemons, Tolliday and Wagner, 2009; Zheng, Thorne and McKew, 2013).

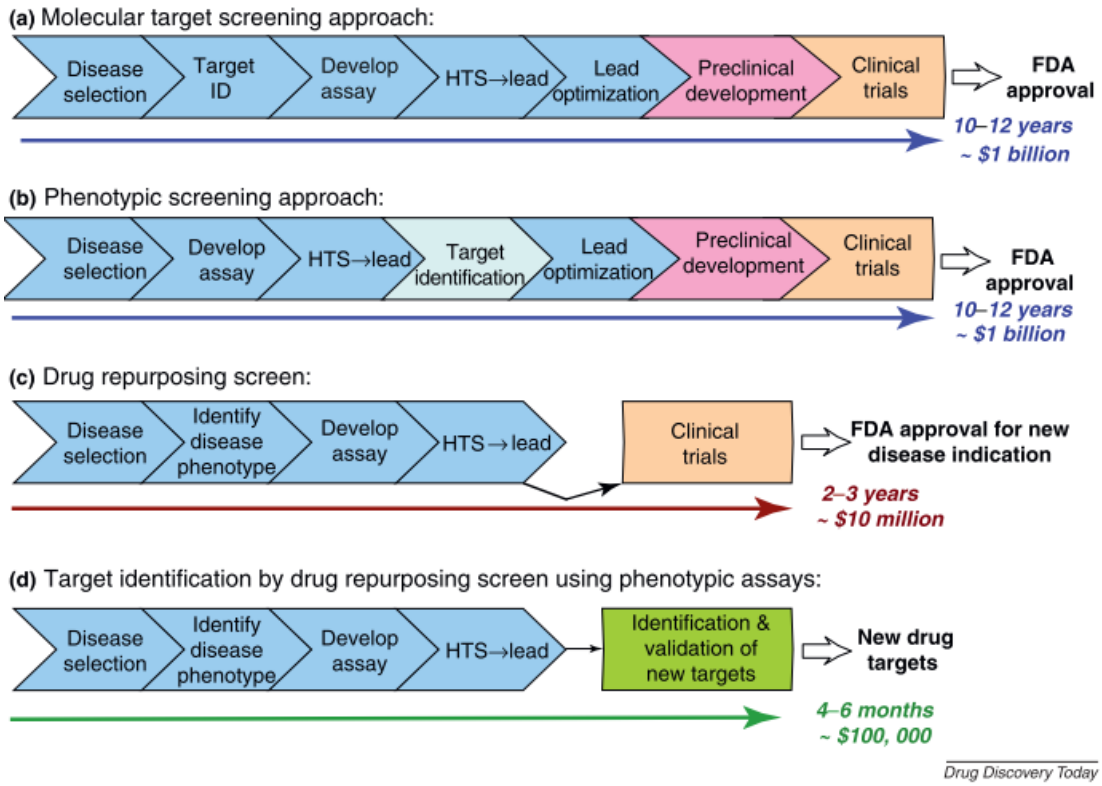

Figure 5.1 Comparisons of various drug discovery pipelines

Screening approaches can be divided into two main types: screening approaches, as shown in (a) molecular target and (b) phenotypic, and drug repurposing screens, as shown in (c) and (d).

The molecular target-based screening approach identifies the target molecule for the disease selected, and develop a screen specific for this molecule to identify a lead compound to optimise (i.e. improve the potency by working with medicinal chemists by studying and adjusting the molecular structure of the lead compound) and move forward towards *in vivo* validation and clinical trials. The phenotypic screening approach develops a screen to identify the phenotype that indicates a positive outcome for the disease selected in order to identify a hit, with the hit compound subsequently needing to undergo target deconvolution to find the molecule and pathways involved before moving on to lead compound optimisation.

The use of repurposing screens is to reduce the time and money required in this drug discovery process by using compounds that already have known profiles for other diseases, such as the molecular pathways it targets, and its safety and efficacy profile, allowing the money- and time-intensive process to be reduced.

(Figure from Zheng, Thorne and McKew, 2013)

The increasing rate of failure of compounds identified as hits making it through clinical trials (Pammolli, Magazzini and Riccaboni, 2011; Scannell *et al.*, 2012), the limit in the number of novel validated druggable targets, and the recent advances in cell-based assay screening technologies such as high-throughput imaging, iPSC technology, CRISPR gene editing, and more relevant 3D *in vitro* models, has resulted in renewed interest in phenotypic-based screens over the past decade (Clemons, Tolliday and Wagner, 2009; Zheng, Thorne and McKew, 2013). The phenotypic screen is generally more biologically and clinically relevant, but also more complex to develop and comparatively lower in throughput compared to the cell-free target-based screens. However this may be offset by the lower attrition rate in later stages of the drug discovery pipeline, although more data is still needed to provide evidence for this, and improved upon by the development of robotic platforms for automation, miniaturisation, and throughput. Although the retrospective identification of the mechanism of action and target may be complicated and lengthy, drugs shown to be safe and efficacious may still be approved for clinical use, and lead identification with repurposed drugs can speed up and reduce the cost of bringing a compound to market, with the validation of the target by a phenotypic screen also possibly leading to the identification of further drug targets (**Figure 5.1**) (Clemons, Tolliday and Wagner, 2009; Zheng, Thorne and McKew, 2013).

5.1.2 Assay development

The construction of a high-throughput cell-based phenotypic assay requires the balance of biological-relevance with the ability to adopt automation, including the readout and data analysis of the assay. High content screening is the technique by which multiple measurements are obtained per well, providing more dynamic and mechanistic information than uniform single well measurements, and can include the use of an image-based automated microscope system. The development of an assay itself requires optimisation of

the throughput, sensitivity of the signal and readout, variability, degree of miniaturisation appropriate, and adaptation to the available screening platforms, and expand to cell density, optimal concentration of tested compounds, sensitivity to the compound solvent (which is usually DMSO), and length of culturing with the compounds among other factors with cell-based assays (Buchser *et al.*, 2004; Clemons, Tolliday and Wagner, 2009; Bray, Carpenter and Broad Institute of MIT and Harvard Imaging Platform, 2012).

Liquid-handling robots can improve the precision, throughput, and the ability to miniaturise the assay. However, this requires careful testing of the volume of dispensing, speed of dispensing and aspirating, and height and position of the tips, to prevent damage to the cells, especially if repeated use is required. Reproducibility between wells of the same plate (intra-plate), between different plates (inter-plate), and between different biological replicates and batches require testing and optimisation using a DMSO-control and a compound shown to produce positive activity when one is available, as well as quality control to eliminate data that are due to non-compound-related variables, such as cell density or imaging artefacts. As discussed further below, the Z' factor is one of the most widely accepted measures of the quality of the assay, allowing for the determination of whether the assay can determine positive activity from background control, with a large number of replicates being required for this calculation. Various techniques for data normalisation also exist to account for inter- and intra-plate variability based on errors, such as changes in compound concentrations due to evaporation, anomalies from external factors such as robotic failures or pipette malfunction, and variations in incubation times and temperature differences of the incubators, or other sources of systematic errors, which are often identifiable as repeated artefacts (Clemons, Tolliday and Wagner, 2009; Bray, Carpenter and Broad Institute of MIT and Harvard Imaging Platform, 2012).

5.1.3 3D cellular models for drug discovery

In addition to the complexities of a cell-based phenotypic assay, there are additional considerations for a 3D cellular model, such as our *in vitro* myelination system. As summarised in the SWOT analysis by Carragher *et al.* (2018), 3D models provide the promise of being able to provide a more physiologically-relevant model of the disease-relevant cells, and may provide new and richer data that is more innovative and intelligent in its design.

However, the complexity of such models also brings about complications, such as the expense and additional difficulties of validating such multifaceted and heterogeneous models, as well as the difficulties of imaging, screening, and analysing such large and rich data sets which pushes the limits of the imaging platforms currently available and the balance between image quality and working distance with long acquisition times, and the computational demands of storing and analysing the extensive data when few 3D-compatible image analysis software packages are available (Horvath *et al.*, 2016; Carragher *et al.*, 2018). Despite the caution required in not yet overestimating the translation of the physiologically more relevant 3D models to increased clinical relevance when the data is not yet available to support this (Carragher *et al.*, 2018), the development of more complex 3D cellular models along with the expanding ability to increase the throughput of their readouts with the development of more high-throughput and high content-compatible robots and software may provide important advancements in our ability to understand and treat diseases in the near future.

5.2 Results

5.2.1 Testing of the compatibility of the 96-well microfibre plate with high-throughput liquid handling machines and high content imaging platforms

In order to be able to use the 96-well microfibre plates for high-throughput drug screening, I needed to verify that the plates could be incorporated into a high-throughput pipeline, including the use of liquid handling machines and high content imaging platforms, which allows for the reduction of human error, increase in reproducibility and reduction in variability (i.e. CV), as well as decrease in timescale of sample processing. Firstly, I used the ImageJ Cell Counter plugin to quantify the number of Hoechst+ cells in DMSO control when OPCs isolated from mixed glia cultures were plated onto a 96-well microfibre plate using a Multidrop™ (**Figure 5.2** A). When imaged using the Leica SP8 MatrixScreener and the cell numbers counted from the maximum projected image, the coefficient of variation was 7.8% (individual values: 207, 205, 181, 219 cells) (n = 1), showing both that the Multidrop™ could be used to plate cells in the 96-well microfibre plates, and that, at least based on preliminary

results, there is a high degree of intra-plate plating density consistency even accounting for some of the cells that may have fallen through in between the fibres if the distance is larger than 10µm.

In addition, in order the process the plates for imaging, the Multidrop™ and the BioTek LS 405 microplate washer can be used to dispense liquids (fixative and antibody solutions) and rinse with PBS in between the steps, respectively. The microplate washer, due to the repeated aspiration directly from the centre of the well, as opposed to the dispensing which is performed towards the side of the well, could result in cells and fibres being detached. I therefore took a 96-well microfibre plate with immunopanned OLs cultured for 14 days, fixed and stained it by manual pipetting, and imaged the plate on the Operetta before using the BioTek LS 405 microplate washer (**Figure 5.2** B). I then calculated the minimum number of aspiration-dispensing cycles required to be able to use the BioTek LS 405 as 10x, estimated the aspiration distance from the bottom of the well as 6.987mm using a standard 96-well plate to leave approximately 125 to 130µl of liquid in each well of a 96-well microfibre plate after aspiration, and re-imaged the same wells on the Operetta after the 10x cycles (**Figure 5.2** C). I repeated this experiment with a further 3x cycles on the microplate washer to account for the potential maximum number of cycles before imaging the plate again (**Figure 5.2** D). As shown in **Figure 5.2** B-D, in this preliminary test, there does not appear to be any cell loss after 10x or 13x cycles on the microplate washer, verifying that the 96-well microfibre plate appears to be compatible with both the Multidrop™ and BioTek microplate liquid-handling robots.

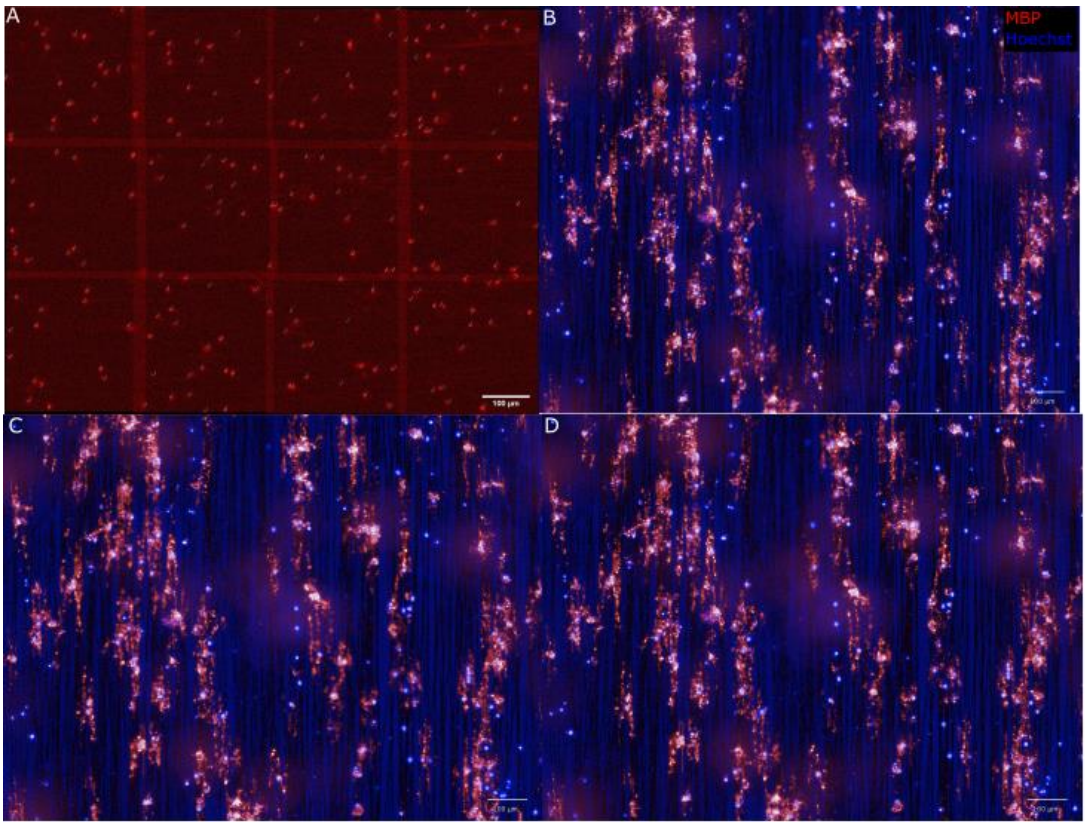

Figure 5.2 The 3D 96-well microfibre plates are compatible with high-throughput liquid-handling robots

A. Maximum projected confocal image of the Hoechst nuclei staining of OPCs isolated from mixed glia cultures plated on the 96-well microfibre plates with the Multidrop taken with the SP8 MatrixScreener. The number of nuclei in the 4x DMSO control wells (individual values: 207, 205, 181, 219 cells) were counted using the Cell Counter plugin on Fiji to calculate the coefficient of variation (CV = 7.8%) in a single plate. n = 1
B. Representative Operetta non-confocal image of a single well of a 96-well microfibre plate with OPCs isolated from immunopanning and plated at 5,000 OPCs per well. n = 1
C. Well from (B) after 10x cycles of aspiration and dispensing with the BioTek LS 405 microplate washer, the minimum number of cycles required for fixation and staining.
D. Well from (C) after a further 3x cycles with the BioTek LS 405 microplate washer, to include additional cycles to improve fixation and staining.

Although we are able to automate the imaging of the 3D 96-well microfibre system using the Leica SP8 MatrixScreener, as the SP8 is not a high content imaging system, it is inherently slow and incompatible with a high-throughput pipeline. In addition, due to the objectives

available and the stage set-up of the microscope at SCRM, only the 25x water objective has the working distance to be able to image the suspended microfibres compared to the 40x oil objective used when imaging the coverslips of the 12-well microfibre scaffold, and only the central 32 wells can be accessed due to the distance from the skirt to the base of the plate, excluding two-thirds of the wells. As discussed below, the Operetta and Opera do not provide the resolution to distinguish between membrane extension and ensheathment, and therefore is incompatible with our myelination assay. Therefore, I also explored the Yokogawa CV7000 and the Opera Phenix high content imaging systems in Dundee (National Phenotypic Screening Centre) and Glasgow (Dr. Lynn McGarry, Beatson Institute for Cancer Research), respectively. The Yokogawa CV7000 was able to register my custom-made plate and detect the fibres using the 20x long working distance, but was not able to using the 60x objective based on initial tests. Interestingly, a commercial custom-ordered 96-well plate (by Dr. Marie Bechler) with suspended microfibres by The Electrospinning Company could not be registered on any of the objectives tested on the Yokogawa CV7000, suggesting that my plates were more compatible for high content imaging platforms than what could be purchased commercially. The Opera Phenix could access the central 60 wells with a plate constructed using the standard PerkinElmer CellCarrier plate, and all 96 wells using the CellCarrier Ultra plates with the shorter skirt, as exemplified with the brightfield transmission images of the fibres across an entire plate taken on the Opera Phenix in **Figure 5.3** A. Additionally, using the 63x objective, it was possible to image individual oligodendrocytes and their respective myelin sheath at 0.5µm z-step sizes (**Figure 5.3** B), therefore confirming that the 96-well microfibre plate is compatible with the high content Opera Phenix imaging platform.

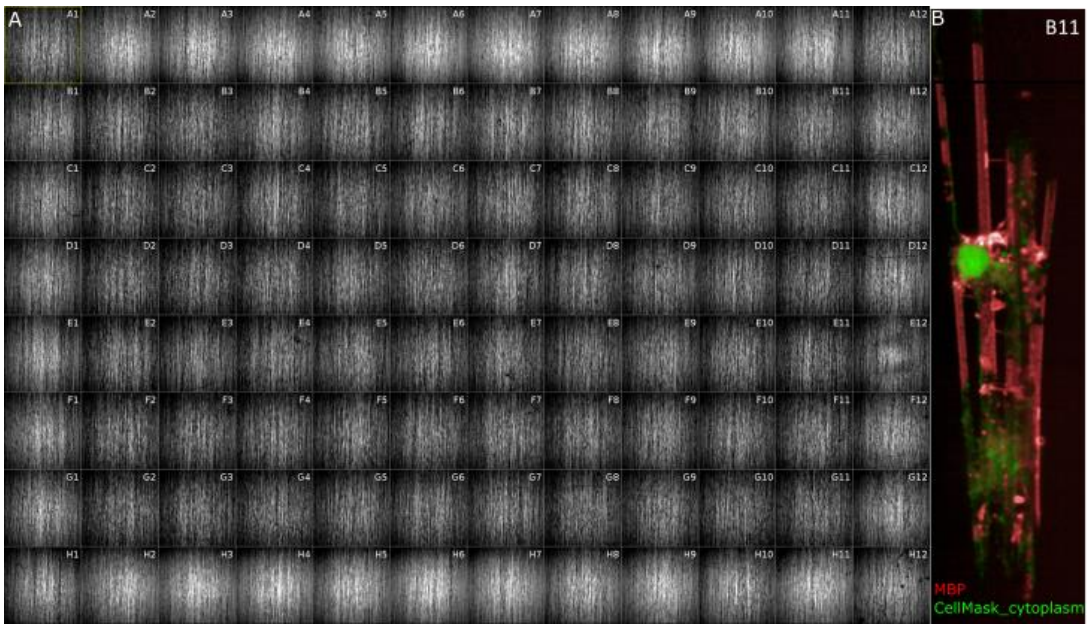

Figure 5.3 The 3D 96-well microfibre plates with suspended microfibres is compatible with the PerkinElmer Opera Phenix as a high content imaging platform

A. Brightfield images of the fibres in focus in a 96-well microfibre plate constructed using the PerkinElmer CellCarrier Ultra plates as taken on the Opera Phenix. As shown, all wells are accessible and can be imaged using the CellCarrier Ultra plates versus the standard CellCarrier plates, where the outer wells cannot be accessed.
B. Confocal image of a single cell taken using the 63x objective at 0.5µm z-step on the Opera Phenix on a 96-well microfibre plate constructed using the PerkinElmer CellCarrier Ultra plate. This highlights that individual myelin sheaths can be visualised for quantification using this high content-compatible imaging platform.

5.2.2 Optimising the OPC isolation method and cell density required for individual oligodendrocytes and their respective myelin sheaths to be identifiable in the high-throughput format

On the 96-well microfibre plates constructed and verified to be water-tight in Chapter 4, OPCs isolated using the mechanical isolation technique from mixed cultures were plated at 8,000 cells per well in myelination media. An initial drug screening experiment was performed using compounds identified in the published differentiation drug screens that had also been tested in 2D 96-well flat culture and 3D 12-well scaffolds in Chapter 3 to test

whether there was a difference between 2D pro-differentiation and 3D pro-remyelination assays, and whether the results obtained in the 3D 12-well scaffolds could be recapitulated in the 96-well plate format. The experiment was adjusted to include the small molecule PKCε activator, FR236924, and the endothelin receptor agonist peptide, BQ-3020 (Swire *et al.*, 2019; Yuen *et al.*, 2013), to test whether the plate could detect compounds that have been confirmed to enhance myelin sheath formation. However, for the reasons listed below, these experiments did not yield myelin sheath-producing oligodendrocytes to quantify.

As shown with an example image in **Figure 5.4**, several wells in different plates showed an abundance of the appearance of CellMask cytoplasm-positive cells that were morphologically distinct from oligodendrocytes and not MBP-positive, appearing to be closer to astrocytes by morphology. Due to a combination of the contaminating cells and the myelination media issue, as discussed further in Chapter 3 and below, only one repeat of the four initial repeats of the experiment yielded oligodendrocytes with myelin sheaths in a majority of its wells (18 out of 32 wells), and could therefore be quantified (**Figure 5.1** B and C). It was therefore not possible to draw conclusions about the effect of the compounds from this experimental set-up.

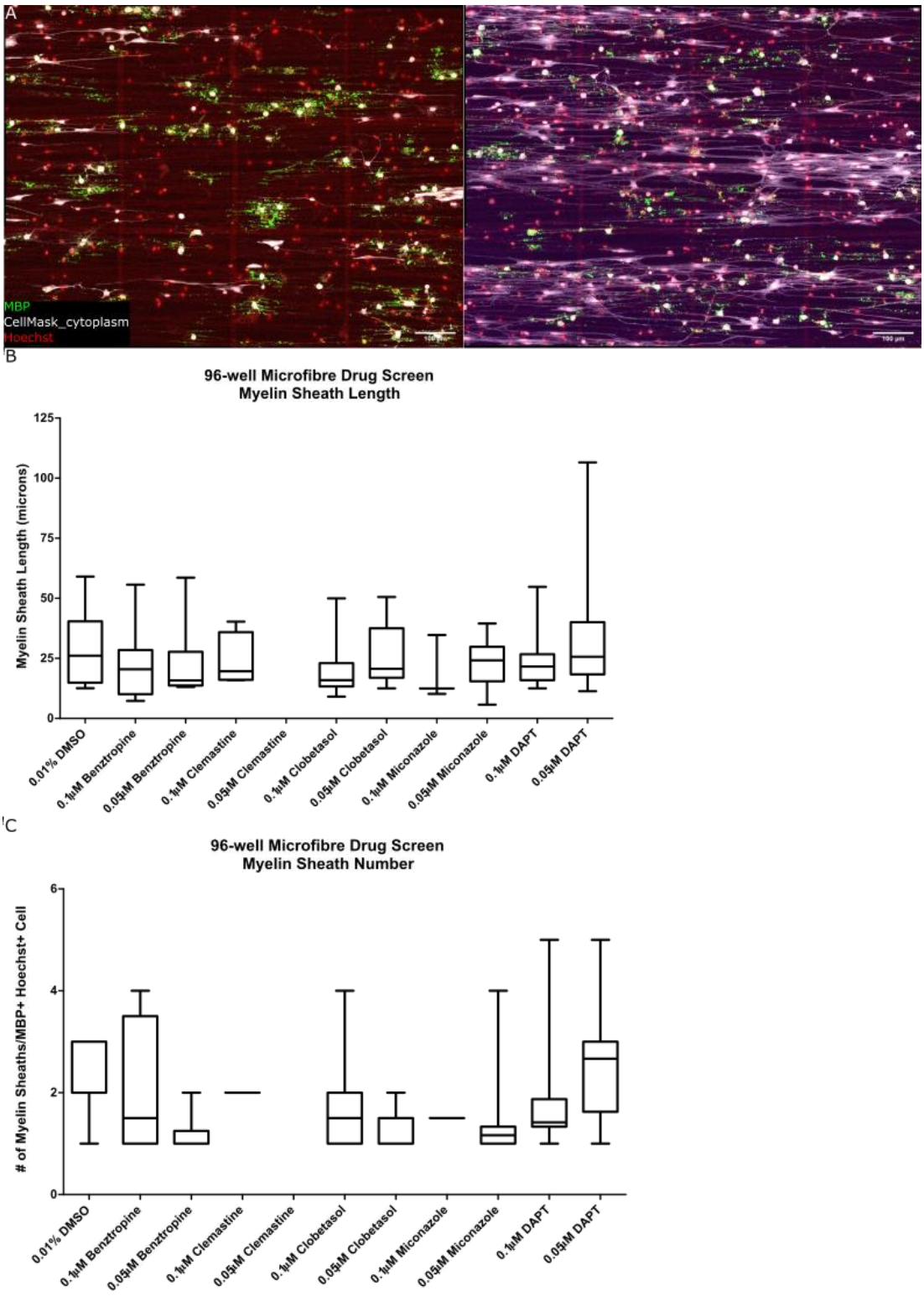

Figure 5.4 There is an abundance of contaminating cells when OPCs isolated using the mechanical isolation technique from mixed glia cultures are cultured on the 96-well microfibre plates

A. Example images show the presence of cytoplasmic staining (CellMask_cytoplasm) that is not MBP+ and is morphologically distinct from oligodendrocytes, suggesting the presence (left) and abundance (right) of a second type of contaminating cells in the culture.
B. Myelin sheath length measurements quantified by manual measurements on Fiji, recorded on Excel, and plotted and analysed on GraphPad Prism 5. No measurements could be obtained from the 0.05µM Clemastine condition (performed in triplicate) from the 3 wells imaged and analysed. n = 1
C. Number of myelin sheath per MBP+ cell. Sheaths were only counted when MBP+ cells were distinctly separate, and excluded when cell bodies were clumped in close proximity. n = 1

The presence of contaminating cells would create complications in performing a drug screen due to the inability to determine whether the effect of certain compounds was on the oligodendrocytes or indirectly through the contaminating cells, and due to the variability of the oligodendrocyte to contaminating cell ratio in different biological replicates. It was difficult to determine whether there was a high percentage of contaminating astrocytes from the isolation technique when plating, promotion of proliferation of the contaminating astrocytes, or whether the 96-well plate format was more conducive to the trans-differentiation of OPCs into astrocytes (Raff, Miller and Noble, 1983). Should the cause be the first two possibilities, increasing the purity of the OPCs in the isolation technique should decrease the appearance of these contaminating cells, such as through immunopanning.

Next, therefore, and as part of a 4-month industry research internship I undertook at Roche in Basel, Switzerland as part of my PhD training and an ongoing industry-academic collaboration based on the 96-well microfibre plates that I had constructed, I used the immunopanning technique developed by Foo *et al.* (2011). Under her guidance I isolated O4+ OPCs to use for drug screening on the 96-well microfibre plates to compare them to those obtained by mechanical isolation of the mixed glia cultures as used at SCRM in Edinburgh, UK. The 3 compounds tested, in addition to the DMSO control, were Clemastine, due to its identification in the BIMA screen (Mei *et al.*, 2014) and positive Phase 1 trial results (Green *et al.*, 2017), DAPT, which was used as a positive control for Lariosa-Willingham *et al.* (2016)'s axonal co-culture screen of myelination rather than differentiation, and Compound R, a compound undergoing early research studies at Roche.

I initially dissected and isolated O4+ OPCs and plated them into my 96-well microfibre plates at a density of 8-10,000 cells/well. However, very few cells were present in each well, suggesting either poor survival and/or low plating density. Therefore, reasoning that the vigorous immunopanning protocol might compromise viability, I plated the O4+ OPCs onto normal tissue culture-treated dishes for 2-3 days in a 'recovery phase' prior to lifting them up and re-plating on my fibres, as well as plating these cells at multiple densities. Plating at higher than 10,000 cells/well (**Figure 5.5** A-C) resulted in the density being too high, and therefore unable to distinguish individual oligodendrocytes and their respective myelin sheaths. 8,000 cells/well (**Figure 5.5** D) allowed individual oligodendrocytes and their myelin sheaths to form in culture and be detected, although a few clusters of cells could still be identified. Therefore, the optimal plating condition was determined to be the plating density of 6-8,000 cells/well after the O4+ OPCs had undergone a 'recovery phase'.

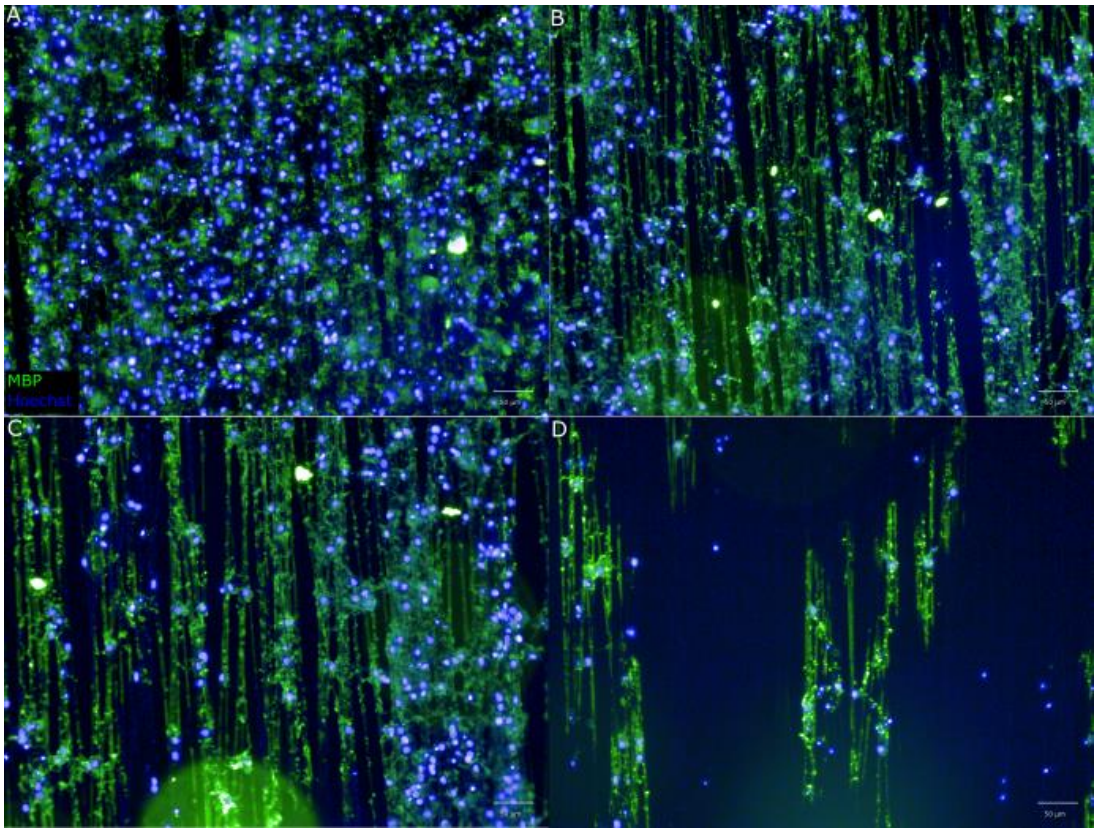

Figure 5.5 Immunopanned OPCs can be plated and cultured in 96-well microfibre plates, and result in lower contamination compared to OPCs isolated from mixed glia cultures

Representative Operetta images when cells are plated at 40,000 (A), 20,000 (B), 10,000 (C), and 8,000 (D) cells per well on the 96-well microfibre plates, with a majority of the Hoechst+ cells also being MBP+. As can be seen, the nuclei density at 40,000 cells per well is too high for process extension. The 20,000 and 10,000 cells per well conditions showed improvement, but was still too dense to identify individual oligodendrocytes and their respective myelin sheaths. At 8,000 cells per well, individual oligodendrocytes and their myelin sheaths could be identified. As a few clusters of cells could still be seen, the optimal density was determined to be approximately 6-8,000 cells per well.

5.2.3 Assessing reproducibility: Intra- and inter-plate coefficient of variation and Z' calculations for the Roche 96-well microfibre drug screening platform

The coefficient of variation (CV) is defined as the standard deviation (SD) of a set of data divided by its mean. It is used to calculate the magnitude of difference that can be attributed to assay variability, i.e. by chance, rather than true difference due to experimental conditions, and can therefore be used as a measure of assay precision and reproducibility (Reed, Lynn and Meade, 2002). To determine the CV of the 96-well microfibre drug screening platform, the average value of myelin sheath length (**Table 5.1**) and myelin sheath number (**Table 5.2**) per well in each plate was calculated, and used to obtain the intra-plate CV for each DMSO control concentration. The inter-plate CV per DMSO concentration across the 3 plates was calculated by taking the average of the CV of the respective DMSO concentration in each of the 3 plates.

A CV of less than 20% is generally the acceptable standard for more complex assays such as the 96-well microfibre drug screen, which, according to Reed *et al.* (2002)'s formula, a CV of 20% would approximate to about 1.3% random twofold changes. When interpreting the CV for myelin sheath length (**Table 5.1Table 5.1** *Coefficient of variation calculations for myelin sheath length from the Roche 96-well drug screen experiment*), there was variable results in intra-plate CV per DMSO concentration, with CV ranging from less than 2% to just under 30%. The inter-plate CV per DMSO concentration was within 20% for 0.1% and 0.01% DMSO, but exceeded the 20% threshold for the 0.001% concentration.

	Per well								
	Plate 1	Plate 2	Plate 3	Plate 1	Plate 2	Plate 3	Plate 1	Plate 2	Plate 3
	DMSO control (0.1%)			DMSO control (0.01%)			DMSO control (0.001%)		
MEAN by well	31.11	28.49	13.98	30.76	17.73	22.86	24.02	15.44	21.83
	31.86	23.85	15.69	25.69	29.21	17.47	24.14	23.33	12.45
				29.07	27.45	27.34	28.74		17.57
SD	0.52	3.28	1.21	2.58	6.19	4.94	2.69	5.58	4.70
MEAN	31.49	26.17	14.83	28.51	24.80	22.56	25.63	19.38	17.28
Intra-plate CV	1.67%	12.54%	8.14%	9.05%	24.94%	21.92%	10.49%	28.79%	27.19%
	DMSO control (0.1%)			DMSO control (0.01%)			DMSO control (0.001%)		
Inter-plate CV	7.45%			18.64%			22.16%		

Table 5.1 Coefficient of variation calculations for myelin sheath length from the Roche 96-well drug screen experiment

The CV of the myelin sheath number (**Table 5.2**) showed more random variability, with intra-plate CV reaching almost 50% in 0.001% DMSO in plate 2, and inter-plate CV being over 20% in the 0.01% and 0.001% DMSO condition. These CV calculations highlight the variability of both the myelin sheath length and myelin sheath number potentially by random chance in the 96-well microfibre plates. Although some of this will be down to technical issues from the transport and the lack of cells to quantify in some wells as discussed below, the use of liquid handling machines to decrease human error in areas such as plating density could be used to improve the assay precision.

	Per well								
	Plate 1	Plate 2	Plate 3	Plate 1	Plate 2	Plate 3	Plate 1	Plate 2	Plate 3
	DMSO control (0.1%)			DMSO control (0.01%)			DMSO control (0.001%)		
MEAN by well	1.67	2.33	3.00	3.00	2.10	1.43	1.89	1.50	2.50
	1.57	1.83	2.50	1.57	2.00	3.20	2.43	3.00	1.60
				1.67	2.40	4.00	1.84		2.33
SD	0.07	0.35	0.35	0.80	0.21	1.32	0.33	1.06	0.48
MEAN	1.62	2.08	2.75	2.08	2.17	2.88	2.06	2.25	2.14
Intra-plate CV	4.16%	16.97%	12.86%	38.41%	9.61%	45.75%	15.91%	47.14%	22.33%
	DMSO control (0.1%)			DMSO control (0.01%)			DMSO control (0.001%)		
Inter-plate CV	11.33%			31.26%			28.46%		

Table 5.2 Coefficient of variation calculations for myelin sheath number from the Roche 96-well drug screen experiment

Further experiments were conducted to include compounds, in addition to the differentiation and co-culture myelination compounds used in Chapter 3 that have been shown to have positive and negative effects on myelin sheath formation on the fibre culture system by Dr. Matthew Swire to test the sensitivity of the 96-well microfibre platform (Swire *et al.*, 2019). The aim was to calculate the Z'-factor, defined as 1 - $\frac{3(\sigma_p + \sigma_n)}{|\mu_p - \mu_n|}$, where μ is the mean and σ is the standard deviation of the positive (p) and negative (n) controls, and is widely used in high content screening assays as a measure of assay performance in assessing its ability to pick up hits whilst reducing false positives and negatives (Bray, Carpenter and Broad Institute of MIT and Harvard Imaging Platform, 2012; Zhang, Chung and Oldenburg, 1999). For positive effect, the small molecule PKCε activator FR236924 and endothelin receptor agonist peptide BQ-3020 were included as both were shown to increase sheath number (Swire *et al.*, 2019). For negative effect, MAP kinase inhibitor U0126 shown to decrease sheath length and number and epidermal growth factor receptor kinase inhibitor AG 1478 which decreased sheath number were included. However, as also discussed in Chapter 3, due to media issues which we narrowed this down to be most likely a result from the batch-to-batch variability of the commercial B27 and home-made B21, I was unable to get myelin sheath formation after 15 sets of experiments were performed, including in the media and DMSO controls, using different batches of commercial B27 and home-made B21, using media with lower T3/T4 concentration to reduce stress to the cells and as our lab protocol adds 10x concentration of T3 in comparison to similar media in addition to adding T4, as well as using media components shipped from Roche. Thus, a Z' factor could not yet be determined at the time of completing this thesis.

5.2.4 Determining the changes in myelin sheath formation using Clemastine, DAPT, and Compound R on immunopanned OPCs on 96-well microfibre plates

Once the plating condition had been optimised and the miniature drug screen test performed, an automated high content screening technique with the appropriate imaging resolution was explored. Neither the Opera (**Figure 5.6** A) nor the Operetta (**Figure 5.6** B), the two high content imaging machines available at Roche, offered the z-step size in resolution or the autofocusing capabilities required for automated imaging of these highly complex myelin

sheath structures, with the Opera also not being high content-compatible with these plates. Their Leica SP8 confocal system also didn't have the appropriate MatrixScreener plugin, which is an extension that allows screens to be set up on the confocal system by allowing parameters such as the autofocusing range, and wells and fields-of-view selected for imaging to be set up and run automatically (Eberle *et al.*, 2017). These investigations highlight the limitations of commercial high content and commercial imaging platforms with regards to imaging bespoke 3D cell assay plate formats. Along with the timeline of the experiments performed at Roche and the end of the internship, it was therefore determined that the only feasible method of imaging these microfibre plates would be to ship them back to SCRM and image them using the Leica SP8 MatrixScreener. However, as shown in **Figure 5.6**, comparing the representative images of a single well taken at Roche on the Opera and Operetta compared to on the MatrixScreener post-shipment, with an average well being shown in **Figure 5.6** C with other wells having slightly more cells and others having significantly fewer, there appeared to be a loss of cells during the transportation process despite filling each of the wells with as much PBS as possible to reduce the amount of air, sealing tight with a plate adhesive, parafilming the edge of the plates, and shipping them in thick Styrofoam boxes labelled as 'fragile'.

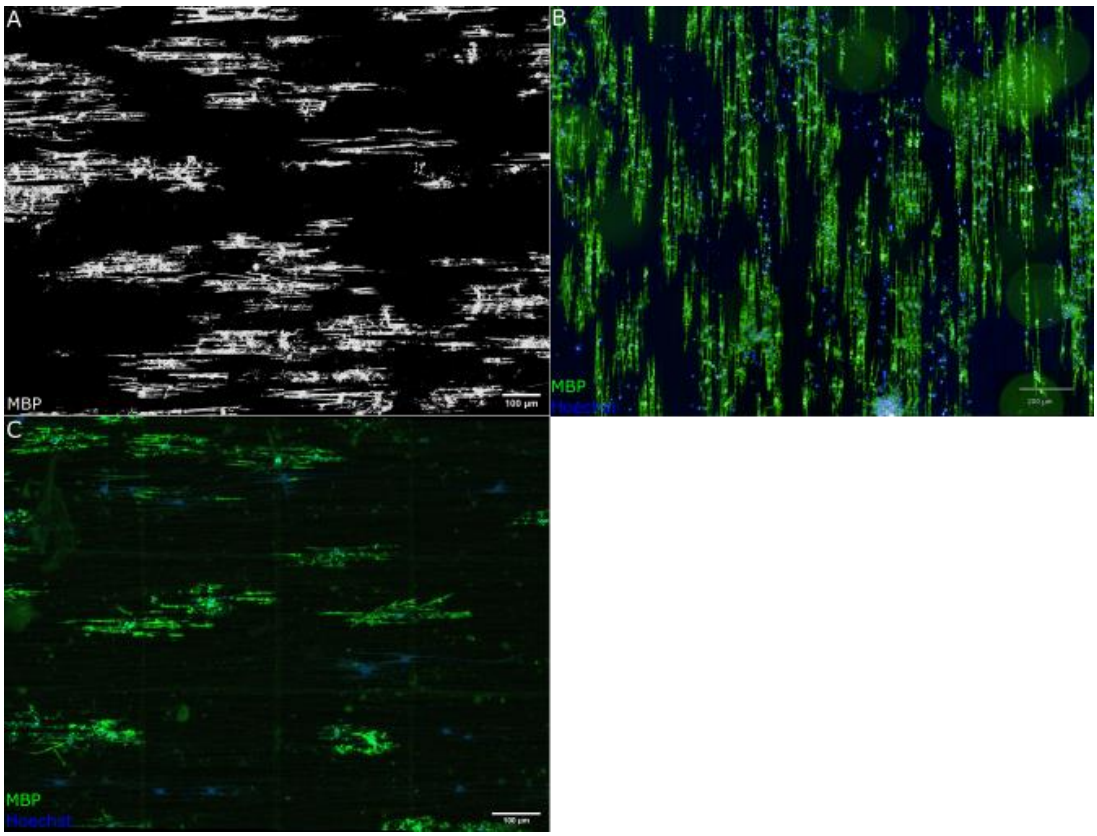

Figure 5.6 96-well microfibre plates transported from Roche (Basel, Switzerland) to SCRM (Edinburgh, UK) show the loss of cells in the wells during the transit process

Representative immunofluorescence microscopy images of single wells in the 96-well microfibre plates with 8,000 cells per well plated at Roche in Basel, Switzerland taken on the (A) Opera and (B) Operetta, and after the plates have been transported to SCRM in Edinburgh, UK on the (C) SP8 MatrixScreener.

Despite these issues, the plates were imaged on the MatrixScreener, and myelin sheath quantification performed using ImageJ (**Figure 5.7** A and B), although interpretation of the data is limited due to the effect of the transportation on these plates and the number of cells available for quantification in each condition in each biological replicate. When sheath length was quantified (**Figure 5.7** C) and the average per biological replicate taken for statistical analysis using the one-way ANOVA with post-hoc Dunn's Multiple Comparison test (**Figure 5.7** D), none of the compounds and concentrations significantly changed the myelin sheath length compared to the DMSO control. Statistical analysis of the myelin sheath number was difficult as the transportation issues resulted in as few as 2 or 3 cells being available for

quantification in some plates due to the additional criteria of excluding myelin sheaths where there were clumps of MBP+ cell bodies, as this makes it difficult to distinguish the originating cell body and results in less than 1 sheath per cell if calculated. When the myelin sheath number was quantified (**Figure 5.8** A), and the average per biological replicate taken for statistical analysis with the available data using the one-way ANOVA with post-hoc Dunn's Multiple Comparison test (**Figure 5.8** B), no statistically significant changes in myelin sheath number could be identified in comparison to the DMSO control. Even taking into account variations between biological replicates by controlling for the DMSO in intra-plate normalisation (Bray, Carpenter and Broad Institute of MIT and Harvard Imaging Platform, 2012), there was no statistically significant changes in sheath number for any of the compounds and concentrations tested (**Figure 5.9** A and B). However, as shown by the wide inter- and intra-plate variability determined by CV calculations (**Table 5.2**) in addition to the lack of quantifiable cells in each condition per biological replicate, caution must be taken in putting any meaning behind these results at this point in time.

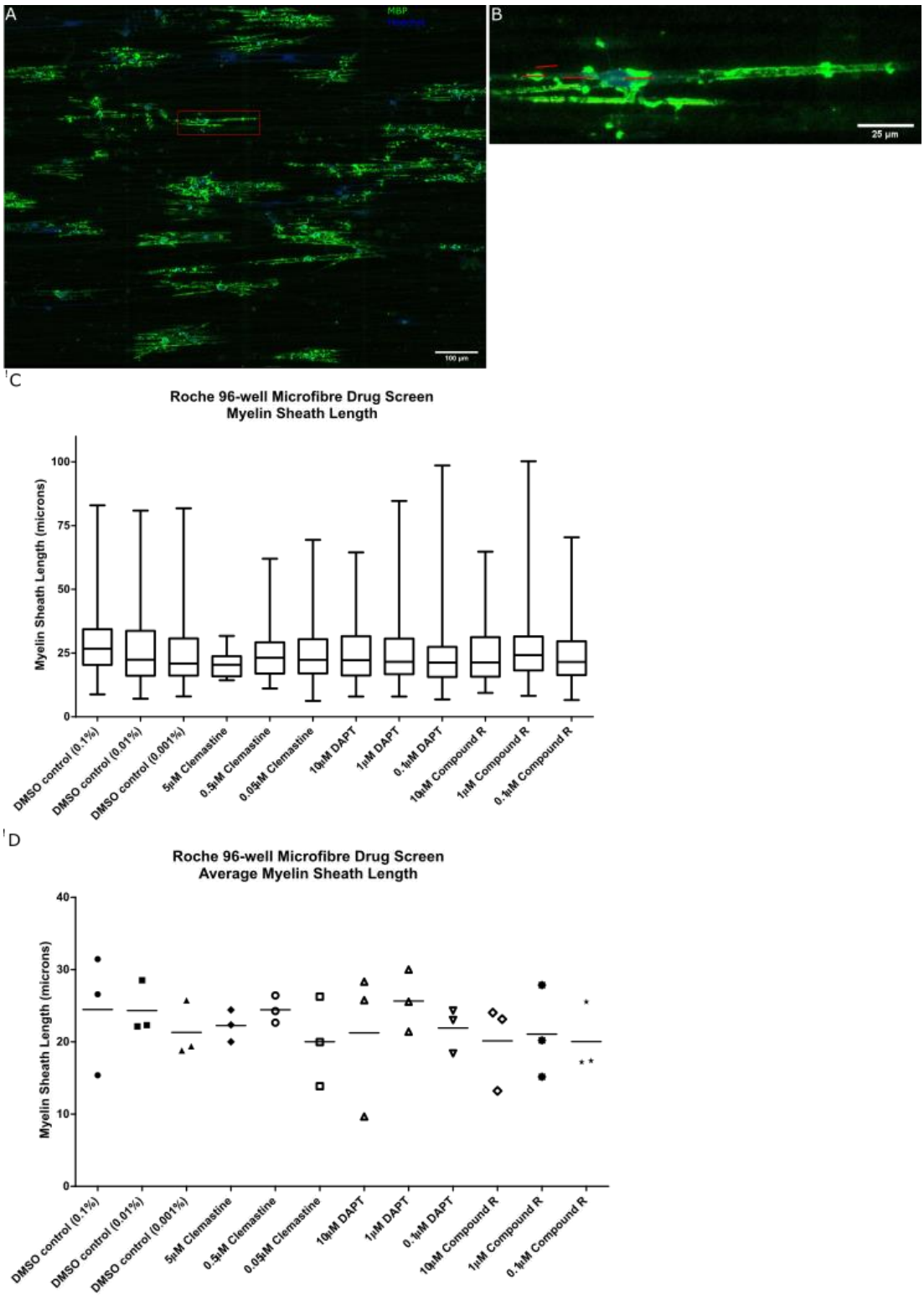

Figure 5.7 No significant changes in myelin sheath length was seen using three compounds tested on immunopanned OPCs at Roche

A. Representative maximum projected confocal image of a single well in the 96-well microfibre plate with the SP8 MatrixScreener.

B. Zoomed in image of the cell in (A). The red lines represent complete myelin sheath formation as determined by observing the z-stack images, and therefore included in the quantification.

C. Myelin sheath length measurements quantified by manual measurements on Fiji, recorded on Excel, and plotted and analysed on GraphPad Prism 5.

   The box-and-whisker plot show the range of measurements obtained as represented by the maximum and minimum at the 'whiskers', and the 75th, 50th, and 25th quartiles with the lines on the 'box' from top to bottom. n = 3

D. The average myelin sheath length per biological replicate from the data in C was used to perform statistical analysis. This showed no significant changes in myelin sheath length for any of the compounds in all concentrations tested.

   The statistical test performed was the one-way ANOVA with post-hoc Dunn's Multiple Comparison test for analysis.

A

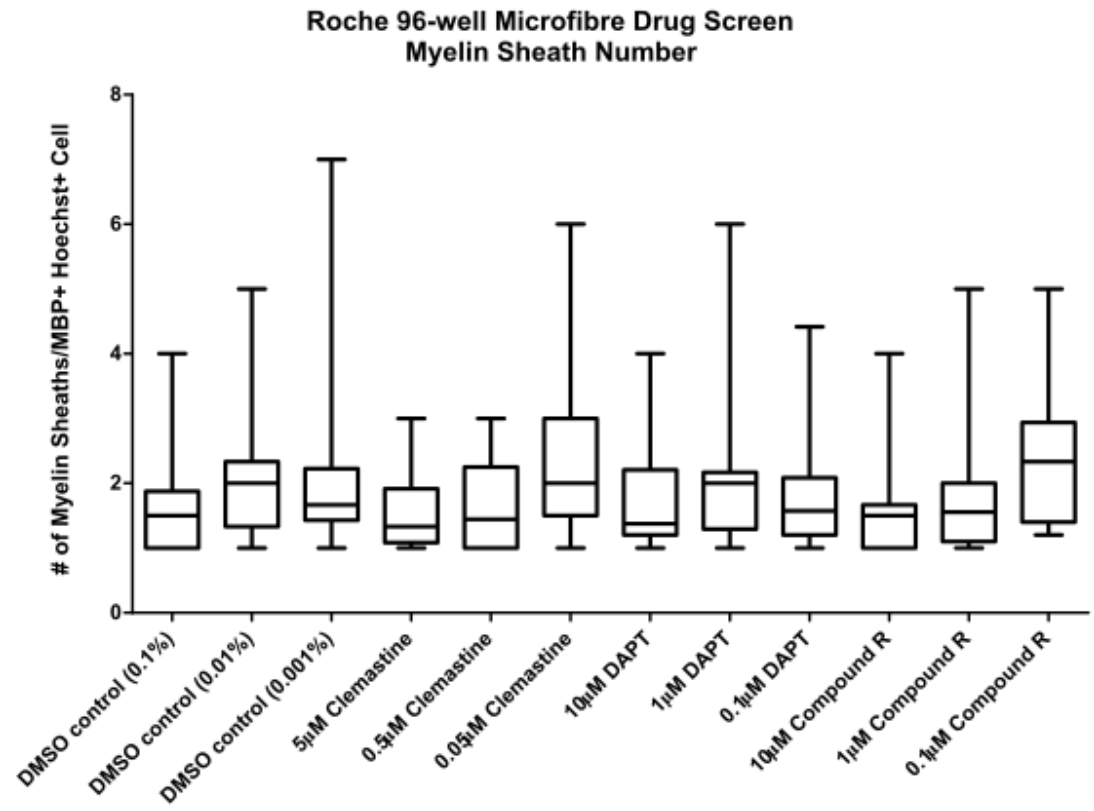
Roche 96-well Microfibre Drug Screen
Myelin Sheath Number
# of Myelin Sheaths/MBP+ Hoechst+ Cell
0
2
4
6
8
DMSO control (0.1%)
DMSO control (0.01%)
DMSO control (0.001%)
5μM Clemastine
0.5μM Clemastine
0.05μM Clemastine
10μM DAPT
1μM DAPT
0.1μM DAPT
10μM Compound R
1μM Compound R
0.1μM Compound R

B

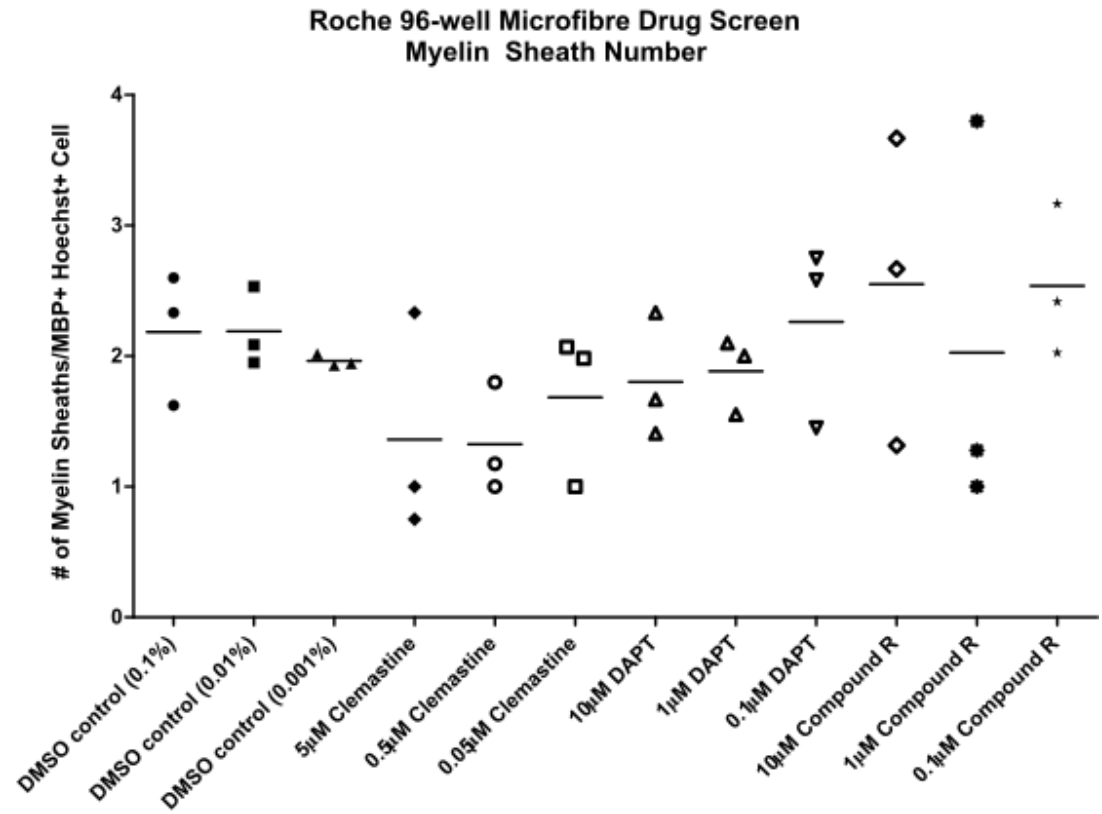
Roche 96-well Microfibre Drug Screen
Myelin Sheath Number
# of Myelin Sheaths/MBP+ Hoechst+ Cell
0
1
2
3
4
DMSO control (0.1%)
DMSO control (0.01%)
DMSO control (0.001%)
5μM Clemastine
0.5μM Clemastine
0.05μM Clemastine
10μM DAPT
1μM DAPT
0.1μM DAPT
10μM Compound R
1μM Compound R
0.1μM Compound R

Figure 5.8 No significant changes in myelin sheath number was seen using three compounds tested on immunopanned OPCs at Roche

A. The number of myelin sheath per MBP+ cell. Sheaths were only counted when MBP+ cells were distinctly separate to allow each process to be traced back to their respective cell body, and excluded when cell bodies were clumped in close proximity. n = 3
B. The average number of myelin sheath per biological replicate from data in A was used to perform statistical analysis. Although the extent to which the results can be interpreted is limited due to the restricted number of qualifying cells for quantification, initial results seem to suggest no significant changes in myelin sheath numbers using any of the compounds at all concentrations tested.

   The statistical test performed was the one-way ANOVA with post-hoc Dunn's Multiple Comparison test for analysis.

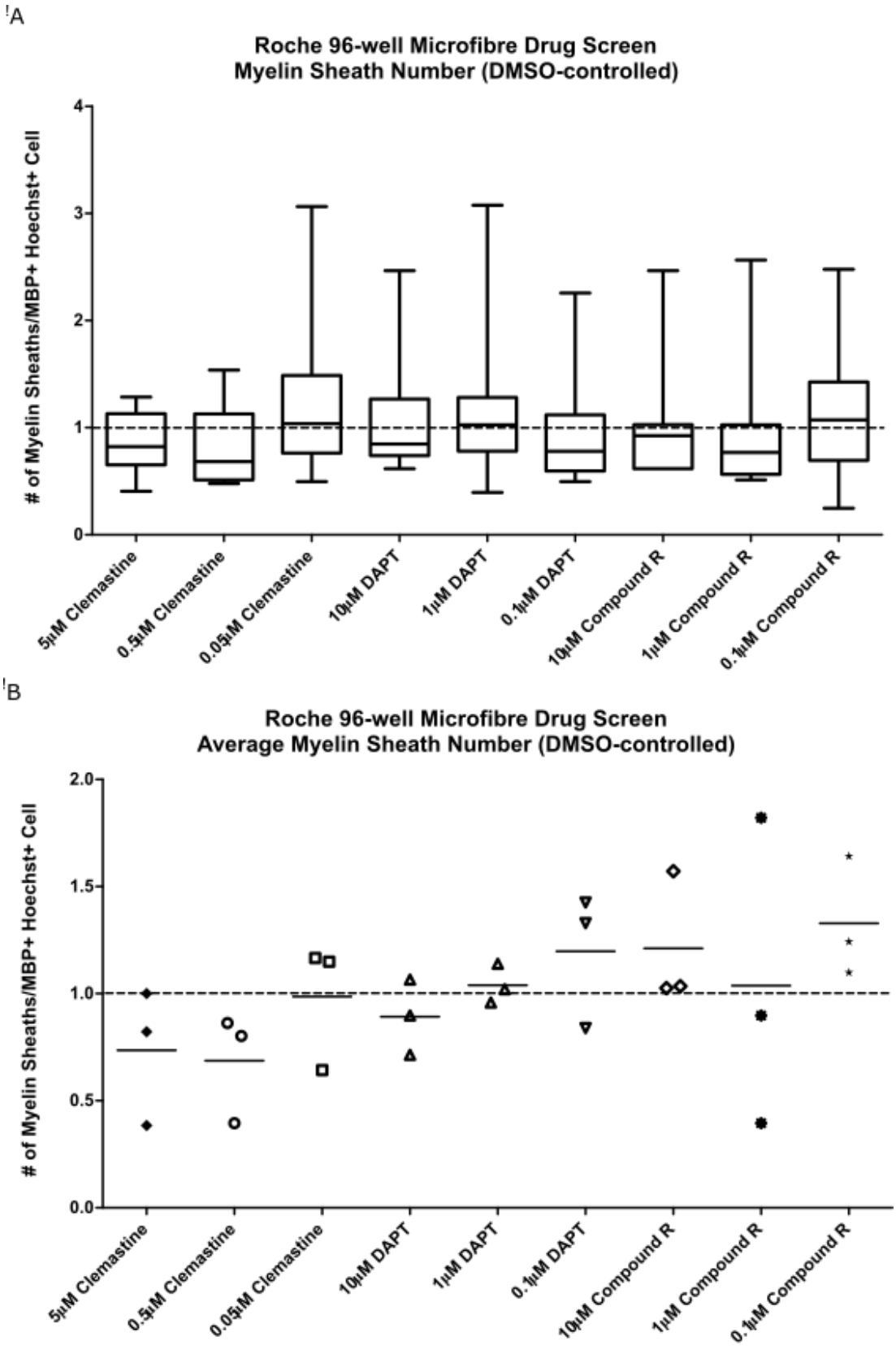

Figure 5.9 No significant changes in DMSO-controlled myelin sheath number was seen using three compounds tested on immunopanned OPCs at Roche

A. The number of myelin sheath per MBP+ cell was normalised for the DMSO control per biological replicate from the data in **Figure 5.8**.
B. The average number of myelin sheath normalised for the DMSO control per biological replicate from the data in A was used to perform statistical analysis. Once again, although the interpretation of the data is limited, the data thus far seems to suggest no significant changes in myelin sheath numbers, even taking into account the average number of sheaths in the DMSO control per biological replicate.

   The statistical test performed was the one-way ANOVA with post-hoc Dunn's Multiple Comparison test on GraphPad Prism 5.

5.2.5 Effect of coating the fibres with fibrin on myelin sheath formation on the 96-well microfibre drug screen

Bechler, Byrne and ffrench-Constant (2015) showed that on these microfibre culture systems, the length of the myelin sheath corresponded to the diameter of the fibre on which they were cultured. One question about this screening platform was that should myelin sheath formation occur at such efficiency that they reached their optimal quantity even in conditions with no compounds added, whether this would result in the masking of the effect of potentially pro-myelinating compounds and therefore result in increased false negatives. Petersen *et al.* (2017) showed that the coagulation factor fibrinogen inhibits the differentiation of OPCs into mature myelinating OLs in primary cultures, OPC/dorsal root ganglion co-cultures, and in nanofibre culture system, by activating the bone morphogenetic protein (BMP) signalling pathway. Evaluation of post-mortem MS lesions suggested the association of fibrinogen and increased BMP signalling occurred at sites of increased blood-brain barrier permeability, and that the administration of a defibrinogenating agent post-LPC demyelination in an *in vivo* model reduced BMP signalling and increased remyelination, highlighting the clinical and therapeutic relevance of this molecule in MS.

Therefore, using Bacakova *et al.* (2016)'s protocol for coating electrospun PLA fibres which showed stable nanocoating for the 14 days in culture media at 37°C tested, with the rate of fibrin coating degradation corresponding to the degree of cell proliferation, I conducted an experiment in which immunopanned O4+ OPCs were plated onto 96-well microfibre plates with or without fibrin coating to test whether the presence of a MS-relevant inhibitory

molecule would increase the sensitivity of the screen. Under the fibrin-coated condition, some cells showed a higher degree of myelin sheath formation on the fibrin-coated fibres (**Figure 5.10** A, 0.05 µM Clemastine) versus other cells where processes and membrane extension could be detected but were not ensheathing the fibres (**Figure 5.10** B, 0.001% DMSO control). Although the same caution in interpretation must be taken as the other experiments plated at Roche and transported to SCRM, initial results seem to show that the average myelin sheath length comparing the non-fibrin-coated (**Figure 5.10** C) and fibrin-coated (**Figure 5.10** D) conditions stayed similar at around 20 to 25µm average across all compounds and concentrations. Conversely, when comparing the myelin sheath number, in the non-fibrin-coated condition (**Figure 5.11** A), the average sheath number across tested compounds and concentrations were around 2 sheaths per MBP+ cell, with a slightly higher value at 2.75 in 0.1 µM DAPT and above 3 in Compound R (3.67 at 10 µM, 3.80 at 1 µM, and 3.17 at 0.1 µM), whereas in the fibrin-coated condition (**Figure 5.11** B), the average sheath number was more variable. Interestingly, despite the potential preliminary slight increase in myelin sheath number with Compound R in the non-fibrin-coated condition, this was not apparent in the fibrin-coated condition at 1 µM and 0.1 µM concentrations. Whilst no significant conclusions can be drawn from this experiment due to the technical issues with transportation and the subsequent low number of cells included in the quantification, as well as the low number of biological replicates thus far (n = 1), the morphology of the cells as seen by confocal microscopy (**Figure 5.10** A and B) and the preliminary quantification does suggest that fibrin-coating of the microfibres may potentially impact the number of myelin sheaths that the OLs are able to form on the microfibre drug screening platform and might be worth exploring in future experiments.

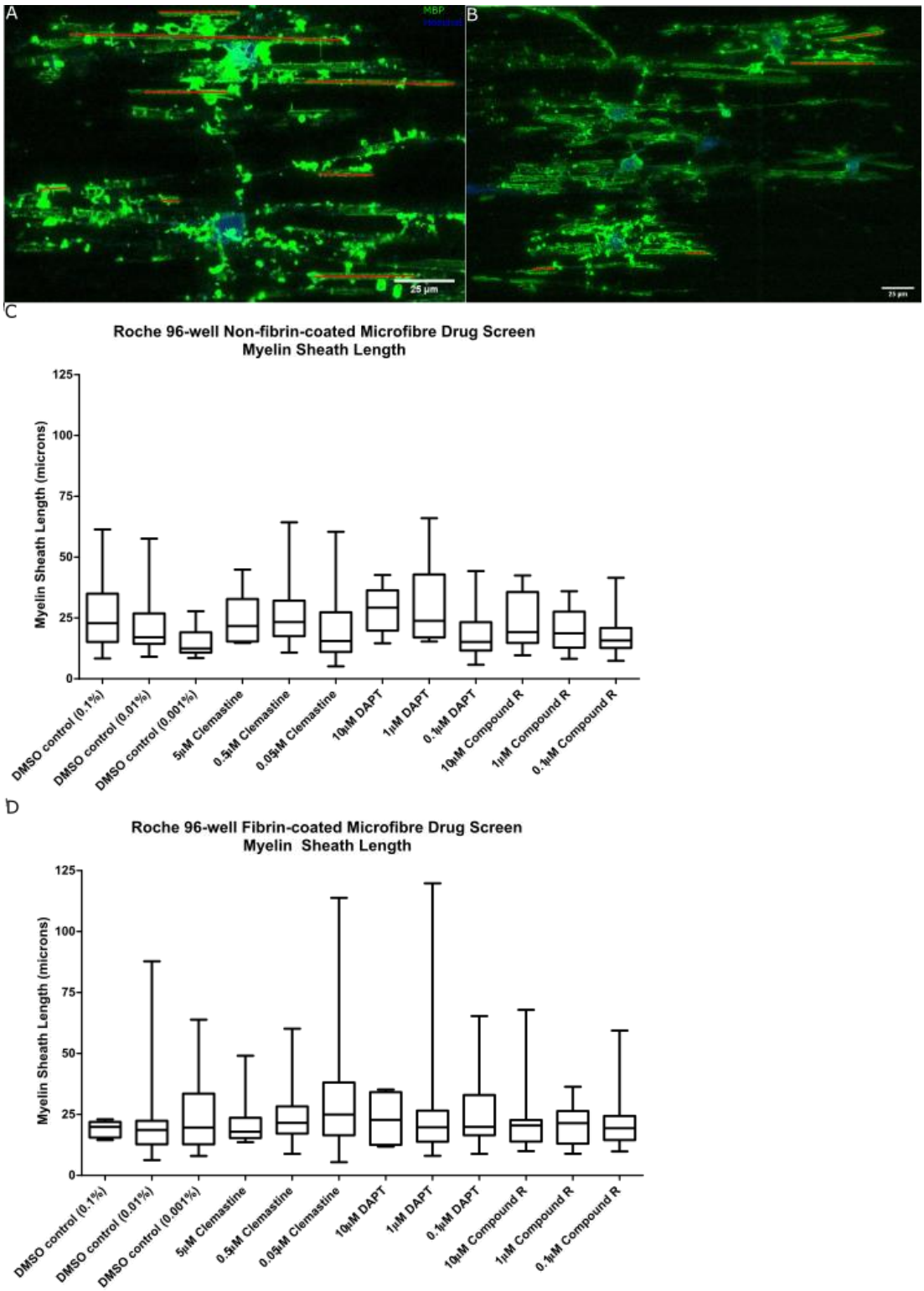

Figure 5.10 Preliminary results from coating the fibres with fibrin shows no change in the average myelin sheath length on the 96-well microfibre drug screen

A. Example of a confocal image of cells isolated by immunopanning on the fibrin-coated microfibres in the 0.05 µM Clemastine condition with myelin sheath formation as verified by

the z-stack images. The red lines represent complete myelin sheaths that were included in the quantification.

B. Example of a confocal image of cells on the fibrin-coated microfibres in the 0.001% DMSO control condition with myelin processes that did not form myelin sheaths as verified by the z-stack images. The red lines represent complete myelin sheaths that were included in the quantification.

C. Myelin sheath length measurements on a 96-well non-fibrin-coated microfibre plate showing an average of 20 to 25µm across all conditions and concentrations. The lengths were quantified by manual measurements on Fiji, recorded on Excel, and plotted on GraphPad Prism 5. n = 1

D. Myelin sheath length measurements on a 96-well fibrin-coated microfibre plate using the same batch of immunopanned OPCs as C showing similar average sheath length across all conditions and concentrations. The lengths were quantified using the same method and criteria as per C. n = 1

A

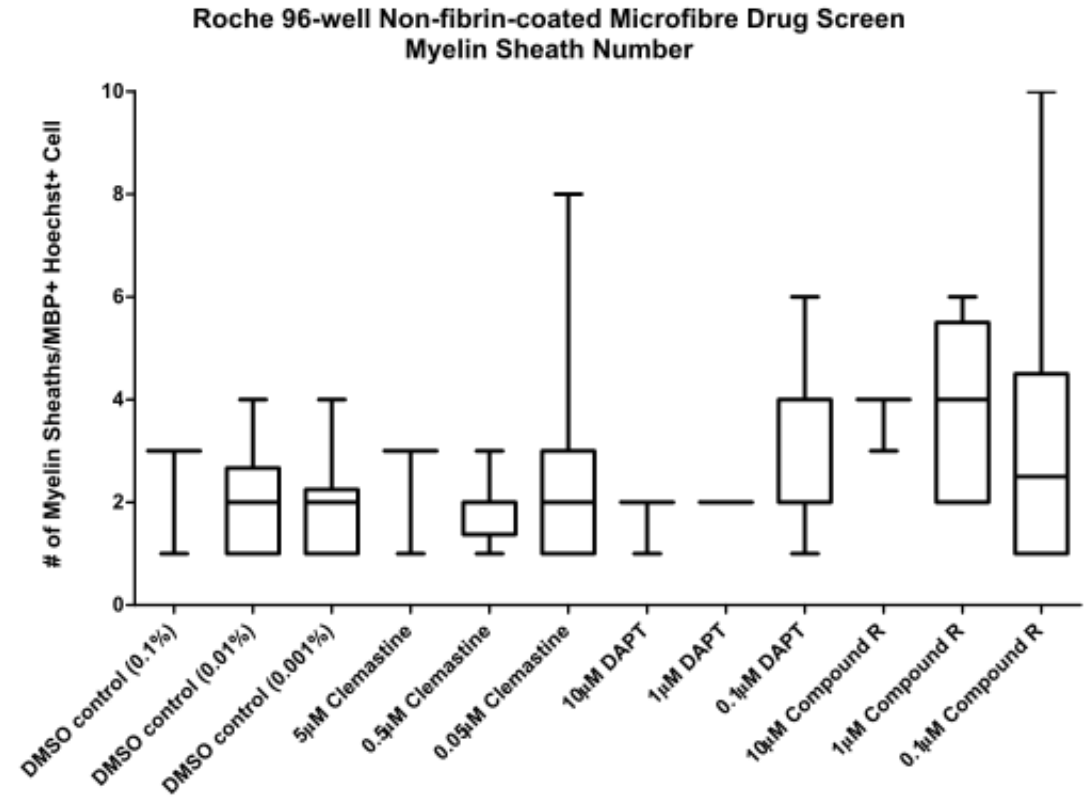
Roche 96-well Non-fibrin-coated Microfibre Drug Screen
Myelin Sheath Number
# of Myelin Sheaths/MBP+ Hoechst+ Cell
0
2
4
6
8
10
DMSO control (0.1%)
DMSO control (0.01%)
DMSO control (0.001%)
5μM Clemastine
0.5μM Clemastine
0.05μM Clemastine
10μM DAPT
1μM DAPT
0.1μM DAPT
10μM Compound R
1μM Compound R
0.1μM Compound R

B

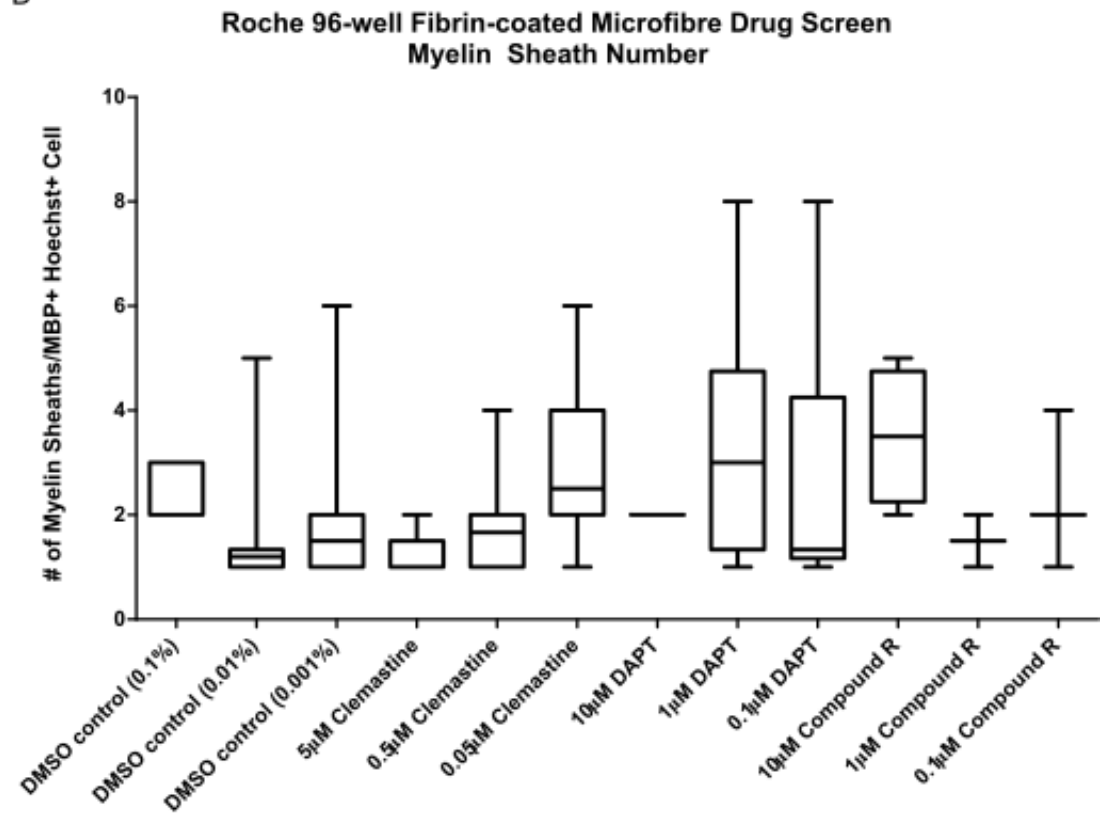
Roche 96-well Fibrin-coated Microfibre Drug Screen
Myelin Sheath Number
# of Myelin Sheaths/MBP+ Hoechst+ Cell
0
2
4
6
8
10
DMSO control (0.1%)
DMSO control (0.01%)
DMSO control (0.001%)
5μM Clemastine
0.5μM Clemastine
0.05μM Clemastine
10μM DAPT
1μM DAPT
0.1μM DAPT
10μM Compound R
1μM Compound R
0.1μM Compound R

Figure 5.11 Preliminary results from coating the fibres with fibrin shows potential differences in the average myelin sheath number for some conditions on the 96-well microfibre drug screen

A. Number of myelin sheath per MBP+ cell on the 96-well non-fibrin-coated microfibre plate, showing an average of 2 sheaths per MBP+ cells across the compounds and concentrations tested, with 0.1 μM DAPT and Compound R showing potentially slightly higher numbers. Sheaths were only counted when MBP+ cells were distinctly separate, and excluded when cell bodies were clumped in close proximity. n = 1
B. Number of myelin sheath per MBP+ cell on the 96-well fibrin-coated microfibre plate using the same batch of immunopanned OPCs and quantified using the same criteria and method as A. The average myelin sheath number was highly variable across all conditions and concentrations. n = 1

5.3 Discussion

In this chapter, I showed that the 96-well microfibre plates that I constructed were compatible with use with liquid-handling machines, specifically the Multidrop™ for plating, fixing, and staining and the BioTek LS 405 microplate washer for staining and washing. The incorporation of these, in addition to the Integra ViaFlo 96/384 liquid-handling pipette machine to increase precision in the media changes with the dissolved compounds, would be essential in future experiments to improve reproducibility and the CV values for the assay. In addressing the issue of imaging the 3D myelin sheaths with the increased working distance of the suspended microfibres and the resolution required to determine complete ensheathment (**Figure 1.19** Challenge and Solution #2), the Leica SP8 Confocal system, Yokogawa CV7000, Operetta, Opera, and Opera Phenix were tested. The Yokogawa CV7000 was eliminated due to the limitations in the objectives compatible with the 96-well microfibre plates, and the practical difficulties of accessing the system for further testing and imaging. The Operetta and Opera were excluded due to their incompatibility for 3D imaging. The Leica SP8 Confocal system with the MatrixScreener plugin is able to automate the imaging, but is not high content. The Opera Phenix appears to be the most promising in terms of high content imaging and resolution for 3D myelin sheath detection.

Due to transport issues of the plates from Roche in Basel, Switzerland, followed by ongoing severe myelination media problems due to the change in the commercial B27 supplement (ThermoFisher Scientific) and the batch-to-batch variability of the homemade B21 (Chen *et al.*, 2008), I had limited scope in performing compound library screening in the 3D myelination assay during the available timeline of my PhD. However, from the experiments conducted, with limited scope for data interpretation due to the technical issues discussed, none of the three drugs tested, Clemastine, DAPT, or Roche's Compound R, seemed to show statistically significant increases in myelin sheath length and number so far. One potential factor with the myelination assay was the possibility that in optimal myelination media, myelin sheath formation would be too efficient to detect increases beyond DMSO control. This issue was addressed by coating the fibres in fibrin, which has been shown by Petersen *et al.* (2017) to inhibit OPC differentiation into mature myelinating OLs, and may also be a clinically and therapeutically relevant inhibitor in MS. Culturing the OPCs on fibrin-coated microfibres showed the presence of extensive incomplete myelin sheath formation in some conditions. Although statistical analysis was not possible to compare fibrin-coating versus non-fibrin-coating results as only one biological replicate was able to be conducted, this shows early promise in potentially increasing the sensitivity of the assay in a clinically-relevant manner in future experiments.

As stated here and in Chapter 3, the lab had persistent problems with myelination media during the course of my PhD, which severely limited the work I could perform. The myelination media for the microfibre culture system, as developed by Bechler, Byrne and ffrench-Constant (2015), is based on neuronal-OPC co-culture media (such as Watkins *et al.*, 2008), requiring multiple components as listed in Chapter 2 (Materials and Methods), including B27. The commercial B-27™ Supplement (ThermoFisher #17504044) and the homemade B21 (based on NS21 (Chen *et al.*, 2008)) were both optimised for use in neuronal cultures to support their growth and activity. It is therefore possible that these media components do not provide optimal conditions for oligodendrocyte differentiation and myelination, and that continued quality control has shifted B27 towards higher neuronal survival and activity which may not be as compatible for oligodendrocytes. An alternative media for oligodendrocyte myelination on microfibres is a B27-free low serum myelination media. However, serum is ill-defined, including undefined growth stimulating factors such as hormones (Barnes and Sato, 1980), and therefore increases batch-to-batch variability between different lots of serum in both cell growth and drug response. It is therefore

imperative to the continued progress of the microfibre culture system and the 96-well microfibre drug screening platform that a third 'B27' is optimised specifically for oligodendrocytes, which may include screening the components of the current homemade B21 to determine which are required for oligodendrocytes and remove superfluous, or potentially even unfavourable, components included specifically for neurons, and determining whether certain sources of media components are preferable for OLs like determined for BSA and transferrin for neuronal cultures by Chen *et al.* (2008).

Some progress has been made in this goal. Subsequent to initial thesis submission, our lab, led by Dr. Marie Bechler, was able to test the various components of B21 and whether their removal affected myelin sheath formation in my 96-well microfibre plate. Different B21 combinations were tested, including the removal of Glutathione, Sato, various combinations of Vitamin components, and lipids, as well as the use of an alternative Vitamin E source, and switching unbound apo-Transferrin to iron-bound holo-Transferrin, with transferrins functioning to mobilise iron. Out of the 24 combinations of B21 in myelination media tested, the use of holo-Transferrin appeared to give the best myelin sheath formation, although this was still poorer than the serum-free myelination media. This suggests an importance of the presence of iron in the myelination media. As reviewed by Todorich *et al.* (2009), iron is an essential trophic factor for vital cell functions in oxygen consumption and ATP production, with OLs having been shown to be a major source of iron accumulation and consumption in the brain and requiring sufficient iron to be acquired from external sources in a timely manner for normal myelination to occur. Infants with iron-deficiency anaemia have been shown to have increased latency in indirect markers of myelination, auditory brain stem potentials and visual evoked potentials (Algarín *et al.*, 2003), and animal models of disrupted iron homeostasis have shown decrease in myelin proteins and lipids levels and loss of myelin compaction (Ortiz *et al.*, 2004). With OLs having been shown to be able to produce transferrin, and its mRNA level increasing uniquely in the brain post-natally with OL maturation (Bartlett, Li and Connor, 1991; Bloch *et al.*, 1985), iron is an essential component for optimal OL function, and suggests the reasoning behind why the availability of iron using holo-Transferrin would improve the *in vitro* microfibre myelinating culture above apo-Transferrin.

Using this variation of B21, my constructed 96-well microfibre plate, optimised immunopanned O4+ OPCs plating protocol, and compounds I had selected as positive (endothelin B receptor agonist BQ-3020 and PKCε agonist FR 236924 (Yuen *et al.*, 2013; Swire

et al., 2019)) and potential negative (MAPK/ERK inhibitor UO126) regulators of myelin sheath formation, Dr. Marie Bechler prepared a plate on which these compounds and their respective controls had been tested, imaging performed by myself, and blind analysis for sheath length and number performed by Dr. Peggy Assinck (**Figure 5.12**). As shown in these preliminary results (n = 1), the endothelin B receptor BQ-3020, shown by Dr. Matthew Swire to increase myelin sheath number on microfibres in 12-well scaffolds (Swire *et al.*, 2019), appears to potentially increase the number of myelin sheaths produced per OL in the 96-well microfibre platform. This gives early promise that pro-myelination compounds could be detected on these 96-well microfibre plates using the holo-Transferrin variant of B21 myelination media, with further experiments being required to increase the number of biological replicates to confirm these initial findings and to determine a compound that decreases myelin sheath formation to calculate the Z' factor for the assay.

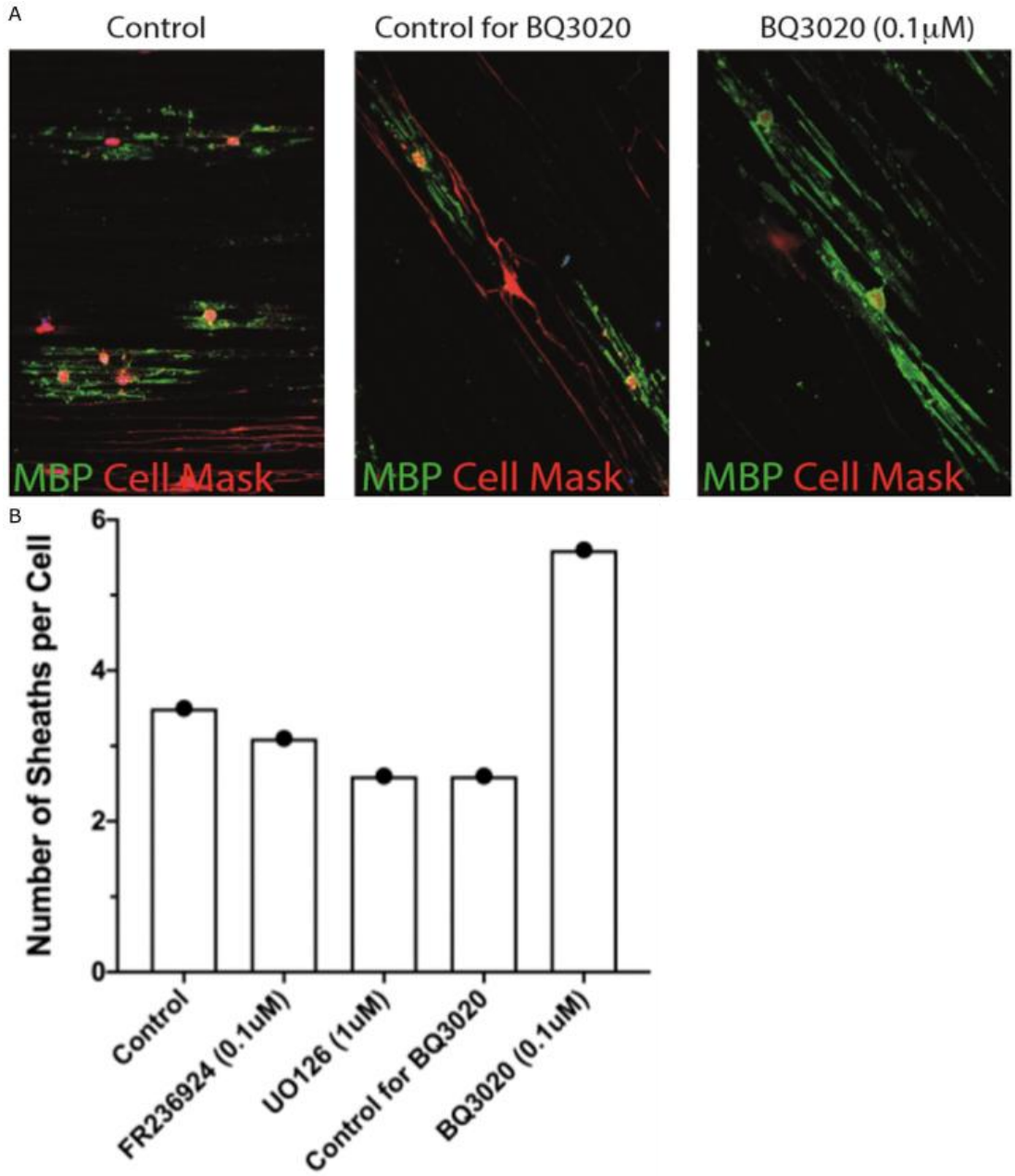

Figure 5.12 Preliminary results from selected compounds tested on the 96-well microfibre plate using the holo-Transferrin variant of B21 myelination media

A. Representative confocal images taken using the 25x water objective on the Leica SP8 confocal system manually for selected conditions: (1) the media control, (2) the control for BQ-3020 (0.03M sodium bicarbonate), and (3) BQ-3020, which showed early results of potentially increasing myelin sheath number.

   The Cell Mask (for cytoplasmic staining) was included to improve the supervised machine learning CellProfiler pipeline as discussed in the 'Discussion'.

B. The average number of myelin sheaths produced per MBP+ Hoechst+ cell per condition. Although FR 236924 and UO126 did not seem to increase or decrease myelin sheath number in comparison to the control, respectively, preliminary results comparing BQ-3020 to its sodium bicarbonate control show a potential increase in myelin sheath number. n = 1

Imaging for A was performed by myself, and the figures were prepared by Dr. Peggy Assinck.

CHAPTER VI. LABEL-FREE RAMAN-BASED IMAGING OF MYELIN

In the final stage of drug discovery for my PhD project, I explored imaging techniques that could be used to validate the compounds that have come up as hits in the 3D high-throughput single cell *in vitro* platform as potentially being pro-myelination in more complex *in vivo* and *ex vivo* models of myelination, and potentially be applicable for live imaging to track changes in *in vivo* and *ex vivo* mouse brains before and after treatment. In order to achieve this, I investigated the use of a label-free imaging techniques based on Raman spectroscopy, Coherent anti-Stokes Raman spectroscopy (CARS) and Stimulated Raman Scattering (SRS) microscopy techniques. Although its application in myelin imaging in itself is not novel, as mentioned in the studies described below, its use in drug discovery for myelination therapies would be a novel application of the technique and provide key benefits such as being label-free and providing potential to track changes pre- and post-treatment. In this final chapter, I explored whether (1) label-free Raman-based imaging techniques could be used to detect myelin in live and fixed tissue, (2) quantification of myelin sheaths was feasible, and (3) if it could be applied to study the effect of a potential pro-myelination compound *in vivo*, including the investigation of whole brain imaging and deuterium labelling of newly formed myelin sheaths.

6.1 Raman Spectroscopy

Raman scattering was described by and named after the Indian physicist Sir Chandrasekhara Venkata Raman in 1928, who first observed the phenomena of inelastic scattering of light in organic liquids predicted by Adolf Smekal in 1923. Raman became the first Asian and first non-white recipient of a Nobel Prize for this discovery, with an award in Physics in 1930 (Raman, 1928; Singh, 2002). Raman spectroscopy is a technique that measures the shift in energy that occurs due to inelastic scattering of light when a photon from the incident light produces a scattered photon when it interacts with matter (**Figure 6.1**). In Rayleigh (elastic) scattering, when the photon of light interacts with a molecule, there is a temporary transition to an increased virtual energy state followed by relaxation back to ground state as the photon is re-emitted in a scattered direction, and therefore no transfer of energy between the

photon and the molecule. However, in Raman (inelastic) scattering, which occurs only in approximately 1 in 10^8 photons, during this molecule and photon interaction, energy transfer results in the molecule releasing a different amount of energy to the incident photon as it equilibrates with its surroundings and relaxes via thermal relaxation. In Stokes scattering, energy is transferred to the molecule from the incident photon by nuclear motion, resulting in reduced energy and frequency of the scattered photon. In anti-Stokes, energy is transferred to the photon, increasing the energy and frequency of the scattered photon. As the shift in energy and the measured wavelength of the scattered light is dependent upon the chemical composition of the matter, and the intensity of the signal proportional to the quantity of the molecules, it can used to "fingerprint" the presence and concentration of molecular bonds in the sample (Ember *et al.*, 2017; Rostron, Gaber and Gaber, 2016; Tarnowski and Morris, 2001).

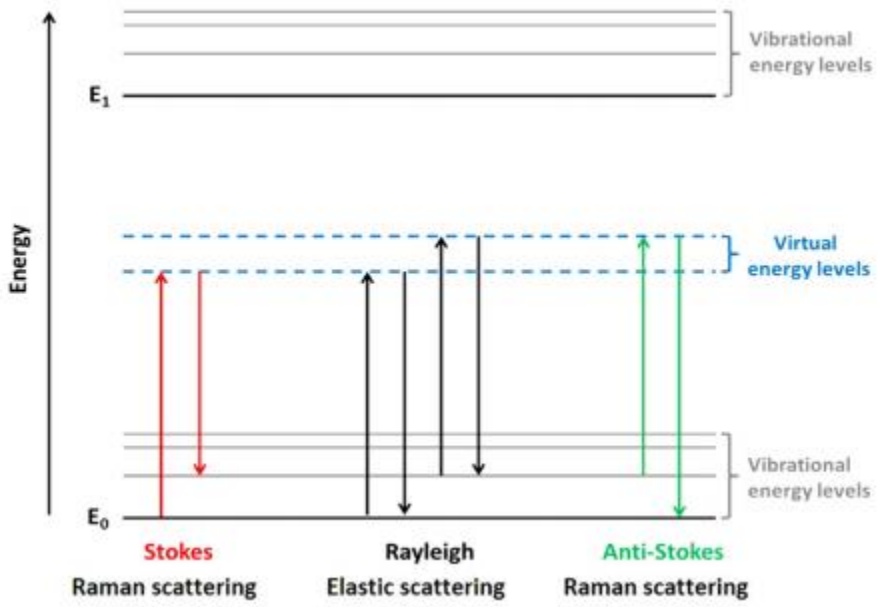

Figure 6.1 Jablonski-style diagram of energetic transitions in Raman

Rayleigh scattering is described as elastic as the incident and scattered photon are of equal energy. In Stokes scattering, the scattered photon is lower in energy than the incident photon, whilst the reverse is true in anti-Stokes scattering where the scattered photon gains energy.

Figure from Ember *et al.*, 2017

Raman Spectroscopy has major advantages compared to complementary vibrational spectroscopy techniques like IR spectroscopy, particularly when it comes to biological samples and imaging. Raman requires minimal sample preparation for good spatial resolution (0.5 to 2μm) and spectral resolution (3-4cm^{-1}, depending on the spectrometer). Unlike IR spectroscopy which is strongly absorbed by water, the Raman scattering intensity of water molecules is very weak and does not overwhelm the generation of more characteristic spectral data. Due to the rarity of Raman scattering occurring, the signal is inherently weak. Therefore, a number of Raman techniques have been developed to enhance the signal generated for various biological questions, including Surface enhanced Raman spectroscopy (SERS) that uses metal nanoparticles, usually gold for its biocompatibility, to increase the signal-to-noise ratio, or Spatially offset Raman spectroscopy (SORS) which detects diffuse Raman scattering to collect measurements from increased depth than can be penetrated by light. Of particular interest to my biological problem were Coherent anti-Stokes Raman spectroscopy (CARS) and stimulated Raman scattering (SRS) (Ember *et al.*, 2017; Rostron, Gaber and Gaber, 2016; Tarnowski and Morris, 2001).

6.2 Coherent anti-Stokes Raman Spectroscopy and Stimulated Raman Scattering Microscopy

CARS and SRS, which overcome the low signal levels of spontaneous Raman and are typically used for imaging, are nonlinear optical processes that involve the use of two pulsed lasers rather than the conventional single continuous laser for Raman spectroscopy (**Figure 6.2** A). The initial idea for CARS is attributed to P.D. Maker and R.W. Terhune, but was first constructed in 1982 by M.D. Duncan (Begley, Harvey and Byer, 1974; Duncan, Reintjes and Manuccia, 1982; Rostron, Gaber and Gaber, 2016). The first publication showing the use of CARS in biological samples, in Gram negative bacterium and HeLa cells, was published in 1999 (Zumbusch, Holtom and Xie, 1999). SRS was initially accidentally discovered by Woodbury and Ng in 1962, and the theory behind its process described by Healthwarth (Rostron, Gaber and Gaber, 2016). The application of SRS in biological samples, including unstained cells, tissues, and drug delivery monitoring was first reported by Freudiger *et al.* (2008), and independently by Ozeki *et al.* (2009).

In CARS (**Figure 6.2** A), the pump field (ω_p) and Stokes field (ω_s) are optically mixed and applied to a sample. If the frequency of the two beams (the 'beat frequency') is matched to the energy gap between the two vibrational energy states of a molecule (the molecular bond "fingerprint"), all of the molecules vibrate 'coherently' between these two energy states. A third beam (ω_p) is used to excite the molecule to a 'virtual' vibrational energy state which emits a Raman-scattered photon (ω_{aS}) as it relaxes back. The 'coherent' vibration results in constructive interference and therefore an increase in signal intensity in a quadratic manner (Ember *et al.*, 2017; Fu *et al.*, 2008; Potma and Xie, 2004; Rostron, Gaber and Gaber, 2016; Wang *et al.*, 2005). By targeting the CH_2 bonds abundant in lipid, CARS has previously been shown to be able to image the myelin fibres in the mouse brain (**Figure 6.2** B) (Fu, T. Brandon Huff, *et al.*, 2008) and in live spinal tissue of guinea pigs (Wang *et al.*, 2005) in label-free and minimally-prepared samples. I therefore wanted to apply CARS to be able to image myelination and quantify myelin sheaths in unlabelled fixed and live brain samples, with the ability to image myelin sheaths in live samples being particularly interesting as this currently requires the use of transgenic animals with membrane-bound GFP labelling under the control of myelin-associated proteins such as MBP (i.e. Chong *et al.*, 2012).

The basic principle of SRS is similar to CARS (**Figure 6.2** A); a pump and a stokes beams are applied to the sample, and when the frequency difference between the two lasers match the molecular vibration frequency of the bond, excitation of the molecule occurs. In SRS, this stimulated excitation results in the loss of intensity in the pump beam (stimulated Raman loss, SRL) and gain in the Stokes beam (stimulated Raman gain, SRG). To detect SRL/SRG, one of the beams in amplitude modulated, and the corresponding modulation in the other beam detected by using a lock-in amplifier. A benefit of using SRS over CARS is that SRL and SRG cannot occur when $\Delta\omega$ does not match the molecular vibration, whereas in CARS, a signal is still generated at the anti-Stokes frequency due to off-resonant electronic transitions that also add coherently. This non-resonant signal can interfere and overwhelm the CARS signal, especially in situations with low concentrations or weak resonances. Although SRS is not entirely free of background (Zhang *et al.*, 2013), it is often more sensitive than CARS, and is therefore more appropriate for sparse labelling and imaging (Rostron, Gaber and Gaber, 2016; Tipping *et al.*, 2016), such as with deuterium labelling as discussed later in this chapter.

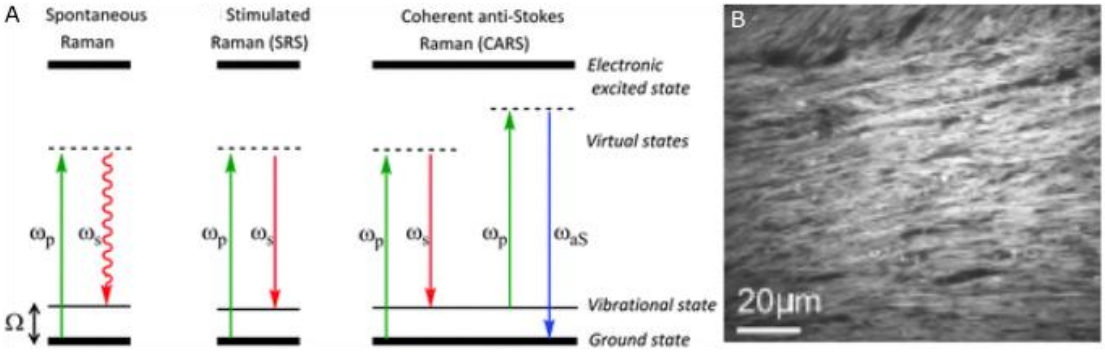

Figure 6.2 CARS and SRS Microscopy

A. Schematic diagram of the energy levels for: (1) spontaneous Raman, where the pump beam (ω_p) interacting with the sample results in a shifted signal (ω_s) due to inelastic scattering; (2) SRS, where two lasers at frequencies ω_p and ω_s are tuned so that the frequency difference ($\Delta\omega = \omega_p - \omega_s$) is equal to the molecular vibration (Ω) being observed, and (3) CARS, which involves a complex four-beam mixing process to probe the anti-Stokes frequency (ω_{aS}) so that $\omega_{aS} = 2\omega_p - \omega_s$ and $\Delta\omega$ tuned to the Ω.
Figure from Tipping *et al.* (2016).

B. CARS image of the mouse brain white matter, showing that the presence of myelin sheaths can be detected by targeting the CH_2 molecular bond using CARS microscopy.
Figure from Fu *et al.* (2008).

6.3 Results

6.3.1 Verifying the use of Coherent anti-Stokes Raman Spectroscopy (CARS) microscopy to detect myelin by targeting the CH_2 bond

Initially, we tested whether we would be able to detect myelin sheaths by using the 2845cm^{-1} wavelength to detect the CH_2 molecular bonds in lipid. Coronal brain sections from 6-week WT mice were stained with MBP for myelin and Olig2 for cell bodies (**Figure 6.3** A). The standard staining protocol for brain sections use the detergent Triton X-100, which contain uncharged and hydrophilic head groups, as the permeabilising agent to non-selectively dissolve lipids from the cell membranes to make them permeable to antibodies. However, the removal of lipid would be incompatible with the sample preparation for CARS due to

requiring the lipid molecules to be present for the detection of myelin sheaths. I therefore developed an adapted staining protocol using saponin, which selectively removes cholesterol to make approximately 100Å holes in the membrane, as the permeabiliser to allow for intracellular antibody binding in the cholesterol-rich brain tissue (Jamur and Oliver, 2009). When simultaneous CARS signals was detected from the same brain sections in the same regions (**Figure 6.3** B), the structures detected by MBP and CARS were almost identical, highlighting that detection of CH_2 bonds by CARS preferentially picks up myelin in the brain. In order to test whether this was not due to cross-talk between the immunofluorescence channel and CARS or artefacts of the CARS imaging, coronal brain sections from the shiverer mutant mice with no compact myelin (**Figure 6.3** C) and LPC-injected mice with focal demyelinated lesions (**Figure 6.3** D and E) were also imaged as negative controls. As can be seen, no distinct CARS signals could be detected in the shiverer mutant brain slice (**Figure 6.3** C), and an absence of signal was seen in the location of the LPC-induced lesion (**Figure 6.3** D), which included structures more similar to lipid droplets from the breaking down of myelin rather than sheath-like structures (**Figure 6.3** E).

An advantage of CARS is that as it is label-free, live imaging of brain slices for myelin may be possible. To test this, unlabelled live coronal brain sections from 6-week old WT mice were imaged by CARS. Imaging a live brain section using the same set-up as with the fixed tissue slices proved more difficult than expected due to the weaker integrity of the brain pre-fixation. This resulted in the slices floating out of range of the working distance of the objective when suspended in media to keep them alive and prevent them from drying out, and becoming severely compressed and losing their structural integrity progressively over the course of an image being taken when a light weight (the same as with the fixed slices or lighter) was applied on top to keep them against the base of the imaging dish. There was therefore a need for balance in keeping the brain slices submerged in sufficient media to keep them alive and prevent drying out with the need to lightly compress the sections in order to have the section lay flat against the base of the imaging dish and reduce its movement for the duration of the imaging. I therefore came up with the solution to 3D print a 500µm-thick ring (with the technical assistance of Dr. Anthony Buchoux) and cut the live brain slices at 500µm on the vibratome, so that the coverslip would rest most of its weight on the ring rather than directly on the brain slice. Although the softness of the live brain when cutting meant that the brain slice was not precisely at 500µm, this set-up was able to reduce tissue motion and compression of the brain slice while preventing it from floating above the

working distance of the objective. Using this set-up, it was possible to image and detect myelin-like structures in the myelin-dense corpus callosum (**Figure 6.3** F).

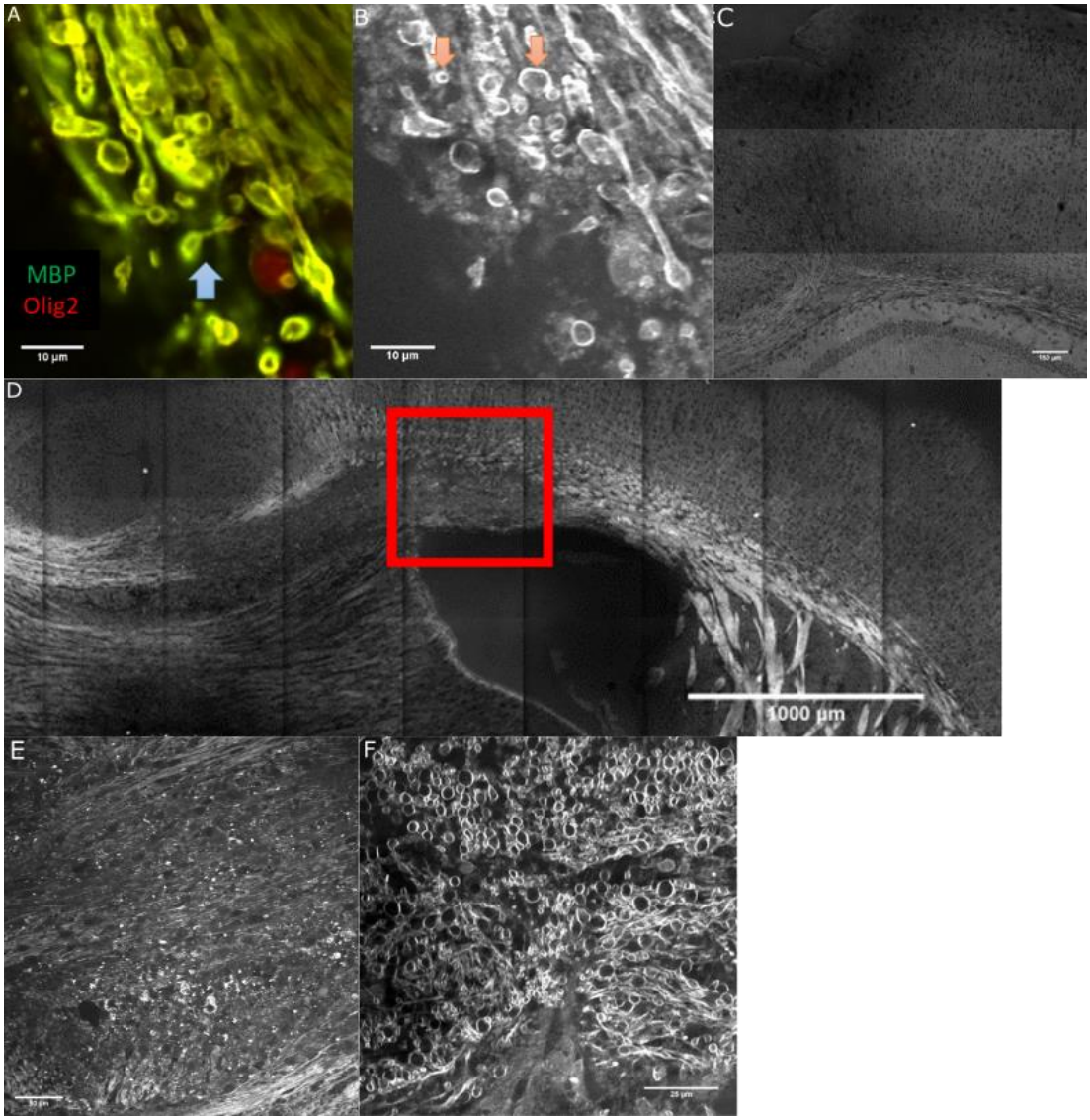

Figure 6.3 CARS microscopy is able to detect myelin by targeting the CH_2 bond

A. Immunofluorescence-labelled 6-week WT male mouse fixed coronal brain slices at the corpus callosum. MBP labelling was used to detect OLs and myelin, and Olig2 for OL-lineage cell bodies. The circular structures appear to be cross-sections of wrapped myelin sheaths, and long structures of full internodes. n = 3
B. The corresponding CARS image for A. Similar structures can be detected in the CARS image versus the immunofluorescence image. The differences between A and B are highlighted with blue (in A) and red (in B) arrows.

C. Shiverer mutant mouse fixed coronal brain slice of the corpus callosum and cerebral cortex regions. There appears to be no significant regions of CH_2-positive CARS signal in this sample with no compact myelin formation. n = 4
D. Fixed coronal brain slice of the corpus callosum of an LPC-injected mouse. The region along the corpus callosum with less intense CARS signal is the location of the demyelinated lesion. n = 1 with lesion out of 3 injected
E. Higher magnification image of the region highlighted with the red box in B showing what appears to be lipid droplets but no distinct myelin sheath-like structures.
F. CARS image of a live coronal brain slice at the corpus callosum. Myelin sheath-like structures can be detected even in the absence of immunofluorescence-labelling (no cross-talk) and without tissue fixation (feasibility of live imaging). n = 5

Scale bars as labelled in individual images.

Next, I wanted to test whether different densities of myelination and individual myelin sheaths could be detected and measured for sheath length. In order to do this, the corpus callosum from WT mice from 4 different time-points (P2, P6, P14, and P21) were imaged (**Figure 6.4** A). The development of the corpus callosum could be observed using CARS, highlighting its ability to detect the increasing density of myelination in the predicted pattern (Wahlsten, 1984) at the time-points observed. To test whether individual myelin sheaths could be imaged and quantified, the cortical layers of 3-week WT mice were imaged, where there are sparser myelin sheaths than the corpus callosum with the highest density closest to the corpus callosum in layer VI, and decreasing density towards the upper layer II, and a layer of denser myelin sheaths in layer I. The different densities of myelin sheaths in the cortical layers of the sections were detectable by CARS (**Figure 6.4** B), and individual myelin sheaths distinguishable (as shown in layers I-III) and quantifiable with the 'Simple Neurite Tracer' plugin on ImageJ (**Figure 6.5** A). When the sheath length was measured from 2 different animals from layers III to V, the regions where individual myelin sheaths was distinguishable by the plugin, the sheath lengths ranged from 30 to 120µm (**Figure 6.5** B), the length of internodes in the cerebral cortex as has been previously reported by Chong *et al.* (2012), providing preliminary results that measurements of myelin sheath length can be obtained by CARS microscopy.

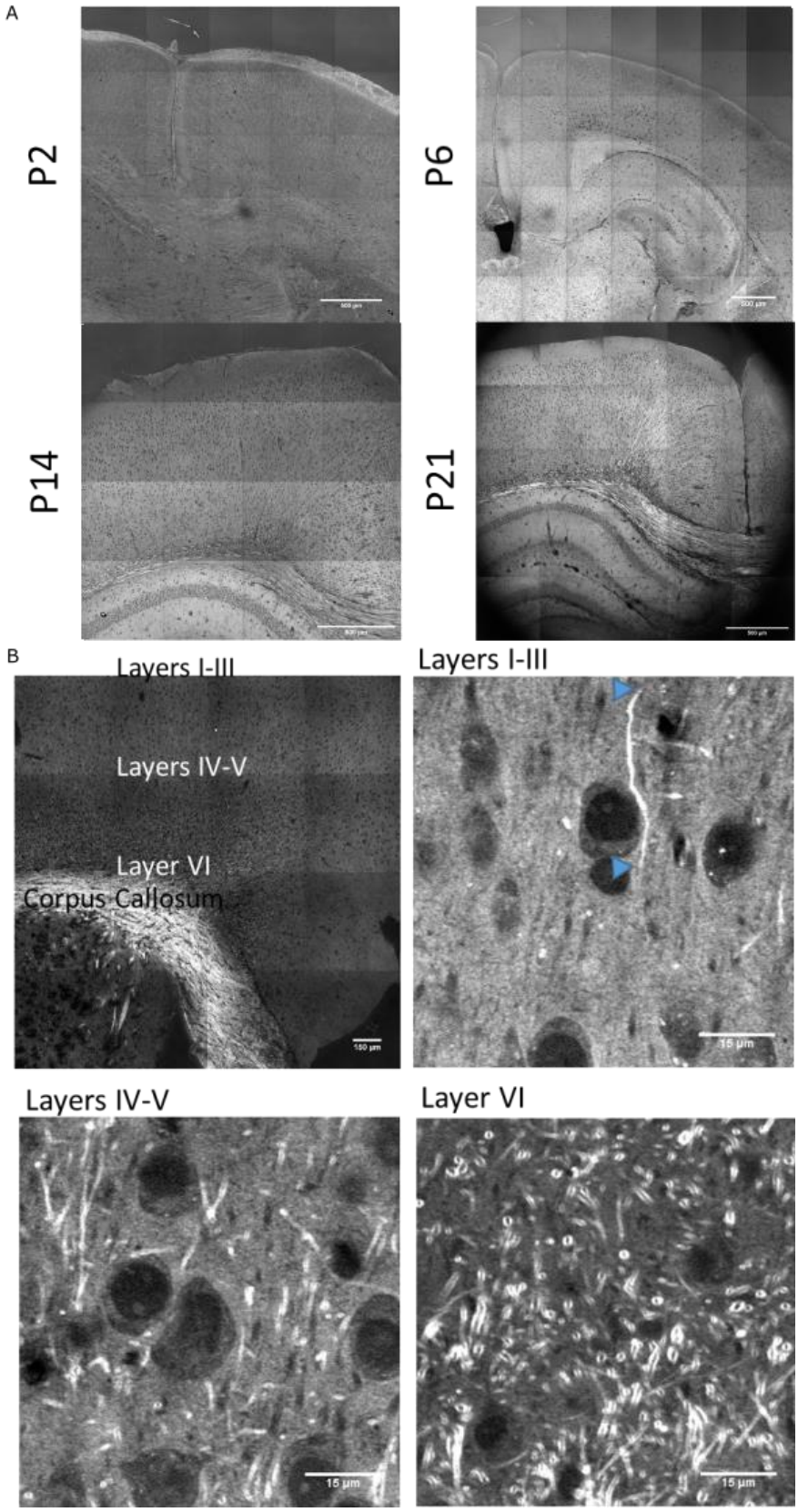

Figure 6.4 Different densities of myelin sheaths, by age and cortical layer, can be detected with CARS microscopy

A. Tilescan images of fixed WT mouse coronal brain slices from different time-points: P2, P6, P14, and P21 (n = 2 per group). Increasing presence of the CH_2-positive CARS signal in the corpus callosum and bright regions in the cortex can be seen with increasing age, as expected for their developmental progress (Wahlsten, 1984).

B. Tilescan overview (top left) and higher magnification images of the cerebral cortex at various layers (layers I to III, layers IV to V, and layer VI) of a 3-week WT male mouse in fixed coronal brain slices, showing increasing density of myelin sheaths at the deeper cortical layers closer to the corpus callosum. The full length of a myelin sheath as detected by CARS is highlighted in 'Layers I-III', with the blue triangles pointed towards the ends of a complete sheath. n = 9

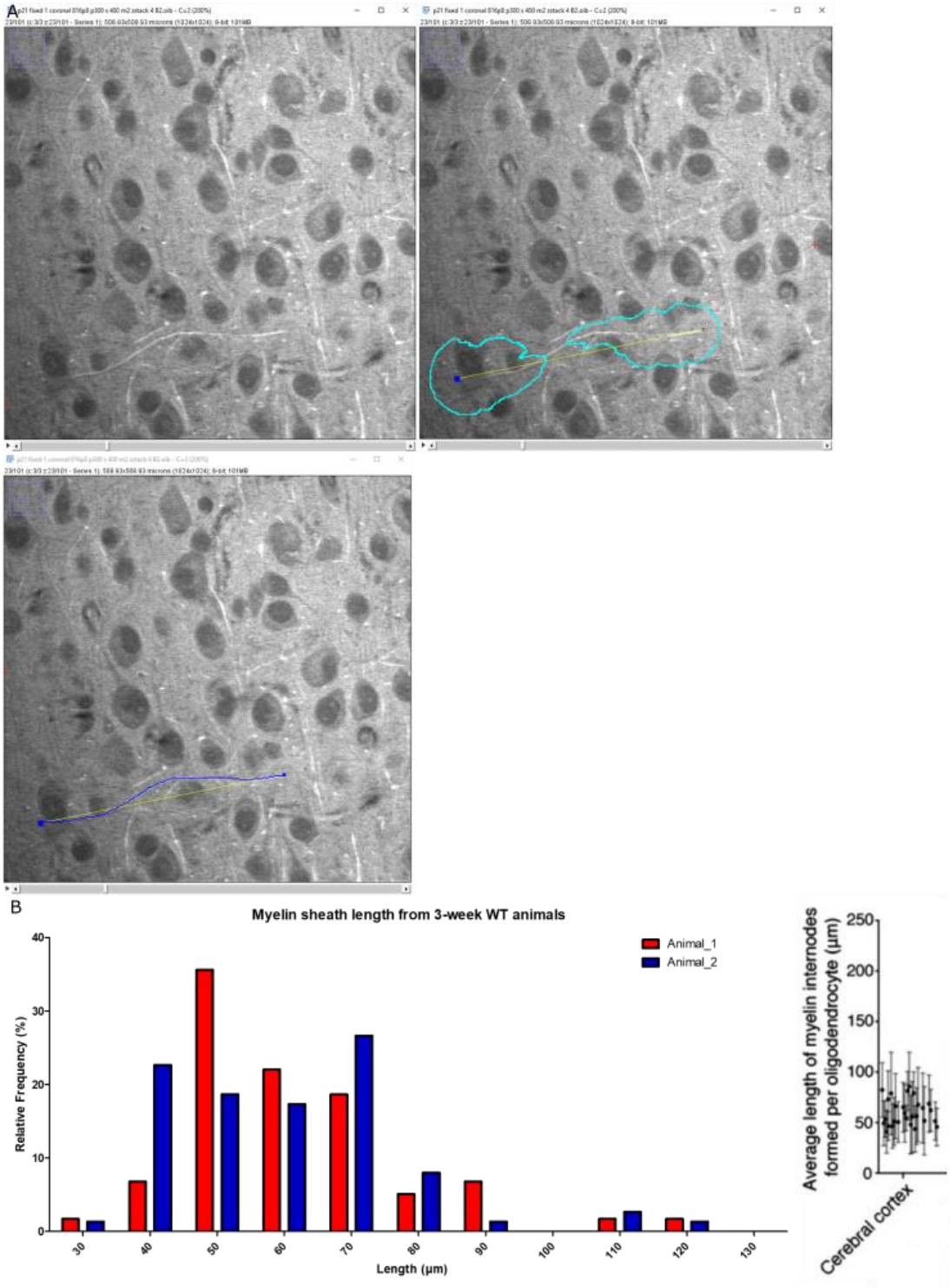

Figure 6.5 Individual myelin sheaths can be quantified using an ImageJ plugin and appear to be the expected range of sheath length for the brain region

A. Myelin sheath length quantification was performed using the 'Simple Neurite Tracer' plugin on ImageJ. The image was adjusted by setting the brightness and contrast automatically at the brightest z-stack, and zooming to 200% (left). The 'Simple Neurite Tracer' plugin was used

to manually detect the two ends of a single myelin sheath (dark blue dots joint by yellow line, middle). The plugin automatically scanned in between the two dots to identify the path of the myelin sheath (light blue, middle) to predict the location and length of the myelin sheath (dark blue, right), which was then manually verified and accepted for sheath length quantification. n = 1

B. Quantification of the lengths of myelin sheaths from layers III-V (where individual myelin sheaths can be detected) of 2 different 3-week WT male mouse from fixed coronal brain slices as described in A (on left). The sheath lengths from both animals ranged from 30 to 120µm, the expected internodal range for the cerebral cortex as reported by Chong *et al.* (2012) (on right).

As live imaging and sheath length quantification is feasible using CARS, I next tested whether *in vivo* imaging of myelin sheaths may be possible by removing a whole brain from a 5-week male mouse and placing it onto the imaging dish with the cortex facing towards the objective. As shown in **Figure 6.6** A, individual myelin sheaths can be detected clearly at 85µm, and as far as 120µm into the whole brain. However, CARS is limited by how far the light can penetrate the sample, with the dark shadows across the top being due to blood vessels obstructing the light. Considering that these brains would have become partially drained of blood due to its position on the imaging dish during the image acquisition, which would not occur if imaging through a cranial window in a whole animal, the depth of penetration *in vivo* would be significantly less with our current set-up. Alternative methods of tracking myelination, as discussed below with SRS microscopy and D_2O labelling, was therefore explored. Additionally, it is possible to image sections of the spinal cord (**Figure 6.6** B), although the resolution with the lenses available means that meaningful quantifications such as measurements of g-ratio (**Figure 6.6** C) would not be feasible.

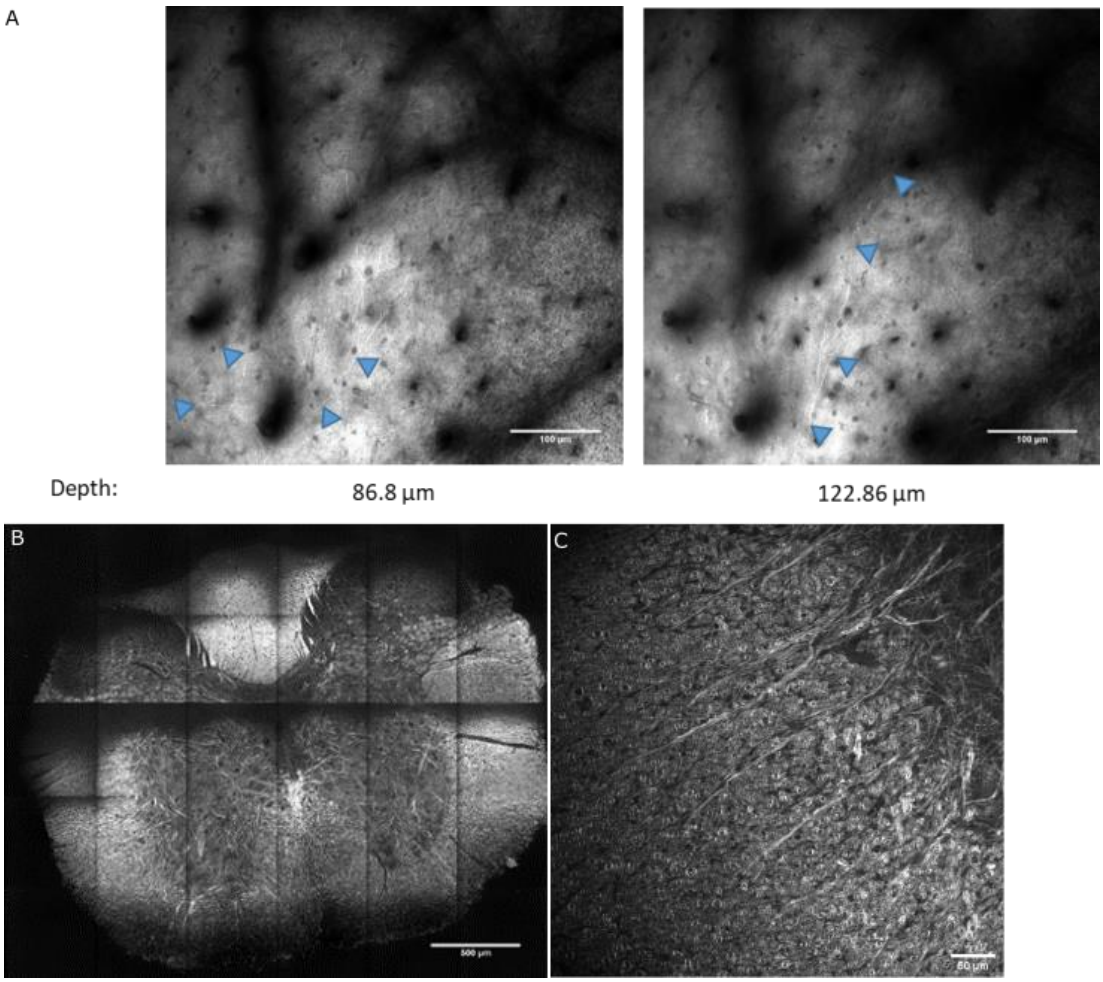

Figure 6.6 CARS microscopy can image the whole adult mouse brain and the spinal cord

A. Images from the z-stack of a whole 5-week male mouse brain. The depths at which the images were taken are written below, showing a working distance of approximately 120µm at which individual myelin sheaths are still visible. The blue triangles highlight the ends of the observed myelin sheaths. The dark shadow across the top of the image is most likely due to blood vessels obstructing light penetration to the underlying tissue, therefore limiting the working distance of imaging, especially in live *in vivo* animals. n = 1
B. Composite image from two consecutive z-stacks from a fixed spinal cord slice of a 6-week male WT mouse, showing the feasibility of using CARS microscopy to visualise myelin in the spinal cord. The composite image was constructed from the z-stack sections where the slice was most in focus due to the spinal cord slice not laying completely flat during imaging. n = 2
C. Higher magnification image from B, showing the circular cross-sections and long internodal structures of myelin sheaths. However, the resolution of the images with the objectives currently available in our set-up makes it difficult to distinguish the clear outlines of the cross-sections of myelin sheaths.

6.3.2 Early exploration of Stimulated Raman Scattering (SRS) microscopy as an alternative method to distinguish newly formed myelin sheaths by labelling with deuterium (heavy) water

As an alternative method for detecting myelin sheath changes to live time-point imaging would be to label newly formed myelin sheaths that were formed subsequent to the initiation of drug administration, and therefore more likely to have formed as a direct result of the treatment. The current technique for detecting new oligodendrocytes is through the crossing of two transgenic mouse lines: *Pdgfra-creER*^{T2} for transcriptional control under *Pdgfra* for OPCs and *creER*^{T2} so that they are tamoxifen-inducible and therefore the expression controllable, and a reporter line such as *Rosa26-YFP* for oligodendrocyte cytoplasm, showing cell bodies and processes (Rivers *et al.*, 2008), or *Rosa26-mGFP* for membrane-bound labelling that allows myelin sheath tracking (Kang *et al.*, 2010). However, the cost of producing and maintaining transgenic animals is high, and also restricts being able to track newly formed myelin to species where the production of transgenic animals is currently possible, i.e. specific mouse lines. The administration of heavy water (D_2O) containing deuterium (heavy hydrogen, ^2H) has previously been used in drinking water to label myelin for analysis of its turnover by mass spectrometry (Ando *et al.*, 2003), and was more recently shown to also work with SRS by Shi *et al.* (2018). In their paper, they were able to show that HeLa cells incorporated deuterium, and that molecular bonds containing deuterium produced distinct Raman peaks to their hydrogen counterparts (**Figure 6.7** A), allowing them to be targeted for Raman detection and imaging.

Shi *et al.* (2018) were also able to show that animals fed D_2O either indirectly through their mother's milk as pups or through direct consumption as adults had deuterium incorporated into the brain. This was confirmed using SRS imaging on P11 animals at the internal capsule (**Figure 6.7** B). Although individual myelin sheaths were not shown in their article, it is promising that deuterium is incorporated and is detectable in CH/CD bonds in the brain. As an alternative to expensive and complex transgenic and virus labelling, deuterium delivery through drinking water may therefore provide a relatively easy method to distinguish newly formed myelin sheaths through its incorporation into the CH_2 bonds to form CD_2 bonds, which would then have a different Raman molecular wavelength signature (2845cm^{-1} for CH_2 bonds versus 2141cm^{-1} for CD_2 bonds). Due to the non-resonant background signals in CARS

microscopy, Stimulated Raman Scattering (SRS) microscopy was used for deuterium imaging. I wanted to test whether: (1) I could recapitulate the labelling of the brain with deuterium administration as D_2O water, (2) verify whether the deuterium incorporation and signal was real, and (3) further test whether this could be used to detect individual myelin sheaths for future experiments in labelling newly formed myelin sheaths in a demyelination and remyelination model of MS for drug testing.

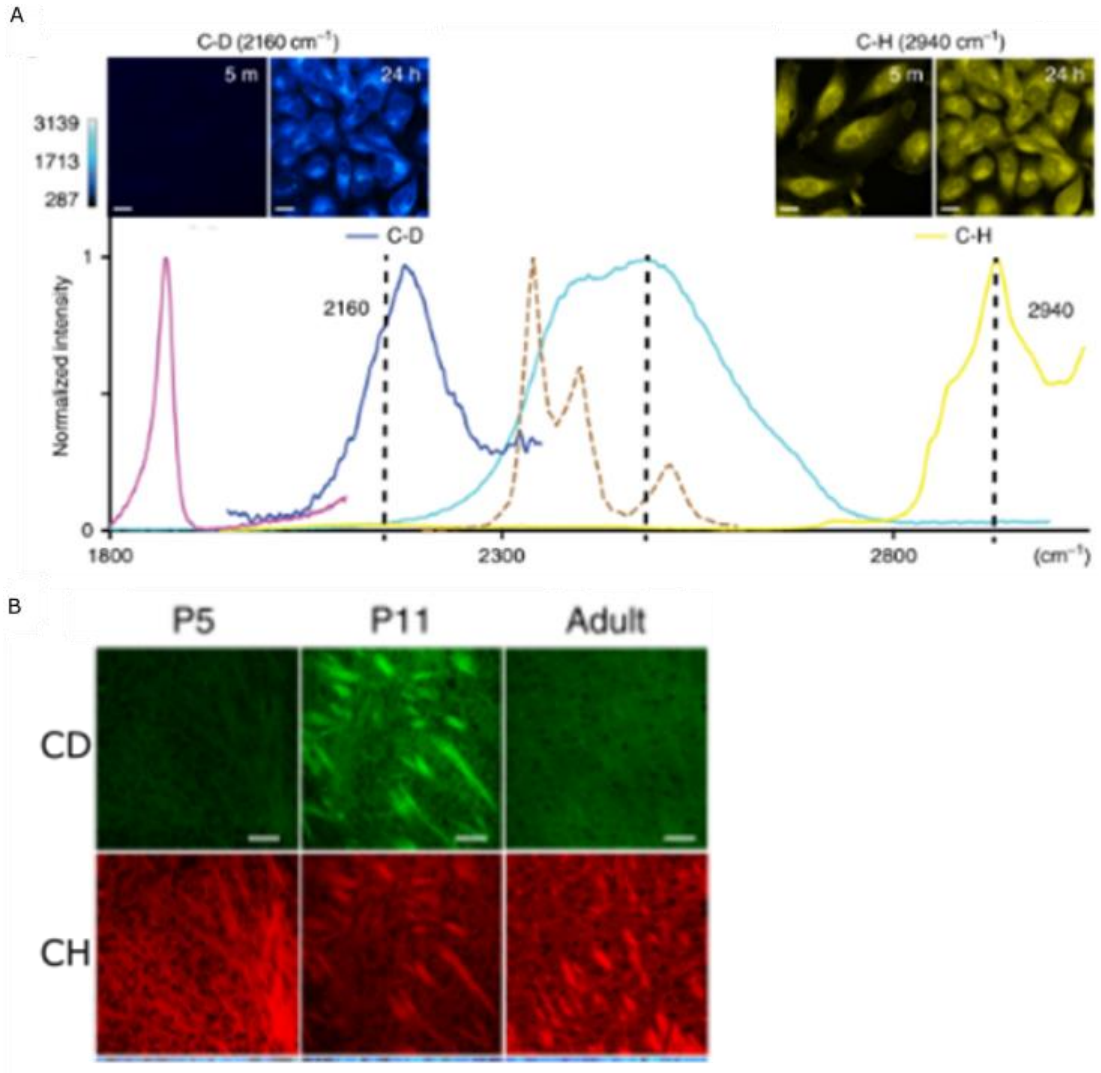

Figure 6.7 Stimulated Raman Scattering (SRS) microscopy is able to distinguish between CH and CD bonds and has been shown to be incorporated into the brain

A. SRS microscopy images of HeLa cells cultured in 70% D_2O medium 5 minutes and 24 hours after medium addition, showing the absence and subsequent increase in C-D detection from

deuterium incorporation into lipids and proteins, versus non-deuterium-related C-H detection. The Raman spectrum shows the shift in Raman peak between C-H (2940cm^{-1}) and C-D (2160cm^{-1}), allowing their distinct detection.

Figure adapted from Shi *et al.* (2018).

B. SRS microscopy images from the internal capsule of mouse brains. Pups (P5 and P11) were fed on the milk of animals drinking 25% D_2O for 6 days, and adult animals were fed 25% D_2O water for 9 days prior to imaging. CD bonds can be detected in the internal capsule of P11 animals, showing the incorporation of deuterium labelling in the brain and in the same areas as the SRS signals for CH bonds.

Figure adapted from Shi *et al.* (2018).

Mice from the same litter that had been weaned, at P23, were divided into two groups: one group receiving 70% deuterium water mixed with 30% normal drinking water (D_2O group), and the other receiving normal drinking water (H_2O group). Water drinking was otherwise not controlled and restricted, with the water bottles from each group measured daily by the SCRM animal facility technician to ensure levels of water drinking was not impacted by the presence of deuterium. The mice were kept on this water for 2 weeks to allow sufficient time for deuterium incorporation and as it would be a similar length of time used for future potential LPC remyelination experiments, after which they were perfused and their organs removed. As shown in **Figure 6.8**, deuterium appears to have incorporated into the D_2O mice but not the H_2O animals in both the corpus callosum and cortex. Although the data is still too preliminary to draw any conclusions from yet, interestingly, the signal intensity of the deuterium in the corpus callosum was relatively weak compared to the cortex, with the corpus callosum reaching myelination maturity earlier than the cortex. In addition, the locations of the highest deuterium signals as detected by CD_2 bonds correlated to the locations of the myelin sheaths detected using CH_2, suggesting that they were preferentially incorporated into myelin sheaths. This suggests a preliminary proof-of-principle (n = 2 for each group with 2 weeks of deuterium water feeding, and additional n = 1 for 1 week of heavy water administration (data not shown)) that we are able to recapitulate the deuterium labelling of the brain, and that it may be preferentially incorporated into the lipid-rich myelin at regions of increased myelination at the time of heavy water administration. This supports the potential for further samples to be prepared to verify these concepts, and the requirement for examples of deuterium-labelled and non-labelled myelin sheaths in the

cortex of deuterium-fed animals to confirm whether deuterium was preferentially labelling newly formed myelin versus all myelin.

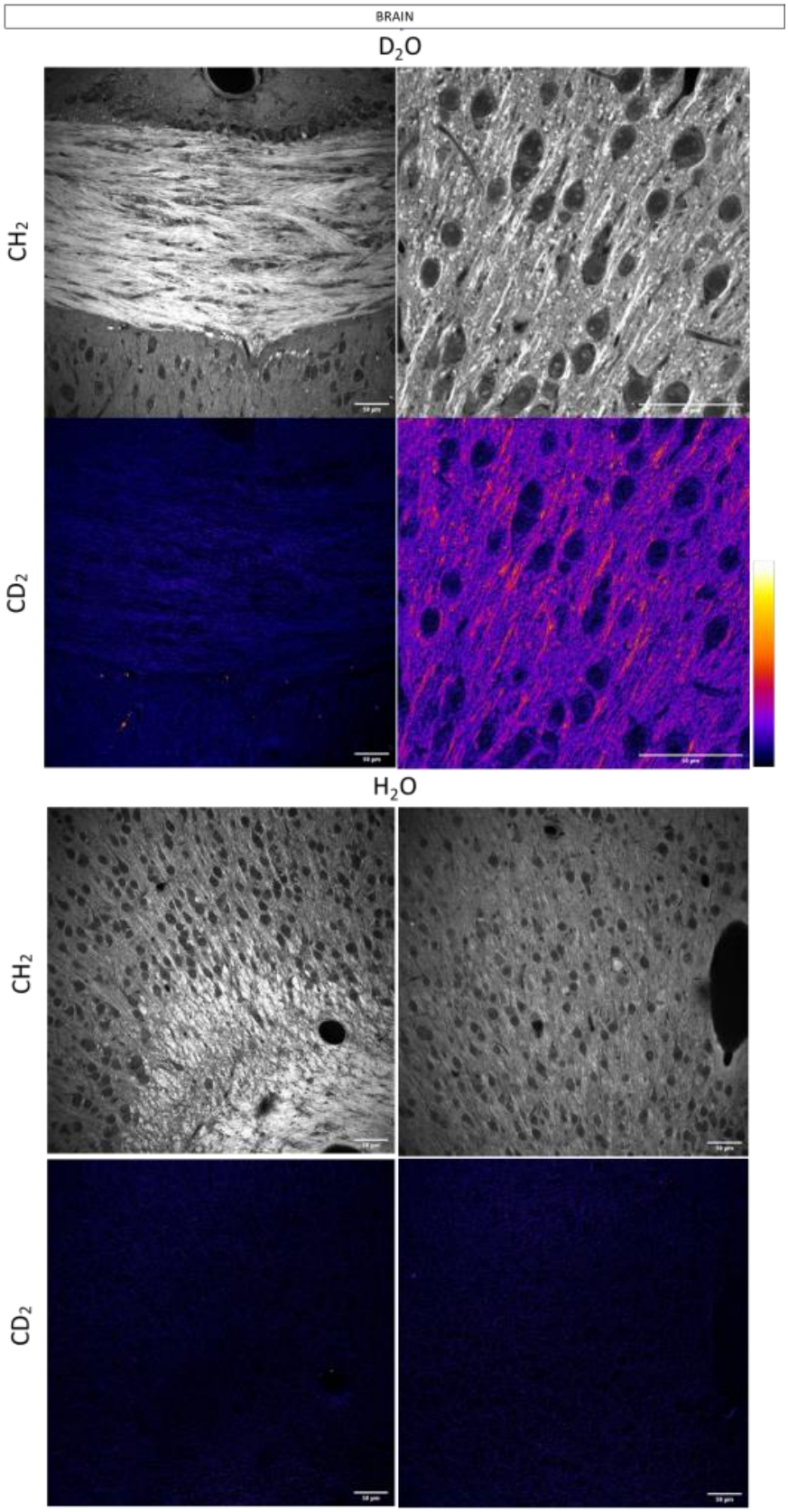
BRAIN
D2O
CH2
CD2
H2O
CH2
CD2

Figure 6.8 Deuterium signal is only detected by SRS in the brain of the animal fed deuterium water

SRS images for CH_2 and CD_2 (as labelled) from WT mice fed 70% deuterium water from P23 for 2 weeks (top panel) and from animals fed normal water (bottom panel), with the corpus callosum on the left and cortex on the right for each condition. n = 2

The top row are images from detecting the CH_2 molecular bond for lipid. The bottom row is the images for the CD_2 molecular bond based on intensity of the SRS signal with the off-resonant background subtracted The calibration bar for signal intensity is in the figure, with white being the highest intensity, and black being no signal.

Note the weak CD_2 signals of the deuterium-fed animals in the corpus callosum, where there would be reduced active myelination at the stage when heavy water was administered, and the stronger signals in the actively myelinating cortex, with apparently increased CD_2 intensity at the locations of myelin sheaths as detected with the presence of CH_2 bonds. The lack of CD_2 signals in the non-deterium water-fed animals confirms that the signal detected in the deuterium water-fed animals is likely due to the incorporation of ^2H.

Scale bar as shown on image (50µm).

In order to confirm whether the signal we were obtaining from the deuterium samples were true, incremental step changes in the wavelength between 850 to 870nm were obtained, and the peaks of the signal intensities plotted using ImageJ. As shown in **Figure 6.9** A, two peaks were identified, with the first peak at approximately 863nm, which lines up with the CD_3 protein molecular bond, and the second peak at 866nm, at the CD_2 lipid bond. In addition, Raman spectroscopy was also performed on the corpus callosum of the D_2O slices (**Figure 6.9** B and C) on the Renishaw Raman spectrometer/microscope. Measurements were taken between 2500cm^{-1} and 3300cm^{-1} to detect the CH_2 bond at 2845cm^{-1} (and CH_3 at 2930cm^{-1}) (**Figure 6.9** B) and between 1700cm^{-1} and 2600cm^{-1} to detect the CD_2 bond at 2141cm^{-1} (and CD_3 at 2189cm^{-1}) (**Figure 6.9** C). The resulting spectra was corrected on the WiRE software with the help of an experienced Raman spectrometrist (Katie Ember, Forbes (SCRM) and Campbell (School of Chemistry) Labs). Firstly, the cosmic rays, which are high energy particles that produce false peaks, were removed by processing features that had the width of 3 and height of 13, or width of 4 and height of 12 (AU). Then, the baseline of measurement was adjusted by changing the polynomial order between 3, 5, and 8 and taking the lowest value

to remove the baseline without introducing an artefact. Lastly, Principal Component Analysis was performed, and the PCA with the closest fit to the expected spectra taken as the reference to compare our spectra with. Although the signal intensity was approximately 100-fold lower, a potential peak at the CD_2 bond was also detectable by Raman spectroscopy, with the shape and position of the peaks also matching well to **Figure 6.9** A. These initial measurements (n = 1 for each) further indicated that deuterium appears to be incorporated into the brain, further highlighting the potential for future experiments in order to validate the replicability of these measurements and take this technique forward.

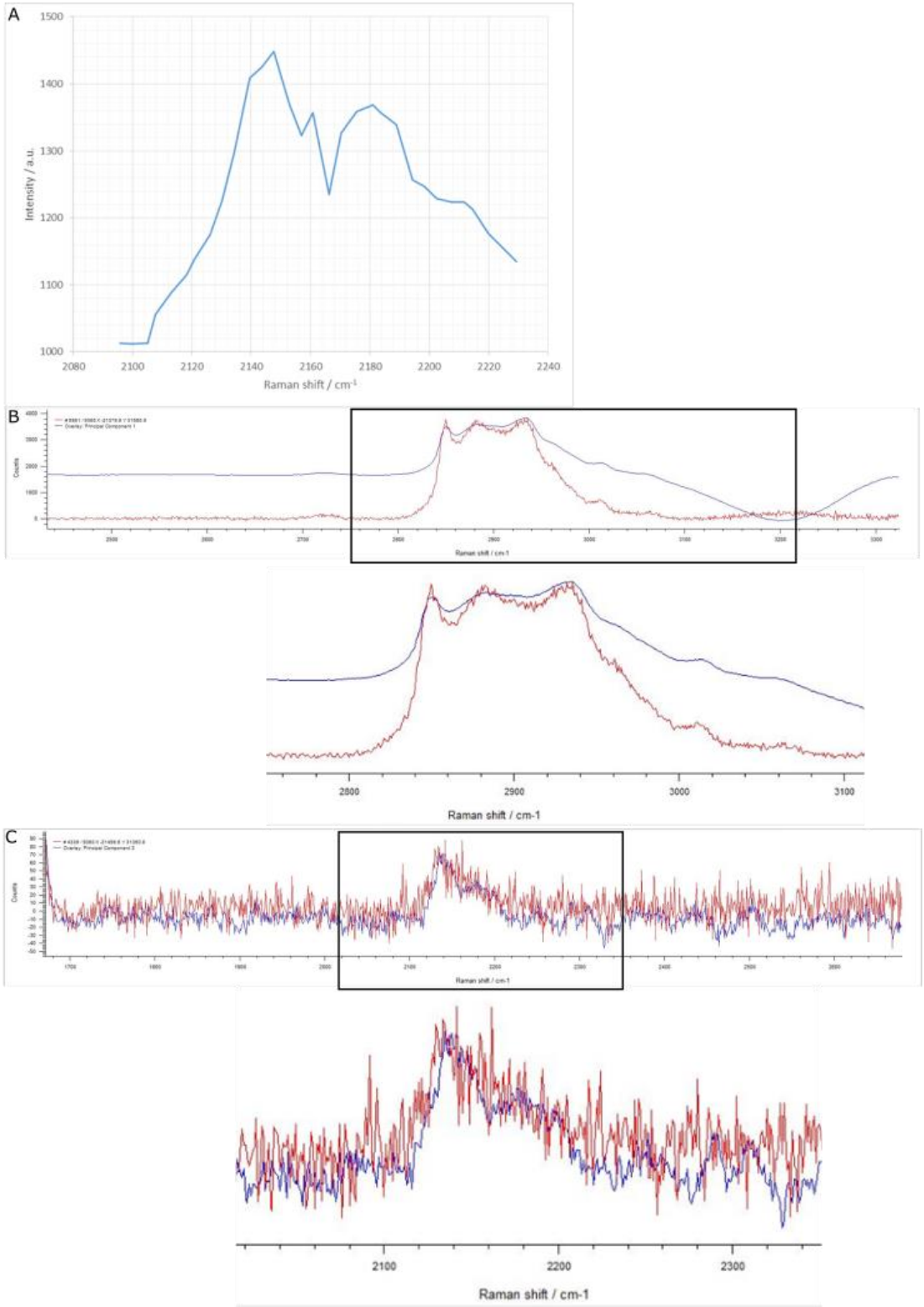

Figure 6.9 Measurements taken on the SRS microscope and Renishaw Raman spectrometer show evidence towards the incorporation of deuterium into the brain

A. Measurements taken with the SRS microscope used for **Figure 6.8** between 860 to 870nm, the expected range at which the deuterium signal should be detected, show increased signal at two peaks. The left peak lines up to the CD_3 protein molecular bond, and the right peak the CD_2 lipid molecular bond. n = 1

B. Raman spectroscopy of 2500cm^{-1} to 3300cm^{-1} from the corpus callosum of the deuterium water fed mice to detect the CH_2 molecular bond located at 2845cm^{-1}. n = 1
The blue line represents the Principal Component Analysis (PCA), and the red line the cosmic ray and baseline-adjusted Raman measurement from the tissue sample.
The black box highlights the location of the peak for CH_2, and a magnified image of this region of the spectroscopy graph shown below.

C. Raman spectroscopy of 1700cm^{-1} to 2600cm^{-1} from the same brain slice and region as B to detect the CD_2 molecular bond located at 2141cm^{-1}. The signal was less intense than that for the CH_2. n = 1
The black box highlights the location of the peak for CD_2, and a magnified image of this region of the spectroscopy graph shown below.

Lastly, to test whether the signals obtained in the brain samples were not an artefact, SRS imaging was performed on other organs of the same animals, including the liver (**Figure 6.10** A), fat cells from the lower abdomen (**Figure 6.10** B), pancreas (**Figure 6.10** C), and kidney (**Figure 6.10** D). This confirmed that the structures identified by CH_2 imaging were also observed with CD_2, especially prominent in the pancreas and kidney due to their distinct morphology. Although some "signals" were detected in the H_2O negative controls, repeated measurements of the same region confirmed that these non-specific "signals" were due to artefact from the tissue moving during and in between imaging as the lasers were being switched from D_2O to off-resonance, which took a few minutes, and therefore being detected as "differences" between the D_2O and off-resonance images in the subtraction, as well as another potential source being background noise (Zhang *et al.*, 2013). The incorporation of the deuterium in the lipid-dense fat cells was particularly interesting to my question due to the composition of myelin sheaths being predominantly lipid. These samples therefore added confidence, although preliminary (n = 1 for each group) at this point, to the seeming incorporation of deuterium by the organs and its specific detection by SRS. SRS combined with deuterium labelling, based on these early results, therefore may be a viable option for further experiments to confirm its use in newly formed myelin sheath quantification in *in vivo*

demyelination and remyelination in the presence of remyelination-promoting compounds, with remyelination being detected by deuterium labelling.

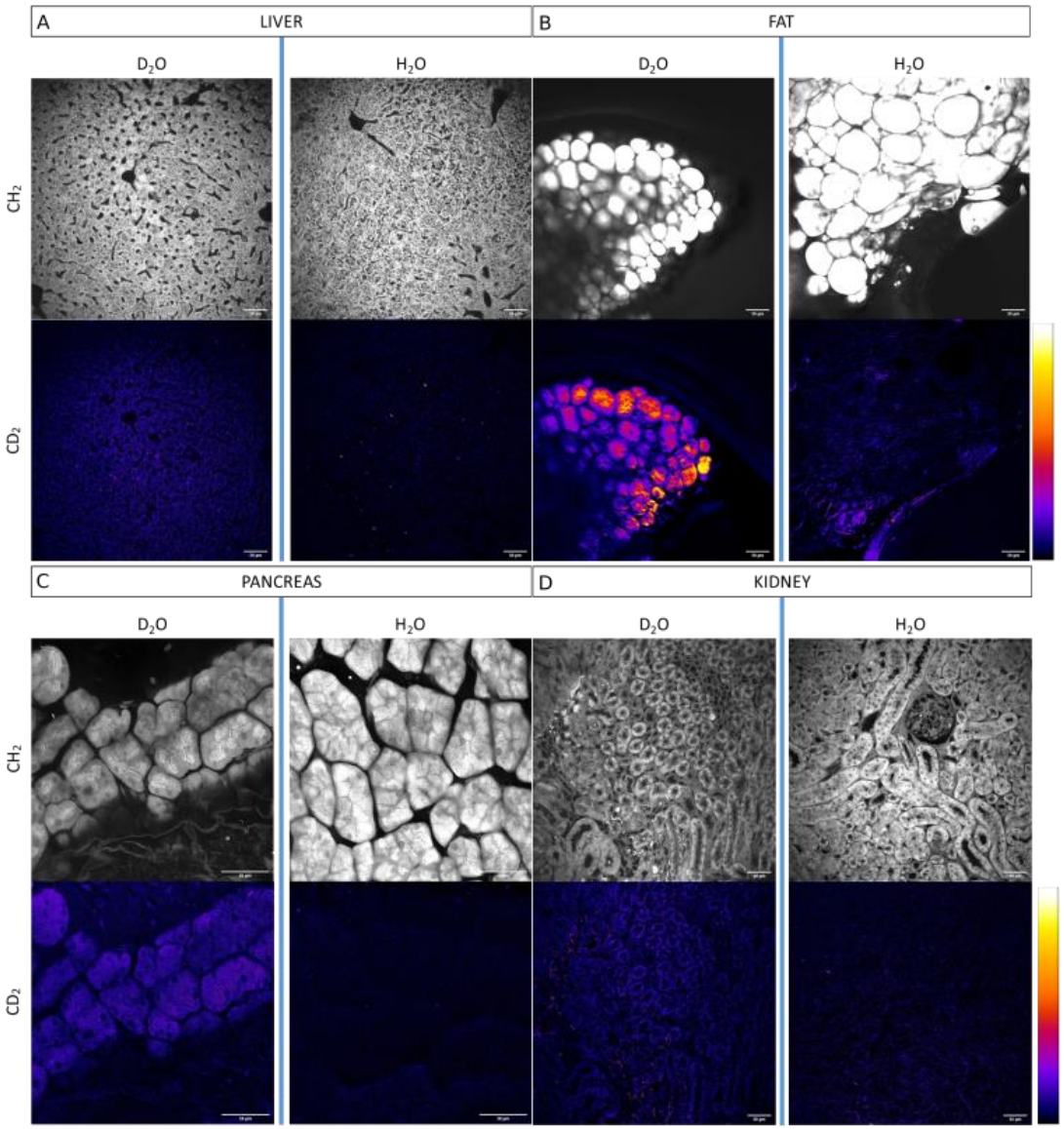

Figure 6.10 Deuterium-labelled and non-labelled sections from other organs confirm the specific incorporation and signal detection in the deuterium administered animal only

Deuterium-labelled and non-labelled slices from A. the liver, B. fat, C. the pancreas, and D. kidney (n = 1-2 per organ per group). Low to mid signal intensities were detected in the liver, pancreas, and kidney, whereas high signal intensity was detected in the fat of the deuterium-labelled animals for the CD_2 bond (calibration bars in figure). Low to no signals were detected in the non-labelled slices as expected. The low signals in these samples may have appeared due to potential background noise, and due to

the slice moving in between the imaging for the deuterium and the off-resonance wavelengths, resulting in a false difference being detected when the off-resonance was subtracted from the deuterium image.

6.4 Discussion

In order to explore an imaging technique to validate hits from high-throughput drug screens in more relevant ex-vivo and in vivo models, I explored the use of label-free CARS and SRS to validate the hits in an *ex vivo* and *in vivo* system (**Figure 1.20** Challenge and Solution #4). CARS microscopy could be used to detect myelin in fixed and live *ex vivo* slices by targeting the CH_2 bonds that are abundant in lipids, and showed preliminary results as being able to be used to quantify myelin sheath lengths in fixed slices. The potential for live *in vivo* imaging was explored by imaging through the upper layers of the cortex of a whole mouse brain that had been removed from the animal (**Figure 6.6**), with a prospective use being for time-point quantification of myelination changes in the presence of potential pro-myelination compounds. In order for longitudinal *in vivo* live CARS imaging to be performed, invasive surgical procedures would need to be performed to implant a cranial window or thin the skull, and potentially expose the underlying brain tissue to more meaningful regions, such as the corpus callosum for LPC injected models of demyelination, in order to be able to artificially achieve the working depth. Not only would this impact animal survivability post-surgery, the formation of scar tissue and related blood deposition would complicate subsequent imaging and reduce the optical penetration (Fu *et al.*, 2008; Shi *et al.*, 2011), as well as likely impacting the biologically relevant regeneration process of the potential pro-remyelination compound versus post-surgery healing. In addition to the impact of motion artifacts when imaging the brain due to vital functions such as breathing and the beating of the heart that needs to be accounted for with *in vivo* imaging (Shi *et al.*, 2011; Paukert and Bergles, 2012), the working depth of CARS for live *in vivo* imaging, limited by the depth of penetration of light, as well as the repeatability of imaging the same regions with post-surgical complications to consider, especially if the region of interest is well below the upper cortical layers, would prove to be challenging to overcome.

I therefore started to explore an alternative method by which an animal could undergo demyelination, such as by LPC injection to form a demyelinated lesion, and deuterium water

given to label newly formed myelin sheaths in the presence or absence of the potential pro-myelination compounds identified in the high-throughput screen. Although further verification is required to confirm the results obtained thus far by increasing the number of biological replicates, initial tests seem to suggest that deuterium is incorporated into the brain after 2 weeks of drinking 30% deuterium water, that the signal detected by SRS is likely specific for deuterium, and that there may potentially be preferentially higher intensity of deuterium signal in myelin sheaths in the brain. Although still early in the validation process, this highlights the future promise of the use of this technique to potentially specifically label and detect newly formed myelin sheaths using deuterium administration.

6.3.1 Implications of the Raman-based imaging and deuterium water labelling

Currently, the ability to detect newly formed myelin sheaths is restricted to the creation of double-transgenic mouse lines, such as the Pdgfrα-creER^{T2} x Rosa-mGFP (Kang *et al.*, 2010). One of the considerations of this is the cost. In order to obtain the animals required to perform a set of experiments, as estimated with the guidance of Dr. Peggy Assinck from our lab, who uses this double-transgenic animal line, and Vince Ranaldi, Senior Research Support Manager of the University's Bioresearch & Veterinary Services, you need to purchase a male and female Rosa-mGFP transgenic mouse line and a male and female Pdgfrα-creER^{T2} mouse line. Similar transgenic animals on the Jackson Laboratory website range from £300-800 per animal, and costs between £1500-2000 for the breeding pair plus shipping, and a further £600 for the quarantine holding and screening, totalling up to £2,500+. A male and female need to be obtained from each of these breeding pairs to obtain at least 3 sets of breeding pairs for cross-breeding, which would result in approximately 18 pups total, of which 6 would likely be double-transgenic and therefore usable in the experiment. Each of these breeding pairs and male and female pups would need to be kept in separate cages, and the entire breeding process would take approximately 6 months, with each cage costing about £2-3 per day, or £7.21 maintenance costs per week excluding estates, throughout this entire process. A further cost would be incurred when the successfully breeded double-transgenic animals are induced with tamoxifen to label the newly formed myelin, which requires once a day injection for 5 days, for approximately £40 for 6 animals. For reference, the maintenance of Peggy's Pdgfrα animals requires 40 to 50 cages per line per week, and cost £1,500 in

maintenance alone for 4 weeks. In contrast, my deuterium water labelling experiment was performed through a wild-type pregnant female mouse, and the pups separated into two different cages to be given either normal or deuterium water once they were weaned with no additional breeding time required. A wild-type C57BL/6 female with a litter costs about £110 from Envigo, and the SCRM facility charges £15 per wild-type adult mouse, plus the £7.21 maintenance per week. Although exact pricing per experimental animal or for a set of experiment is difficult to calculate due to the multitude of factors that influence the actual costs, the estimated cost of obtaining one litter of double-transgenic animals is in the £1000s, whereas it is in the £100s using the deuterium method. Although access to the method is restricted by the availability of a CARS/SRS microscope, deuterium-labelling could provide a cheaper and non-invasive method for labelling newly formed myelin and other hydrogen-dependent processes should this pre-requisite be met.

A potentially more significant implication for the deuterium water labelling of newly formed myelin is its potential for application in non-mouse models of myelination. Due to our current ability to create transgenic animals being restricted mostly to mice, the double-transgenic technique of labelling newly formed myelin sheaths is currently limited to one species in mammals. The ability to observe this process in rats would open up the possibility of correlating the myelination process with more sophisticated behavioural studies than possible in mice. Myelination has also been studied in larger mammals, including in pigs in traumatic spinal cord injury (Kim *et al.*, 2018), and in models of MS in guinea pigs, rabbits, and non-human primates (’T Hart *et al.*, 2000; Brok *et al.*, 2008). The autoimmune EAE models in common marmoset and rhesus monkeys in particular better recapitulate the clinical and neuropathological heterogeneity seen in MS patients that are poorly represented in the more stereotypical rodent models (Brok *et al.*, 2008). They may therefore provide a better insight into the myelination process in a disease model of MS beyond what we can currently infer from rodent models by studying them using the minimally-invasive deuterium labelling technique. In addition, as potentially both a limitation and benefit, as the deuterium labelling is non-specific for myelin labelling, it could be used to observe other organs and hydrogen-dependent processes in the animal and therefore represent a significant contribution to the Three Rs (Replacement, Reduction and Refinement) in animal research, especially with the larger mammals.

CHAPTER VII: DISCUSSION

7.1 Summary of results

As discussed more extensively in 'CHAPTER I. LITERATURE REVIEW', the existing disease-modifying treatments for MS are aimed towards modulating the immune response to suppress and prevent new inflammatory attacks and the formation of new lesions, therefore being most efficient in RRMS (Filippini *et al.*, 2013; Mulero, Midaglia and Montalban, 2018), while not being able to target the non-inflammatory degenerative phase of the disease. The majority of current published high-throughput phenotypic drug screens to discover remyelination therapies have been focused on discovering pro-differentiation compounds by using antibody-based markers of endogenous MBP and the detection of increased numbers of MBP+ OLs as their primary output (Deshmukh *et al.*, 2013; Eleuteri *et al.*, 2017; Lariosa-Willingham *et al.*, 2016a, 2016c; Mei *et al.*, 2014; Najm *et al.*, 2015). However, recent data indicate that a more complex interplay between oligodendrocyte biology and the pathophysiology of MS exists beyond simple differentiation of oligodendrocyte precursor cells. For example, there is evidence towards MS lesions containing premyelinating OLs that have differentiated but have not produced complete myelin sheaths (Chang *et al.*, 2002). In addition, single-cell transcriptomic analysis of OL lineage cells from an EAE model of MS showed a skewing of OLs towards immunomodulating roles (Falcão *et al.*, 2018), and post-mortem control versus MS brain tissue showed a shift of OL subclusters towards immature and intermediate populations of oligodendrocytes in MS (Jäkel *et al.*, 2019), rather than the simple absence of differentiated oligodendrocytes that could myelinate. Based on these studies it could be argued that a broader variety of more physiologically-relevant high-throughput phenotypic drug screening assays are required to support a more clinically relevant platform for remyelination drug discovery in MS.

For my PhD project, I therefore identified a clinical need in the lack of remyelination therapies in treating MS, and the biological problem in current drug screens not targeting the key myelination phase in OL development and only being able to recapitulate the differentiation phase *in vitro*. In order to address these issues, I came up with a bioengineering solution to be able to construct a high throughput-compatible phenotypic drug screening platform in

which we would be able to identify compounds that influenced myelin sheath formation. First, in order to validate the difference between 2D differentiation and 3D myelination assays, I tested whether (1) pro-myelination compounds increased differentiation in 2D assays, and (2) pro-differentiation compounds increased myelination in 3D assays. As discussed in Chapter 3, Benztropine (Deshmukh *et al.*, 2013) and Clemastine (Mei *et al.*, 2014) were detected to statistically significantly increase differentiation at certain concentrations when tested on our 2D flat culture system. However, based on early results due to myelination media issues resulting in a low number of usable biological replicates, the pro-myelination compound, small molecule PKCε activator FR236924 (Swire *et al.*, 2019), did not seem to increase differentiation in the 2D assay. In addition, when the pro-differentiation compounds were tested on the 3D microfibre culture system, none of these compounds increased either myelin sheath length or number. Collectively, these data provide preliminary evidence, which increasing the number of biological replicates in the correct batch of B21 for the myelination media could further support, towards the idea that (1) pro-differentiation screens may not necessarily identify pro-myelination compounds, and (2) pro-differentiation compounds may not also be pro-myelination, and therefore validate the development of more complex and better *in vitro* cell models for MS in high-throughput drug discovery.

The first stage in the development of a high throughput-compatible drug screening platform to allow for a more disease-relevant cell model was the bioengineering of a 96-well plate with suspended microfibres to miniaturise the 3D myelination microfibre system as previously described by Bechler, Byrne and ffrench-Constant (2015) and Lee *et al.* (2012, 2013) ('CHAPTER IV. CONSTRUCTION OF A HIGH-THROUGHPUT-COMPATIBLE 96-WELL MICROFIBRE PLATE'; **Figure 7.1** Challenge and Solution #1). I was able to achieve this by optimising the electrospinning process using 10% poly-L-lactic acid (PLA) dissolved in hexafluoroisopropanol (HFIP) to control the fibre diameter, and by using a moving needle and a rotating collector covered with release paper for equal distribution and easy transfer of fibres. The sheet of electrospun fibres was then inserted into the base of a 96-well plate, and sealed and suspended with layers of adhesives above the optically-compatible cyclic olefin copolymer (COC) film as the base. As described in 'CHAPTER V. VERIFICATION OF THE HIGH-THROUGHPUT 96-WELL MICROFIBRE PLATE PLATFORM', OPCs purified by immunopanning, rather than mechanical isolation from mixed glia cultures, resulted in the lower appearance of contaminating cells, with plating at the density of 6-8,000 cells per well being optimal to detect individual oligodendrocytes and their respective myelin sheaths.

Although ongoing media issues restricted the extent to which the platform could be used to screen compounds during the scope of my PhD, I was also able to show that the plate appears to be compatible with high-throughput liquid-handling robots such as the Thermo Fisher Multidrop™ and BioTek LS405 multiplate washer, and more suitable for high content imaging, such as on the Opera Phenix, than any similar products that are commercially available (**Figure 7.1** Challenge and Solution #2). Preliminary results also suggest the potential of being able to adapt the assay to increase the sensitivity with fibrin coating.

Lastly, I explored a label-free imaging technique that could be used to validate the pro-myelination compounds that are identified from the 3D myelination 96-well microfibre assay in more complex *in vivo* and *ex vivo* models of myelination ('CHAPTER VI. LABEL-FREE RAMAN-BASED IMAGING OF MYELIN'; **Figure 7.1** Challenge and Solution #4). By targeting the CH_2 bonds that are abundant in lipids, Coherent anti-Stokes Raman Spectroscopy (CARS) microscopy could be used to detect myelin in fixed and live *ex vivo* slices, and quantify their lengths in fixed slices. Although live *in vivo* imaging is restricted by the depth of penetration of light required for CARS microscopy, early results using Stimulated Raman Scattering (SRS) microscopy and deuterium in drinking water suggests that the ^2H in deuterium may be incorporated into the myelin sheaths in the brains of these mice. Although extremely early in the validation process with increased numbers of biological replicates required to confirm initial observations, this preliminary result is promising as it suggests that it may be possible for an animal to undergo demyelination, and be simultaneously given the potential pro-myelination compound and deuterium water to label the newly formed myelin sheaths that are formed during treatment and remyelination, and subsequently allow us to assess the pro-remyelination capabilities of the compound.

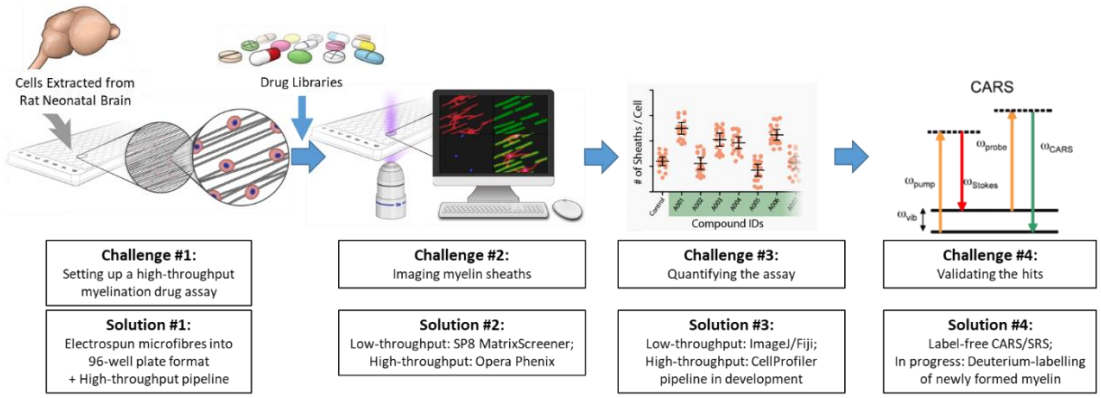

Figure 7.1 Project overview of the high-throughput screening for remyelination treatment in MS

The main high-throughput drug screening challenges of my thesis as introduced in the 'CHAPTER I. LITERATURE REVIEW', and the corresponding solutions explored throughout my project.

1. 'CHAPTER IV. CONSTRUCTION OF A HIGH-THROUGHPUT-COMPATIBLE 96-WELL MICROFIBRE PLATE': The bioengineering of high-throughput-compatible 96-well plates with suspended electrospun microfibres.
2. 'CHAPTER V. VERIFICATION OF THE HIGH-THROUGHPUT 96-WELL MICROFIBRE PLATE PLATFORM': The imaging of the 3D myelin sheaths on the microfibres with the resolution to determine complete ensheathment.
3. The quantification of complete myelin sheath formation, with the high-throughput automated pipeline using CellProfiler image analysis software being in development by Dr. Marie E. Bechler in collaboration with Dr. Beth A. Cimini and Professor Anne E. Carpenter of the Broad Institute.
4. 'CHAPTER VI. LABEL-FREE RAMAN-BASED IMAGING OF MYELIN': The verification of CARS and SRS as label-free techniques of *ex vivo* myelin sheath imaging and quantification, with in progress exploration of deuterium to label newly formed myelin.

(Figure adapted from ScideLight and Potma and Xie, 2004)

7.2 Future prospects

Due to the severe myelination media issues incurred during the PhD, there were limitations to the compound screens that could be performed and the optimisation of assay reproducibility. In the next stages of this research, once the myelination media issues have

been resolved, with several potential methods of resolution currently being explored and acted upon as discussed at the end of Chapter 5, there are various methods that could be explored to increase the reproducibility and throughput of the assay: 1) the incorporation of more liquid-handling robots into the high-throughput pipeline, 2) improved high content imaging platform, 3) the use of an automated image analysis pipeline, 4) the application of more physiological substrates to the electrospun fibres, 5) the optimisation of myelinating human cells on the microfibres, and 6) the development of the Raman-based imaging strategies as discussed in Chapter 6.

As discussed in the chapter, the ThermoScientific Multidrop™ and BioTek LS 405 microplate washer is compatible with the 96-well microfibre plate for plating, fixing, and staining. The Integra VIAFLO 96 is a power-assisted handheld microplate pipetting robot that enables the pipetting and transfer of liquids from 96 wells simultaneously. The use of this robot would increase the speed and accuracy of pipetting during media changes and drug additions, with 4 to 5 changes required for the 14 days of culturing. This would increase the accuracy of compounds/DMSO added and the throughput of the assay, and decrease the amount of time the plates are out of the incubator (set at 37°C and 7.5% CO_2) and in an uncontrolled environment.

The PerkinElmer Opera Phenix imaging platform is also promising to increase the imaging capabilities and throughput beyond the limitations of the Leica SP8 MatrixScreener. This imaging system uses an advanced spinning-disk technology, called Synchrony™ Optics, which reduces the spectral cross talk between different lasers to allow up to 4 channels to be imaged simultaneously, and has an increased pinhole-to-pinhole distance which reduces spatial cross talk, an essential aspect for 3D imaging (Li *et al.*, 2016). The Opera Phenix has been reported to have been used for complex 3D cellular models, such as the quantification of nuclei in hiPSC-derived 3D cardiac spheroids (Christoffersson *et al.*, 2018), and is therefore extremely promising in increasing the speed and throughput of the imaging in the 96-well microfibre myelination assay.

Lastly, in addition to the imaging, a major hurdle in increasing the throughput of the 3D myelination assay is image analysis, which currently requires manual quantification on Fiji. Dr. Marie Bechler in our lab has been working in collaboration with Dr. Beth A. Cimini and Professor Anne E. Carpenter, from the Broad Institute of MIT and Harvard, to develop a CellProfiler pipeline with machine learning targeted towards the automated quantification

of complete myelin sheath formation on the microfibre culture system (**Figure 7.1** Challenge and Solution #3). As summarised in **Figure 7.2** A, the pipeline takes the maximum projection of the original image, segments it, and then classifies what it has been taught with machine learning as complete myelin sheaths. The pipeline is currently able to perform this with 85% accuracy (**Figure 7.2** B), and is able to detect the difference in the area of complete myelin sheaths produced by cortical- and spinal cord-derived oligodendrocytes on the microfibre culture system as previously reported by Bechler, Byrne and ffrench-Constant (2015) (**Figure 7.2** C). As the pipeline was developed and the machine learning performed on oligodendrocytes cultured on the 12-well microfibre scaffolds, mounted in Fluoromount G, and imaged with the 40x objective on the Leica SP8 imaging system, there will likely be differences in the segmentation and classification of myelin sheaths in 96-well plates filled with PBS, with images taken on the PerkinElmer Opera Phenix system. However, with adjustments and re-training of the CellProfiler pipeline with images taken on the Opera Phenix system, we should be able to significantly increase the throughput of the image analysis of the 96-well myelination assay in the future.

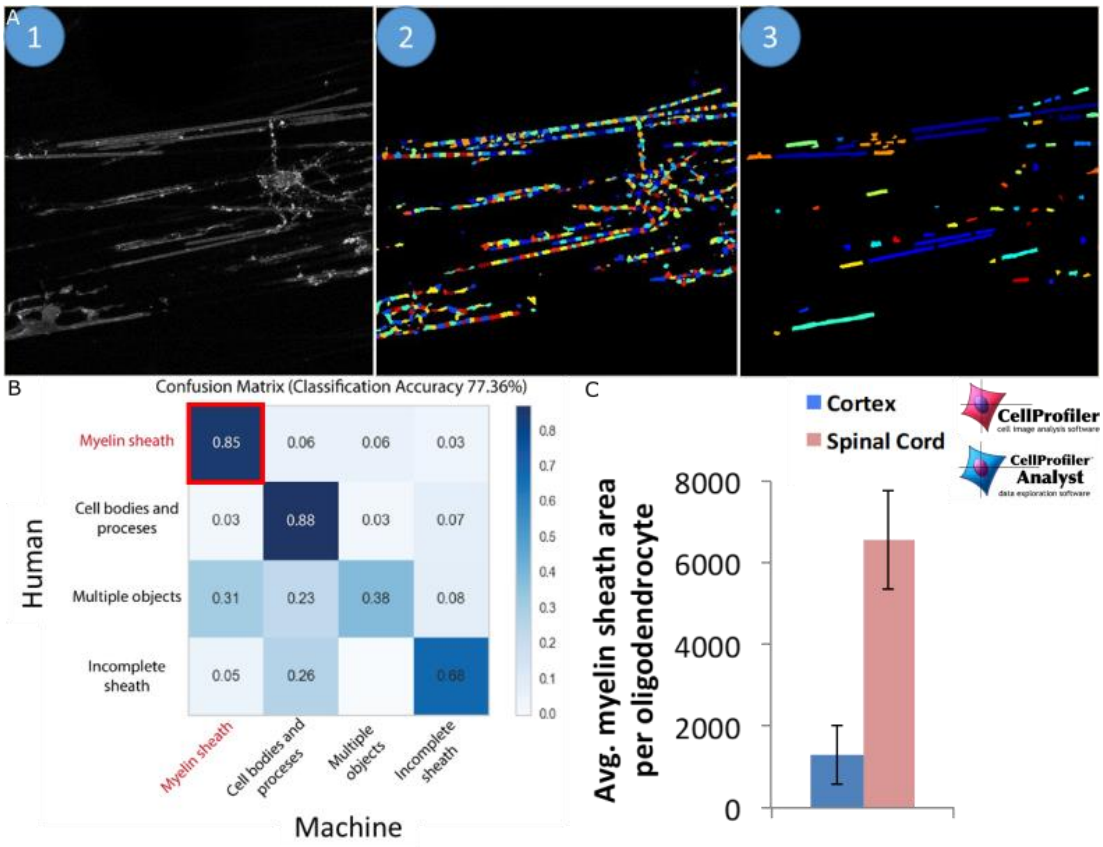

Figure 7.2 CellProfiler pipeline with supervised machine learning for automated image analysis shows 85% classification accuracy for myelin sheaths and the ability to detect increased myelin sheath formation

A. The stages of image processing by the CellProfiler pipeline: (1) Maximum projection of the original z-stack image, (2) segmentation, (3) classification into myelin sheaths, cell bodies and processes, multiple objects, and incomplete myelin sheaths.
B. The comparison of classification between a human expert (Dr. Marie Bechler) and the CellProfiler pipeline with supervised machine learning, showing 77% overall accuracy and 85% accuracy in detecting complete myelin sheaths.
C. The quantification of the average myelin sheath area per oligodendrocyte between cortical- and spinal cord-derived oligodendrocytes, showing the ability to detect the increased myelin sheath produced by spinal cord OLs as previously reported by Bechler, Byrne and ffrench-Constant (2015).

   This CellProfiler pipeline and the supervised machine learning was performed by Dr. Marie Bechler (ffrench-Constant Lab), and Dr. Beth A. Cimini and Professor Anne E. Carpenter (Broad Institute of MIT and Harvard)

The 96-well microfibre plates produced in this thesis provides a basis for the ability to perform high-throughput screens in a more phenotypically-relevant 3D model than the current standard 2D flat culture screens. However, our drug screening platform still faces one of the key limitations of current disease models, which often lack the disease-relevant substrates and bioengineering tools to better recapitulate the mechanical and physiological environment that the cells are exposed to *in vivo* (Horvath *et al.*, 2016). Using a technique called atomic force microscopy, which uses a cantilever across a surface to measure its deflection, the mechanical property of a PLA fibre was measured to be approximately 10GPa (Iqbal *et al.*, 2015), whereas it is in the range of less than 7.5kPa in the neurite of fixed rat tissue and between approximately 50 to 300Pa in live rat hippocampal slices (Spedden and Staii, 2013), making the stiffness of the electrospun PLA fibre in the orders of magnitudes higher than *in vivo*. One method of tackling this would be to use another polymer, such as poly-glycerol-dodecanoate (PDG), which has distinct temperature-related properties, with its mechanical properties being approximately 1 MPa at 37°C (Migneco *et al.*, 2009), the temperature at which the cells are cultured, with PDG also being shown to be biocompatible and compatible with electrospinning (Dai and Huang, 2014). Although these values are still

higher than neurons, the stiffness of PDG is approximately 10,000x lower than that of PLA, making it 10,000x stiffer than live brain tissue (calculated at 100Pa for this comparison) versus 100,000,000x. By additionally coating the fibres with matrigel (Dai and Huang, 2014), it may be possible to bring the mechanical stiffness of the electrospun fibres down even further. In targeting the physiological environment, it has recently been shown that it is possible to combine the decellularisation of human liver tissue with electrospun polymers to create a more physiologically relevant niche for hepatocytes (Grant *et al.*, 2019). It may therefore be feasible to combine this technique with brain tissue and our electrospun fibres to create a more physiologically-relevant environment, either by using control brain tissue or even brain tissue from models or patients of MS in increasing the predictive validity by creating a more physiologically-relevant model, and therefore increasing the positive predictive value in drug discovery.

Another aspect for consideration in enhancing the disease modelling is through the use of human cell models (Horvath *et al.*, 2016). It has already been shown that it is possible to obtain human oligodendrocytes from pluripotent stem cells that show maturation-specific physiological and transcriptomic properties (Livesey *et al.*, 2016; García-León *et al.*, 2018), that this can be performed using patient-derived samples including MS (Livesey *et al.*, 2016; García-León *et al.*, 2018), and can be adapted to be high-throughput-compatible (García-León *et al.*, 2018). The current fibre culture system has been optimised for rodent-derived cells, and the human pluripotent stem cell-derived oligodendrocytes for single cell 2D flat-culture or in neuronal co-cultures. However, with the optimisation of the appropriate myelination media and culture conditions and further development of its robustness for 3D *in vitro* myelination, it has already shown a degree of flexibility in working with control and patient-derived cells and scalability by García-León *et al.* (2018) to be feasible to use in high-throughput drug screens with improved cellular models of physiological and clinical relevancy than the current model developed in this thesis for future development. The ability to use patient-derived cells may offer the potential for personalised medicine in screening for the compound that is most likely to show pro-remyelinating effects on a patient-specific level from a selection of approved treatments in the future.

The next major step in the CARS/SRS imaging with deuterium labelling would be to verify its presence in specifically newly formed myelin sheaths. This could be performed using two main methods: (1) by creating a focal lesion using LPC and detecting whether there is a higher

degree of deuterium labelling at this site of demyelination and remyelination, or (2) by co-administering tamoxifen and deuterium water to the Pdgfrα-creER^{T2} x Rosa-mGFP double-transgenic mouse line (Kang *et al.*, 2010) during developmental myelination or remyelination to detect newly formed myelin sheaths as confirmed by the GFP labelling and correlating to the SRS deuterium signal as validation. These techniques, in particular the latter, would justify the use of the less invasive and cheaper deuterium labelling technique to the myelin research community in its acceptance as a viable method. In addition, as shown in Chapter 6, although deuterium seems to be detectable in individual myelin sheaths, the signal intensity, due to the lower presence of CD_2 bonds versus CH_2 bonds, is low. Ando *et al.* (2003) used 30% D_2O for 4 to 6 weeks in their mass spectrometry quantification of newly formed myelin, and Shi *et al.* (2018) administered 25% for SRS microscopy. It is difficult to justify increasing the dosage of deuterium due to its reported toxic effects at high concentrations, as reported by Thomson (1960). However, by combining CH_2 and CD_2 imaging, and verification with the proposed techniques, it may be possible to label newly formed myelin sheath using deuterium, and quantify their lengths using the corresponding CH_2 imaging. These would allow for the *in vivo* testing of positive hits from the 96-well microfibre plates in improving remyelination while more accurately being able to take into consideration the degree of myelination left and the extent of demyelination caused by the demyelination model of MS used.

Overall, the two main components of my PhD project were aimed at and have the potential to: (1) increase the identification of pro-myelinating compounds by increasing the complexity to a more physiologically-relevant model in a novel high-throughput drug screening platform for multiple sclerosis, and (2) expand our ability to test these compounds *in vivo* in terms of detecting the degree of remyelination more accurately, and in the number of animal models of MS available. Although the degree to which the 96-well drug screening platform could be biologically and pharmacologically verified was severely restricted during the scope of my PhD by the ongoing media issues from an as of yet undetermined change to the B27/B21 media supplement, the resolution of this issue would provide a highly valuable asset towards the screening and identification of novel compounds and therapeutic targets and thus provide and important piece in the puzzle towards developing effective treatments which address the lack of remyelination in MS.

REFERENCES

'T Hart, B. A. *et al.* (2000) 'A new primate model for multiple sclerosis in the common marmoset', *Immunology Today*, 21(6), pp. 290–297. doi: 10.1016/S0167-5699(00)01627-3.

Agrawal, H. C. *et al.* (1977) 'Purification and Immunohistochemical Localization of Rat Brain Myelin Proteolipid Protein', *Journal of Neurochemistry*, 28(3), pp. 495–508. doi: 10.1111/j.1471-4159.1977.tb10420.x.

Alberta, J. A. *et al.* (2001) 'Sonic hedgehog is required during an early phase of oligodendrocyte development in mammalian brain', *Molecular and Cellular Neuroscience*, 18(4), pp. 434–441. doi: 10.1006/mcne.2001.1026.

Alavijeh, M. S. *et al.* (2005) 'Drug metabolism and pharmacokinetics, the blood-brain barrier, and central nervous system drug discovery', *NeuroRx*, 2(4), pp. 554–571. doi: 10.1602/neurorx.2.4.554.

Ando, S. *et al.* (2003) 'Turnover of myelin lipids in aging brain.', *Neurochemical research*, 28(1), pp. 5–13. Available at: http://www.ncbi.nlm.nih.gov/pubmed/12587659.

Armstrong, R. C. *et al.* (1992) 'Pre-oligodendrocytes from adult human CNS', *The Journal of Neuroscience*, 12(4), pp. 1538–1547.

Aronson, J. K. (2007) 'Concentration-effect and dose-response relations in clinical pharmacology', *British Journal of Clinical Pharmacology*, 63(3), pp. 255–257. doi: 10.1111/j.1365-2125.2007.02871.x.

Asai, D. (2015) 'Immunofluorescence Microscopy', *Current Protocols Essential Laboratory Techniques*, 10(1), pp.9.2.1-9.2.23.

Back, S. A. *et al.* (2005) 'Hyaluronan accumulates in demyelinated lesions and inhibits oligodendrocyte progenitor maturation', *Nature Medicine*, 11(9), pp. 966–972. doi: 10.1038/nm1279.

Bacakova, M. *et al.* (2016) 'The potential applications of fibrin-coated electrospun polylactide nanofibers in skin tissue engineering', *International Journal of Nanomedicine*, 11, pp. 771–789. doi: 10.2147/IJN.S99317.

Baer, A. S. *et al.* (2009) 'Myelin-mediated inhibition of oligodendrocyte precursor differentiation can be overcome by pharmacological modulation of Fyn-RhoA and protein kinase C signalling', *Brain*, 132, pp. 465–481. doi: 10.1093/brain/awn334.

Baker, G. E. and Stryker, M. P. (1990) 'Retinofugal fibres change conduction velocity and diameter between the optic nerve and tracts in ferrets', *Nature*, 344(March), pp. 342–345.

Bansal, R., Gard, A. and Pfeiffer, S. (1988) 'Stimulation of oligodendrocyte differentiation in culture by growth in the presence of a monoclonal antibody to sulfated glycolipid', *Journal of Neuroscience Research*, 21(2-4), pp.260-267.

Bansal, R., Warrington, A., Gard, A., Ranscht, B. and Pfeiffer, S. (1989) 'Multiple and novel specificities of monoclonal antibodies O1, O4, and R-mAb used in the analysis of oligodendrocyte development', *Journal of Neuroscience Research*, 24(4), pp.548-557.

Baraban, M., Koudelka, S. and Lyons, D. A. (2017) 'Ca 2+ activity signatures of myelin sheath formation and growth in vivo', *Nature Neuroscience*. Springer US, 21(January). doi: 10.1038/s41593-017-0040-x.

Baraban, M., Koudelka, S. and Lyons, D. A. (2018) 'Ca2+ activity signatures of myelin sheath formation and growth in vivo', *Nature Neuroscience*. Springer US, 21(January), pp. 19–23. doi: 10.1038/s41593-017-0040-x.

Barnes, D. and Sato, G. (1980) 'Serum-free cell culture: a unifying approach', *Cell*, 22(3), pp. 649–655. doi: 10.1016/0092-8674(80)90540-1.

Barnett, S. C. and Linington, C. (2013) 'Myelination: Do astrocytes play a role?', *Neuroscientist*, 19(5), pp. 442–450. doi: 10.1177/1073858412465655.

Barres, B. A. *et al.* (1990) 'Ion channel expression by white matter glia: The O-2A glial progenitor cell', *Neuron*, 4(4), pp. 507–524. doi: 10.1016/0896-6273(90)90109-S.

Barres, B. A. *et al.* (1992a) 'Cell death and control of cell survival in the oligodendrocyte lineage', *Cell*, 70(1), pp. 31–46. doi: 10.1016/0092-8674(92)90531-G.

Barres, B. A. *et al.* (1992b) 'Cell death in the oligodendrocyte lineage', *Journal of Neurobiology*, 23(9), pp. 1221–1230. doi: 10.1002/neu.480230912.

Barres, B. A. and Raff, M. C. (1993a) 'Proliferation of oligodendrocyte precursor cells depends on electrical activity in axons', *Nature*, 361(6409), pp. 258–260. doi: 10.1038/361258a0.

Barres, B. A. *et al.* (1993b) 'Multiple extracellular signals are required for long-term oligodendrocyte survival', *Development*, 118(1), pp. 283–295.

Barres, B. A. *et al.* (1994a) 'A crucial role for neurotrophin-3 in oligodendrocyte development', *Nature*, 367, pp. 371–375. doi: 10.1038/246170a0.

Barres, B. A., Lazar, M. A. and Raff, M. C. (1994b) 'A novel role for thyroid hormone, glucocorticoids and retinoic acid in timing oligodendrocyte development', *Development*, 120, pp. 1097–1106.

Bechler, M. E., Byrne, L. and ffrench-Constant, C. (2015) 'CNS Myelin Sheath Lengths Are an Intrinsic Property of Oligodendrocytes', *Current Biology*. The Authors, 25(18), pp. 2411–2416. doi: 10.1016/j.cub.2015.07.056.

Bechler, M. E., Swire, M. and ffrench-Constant, C. (2018) 'Intrinsic and adaptive myelination—A sequential mechanism for smart wiring in the brain', *Developmental Neurobiology*, 78(2), pp. 68–79. doi: 10.1002/dneu.22518.

Begley, R. F., Harvey, A. B. and Byer, R. L. (1974) 'Coherent anti-Stokes Raman spectroscopy', *Applied Physics Letters*, 25(7), p. 387. doi: 10.1063/1.1655519.

Behar, T. *et al.* (1988) 'Growth and differentiation properties of O-2A Progenitors purified from rat cerebral hemispheres', *Journal of Neuroscience Research*, 21(2–4), pp. 168–180. doi: 10.1002/jnr.490210209.

Belbasis, L. *et al.* (2014) 'Environmental risk factors and multiple sclerosis : an umbrella review of systematic reviews and meta-analyses', *The Lancet Neurology*. Elsevier Ltd, 14(3), pp. 263–273. doi: 10.1016/S1474-4422(14)70267-4.

Ben Arous, J. (2011) 'Single myelin fiber imaging in living rodents without labeling by deep optical coherence microscopy', *Journal of Biomedical Optics*, 16(11), p. 116012. doi: 10.1117/1.3650770.

Bengtsson, S. L. *et al.* (2005) 'Extensive piano practicing has regionally specific effects on white matter development', *Nature Neuroscience*, 8(9), pp. 1148–1150. doi: 10.1038/nn1516.

Berger, T. *et al.* (1992a) 'GABA- and glutamate-activated currents in glial cells of the mouse corpus callosum slice', *Journal of Neuroscience Research*, 31(1), pp. 21–27. doi: 10.1002/jnr.490310104.

Berger, Thomas *et al.* (1992b) 'Sodium and Calcium Currents in Glial Cells of the Mouse Corpus Callosum Slice', *European Journal of Neuroscience*, 4(12), pp. 1271–1284. doi: 10.1111/j.1460-9568.1992.tb00153.x.

Bergles, D. E. *et al.* (2000) 'Glutamatergic synapses on OPCs in the hippocampus', *Nature*, 405(1996), pp. 187–191.

Bhardwaj, N. and Kundu, S. C. (2010) 'Electrospinning: A fascinating fiber fabrication technique', *Biotechnology Advances*, 28(3), pp. 325–347. doi: 10.1016/j.biotechadv.2010.01.004.

Bhat, S. and Pfeiffer, S. E. (1986) 'Stimulation of oligodendrocytes by extracts from astrocyte-enriched cultures', *Journal of Neuroscience Research*, 15(1), pp. 19–27. doi: 10.1002/jnr.490150103.

Biase, L. M. De, Nishiyama, A. and Bergles, D. E. (2010) 'Excitability and Synaptic Communication within the Oligodendrocyte Lineage', *Journal of Neuroscience*, 30(10), pp. 3600–3611. doi: 10.1523/JNEUROSCI.6000-09.2010.

Bieber, A. J., Kerr, S. and Rodriguez, M. (2003) 'Efficient Central Nervous System Remyelination Requires T Cells', *Annals of Neurology*, 53, pp. 680–684.

Bijland, S. *et al.* (2019) 'An in vitro model for studying CNS white matter: Functional properties and experimental approaches', *F1000Research*, 8, pp. 1–27. doi: 10.12688/f1000research.16802.1.

Biswas, S. *et al.* (2019) 'Development of glial restricted human neural stem cells for oligodendrocyte differentiation in vitro and in vivo', *Scientific Reports*. Springer US, 9(1), pp. 1–14. doi: 10.1038/s41598-019-45247-3.

Bitsch, A. and Brück, W. (2002) 'Differentiation of Multiple Sclerosis Subtypes Implications for Treatment', *CNS Drugs*, 16(6), pp. 405–418.

Blakemore, W. F. (1974) 'Pattern of remyelination in the CNS', *Nature*, 249, pp. 577–578.

Bögler, O. *et al.* (1990) 'Cooperation between two growth factors promotes extended self-renewal and inhibits differentiation of oligodendrocyte-type-2 astrocyte (O-2A) progenitor cells', *Proceedings of the National Academy of Sciences of the United States of America*, 87(16), pp. 6368–6372. doi: 10.1073/pnas.87.16.6368.

Bognitzki, M. *et al.* (2001) 'Nanostructured Fibers via Electrospinning', *Advanced Materials*, 13(1), pp. 70–72.

Boiko, T. *et al.* (2001) 'Compact myelin dictates the differential targeting of two sodium channel isoforms in the same axon', *Neuron*, 30(1), pp. 91–104. doi: 10.1016/S0896-6273(01)00265-3.

Boullerne, A. I. (2016) 'The history of myelin', *Experimental Neurology*. Elsevier Inc., 283, pp. 431–445. doi: 10.1016/j.expneurol.2016.06.005.

Boyd, A., Zhang, H. and Williams, A. (2013) 'Insufficient OPC migration into demyelinated lesions is a cause of poor remyelination in MS and mouse models', *Acta Neuropathologica*, 125(6), pp. 841–859. doi: 10.1007/s00401-013-1112-y.

Boys, C. V (1887) 'On the Production, Properties, and some suggested Uses of the Finest Threads', *Proceedings of the Physical Society of London*, 9(1), pp. 8–19. doi: 10.1088/1478-7814/9/1/303.

Bray, M.-A., Carpenter, A. and Broad Institute of MIT and Harvard Imaging Platform, . (2012) 'Advanced Assay Development Guidelines for Image-Based High Content Screening and Analysis', *Assay Guidance Manual*. Available at: http://www.ncbi.nlm.nih.gov/pubmed/23469374.

Brinkmann, B. G. *et al.* (2008) 'Neuregulin-1/ErbB Signaling Serves Distinct Functions in Myelination of the Peripheral and Central Nervous System', *Neuron*, 59, pp. 581–595. doi: 10.1016/j.neuron.2008.06.028.

Brody, B. A. *et al.* (1987) 'Sequence of Central Nervous System Myelination in Human Infancy. I. An Autopsy Study of Myelination', *Journal of Neuropathology & Experimental Neurology*, 46(3), pp. 283–301.

Brok, H. P. M. *et al.* (2008) 'Non-human primate models of multiple sclerosis', *Drug Discovery Today: Disease Models*, 5(2), pp. 97–104. doi: 10.1016/j.ddmod.2008.06.001.

Bruck, W. (2005) 'The pathology of multiple sclerosis is the result of focal inflammatory demyelination with axonal damage', *Journal of Neuroscience*, 252([Suppl 5]), p. V/3-V/9. doi: 10.1007/s00415-005-5002-7.

Buchser, W. *et al.* (2004) 'Advanced Assay Development Guidelines for Image-Based High

Content Screening and Analysis', *Assay Guidance Manual*, (Md), pp. 1–60. Available at: http://www.ncbi.nlm.nih.gov/pubmed/23469374.

Bujalka, H., Koenning, M., Jackson, S., Perreau, V., Pope, B., Hay, C., Mitew, S., Hill, A., Lu, Q., Wegner, M., Srinivasan, R., Svaren, J., Willingham, M., Barres, B. and Emery, B. (2013) 'MYRF Is a Membrane-Associated Transcription Factor That Autoproteolytically Cleaves to Directly Activate Myelin Genes', *PLoS Biology*, 11(8), p.e1001625.

Bullock, P. N. and Rome, L. H. (1990) 'Glass micro-fibers: A model system for study of early events in myelination', *Journal of Neuroscience Research*, 27(3), pp. 383–393. doi: 10.1002/jnr.490270317.

Bunge, R. P., Bunge, M. B. and Bates, M. (1989) 'Movements of the Schwann Cell Nucleus Implicate Progression of the Inner (Axon-related) Schwann Cell Process During Myelination', *The Journal of Cell Biology*, 109(July), pp. 273–284.

Butt, A. M. and Dinsdale, J. (2005) 'Opposing actions of fibroblast growth factor-2 on early and late oligodendrocyte lineage cells in vivo', *Journal of Neuroimmunology*, 166(1–2), pp. 75–87. doi: 10.1016/j.jneuroim.2005.05.015.

Cadavid, D. *et al.* (2019) 'Safety and efficacy of opicinumab in patients with relapsing multiple sclerosis (SYNERGY): a randomised, placebo-controlled, phase 2 trial', *The Lancet Neurology*, 18, pp. 845–856. doi: 10.1016/S1474-4422(19)30137-1.

Cahoy, J. D. *et al.* (2008) 'A transcriptome database for astrocytes, neurons, and oligodendrocytes: A new resource for understanding brain development and function', *Journal of Neuroscience*, 28(1), pp. 264–278. doi: 10.1523/JNEUROSCI.4178-07.2008.

Cai, J. *et al.* (2005) 'Generation of oligodendrocyte precursor cells from mouse dorsal spinal cord independent of Nkx6 regulation and Shh signaling', *Neuron*, 45(1), pp. 41–53. doi: 10.1016/j.neuron.2004.12.028.

Calver, A. R. *et al.* (1998) 'Oligodendrocyte population dynamics and the role of PDGF in vivo', *Neuron*, 20(5), pp. 869–882. doi: 10.1016/S0896-6273(00)80469-9.

Câmara, J. *et al.* (2009) 'Integrin-mediated axoglial interactions initiate myelination in the central nervous system', *The Journal of Cell Biology*, 185(4), pp. 699–712. doi: 10.1083/jcb.200807010.

Canoll, P. D. *et al.* (1996) 'GGF/neuregulin is a neuronal signal that promotes the proliferation and survival and inhibits the differentiation of oligodendrocyte progenitors', *Neuron*, 17(2), pp. 229–243. doi: 10.1016/S0896-6273(00)80155-5.

Carragher, N. *et al.* (2018) 'Concerns, challenges and promises of high-content analysis of 3D cellular models', *Nature Reviews Drug Discovery*. Nature Publishing Group. doi: 10.1038/nrd.2018.99.

Carteron, C., Ferrer-Montiel, A. and Cabedo, H. (2006) 'Characterization of a neural-specific splicing form of the human neuregulin 3 gene involved in oligodendrocyte survival', *Journal of Cell Science*, 119(5), pp. 898–909. doi: 10.1242/jcs.02799.

Chang, A. *et al.* (2000) 'NG2-Positive Oligodendrocyte Progenitor Cells in Adult Human Brain and Multiple Sclerosis Lesions', *Journal of Neuroscience*, 20(17), pp. 6404–6412.

Chang, A. *et al.* (2002) 'Premyelinating oligodendrocytes in chronic lesions of multiple sclerosis', *New England Journal of MedicineMedicine*, 346(3), pp. 165–173.

Charles, P. *et al.* (2000) 'Negative regulation of central nervous system myelination by polysialylated-neural cell adhesion molecule.', *Proceedings of the National Academy of Sciences of the United States of America*, 97(13), pp. 7585–90. doi: 10.1073/pnas.100076197.

Chen, Y. *et al.* (2008) 'NS21: Re-defined and modified supplement B27 for neuronal cultures', *Journal of Neuroscience Methods*, 171(2), pp. 239–247. doi: 10.1016/j.jneumeth.2008.03.013.

Chen, Y. *et al.* (2009) 'The oligodendrocyte-specific G protein-coupled receptor GPR17 is a cell-intrinsic timer of myelination', *Nature Neuroscience*, 12(11), pp. 1398–1406. doi: 10.1038/nn.2410.

Chong, S. Y. C. *et al.* (2012) 'Neurite outgrowth inhibitor Nogo-A establishes spatial segregation and extent of oligodendrocyte myelination', *Proceedings of the National Academy of Sciences*, 109(4), pp. 1299–1304. doi: 10.1073/pnas.1113540109.

Choi, S. H. *et al.* (2014) 'A three-dimensional human neural cell culture model of Alzheimer's disease', *Nature*. Nature Publishing Group, 515(7526), pp. 274–278. doi: 10.1038/nature13800.

Choi, S. H. and Tanzi, R. E. (2012) 'IPSCs to the rescue in Alzheimer's research', *Cell Stem Cell*. Elsevier Inc., 10(3), pp. 235–236. doi: 10.1016/j.stem.2012.02.011.

Christoffersson, J. *et al.* (2018) 'A Cardiac Cell Outgrowth Assay for Evaluating Drug Compounds Using a Cardiac Spheroid-on-a-Chip Device', *Bioengineering*, 5(2), p. 36. doi: 10.3390/bioengineering5020036.

Citterio, A. *et al.* (2013) 'Corticosteroids or ACTH for acute exacerbations in multiple sclerosis', *Cochrane Database of Systematic Reviews*, (4). doi: 10.1002/14651858.CD001331.www.cochranelibrary.com.

Clarke, L. E. *et al.* (2012) 'Properties and Fate of Oligodendrocyte Progenitor Cells in the Corpus Callosum, Motor Cortex, and Piriform Cortex of the Mouse', *Journal of Neuroscience*, 32(24), pp. 8173–8185. doi: 10.1523/JNEUROSCI.0928-12.2012.

Claus Stolt, C. *et al.* (2002) 'Terminal differentiation of myelin-forming oligodendrocytes depends on the transcription factor Sox10', *Genes and Development*, 16(2), pp. 165–170. doi: 10.1101/gad.215802.

Clemons, P. A., Tolliday, N. J. and Wagner, B. K. (2009) *Cell-Based Assays for High-Throughput Screening: Methods and Protocols*. doi: 10.1007/978-1-59745-542-8_3.

Cohen, R. I. *et al.* (1996) 'Nerve growth factor and neurotrophin-3 differentially regulate the proliferation and survival of developing rat brain oligodendrocytes', *Journal of Neuroscience*, 16(20), pp. 6433–6442. doi: 10.1523/jneurosci.16-20-06433.1996.

Colello, R. J. *et al.* (1995) 'The chronology of oligodendrocyte differentiation in the rat optic nerve: evidence for a signaling step initiating myelination in the CNS.', *The Journal of neuroscience : the official journal of the Society for Neuroscience*, 15(November), pp. 7665–7672.

Colognato, H. *et al.* (2002) 'CNS integrins switch growth factor signalling to promote target-dependent survival', *Nature Cell Biology*, 4(11), pp. 1–9. doi: 10.1038/ncb865.

Colognato, H. *et al.* (2004) 'Integrins direct Src family kinases to regulate distinct phases of oligodendrocyte development', *Journal of Cell Biology*, 167(2), pp. 365–375. doi: 10.1083/jcb.200404076.

Colognato, H. *et al.* (2007) 'Identification of dystroglycan as a second laminin receptor in oligodendrocytes, with a role in myelination', *Development*, 134(9), pp. 1723–1736. doi: 10.1242/dev.02819.

Compston, A. and Coles, A. (2002) 'Multiple sclerosis', *The Lancet*, 359, pp. 1221–1231.

Confavreux, C. and Vukusic, S. (2006) 'Age at disability milestones in multiple sclerosis', *Brain*, 129, pp. 595–605. doi: 10.1093/brain/awh714.

Crawford, A. H. *et al.* (2016) 'Pre-existing mature oligodendrocytes do not contribute to remyelination following toxin-induced spinal cord demyelination', *American Journal of Pathology*. American Society for Investigative Pathology, 186(3), pp. 511–516. doi: 10.1016/j.ajpath.2015.11.005.

Czopka, T., ffrench-Constant, C. and Lyons, David A. (2013) 'Individual Oligodendrocytes Have Only a Few Hours in which to Generate New Myelin Sheaths In Vivo', *Developmental Cell*. Elsevier Inc., 25(6), pp. 599–609. doi: 10.1016/j.devcel.2013.05.013.

Czopka, T., ffrench-Constant, C. and Lyons, David A (2013) 'Individual Oligodendrocytes Have Only a Few Hours in which to Generate New Myelin Sheaths In Vivo', *Developmental Cell*. Elsevier Inc., 25(6), pp. 599–609. doi: 10.1016/j.devcel.2013.05.013.

D'Este, E. *et al.* (2017) 'Ultrastructural anatomy of nodes of Ranvier in the peripheral nervous system as revealed by STED microscopy', *Proceedings of the National Academy of Sciences of the United States of America*, 114(2), pp. E191–E199. doi: 10.1073/pnas.1619553114.

Dai, X. and Huang, Y.-C. (2014) 'Electrospun Fibrous Scaffolds of Poly(glycerol-dodecanedioate) for Engineering Neural Tissues From Mouse Embryonic Stem Cells', *Journal of Visualized Experiments*, (88). doi: 10.3791/51587.

Dawson, M. R. L. *et al.* (2003) 'NG2-expressing glial progenitor cells: An abundant and widespread population of cycling cells in the adult rat CNS', *Molecular and Cellular Neuroscience*, 24(2), pp. 476–488. doi: 10.1016/S1044-7431(03)00210-0.

de Boer, A. G. and Gaillard, P. J. (2007) 'Drug Targeting to the Brain', *Annual Review of Pharmacology and Toxicology*, 47(1), pp. 323–355. doi: 10.1146/annurev.pharmtox.47.120505.105237.

de Robertis, E. and Schmitt, F. O. (1948) 'An electron microscope analysis of certain nerve axon constituents', *Journal of Cellular and Comparative Physiology*, 31(1), pp. 1–23. doi: 10.1002/jcp.1030310102.

Demerens, C. *et al.* (1996) 'Induction of myelination in the central nervous system by

electrical activity', *Proceedings of the National Academy of Sciences of the United States of America*, 93(18), pp. 9887–9892. doi: 10.1073/pnas.93.18.9887.

Denic, A. *et al.* (2011) 'The relevance of animal models in multiple sclerosis research', *Pathophysiology*. Elsevier Ireland Ltd, 18(1), pp. 21–29. doi: 10.1016/j.pathophys.2010.04.004.

Deo, A. K., Theil, F. P. and Nicolas, J. M. (2013) 'Confounding parameters in preclinical assessment of blood-brain barrier permeation: An overview with emphasis on species differences and effect of disease states', *Molecular Pharmaceutics*, 10(5), pp. 1581–1595. doi: 10.1021/mp300570z.

Deshmukh, V. A. *et al.* (2013) 'A regenerative approach to the treatment of multiple sclerosis.', *Nature*. Nature Publishing Group, 502(7471), pp. 327–32. doi: 10.1038/nature12647.

Deun, I. S. L. Van and Pesch, C. B. V. Van (2017) 'Corticosteroids in the management of acute multiple sclerosis exacerbations', *Acta Neurologica Belgica*. Springer International Publishing, 117(3), pp. 623–633. doi: 10.1007/s13760-017-0772-0.

Deyati, A. *et al.* (2013) 'Challenges and opportunities for oncology biomarker discovery', *Drug Discovery Today*. Elsevier Ltd, 18(13–14), pp. 614–624. doi: 10.1016/j.drudis.2012.12.011.

Diemel, L. T. *et al.* (2004) 'Remyelination of Cytokine- or Antibody-Demyelinated CNS Aggregate Cultures Is Inhibited by Macrophage Supplementation', *Glia*, 45(3), pp. 278–286. doi: 10.1002/glia.10335.

Dombrowski, Y. *et al.* (2015) 'Regulatory T cells directly promote myelin regeneration in the Central Nervous System', *Cell & Bioscienceell Stem Cell*. Nature Publishing Group, 20(August 2016), pp. 1–10. doi: 10.1038/nn.4528.

Doshi, J. and Reneker, D. H. (1995) 'Electrospinning Process and Applications of Electrospun Fibers', *Journal of Electrostatics*, 35(2–3), pp. 151–160. doi: 10.1109/IAS.1993.299067.

Dubois-Dalcq, M. *et al.* (1986) 'Emergence of three myelin proteins in oligodendrocytes cultured without neurons', *The Journal of Cell Biology*, 102(February), pp. 384–392.

Dubois-Dalcq, M. (1987) 'Characterization of a slowly proliferative cell along the oligodendrocyte differentiation pathway.', *The EMBO Journal*, 6(9), pp. 2587–2595. doi:

10.1002/j.1460-2075.1987.tb02549.x.

Dugas, J. C. *et al.* (2010) 'Dicer1 and miR-219 Are Required for Normal Oligodendrocyte Differentiation and Myelination', *Neuron*. Elsevier Ltd, 65(5), pp. 597–611. doi: 10.1016/j.neuron.2010.01.027.

Duncan, I. D. *et al.* (2009) 'Extensive remyelination of the CNS leads to functional recovery', *Proceedings of the National Academy of Sciences*, 106(16), pp. 6832–6836. doi: 10.1073/pnas.0906701106.

Duncan, I. D. *et al.* (2017) 'Thin myelin sheaths as the hallmark of remyelination persist over time and preserve axon function', *Proceedings of the National Academy of Sciences*, p. 201714183. doi: 10.1073/pnas.1714183114.

Duncan, I. D. *et al.* (2018) 'The adult oligodendrocyte can participate in remyelination', *Proceedings of the National Academy of Sciences*, 115(50), pp. E11807–E11816. doi: 10.1073/pnas.1808064115.

Duncan, M. D., Reintjes, J. and Manuccia, T. J. (1982) 'Scanning coherent anti-Stokes Raman microscope.', *Optics letters*, 7(8), pp. 350–2. Available at: http://www.ncbi.nlm.nih.gov/pubmed/19714017.

Durand, B. *et al.* (1998) 'p27(Kip1) alters the response of cells to mitogen and is part of a cell-intrinsic timer that arrests the cell cycle and initiates differentiation', *Current Biology*, 8(8), pp. 431–440. doi: 10.1016/S0960-9822(98)70177-0.

Durand, B. and Raff, M. (2000) 'A cell-intrinsic timer that operates during oligodendrocyte development', *BioEssays*, 22(1), pp. 64–71. doi: 10.1002/(SICI)1521-1878(200001)22:1<64::AID-BIES11>3.0.CO;2-Q.

Dziembowska, M. *et al.* (2005) 'A role for CXCR4 signaling in survival and migration of neural and oligodendrocyte precursors', *Glia*, 50(3), pp. 258–269. doi: 10.1002/glia.20170.

Eberle, J. P. *et al.* (2017) *Super-resolution microscopy: Fully automated targeted confocal and single-molecular localisation microscopy*, *Methods in Molecular Biology*. doi: 10.1007/978-1-4939-7265-4_15.

Ehrlich, M. *et al.* (2017) 'Rapid and efficient generation of oligodendrocytes from human induced pluripotent stem cells using transcription factors', *Proceedings of the National*

Academy of Sciences of the United States of America, 114(11), pp. E2243–E2252. doi: 10.1073/pnas.1614412114.

Eleuteri, C. *et al.* (2017) 'A staged screening of registered drugs highlights remyelinating drug candidates for clinical trials', *Scientific Reports*. Nature Publishing Group, 7(March), p. 45780. doi: 10.1038/srep45780.

Eluvathingal, T. J. *et al.* (2006) 'Abnormal Brain Connectivity in Children After Early Severe Socioemotional Deprivation: A Diffusion Tensor Imaging Study', *Pediatrics*, 117(6), pp. 2093–2100. doi: 10.1542/peds.2005-1727.

Ember, K. J. I. *et al.* (2017) 'Raman spectroscopy and regenerative medicine: a review', *npj Regenerative Medicine*. Springer US, 2(1). doi: 10.1038/s41536-017-0014-3.

Emery, B. *et al.* (2009) 'Myelin Gene Regulatory Factor Is a Critical Transcriptional Regulator Required for CNS Myelination', *Cell*. Elsevier Ltd, 138(1), pp. 172–185. doi: 10.1016/j.cell.2009.04.031.

Falcão, A. M. *et al.* (2018) 'Disease-specific oligodendrocyte lineage cells arise in multiple sclerosis', *Nature Medicine*. Springer US, 24(December). doi: 10.1038/s41591-018-0236-y.

Fancy, S. P. J. *et al.* (2009) 'Dysregulation of the Wnt pathway inhibits timely myelination and remyelination in the mammalian CNS', *Genes and Development*, 23(13), pp. 1571–1585. doi: 10.1101/gad.1806309.

Fard, M. K. *et al.* (2017) 'BCAS1 expression defines a population of early myelinating oligodendrocytes in multiple sclerosis lesions', *Science Translational Medicine*, 9(December), p. eaam7816.

Farrar, M. J. *et al.* (2011) 'In vivo imaging of myelin in the vertebrate central nervous system using third harmonic generation microscopy', *Biophysical Journal*. Biophysical Society, 100(5), pp. 1362–1371. doi: 10.1016/j.bpj.2011.01.031.

Feirabend, H. K. P., Choufoer, H. and Ploeger, S. (1998) 'Preservation and staining of myelinated nerve fibers', *Methods: A Companion to Methods in Enzymology*, 15(2), pp. 123–131. doi: 10.1006/meth.1998.0615.

Feng, B. *et al.* (2019) 'Validation of Human MDR1-MDCK and BCRP-MDCK Cell Lines to Improve the Prediction of Brain Penetration', *Journal of Pharmaceutical Sciences*. Elsevier Ltd,

108(7), pp. 2476–2483. doi: 10.1016/j.xphs.2019.02.005.

Ferrer, I. *et al.* (2008) 'Brain banks: Benefits, limitations and cautions concerning the use of post-mortem brain tissue for molecular studies', *Cell and Tissue Banking*, 9(3), pp. 181–194. doi: 10.1007/s10561-008-9077-0.

Fernandez, P. A. *et al.* (2000) 'Evidence that axon-derived neuregulin promotes oligodendrocyte survival in the developing rat optic nerve', *Neuron*, 28(1), pp. 81–90. doi: 10.1016/S0896-6273(00)00087-8.

ffrench-Constant, C. and Raff, M. C. (1986) 'Proliferating bipotential glial progenitor cells in adult rat optic nerve', *Nature*, 319(6053), pp. 499–502. doi: 10.1038/319499a0.

ffrench-Constant, C. *et al.* (1988) 'Evidence that migratory oligodendrocyte-type-2 astrocyte (O-2A) progenitor cells are kept out of the rat retina by a barrier at the eye-end of the optic nerve', *Journal of Neurocytology*, 17(1), pp. 13–25. doi: 10.1007/BF01735374.

Filippini, G. *et al.* (2013) 'Immunomodulators and immunosuppressants for multiple sclerosis : a network meta-analysis', *Cochrane Database of Systematic Reviews*, (6). doi: 10.1002/14651858.CD008933.pub2.www.cochranelibrary.com.

Fitch, M. T. and Silver, J. (2008) 'CNS injury, glial scars, and inflammation: Inhibitory extracellular matrices and regeneration failure', *Experimental Neurology*, 209(2), pp. 294–301. doi: 10.1016/j.expneurol.2007.05.014.

Flores, A. I. *et al.* (2008) 'Constitutively Active Akt Induces Enhanced Myelination in the CNS', *Journal of Neuroscience*, 28(28), pp. 7174–7183. doi: 10.1523/JNEUROSCI.0150-08.2008.

Foo, L. C. *et al.* (2011) 'Development of a method for the purification and culture of rodent astrocytes.', *Neuron*. Elsevier Inc., 71(5), pp. 799–811. doi: 10.1016/j.neuron.2011.07.022.

Foo, L. C. (2013) 'Purification of rat and mouse astrocytes by immunopanning', *Cold Spring Harbor Protocols*, 8(5), pp. 421–432. doi: 10.1101/pdb.prot074211.

Fogarty, M., Richardson, W. D. and Kessaris, N. (2005) 'A subset of oligodendrocytes generated from radial glia in the dorsal spinal cord', *Development*, 132(8), pp. 1951–1959. doi: 10.1242/dev.01777.

Fortin, D. *et al.* (2005) 'Distinct fibroblast growth factor (FGF)/FGF receptor signaling pairs initiate diverse cellular responses in the oligodendrocyte lineage', *Journal of Neuroscience*,

25(32), pp. 7470–7479. doi: 10.1523/JNEUROSCI.2120-05.2005.

Freeman, S. A. *et al.* (2015) 'Acceleration of conduction velocity linked to clustering of nodal components precedes myelination', *Proceedings of the National Academy of Sciences*, 112(3), pp. E321–E328. doi: 10.1073/pnas.1419099112.

Freudiger, C. W. *et al.* (2008) 'Label-free biomedical imaging with high sensitivity by stimulated Raman scattering microscopy', *Science*, 322, pp. 1857–1861. doi: 10.1126/science.1165758.

Frühbeis, C. *et al.* (2013) 'Neurotransmitter-Triggered Transfer of Exosomes Mediates Oligodendrocyte–Neuron Communication', *PLoS Biology*, 11(7), p. e1001604. doi: 10.1371/journal.pbio.1001604.

Fruttiger, M. *et al.* (1999) 'Defective oligodendrocyte development and severe hypomyelination in PDGF-A knockout mice', *Development*, 126(3), pp. 457–467.

Fu, Y. *et al.* (2008) 'Ex vivo and in vivo imaging of myelin fibers in mouse brain by coherent anti-Stokes Raman scattering microscopy', *Opt Express*, 16(24), pp. 19396–19409. doi: 10.1016/j.biotechadv.2011.08.021.Secreted.

Fu, H. *et al.* (2009) 'A genome-wide screen for spatially restricted expression patterns identifies transcription factors that regulate glial development', *Journal of Neuroscience*, 29(36), pp. 11399–11408. doi: 10.1523/JNEUROSCI.0160-09.2009.

Fünfschilling, U. *et al.* (2012) 'Glycolytic oligodendrocytes maintain myelin and long-term axonal integrity', *Nature*, 485(7399), pp. 517–521. doi: 10.1038/nature11007.

Furusho, M. *et al.* (2011) 'Fibroblast growth factor signaling is required for the generation of oligodendrocyte progenitors from the embryonic forebrain', *Journal of Neuroscience*, 31(13), pp. 5055–5066. doi: 10.1523/JNEUROSCI.4800-10.2011.

Furusho, M. *et al.* (2012) 'Fibroblast growth factor receptor signaling in oligodendrocytes regulates myelin sheath thickness', *Journal of Neuroscience*, 32(19), pp. 6631–6641. doi: 10.1523/JNEUROSCI.6005-11.2012.

Gaillard, P. J. *et al.* (2012) 'Enhanced brain drug delivery: Safely crossing the blood-brain barrier', *Drug Discovery Today: Technologies*. Elsevier Ltd, 9(2), pp. e155–e160. doi: 10.1016/j.ddtec.2011.12.002.

Galbraith, C. G. and Galbraith, J. A. (2011) 'Super-resolution microscopy at a glance', *Journal of Cell Science*, 124(10), pp. 1607–1611. doi: 10.1242/jcs.080085.

Gallo, V. *et al.* (1996) 'Oligodendrocyte progenitor cell proliferation and lineage progression are regulated by glutamate receptor-mediated K+ channel block', *The Journal of Neuroscience*, 16(8), pp. 2659–2670. doi: 10.1523/jneurosci.16-08-02659.1996.

García-León, J. A. *et al.* (2018) 'SOX10 Single Transcription Factor-Based Fast and Efficient Generation of Oligodendrocytes from Human Pluripotent Stem Cells', *Stem Cell Reports*, 10, pp. 1–18. doi: 10.1016/j.stemcr.2017.12.014.

Garcion, E., Faissner, A. and ffrench-Constant, C. (2001) 'Knockout mice reveal a contribution of the extracellular matrix molecule tenascin-C to neural precursor proliferation and migration', *Development*, 128(13), pp. 2485–2496.

Gard, A. L. and Pfeiffer, S. E. (1989) 'Oligodendrocyte progenitors isolated directly from developing telencephalon at a specific phenotypic stage: myelinogenic potential in a defined environment.', *Development*, 106, pp. 119–32. Available at: http://www.ncbi.nlm.nih.gov/pubmed/2697546.

Gautier, H. O. B. *et al.* (2015) 'Neuronal activity regulates remyelination via glutamate signalling to oligodendrocyte progenitors.', *Nature communications*, 6, p. 8518. doi: 10.1038/ncomms9518.

GBD 2015 Neurological Disorders Collaborator Group (2017) 'Global, regional, and national burden of neurological disorders during 1990 – 2015: a systematic analysis for the Global Burden of Disease Study 2015', *Lancet Neurology*, 16, pp. 977–897. doi: 10.1016/S1474-4422(17)30299-5.

Ghnenis, A. B. *et al.* (2018) 'Toluidine blue staining of resin-embedded sections for evaluation of peripheral nerve morphology', *Journal of Visualized Experiments*, 2018(137), pp. 1–7. doi: 10.3791/58031.

Gibson, E. M., Purger, D., Mount, C. W., Goldstein, A. K., Lin, G. L., Wood, L. S., Inema, I., Miller, Sarah, E., *et al.* (2014) 'Neuronal Activity Promotes Oligodendrogenesis and Adaptive Myelination in the Mammalian Brain', *Science*, 344(6183), pp. 480–481. doi: 10.1126/science.1254446.

Gibson, E. M., Purger, D., Mount, C. W., Goldstein, A. K., Lin, G. L., Wood, L. S., Inema, I.,

Miller, S. E., *et al.* (2014) 'Neuronal Activity Promotes Oligodendrogenesis and Adaptive Myelination in the Mammalian Brain', *Science*, 344. doi: 10.1126/science.1252304.

Giera, S. *et al.* (2015) 'The adhesion G protein-coupled receptor GPR56 is a cell-autonomous regulator of oligodendrocyte development', *Nature Communications*. Nature Publishing Group, 6(May 2014). doi: 10.1038/ncomms7121.

Goebbels, S. *et al.* (2010) 'Elevated Phosphatidylinositol 3,4,5-Trisphosphate in Glia Triggers Cell-Autonomous Membrane Wrapping and Myelination', *Journal of Neuroscience*, 30(26), pp. 8953–8964. doi: 10.1523/JNEUROSCI.0219-10.2010.

Goldberg, J. L. *et al.* (2004) 'An oligodendrocyte lineage-specific semaphorin, sema5A, inhibits axon growth by retinal ganglion cells', *Journal of Neuroscience*, 24(21), pp. 4989–4999. doi: 10.1523/JNEUROSCI.4390-03.2004.

Gonsalvez, D. G. *et al.* (2019) 'Imaging and Quantification of Myelin Integrity After Injury With Spectral Confocal Reflectance Microscopy', *Frontiers in Molecular Neuroscience*, 12(November), pp. 1–13. doi: 10.3389/fnmol.2019.00275.

Göttle, P. *et al.* (2010) 'Activation of CXCR7 receptor promotes oligodendroglial cell maturation', *Annals of Neurology*, 68(6), pp. 915–924. doi: 10.1002/ana.22214.

Grant, R. *et al.* (2019) 'Blended electrospinning with human liver extracellular matrix for engineering new hepatic microenvironments', *Scientific Reports*, 9(1), pp. 1–12. doi: 10.1038/s41598-019-42627-7.

Green, A. J. *et al.* (2017) 'Clemastine fumarate as a remyelinating therapy for multiple sclerosis (ReBUILD) : a randomised , controlled , double-blind , crossover trial', *The Lancet*, 390, pp. 2481–2489. doi: 10.1016/S0140-6736(17)32346-2.

Griffiths, I. *et al.* (1998) 'Axonal Swellings and Degeneration in Mice Lacking the Major Proteolipid of Myelin Axonal Swellings and Degeneration in Mice Lacking the Major Proteolipid of Myelin', *Science*, 280, pp. 1610–1613. doi: 10.1126/science.280.5369.1610.

Guan, Y. *et al.* (2019) 'The role of Epstein-Barr virus in multiple sclerosis : from molecular pathophysiology to in vivo imaging', *Neural Regeneration Research*, 14(2), pp. 373–386. doi: 10.4103/1673-5374.245462.

Gudz, T. I., Komuro, H. and Macklin, W. B. (2006) 'Glutamate stimulates oligodendrocyte

progenitor migration mediated via an αv integrin/myelin proteolipid protein complex', *Journal of Neuroscience*, 26(9), pp. 2458–2466. doi: 10.1523/JNEUROSCI.4054-05.2006.

Gustafsson, M. G. L. (2000) 'Surpassing the lateral resolution limit by a factor of two using structured illumination microscopy', *Journal of Microscopy*, 198(2), pp. 82–87. doi: 10.1046/j.1365-2818.2000.00710.x.

Gustavsson, A. *et al.* (2011) 'Cost of disorders of the brain in Europe 2010', *European Neuropsychopharmacology*, 21(10), pp. 718–779. doi: 10.1016/j.euroneuro.2011.08.008.

Gyllensten, L. and Malmfors, T. (1963) 'Myelinization of the optic nerve and its dependence on visual function--a quantitative investigation in mice.', *Journal of embryology and experimental morphology*, 11(March), pp. 255–66. Available at: http://www.ncbi.nlm.nih.gov/pubmed/13963537.

Hagström, H. *et al.* (2018) 'Risk for development of severe liver disease in lean patients with nonalcoholic fatty liver disease: A long-term follow-up study', *Hepatology Communications*, 2(1), pp. 48–57. doi: 10.1002/hep4.1124.

Hajihosseini, M., Tham, T. N. and Dubois-Dalcq, M. (1996) 'Origin of oligodendrocytes within the human spinal cord', *Journal of Neuroscience*, 16(24), pp. 7981–7994. doi: 10.1523/jneurosci.16-24-07981.1996.

Hampton, D. W. *et al.* (2012) 'Focal Immune-Mediated White Matter Demyelination Reveals an Age-Associated Increase in Axonal Vulnerability and Decreased Remyelination Efficiency', *The American Journal of Pathology*. Elsevier Inc., 180(5), pp. 1897–1905. doi: 10.1016/j.ajpath.2012.01.018.

Handel, A. E. *et al.* (2011) 'The epidemiology of multiple sclerosis in Scotland: Inferences from hospital admissions', *PLoS ONE*, 6(1), pp. 1–5. doi: 10.1371/journal.pone.0014606.

Hart, I. K. *et al.* (1989) 'Timing of Oligodendrocyte Differentiation', *Cell*, 109(6), pp. 3411–3417.

Hartman, B. K. *et al.* (1982) 'Development and maturation of central nervous system myelin: Comparison of immunohistochemical localization of proteolipid protein and basic protein in myelin and oligodendrocytes', *Proceedings of the National Academy of Sciences of the United States of America*, 79(13), pp. 4217–4220. doi: 10.1073/pnas.79.13.4217.

Hay, M. *et al.* (2014) 'Clinical development success rates for investigational drugs', *Nature Biotechnology*, 32(1), pp. 40–51. doi: 10.1038/nbt.2786.

He, Y. *et al.* (2007) 'The Transcription Factor Yin Yang 1 Is Essential for Oligodendrocyte Progenitor Differentiation', *Neuron*, 55(2), pp. 217–230. doi: 10.1016/j.neuron.2007.06.029.

Heilemann, M. *et al.* (2008) 'Subdiffraction-resolution fluorescence imaging with conventional fluorescent probes', *Angewandte Chemie - International Edition*, 47(33), pp. 6172–6176. doi: 10.1002/anie.200802376.

Hejgaard Laursen, J. *et al.* (2016) 'Vitamin D supplementation reduces relapse rate in relapsing-remitting multiple sclerosis patients treated with natalizumab', *Multiple Sclerosis and Related Disorders*. Elsevier, 10(October), pp. 169–173. doi: 10.1016/j.msard.2016.10.005.

Hell, S. W. and Wichmann, J. (1994) 'Breaking the diffraction resolution limit by stimulated emission: stimulated-emission-depletion fluorescence microscopy', *Optics Letters*, 19(11), p. 780. doi: 10.1364/ol.19.000780.

Hess, S. T., Girirajan, T. P. K. and Mason, M. D. (2006) 'Ultra-high resolution imaging by fluorescence photoactivation localization microscopy', *Biophysical Journal*. Elsevier, 91(11), pp. 4258–4272. doi: 10.1529/biophysj.106.091116.

Hill, R. A. *et al.* (2014) 'Modulation of oligodendrocyte generation during a critical temporal window after NG2 cell division', *Nature Neuroscience*, 17(11), pp. 1518–1527. doi: 10.1038/nn.3815.

Hill, R. A., Li, A. M. and Grutzendler, J. (2018) 'Lifelong cortical myelin plasticity and age-related degeneration in the live mammalian brain', *Nature Neuroscience*. Springer US, 21(5), pp. 683–695. doi: 10.1038/s41593-018-0120-6.

Hodgkin, A. L. and Huxley, A. F. (1952) 'A quantitative description of membrane current and its application to conduction and excitation in nerve', *Journal of Physiology*, 117, pp. 500–544. doi: 10.1080/00062278.1939.10600645.

Horvath, P. *et al.* (2016) 'Screening out irrelevant cell-based models of disease', *Nature Reviews Drug Discovery*. Nature Publishing Group. doi: 10.1038/nrd.2016.175.

Howe, C. L. (2006) 'Coated glass and vicryl microfibers as artificial axons', *Cells Tissues Organs*, 183(4), pp. 180–194. doi: 10.1159/000096509.

Hu, J. *et al.* (2009) 'Effects of extracellular matrix molecules on the growth properties of oligodendrocyte progenitor cells in vitro', *Journal of Neuroscience Research*, 87(13), pp. 2854–2862. doi: 10.1002/jnr.22111.

Huang, J. K. *et al.* (2010) 'Retinoid X receptor gamma signaling accelerates CNS remyelination', *Nature Neuroscience*. Nature Publishing Group, 14(1), pp. 45–53. doi: 10.1038/nn.2702.

Huang, Z. M. *et al.* (2003) 'A review on polymer nanofibers by electrospinning and their applications in nanocomposites', *Composites Science and Technology*, 63(15), pp. 2223–2253. doi: 10.1016/S0266-3538(03)00178-7.

Hughes, E. G. *et al.* (2013) 'Oligodendrocyte progenitors balance growth with self-repulsion to achieve homeostasis in the adult brain', *Nature Neuroscience*. Nature Publishing Group, 16(6), pp. 668–676. doi: 10.1038/nn.3390.

Hughes, E. G. *et al.* (2018) 'Myelin remodeling through experience-dependent oligodendrogenesis in the adult somatosensory cortex', *Nature Neuroscience*. Springer US, 21(5), pp. 696–706. doi: 10.1038/s41593-018-0121-5.

Huxley, B. Y. A. F. and Stampfli, A. D. R. (1949) 'Evidence for Saltatory Conduction in Peripheral Myelinated Nerve Fibers', *Journal of physiology*, 108(1946), pp. 315–339.

IMSGC, T. I. M. S. G. C. and WTCCC, T. W. T. C. C. C. (2011) 'Genetic risk and a primary role for cell-mediated immune mechanisms in multiple sclerosis', *Nature*, 476, pp. 214–219. doi: 10.1038/nature10251.

Ineichen, B. V. *et al.* (2017) 'Sudan black: a fast, easy and non-toxic method to assess myelin repair in demyelinating diseases', *Neuropathology and Applied Neurobiology*, 43(3), pp. 242–251. doi: 10.1111/nan.12373.

Iqbal, Q. *et al.* (2015) 'Quantitative analysis of mechanical and electrostatic properties of poly(lactic) acid fibers and poly(lactic) acid - Carbon nanotube composites using atomic force microscopy', *Nanotechnology*. IOP Publishing, 26(10). doi: 10.1088/0957-4484/26/10/105702.

Irvine, K. A. and Blakemore, W. F. (2008) 'Remyelination protects axons from demyelination-associated axon degeneration', *Brain*, 131, pp. 1464–1477. doi: 10.1093/brain/awn080.

Irvine, K. and Blakemore, W. F. (2006) 'Age increases axon loss associated with primary

demyelination in cuprizone-induced demyelination in C57BL / 6 mice', *Journal of Neuroimmunology*, 175, pp. 69–76. doi: 10.1016/j.jneuroim.2006.03.002.

Ishibashi, T. *et al.* (2006) 'Astrocytes promote myelination in response to electrical impulses', *Neuron*, 49(6), pp. 823–832. doi: 10.1016/j.neuron.2006.02.006.

Ishii, A., Furusho, M. and Bansal, R. (2013) 'Sustained Activation of ERK1 / 2 MAPK in Oligodendrocytes and Schwann Cells Enhances Myelin Growth and Stimulates Oligodendrocyte Progenitor Expansion', *Journal of Neuroscience*, 33(1), pp. 175–186. doi: 10.1523/JNEUROSCI.4403-12.2013.

Israel, M. A. *et al.* (2012) 'Probing sporadic and familial Alzheimer's disease using induced pluripotent stem cells', *Nature*. Nature Publishing Group, 482(7384), pp. 216–220. doi: 10.1038/nature10821.

Itoh, K. *et al.* (1995) 'Regulated expression of the neural cell adhesion molecule L1 by specific patterns of neural impulses', *Science*, 270(5240), pp. 1369–1372. doi: 10.1126/science.270.5240.1369.

Jabs, R. *et al.* (1994) 'Kainate activates Ca2+-permeable glutamate receptors and blocks voltage-gated K+ currents in glial cells of mouse hippocampal slices', *Pflügers Archiv European Journal of Physiology*, 426(3–4), pp. 310–319. doi: 10.1007/BF00374787.

Jäkel, S., *et al.* (2019) 'Altered human oligodendrocyte heterogeneity in multiple sclerosis', *Nature*. Springer US, 566(7745), pp. 543–547. doi: 10.1038/s41586-019-0903-2.

Jamur M.C., Oliver C. (2010) Permeabilization of Cell Membranes. In: Oliver C., Jamur M. (eds) Immunocytochemical Methods and Protocols. Methods in Molecular Biology (Methods and Protocols), vol 588. Humana Press.

Jarjour, A. A. *et al.* (2015) 'The Polarity Protein Scribble Regulates Myelination and Remyelination in the Central Nervous System', *PLoS Biology*, 13(3), pp. 1–23. doi: 10.1371/journal.pbio.1002107.

Jeffries, M. A. *et al.* (2016) 'ERK1/2 Activation in Preexisting Oligodendrocytes of Adult Mice Drives New Myelin Synthesis and Enhanced CNS Function', *Journal of Neuroscience*, 36(35), pp. 9186–9200. doi: 10.1523/JNEUROSCI.1444-16.2016.

Kang, S. H. *et al.* (2010) 'NG2+ CNS glial progenitors remain committed to the

oligodendrocyte lineage in postnatal life and following neurodegeneration', *Neuron*. Elsevier Inc., 68(4), pp. 668–681. doi: 10.1016/j.neuron.2010.09.009.

Kaplan, M. R. *et al.* (1997) 'Induction of sodium channel clustering by oligodendrocytes', *Nature*, 386(April), pp. 724–728.

Kaplan, M. R. *et al.* (2001) 'Differential Control of Clustering of the Sodium Channels Na v 1.2 and Na v 1.6 at Developing CNS Nodes of Ranvier purification and culture of retinal ganglion cells (RGCs), optic nerve astrocytes, and optic nerve oligodendrocytes', *Neuron*, 30, pp. 105–119. Available at: https://www.cell.com/action/showPdf?pii=S0896-6273%2801%2900266-5.

Káradóttir, R. *et al.* (2005) 'NMDA receptors are expressed in oligodendrocytes and activated in ischaemia', *Nature*, 438(7071), pp. 1162–1166. doi: 10.1038/nature04302.

Kessaris, N. *et al.* (2006) 'Competing waves of oligodendrocytes in the forebrain and postnatal elimination of an embryonic lineage', *Nature Neuroscience*, 9(2), pp. 173–179. doi: 10.1038/nn1620.

Kim, K. T. *et al.* (2018) 'Review of the UBC porcine model of traumatic spinal cord injury', *Journal of Korean Neurosurgical Society*, 61(5), pp. 539–547. doi: 10.3340/jkns.2017.0276.

Kim, H. *et al.* (2019) 'Pluripotent Stem Cell-Derived Cerebral Organoids Reveal Human Oligodendrogenesis with Dorsal and Ventral Origins', *Stem Cell Reports*. ElsevierCompany., 12(5), pp. 890–905. doi: 10.1016/j.stemcr.2019.04.011.

Kinney, H. C. *et al.* (1988) 'Sequence of Central Nervous System Myelination in Human Infancy. II. Patterns of Myelination in Autopsied Infants', *Journal of Neuropathology & Experimental Neurology*, 47(3), pp. 217–234.

Kirby, B. B. *et al.* (2006) 'In vivo time-lapse imaging shows dynamic oligodendrocyte progenitor behavior during zebrafish development', *Nature Neuroscience*, 9(12), pp. 1506–1511. doi: 10.1038/nn1803.

Kola, I. and Landis, J. (2004) 'Can the pharmaceutical industry reduce attrition rates?', *Nature Reviews Drug Discovery*, 3(8), pp. 711–715. doi: 10.1038/nrd1470.

Kotter, M. R. *et al.* (2006) 'Myelin Impairs CNS Remyelination by Inhibiting Oligodendrocyte Precursor Cell Differentiation', *Journal of Neuroscience*, 26(1), pp. 328–332. doi:

10.1523/JNEUROSCI.2615-05.2006.

Krasnow, A. M. *et al.* (2017) 'Regulation of developing myelin sheath elongation by oligodendrocyte calcium transients in vivo', *Nature Neuroscience*. Springer US, 21(January). doi: 10.1038/s41593-017-0031-y.

Kuhlbrodt, K. *et al.* (1998) 'Sox10, a Novel Transcriptional Modulator in Glial Cells', *The Journal of Neuroscience*, 18(1), pp. 237–250. doi: 10.1523/jneurosci.18-01-00237.1998.

Kuhlmann, T. *et al.* (2016) 'An updated histological classification system for multiple sclerosis lesions', *Acta Neuropathologica*. Springer Berlin Heidelberg, 133(1), pp. 13–24. doi: 10.1007/s00401-016-1653-y.

Kukley, M., Nishiyama, A. and Dietrich, D. (2010) 'The fate of synaptic input to NG2 glial cells: Neurons specifically downregulate transmitter release onto differentiating oligodendroglial cells', *Journal of Neuroscience*, 30(24), pp. 8320–8331. doi: 10.1523/JNEUROSCI.0854-10.2010.

Kutzelnigg, A. *et al.* (2005) 'Cortical demyelination and diffuse white matter injury in multiple sclerosis', *Brain*, 128, pp. 2705–2712. doi: 10.1093/brain/awh641.

Laabs, T. *et al.* (2005) 'Chondroitin sulfate proteoglycans in neural development and regeneration', *Current Opinion in Neurobiology*, 15(1), pp. 116–120. doi: 10.1016/j.conb.2005.01.014.

Lamonte, R. R. and McNally, D. (2001) 'Cyclic Olefin Copolymers', *Advanced Materials and Processes*, 159(3), pp. 33–36.

Lampron, A. *et al.* (2015) 'Inefficient clearance of myelin debris by microglia impairs remyelinating processes', *Journal of Experimental Medicine*, 212(4), pp. 481–495. doi: 10.1084/jem.20141656.

Lappe-Siefke, C. *et al.* (2003) 'Disruption of Cnp1 uncouples oligodendroglial functions in axonal support and myelination', *Nature Genetics*, 33(3), pp. 366–374. doi: 10.1038/ng1095.

Lariosa-Willingham, K. D. *et al.* (2016a) 'A high throughput drug screening assay to identify compounds that promote oligodendrocyte differentiation using acutely dissociated and purified oligodendrocyte precursor cells', *BMC Research Notes*. BioMed Central, 9(1), p. 419. doi: 10.1186/s13104-016-2220-2.

Lariosa-Willingham, K. D. *et al.* (2016b) 'Development of a central nervous system axonal myelination assay for high throughput screening', *BMC Neuroscience*. BioMed Central, 17(1), p. 16. doi: 10.1186/s12868-016-0250-2.

Lariosa-Willingham, K. D. *et al.* (2016c) 'Development of a high throughput drug screening assay to identify compounds that protect oligodendrocyte viability and differentiation under inflammatory conditions', *BMC Research Notes*. BioMed Central, 9(1), p. 419. doi: 10.1186/s13104-016-2220-2.

Lassmann, H. and Bradl, M. (2017) 'Multiple sclerosis: experimental models and reality', *Acta Neuropathologica*. Springer Berlin Heidelberg, 133(2), pp. 223–244. doi: 10.1007/s00401-016-1631-4.

Laursen, L. S., Chan, C. W. and ffrench-Constant, C. (2009) 'An integrin-contactin complex regulates CNS myelination by differential Fyn phosphorylation', *Journal of Neuroscience*, 29(29), pp. 9174–9185. doi: 10.1523/JNEUROSCI.5942-08.2009.

Lee, B. *et al.* (2010) 'White matter neuroplastic changes in long-term trained players of the game of "Baduk"11"Baduk" is the Korean name which replaces the Japanese name "GO," designating a traditional Far Eastern board game with two kinds of pieces (black and white stones) man', *NeuroImage*. Elsevier Inc., 52(1), pp. 9–19. doi: 10.1016/j.neuroimage.2010.04.014.

Lee, M. *et al.* (2015) 'In vivo imaging of the tumor and its associated microenvironment using combined CARS / two- photon microscopy', *IntraVital*, 4(June), pp. 37–41. doi: 10.1080/21659087.2015.1055430.

Lee, S. *et al.* (2012) 'A culture system to study oligodendrocyte myelination processes using engineered nanofibers', *Nature Methods*, 9(9), pp. 917–922. doi: 10.1038/nmeth.2105.

Lee, S. *et al.* (2013) 'A rapid and reproducible assay for modeling myelination by oligodendrocytes using engineered nanofibers', *Nature Protocols*, 8(4), pp. 771–782. doi: 10.1038/nprot.2013.039.

Lee, X. *et al.* (2007) 'NGF Regulates the Expression of Axonal LINGO-1 to Inhibit Oligodendrocyte Differentiation and Myelination', *Journal of Neuroscience*, 27(1), pp. 220–225. doi: 10.1523/JNEUROSCI.4175-06.2007.

Lee, Y. *et al.* (2012) 'Oligodendroglia metabolically support axons and contribute to

neurodegeneration', *Nature*. Nature Publishing Group, 487(7408), pp. 443–448. doi: 10.1038/nature11314.

Li, L. *et al.* (2016) 'High-throughput imaging: Focusing in on drug discovery in 3D', *Methods*. Elsevier Inc., 96, pp. 97–102. doi: 10.1016/j.ymeth.2015.11.013.

Lin, S. C. and Bergles, D. E. (2004) 'Synaptic signaling between GABAergic interneurons and oligodendrocyte precursor cells in the hippocampus', *Nature Neuroscience*, 7(1), pp. 24–32. doi: 10.1038/nn1162.

Li, L. *et al.* (2016) 'High-throughput imaging: Focusing in on drug discovery in 3D', *Methods*. Elsevier Inc., 96, pp. 97–102. doi: 10.1016/j.ymeth.2015.11.013.

Linnington, C., Webb, M. and Woodhams, P. L. (1984) 'A novel myelin-associated glycoprotein defined by a mouse monoclonal antibody', *Journal of Neuroimmunology*, 6(6), pp. 387–396. doi: 10.1016/0165-5728(84)90064-X.

Liu, J. *et al.* (2012) 'Impaired adult myelination in the prefrontal cortex of socially isolated mice.', *Nature Neuroscience*, 15(12), pp. 1621–3. doi: 10.1038/nn.3263.

Livesey, M. R. *et al.* (2016) 'Maturation and Electrophysiological Properties of Human Pluripotent Stem Cell-Derived Oligodendrocytes', *Stem Cells*, 34, pp. 1040–1053.

Longair, M. H., Baker, D. A. and Armstrong, J. D. (2011) 'Simple neurite tracer: Open source software for reconstruction, visualization and analysis of neuronal processes', *Bioinformatics*, 27(17), pp. 2453–2454. doi: 10.1093/bioinformatics/btr390.

Loughlin, A. J. *et al.* (1994) 'Myelin basic protein content of aggregating rat brain cell cultures treated with cytokines and/or demyelinating antibody: Effects of macrophage enrichment', *Journal of Neuroscience Research*, 37(5), pp. 647–653. doi: 10.1002/jnr.490370512.

Lu, Q. R. *et al.* (2002) 'Common developmental requirement for Olig function indicates a motor neuron/oligodendrocyte connection', *Cell*, 109(1), pp. 75–86. doi: 10.1016/S0092-8674(02)00678-5.

Lublin, F. D. *et al.* (2014) 'Defining the clinical course of multiple sclerosis The 2013 revisions', *Neurology*, 83, pp. 278–286.

Lucchinetti, C. F. *et al.* (1996) 'Distinct patterns of multiple sclerosis pathology indicates heterogeneity in pathogenesis', *Brain Pathology*, 6(3), pp. 259–274. doi: 10.1111/j.1750-

3639.1996.tb00854.x.

Lucchinetti, C. F. *et al.* (1999) 'A quantitative analysis of oligodendrocyes in multiple sclerosis lesions', *Brain*, 122(12), pp. 2279–2295. doi: 10.1093/brain/122.12.2279.

Lucchinetti, C. *et al.* (2000) 'Heterogeneity of multiple sclerosis lesions: Implications for the pathogenesis of demyelination', *Annals of Neurology*, 47(6), pp. 707–717. doi: 10.1002/1531-8249(200006)47:6<707::AID-ANA3>3.0.CO;2-Q.

Lysenko, V. *et al.* (2017) 'Humanised mouse models for haematopoiesis and infectious diseases', *Swiss medical weekly*, 147(October), p. w14516. doi: 10.4414/smw.2017.14516.

Madhavan, M. *et al.* (2018) 'Induction of myelinating oligodendrocytes in human cortical spheroids', *Nature Methods*. Springer US, 15(9), pp. 700–706. doi: 10.1038/s41592-018-0081-4.

Makinodan, M. *et al.* (2012) 'A Critical Period for Social Experience-Dependent Oligodendrocyte Maturation and Myelination', *Science*, 337(September), pp. 1357–1360. doi: 10.1126/science.1220845.

Maldonado, P. P. *et al.* (2013) 'Oligodendrocyte Precursor Cells Are Accurate Sensors of Local K+ in Mature Gray Matter', *Journal of Neuroscience*, 33(6), pp. 2432–2442. doi: 10.1523/jneurosci.1961-12.2013.

Markou, A. *et al.* (2009) 'Removing obstacles in neuroscience drug discovery: The future path for animal models', *Neuropsychopharmacology*, 34(1), pp. 74–89. doi: 10.1038/npp.2008.173.

Marques, S. *et al.* (2016) 'Oligodendrocyte heterogeneity in the mouse juvenile and adult central nervous system', *Science*, 352(6291).

Marton, R. M. *et al.* (2019) 'Differentiation and maturation of oligodendrocytes in human three-dimensional neural cultures', *Nature Neuroscience*. Springer US, 22(3), pp. 484–491. doi: 10.1038/s41593-018-0316-9.

Mason, G. F. and Krystal, J. H. (2006) 'MR spectroscopy: its potential role for drug development for the treatment of psychiatric diseases', *NMR in Biomedicine*, 19, pp. 609–701. doi: 10.1002/nbm.

Mcalpine, D. and Finean, J. B. (1961) 'Electron Microscopy of the Myelin', *Journal of the Royal*

Society of Medicine, 54(1), pp. 19–26. doi: 10.1177/003591576105400106.

McCarthy, K. D. and de Vellis, J. (1980) 'Preparation of separate astroglial and oligodendroglial cell cultures from rat cerebral tissue', *Journal of Cell Biology*, 85(June), pp. 890–902.

Mcdonald, J. J. *et al.* (2019) 'Latitudinal variation in MS incidence in Scotland', *Multiple Sclerosis and Related Disorders*. Elsevier B.V. doi: 10.1016/j.msard.2019.04.032.

McDonald, W. I. and Sears, T. A. (1970) 'The Effects of Experimental Demyelination on Conduction in the Central Nervous System', *Brain*, 93, pp. 585–598.

McKenzie, I. A. *et al.* (2014) 'Motor skill learning requires active central myelination', *Science*, 346(6207), pp. 318–323. doi: 10.1126/science.1254960.

McKinnon, R. D. *et al.* (1990) 'FGF modulates the PDGF-driven pathway of oligodendrocyte development', *Neuron*, 5(5), pp. 603–614. doi: 10.1016/0896-6273(90)90215-2.

McMorris, F. A. *et al.* (1986) 'Insulin-like growth factor I/somatomedin C: A potent inducer of oligodendrocyte development', *Proceedings of the National Academy of Sciences of the United States of America*, 83(3), pp. 822–826. doi: 10.1073/pnas.83.3.822.

McTigue, D. M. *et al.* (1998) 'Neurotrophin-3 and brain-derived neurotrophic factor induce oligodendrocyte proliferation and myelination of regenerating axons in the contused adult rat spinal cord', *Journal of Neuroscience*, 18(14), pp. 5354–5365. doi: 10.1523/jneurosci.18-14-05354.1998.

Meesters, G. M. H. *et al.* (1992) 'Generation of micron-sized droplets from the Taylor cone', *Journal of Aerosol Science*, 23(1), pp. 37–49. doi: 10.1016/0021-8502(92)90316-N.

Mei, F. *et al.* (2014) 'Micropillar arrays as a high-throughput screening platform for therapeutics in multiple sclerosis.', *Nature medicine*. Nature Publishing Group, 20(8), pp. 954–960. doi: 10.1038/nm.3618.

Mei, F., Lehmann-Horn, K., *et al.* (2016) 'Accelerated remyelination during inflammatory demyelination prevents axonal loss and improves functional recovery', *eLife*, 5, pp. 1–21. doi: 10.7554/eLife.18246.

Mei, F., Mayoral, X. S. R., *et al.* (2016) 'Identification of the Kappa-Opioid Receptor as a Therapeutic Target for Oligodendrocyte Remyelination', *The Journal of Neuroscience*, 36(30),

pp. 7925–7935. doi: 10.1523/JNEUROSCI.1493-16.2016.

Mensch, S. *et al.* (2015) 'Synaptic vesicle release regulates myelin sheath number of individual oligodendrocytes in vivo.', *Nature Neuroscience*, 18(5), pp. 628–30. doi: 10.1038/nn.3991.

Meyer, N. *et al.* (2018) 'Oligodendrocytes in the Mouse Corpus Callosum Maintain Axonal Function by Delivery of Glucose', *Cell Reports*, 22(9), pp. 2383–2394. doi: 10.1016/j.celrep.2018.02.022.

Mi, S. *et al.* (2005) 'LINGO-1 negatively regulates myelination by oligodendrocytes', *Nature Neuroscience*, 8(6), pp. 745–751. doi: 10.1038/nn1460.

Mi, S. *et al.* (2009) 'Promotion of Central Nervous System Remyelination by Induced Differentiation of Oligodendrocyte Precursor Cells', *Annals of Neurology*, 65, pp. 304–315. doi: 10.1002/ana.21581.

Migneco, F. *et al.* (2009) 'Poly(glycerol-dodecanoate), a biodegradable polyester for medical devices and tissue engineering scaffolds', *Biomaterials*. Elsevier Ltd, 30(33), pp. 6479–6484. doi: 10.1016/j.biomaterials.2009.08.021.

Miller, R. H. (1996) 'Oligodendrocyte origins', *Trends in Neurosciences*, 19(3), pp. 92–96. doi: 10.1016/S0166-2236(96)80036-1.

Milner, R. *et al.* (1997) 'Expression of αvβ3 and αvβ8 integrins during oligodendrocyte precursor differentiation in the presence and absence of axons', *Glia*, 21(4), pp. 350–360. doi: 10.1002/(SICI)1098-1136(199712)21:4<350::AID-GLIA2>3.0.CO;2-7.

Möbius, W., Nave, K. A. and Werner, H. B. (2016) 'Electron microscopy of myelin: Structure preservation by high-pressure freezing', *Brain Research*. Elsevier, 1641, pp. 92–100. doi: 10.1016/j.brainres.2016.02.027.

Mokry, L. E. *et al.* (2015) 'Vitamin D and Risk of Multiple Sclerosis: A Mendelian Randomization Study', *PLoS Medicine*, 12(8), p. e1001866. doi: 10.1371/journal.pmed.1001866.

Molineaux, S. M. *et al.* (1986) 'Recombination within the myelin basic protein gene created the dysmyelinating shiverer mouse mutation', *Proceedings of the National Academy of Sciences of the United States of America*, 83(19), pp. 7542–7546. doi:

10.1073/pnas.83.19.7542.

Moore, J. W. *et al.* (1978) 'Simulations of conduction in uniform myelinated fibers. Relative sensitivity to changes in nodal and internodal parameters', *Biophysical Journal*. Elsevier, 21(2), pp. 147–160. doi: 10.1016/S0006-3495(78)85515-5.

Moyon, S. *et al.* (2015) 'Demyelination Causes Adult CNS Progenitors to Revert to an Immature State and Express Immune Cues That Support Their Migration', *Journal of Neuroscience*, 35(1), pp. 4–20. doi: 10.1523/JNEUROSCI.0849-14.2015.

Mulero, P., Midaglia, L. and Montalban, X. (2018) 'Ocrelizumab: a new milestone in multiple sclerosis therapy', *Therapeutic Advances in Neurological Disorders*, 11, pp. 1–6. doi: 10.1177/https.

Müller, J. *et al.* (2009) 'The principal neurons of the medial nucleus of the trapezoid body and NG2+ glial cells receive coordinated excitatory synaptic input', *Journal of General Physiology*, 134(2), pp. 115–127. doi: 10.1085/jgp.200910194.

Munger, K. L. *et al.* (2004) 'Vitamin D intake and incidence of multiple sclerosis', *Neurology*, 62, pp. 60–65.

Murtie, J. C. *et al.* (2005) 'In vivo analysis of oligodendrocyte lineage development in postnatal FGF2 null mice', *Glia*, 49(4), pp. 542–554. doi: 10.1002/glia.20142.

Murtie, J. C., Macklin, W. B. and Corfas, G. (2007) 'Morphometric Analysis of Oligodendrocytes in the Adult Mouse Frontal Cortex', *Journal of Neuroscience Research*, 85, pp. 2080–2086. doi: 10.1002/jnr.

Nagy, B. *et al.* (2017) *Different patterns of neuronal activity trigger distinct responses of oligodendrocyte precursor cells in the corpus callosum*, *PLoS Biology*. doi: 10.1371/journal.pbio.2001993.

Nait-Oumesmar, B. *et al.* (1999) 'Progenitor cells of the adult mouse subventricular zone proliferate, migrate and differentiate into oligodendrocytes after demyelination', *European Journal of Neuroscience*, 11(12), pp. 4357–4366. doi: 10.1046/j.1460-9568.1999.00873.x.

Najm, F. J. *et al.* (2015) 'Drug-based modulation of endogenous stem cells promotes functional remyelination in vivo.', *Nature*, 522(7555), pp. 216–20. doi: 10.1038/nature14335.

Nawaz, S. *et al.* (2015) 'Actin Filament Turnover Drives Leading Edge Growth during Myelin

Sheath Formation in the Article Actin Filament Turnover Drives Leading Edge Growth during Myelin Sheath Formation in the Central Nervous System', *Developmental Cell*, 34, pp. 139–151. doi: 10.1016/j.devcel.2015.05.013.

Nicaise, A. M. *et al.* (2019) 'Cellular senescence in progenitor cells contributes to diminished remyelination potential in progressive multiple sclerosis', *Proceedings of the National Academy of Sciences*, 116(18), pp. 9030–9039. doi: 10.1073/pnas.1818348116.

Nielsen, H. H. *et al.* (2011) 'Stimulation of Adult Oligodendrogenesis by Myelin-Specific T Cells', *The American Journal of Pathology*. Elsevier Inc., 179(4), pp. 2028–2041. doi: 10.1016/j.ajpath.2011.06.006.

Nishiyama, A. *et al.* (1996) 'Interaction between NG2 proteoglycan and PDGF α-receptor on O2A progenitor cells is required for optimal response to PDGF', *Journal of Neuroscience Research*, 43(3), pp. 315–330. doi: 10.1002/(SICI)1097-4547(19960201)43:3<315::AID-JNR6>3.0.CO;2-M.

Noble, M. *et al.* (1988) 'Platelet-derived growth factor promotes division and motility and inhibits premature differentiation of the oligodendrocyte/type-2 astrocyte progenitor ceil', *Nature*, 333(6173), pp. 560–562. doi: 10.1038/333560a0.

Novak, U. and Kaye, A. H. (2000) 'Extracellular matrix and the brain: Components and function', *Journal of Clinical Neuroscience*, 7(4), pp. 280–290. doi: 10.1054/jocn.1999.0212.

Ntziachristos, V. (2010) 'Going deeper than microscopy: The optical imaging frontier in biology', *Nature Methods*. Nature Publishing Group, 7(8), pp. 603–614. doi: 10.1038/nmeth.1483.

Olesen, J. *et al.* (2012) 'The economic cost of brain disorders in Europe', *European Journal of Neurology*, 19(1), pp. 155–162. doi: 10.1111/j.1468-1331.2011.03590.x.

Olivier, C. *et al.* (2001) 'Monofocal origin of telencephalic oligodendrocytes in the anterior entopeduncular area of the chick embryo', *Development*, 128(10), pp. 1757–1769.

Ong, W. *et al.* (2018) 'Microfiber drug/gene delivery platform for study of myelination', *Acta Biomaterialia*. Acta Materialia Inc., 75, pp. 152–160. doi: 10.1016/j.actbio.2018.06.011.

Ono, K. *et al.* (1997) 'Focal ventricular origin and migration of oligodendrocyte precursors into the chick optic nerve', *Neuron*, 19(2), pp. 283–292. doi: 10.1016/S0896-6273(00)80939-

3.

Orduz, D. *et al.* (2015) 'Interneurons and oligodendrocyte progenitors form a structured synaptic network in the developing neocortex', *eLife*, 2015(4), pp. 1–53. doi: 10.7554/eLife.06953.

Ortega, M. C. *et al.* (2012) 'Neuregulin-1/ErbB4 signaling controls the migration of oligodendrocyte precursor cells during development', *Experimental Neurology*. Elsevier Inc., 235(2), pp. 610–620. doi: 10.1016/j.expneurol.2012.03.015.

Osanai, Y. *et al.* (2017) 'Rabies virus-mediated oligodendrocyte labeling reveals a single oligodendrocyte myelinates axons from distinct brain regions', *Glia*, 65(1), pp. 93–105. doi: 10.1002/glia.23076.

Ozeki, Y. *et al.* (2009) 'Analysis and experimental assessment of the sensitivity of stimulated Raman scattering microscopy', *Optics Express*, 17(5), pp. 3651–3658. doi: 10.1364/oe.17.003651.

Pajouhesh, H. and Lenz, G. R. (2005) 'Medicinal chemical properties of successful central nervous system drugs', *NeuroRx*, 2(4), pp. 541–553. doi: 10.1602/neurorx.2.4.541.

Pammolli, F., Magazzini, L. and Riccaboni, M. (2011) 'The productivity crisis in pharmaceutical R&D', *Nature Reviews Drug Discovery*. Nature Publishing Group, 10(6), pp. 428–438. doi: 10.1038/nrd3405.

Park, H. C. *et al.* (2002) 'Olig2 Is Required for Zebrafish Primary Motor Neuron and Oligodendrocyte Development', *Developmental Biology*, 248(2), pp. 356–368. doi: 10.1006/dbio.2002.0738.

Patani, R. *et al.* (2007) 'Remyelination can be extensive in multiple sclerosis despite a long disease course', *Neuropathology and Applied Neurobiology*, 33, pp. 277–287. doi: 10.1111/j.1365-2990.2007.00805.x.

Patneau, D. K. *et al.* (1994) 'Glial cells of the oligodendrocyte lineage express both kainate- and AMPA-preferring subtypes of glutamate receptor', *Neuron*, 12(2), pp. 357–371. doi: 10.1016/0896-6273(94)90277-1.

Patrikios, P. *et al.* (2006) 'Remyelination is extensive in a subset of multiple sclerosis patients', *Brain*, 129, pp. 3165–3172. doi: 10.1093/brain/awl217.

Paukert, M. and Bergles, D. (2012) 'Reduction of motion artifacts during in vivo two-photon imaging of brain through heartbeat triggered scanning', *The Journal of Physiology*, 590(13), pp.2955-2963.

Pedraza, C. E. *et al.* (2014) 'Induction of oligodendrocyte differentiation and in vitro myelination by inhibition of Rho-associated kinase', *ASN Neuro*, 6(4), pp. 1–17. doi: 10.1177/1759091414538134.

Pérez-Cerdá, F., Sánchez-Gómez, M. V. and Matute, C. (2015) 'Pío del Río Hortega and the discovery of the oligodendrocytes', *Frontiers in Neuroanatomy*, 9(July), pp. 7–12. doi: 10.3389/fnana.2015.00092.

Petersen, M. A. *et al.* (2017) 'Fibrinogen Activates BMP Signaling in Oligodendrocyte Progenitor Cells and Inhibits Remyelination after Vascular Damage', *Neuron*. Elsevier Inc., 96(5), pp. 1003-1012.e7. doi: 10.1016/j.neuron.2017.10.008.

Pfeifenbring, S. *et al.* (2015) 'Remyelination After Cuprizone-Induced Demyelination Is Accelerated in Juvenile Mice', *Journal of Neuropathology & Experimental Neurology*, 74(8), pp. 756–766.

Piaton, G. *et al.* (2011) 'Class 3 semaphorins influence oligodendrocyte precursor recruitment and remyelination in adult central nervous system', *Brain*, 134, pp. 1156–1167. doi: 10.1093/brain/awr022.

Plemel, J. R. *et al.* (2012) 'Myelin Inhibits Oligodendroglial Maturation and Regulates Oligodendrocytic Transcription Factor Expression', *Glia*, 61, pp. 1471–1487. doi: 10.1002/glia.22535.

Plemel, J. R., Liu, W. and Yong, V. W. (2017) 'Remyelination therapies: a new direction and challenge in multiple sclerosis', *Nature Reviews Drug Discovery*, 16, pp. 1–18. doi: 10.1038/nrdnrd.2017.115.

Pluchino, S. *et al.* (2005) 'Neurosphere-derived multipotent precursors promote neuroprotection by an immunomodulatory mechanism', *Nature*, 436(July), pp. 266–271. doi: 10.1038/nature03889.

Poduslo, S. E. and Norton, W. T. (1972) 'Isolation and Some Chemical Properties of Oligodendroglia From Calf Brain', *Journal of Neurochemistry*, 19(3), pp. 727–736. doi: 10.1111/j.1471-4159.1972.tb01388.x.

Pohl, H. B. F. *et al.* (2011) 'Genetically Induced Adult Oligodendrocyte Cell Death Is Associated with Poor Myelin Clearance , Reduced Remyelination , and Axonal Damage', *Journal of Neuroscience*, 31(3), pp. 1069–1080. doi: 10.1523/JNEUROSCI.5035-10.2011.

Potma, E. O. and Xie, X. S. (2004) 'CARS Microscopy for Biology and Medicine', *Optics & Photonics News*, (November).

Prineas, J. W. *et al.* (1993) 'Multiple Sclerosis : Remyelination of Nascent Lesions', *Annals of Neurology*, 33, pp. 137–151.

Prineas, J. W. *et al.* (2001) 'Immunopathology of Secondary-Progressive Multiple Sclerosis', *Annals of Neurology*, 50, pp. 646–657. doi: 10.1002/ana.1255.

Pringle, N. P. *et al.* (1992) 'PDGF receptors in the rat CNS: during late neurogenesis, PDGF alpha-receptor expression appears to be restricted to glial cells of the oligodendrocyte lineage.', *Development (Cambridge, England)*, 115(2), pp. 535–51. Available at: http://www.ncbi.nlm.nih.gov/pubmed/1425339.

Pringle, N. P. and Richardson, W. D. (1993) 'A singularity of PDGF alpha-receptor expression in the dorsoventral axis of the neural tube may define the origin of the oligodendrocyte lineage.', *Development*, 117(2), pp. 525–33. Available at: http://www.ncbi.nlm.nih.gov/pubmed/8330523.

Pugliatti, M., Sotgiu, S. and Rosati, G. (2002) 'The worldwide prevalence of multiple sclerosis', *Clinical Neurology and Neurosurgery*, 104, pp. 182–191.

Qian, X., Song, H. and Ming, G. L. (2019) 'Brain organoids: Advances, applications and challenges', *Development (Cambridge)*, 146(8). doi: 10.1242/dev.166074.

Raasakka, A. *et al.* (2017) 'Membrane Association Landscape of Myelin Basic Protein Portrays Formation of the Myelin Major Dense Line', *Scientific Reports*, 7, pp. 4974–4992. doi: 10.1038/s41598-017-05364-3.

Rachakonda, V., Pan, T. H. and Le, W. D. (2004) 'Biomarkers of neurodegenerative disorders: How good are they?', *Cell Research*, 14(5), pp. 349–358. doi: 10.1038/sj.cr.7290235.

Raff, M. C., Miller, R. H., and Noble, M. (1983) 'A glial progenitor cell that develops in vitro into an astrocyte or an oligodendrocyte depending on culture medium', *Nature*, 303(5916), pp. 390–396. Available at: https://www.nature.com/articles/303390a0.pdf.

Raff, M. C. *et al.* (1988) 'Platelet-derived growth factor from astrocytes drives the clock that times oligodendrocyte development in culture', *Nature*, 333(6173), pp. 562–565. doi: 10.1038/333562a0.

Raman, C. V (1928) 'A new radiation', *Indian Journal of Physics*, 2, pp. 387–398. doi: 10.1016/s0016-0032(28)91546-x.

Rankin, K. A. *et al.* (2019) 'Selective Estrogen Receptor Modulators Enhance CNS Remyelination Independent of Estrogen Receptors', *Journal of Neuroscience*, 39(12), pp. 2184–2194.

Ransohoff, R. M. (2012) 'Animal models of multiple sclerosis: The good, the bad and the bottom line', *Nature Neuroscience*. Nature Publishing Group, 15(8), pp. 1074–1077. doi: 10.1038/nn.3168.

Ravid, R. (2008) 'Standard operating procedures, ethical and legal regulations in BTB (Brain/Tissue/Bio) banking: What is still missing?', *Cell and Tissue Banking*, 9(2), pp. 121–137. doi: 10.1007/s10561-007-9055-y.

Readhead, C. and Hood, L. (1990) 'The dysmyelinating mouse mutations shiverer (shi) and myelin deficient (shimld)', *Behavior Genetics*, 20(2), pp. 213–234. doi: 10.1007/BF01067791.

Redmond, S. A. *et al.* (2016) 'Somatodendritic Expression of JAM2 Inhibits Oligodendrocyte Myelination', *Neuron*. Elsevier Inc., 91(4), pp. 824–836. doi: 10.1016/j.neuron.2016.07.021.

Reed, G. F., Lynn, F. and Meade, B. D. (2002) 'Use of Coefficient of Variation in Assessing Variability of Quantitative Assays', *Clinical and Diagnostic Laboratory Immunology*, 9(6), pp. 1235–1239. doi: 10.1128/CDLI.9.6.1235.

Reich, D. S., Lucchinetti, C. F. and Calabresi, P. A. (2018a) 'Multiple Sclerosis', *New England Journal of Medicine*, 378(2), pp. 169–180. doi: 10.1056/NEJMra1401483.

Reich, D. S., Lucchinetti, C. F. and Calabresi, P. A. (2018b) 'Multiple Sclerosis', *The New England Journal of Medicine*, 378, pp. 169–180. doi: 10.1056/NEJMra1401483.

Richardson, W. D. *et al.* (1988) 'A role for platelet-derived growth factor in normal gliogenesis in the central nervous system', *Cell*, 53(2), pp. 309–319. doi: 10.1016/0092-8674(88)90392-3.

Risacher, S. L. and Saykin, A. J. (2013) 'Neuroimaging biomarkers of neurodegenerative

diseases and dementia', *Seminars in Neurology*, 33(4), pp. 386–416. doi: 10.1055/s-0033-1359312.

Rivers, L. E. *et al.* (2008) 'PDGFRA/NG2 glia generate myelinating oligodendrocytes and piriform projection neurons in adult mice', *Nature Neuroscience*, 11(12), pp. 1392–1401. doi: 10.1038/nn.2220.

Robinson, S. *et al.* (1998) 'The chemokine growth-regulated oncogene-α promotes spinal cord oligodendrocyte precursor proliferation', *Journal of Neuroscience*, 18(24), pp. 10457–10463. doi: 10.1523/jneurosci.18-24-10457.1998.

Robinson, S. and Miller, R. H. (1999) 'Contact with Central Nervous System Myelin Inhibits Oligodendrocyte Progenitor Maturation', *Developmental Biology*, 216, pp. 359–368.

Rodrigues, G. M. C. *et al.* (2017) 'Defined and Scalable Differentiation of Human Oligodendrocyte Precursors from Pluripotent Stem Cells in a 3D Culture System', *Stem Cell Reports*, 8(6), pp. 1770–1783. doi: 10.1016/j.stemcr.2017.04.027.

Rosenberg, S. S. *et al.* (2008) 'The geometric and spatial constraints of the microenvironment induce oligodendrocyte differentiation', *Proceedings of the National Academy of Sciences*, 105(38), pp. 14662–14667.

Rosenberg, S. S., Powell, B. L. and Chan, J. R. (2007) 'Receiving mixed signals: Uncoupling oligodendrocyte differentiation and myelination', *Cellular and Molecular Life Sciences*, 64(23), pp. 3059–3068. doi: 10.1007/s00018-007-7265-x.

Rostron, P., Gaber, S. and Gaber, D. (2016) 'Raman Spectroscopy, Review', *Internation Journal of Engineering and Technical Research (IJETR)*, 6(1), pp. 50–64.

Ruckh, J. M. *et al.* (2011) 'Rejuvenation of Regeneration in the Aging Central Nervous System', *Cell Stem CellStem Cell*. Elsevier Inc., 10, pp. 96–103. doi: 10.1016/j.stem.2011.11.019.

Rushton, W. A. H. (1951) 'A theory of the effects of fibre size in medullated nerve', *Journal of Physiology*, 115, pp. 101–122.

Sakry, D. *et al.* (2014) 'Oligodendrocyte Precursor Cells Modulate the Neuronal Network by Activity-Dependent Ectodomain Cleavage of Glial NG2', *PLoS Biology*, 12(11). doi: 10.1371/journal.pbio.1001993.

Sánchez, M. M. *et al.* (1998) 'Differential rearing affects corpus callosum size and cognitive

function of rhesus monkeys', *Brain Research*, 812(1–2), pp. 38–49. doi: 10.1016/S0006-8993(98)00857-9.

Scannell, J. W. *et al.* (2012) 'Diagnosing the decline in pharmaceutical R&D efficiency', *Nature Reviews Drug Discovery*. Nature Publishing Group, 11(March), pp. 191–200. Available at: http://dx.doi.org/10.1038/nrd3681.

Scannell, J. W. and Bosley, J. (2016) 'When quality beats quantity: Decision theory, drug discovery, and the reproducibility crisis', *PLoS ONE*, 11(2), pp. 1–21. doi: 10.1371/journal.pone.0147215.

Schachner, M. and Sommer, I. (1981) 'Monoclonal Antibodies (01 to 04) to Oligodendrocyte Cell Surfaces : An lmmunocytological Study in the Central Nervous System', *Developmental biology*, 83, pp. 311–327.

Schain, A. J., Hill, R. A. and Grutzendler, J. (2014) 'Label-free in vivo imaging of myelinated axons in health and disease with spectral confocal reflectance microscopy', *Nature Medicine*. Nature Publishing Group, 20(4), pp. 443–449. doi: 10.1038/nm.3495.

Schindelin, J. *et al.* (2012) 'Fiji: An open-source platform for biological-image analysis', *Nature Methods*, 9(7), pp. 676–682. doi: 10.1038/nmeth.2019.

Schmued, L. C. (1990) 'A rapid, sensitive histochemical stain for myelin in frozen brain sections', *Journal of Histochemistry and Cytochemistry*, 38(5), pp. 717–720. doi: 10.1177/38.5.1692056.

Scholz, J. *et al.* (2009) 'Training induces changes in white-matter architecture', *Nature Neuroscience*, 12(11), pp. 1370–1371. doi: 10.1038/nn.2412.

Scholtz, C. L. (1977) 'Quantitative histochemistry of myelin using Luxol Fast Blue MBS', *The Histochemical Journal*, 9(6), pp. 759–765. doi: 10.1007/BF01003070.

Shi, M., Caudle, W. M. and Zhang, J. (2009) 'Biomarker discovery in neurodegenerative diseases: A proteomic approach', *Neurobiology of Disease*. Elsevier B.V., 35(2), pp. 157–164. doi: 10.1016/j.nbd.2008.09.004.

Seeds, N. W. (1971) 'Biochemical differentiation in reaggregating brain cell culture.', *Proceedings of the National Academy of Sciences of the United States of America*, 68(8), pp. 1858–1861. doi: 10.1073/pnas.68.8.1858.

Seidl, A. H., Rubel, E. W. and Barria, A. (2014) 'Differential Conduction Velocity Regulation in Ipsilateral and Contralateral Collaterals Innervating Brainstem Coincidence Detector Neurons', *Journal of Neuroscience*, 34(14), pp. 4914–4919. doi: 10.1523/jneurosci.5460-13.2014.

Seidl, A. H., Rubel, E. W. and Harris, D. M. (2010) 'Mechanisms for Adjusting Interaural Time Differences to Achieve Binaural Coincidence Detection', *Journal of Neuroscience*, 30(1), pp. 70–80. doi: 10.1523/jneurosci.3464-09.2010.

Semwogerere, D. and Weeks, E. R. (2005) 'Confocal Microscopy', *Encyclopedia of Biomaterial and Biomedical Engineering*, p. 97. doi: 10.1081/E-EBBE-120024153.

Shen, S., Li, J. and Casaccia-Bonnefil, P. (2005) 'Histone modifications affect timing of oligodendrocyte progenitor differentiation in the developing rat brain', *Journal of Cell Biology*, 169(4), pp. 577–589. doi: 10.1083/jcb.200412101.

Shi, Y. *et al.* (2011) 'Longitudinal in vivo coherent anti-Stokes Raman scattering imaging of demyelination and remyelination in injured spinal cord', *Journal of Biomedical Optics*, 16(10), p. 106012. doi: 10.1117/1.3641988.

Shi, L., *et al.* (2018) 'Optical Imaging of Metabolic Dynamics in Animals', *Nature Communication*, 9, pp. 2995. doi: 10.1038/s41467-018-05401-3.

Shields, S. A. *et al.* (1999) 'Remyelination Occurs as Extensively But More Slowly in Old Rats Compared to Young Rats Following Gliotoxin-Induced CNS Demyelination', *Glia*, 28, pp. 77–83.

Siebert, J. R. and Osterhout, D. J. (2011) 'The inhibitory effects of chondroitin sulfate proteoglycans on oligodendrocytes', *Journal of Neurochemistry*, 119, pp. 176–188. doi: 10.1111/j.1471-4159.2011.07370.x.

Sim, F. J. *et al.* (2002) 'The age-related decrease in CNS remyelination efficiency is caused by an impairment of both oligodendrocyte progenitor recruitment and differentiation', *The Journal of Neuroscience*, 22(7), pp. 2451–2459. doi: 10.1046/j.1365-2990.2002.39286_16.x.

Singh, R. (2002) 'C. V. Raman and the Discovery of the Raman Effect', *Physics in Perspective*, 4(4), pp. 399–420. doi: 10.1007/s000160200002.

Skripuletz, T. *et al.* (2013) 'Astrocytes regulate myelin clearance through recruitment of

microglia during cuprizone-induced demyelination', *Brain*, 136, pp. 147–167. doi: 10.1093/brain/aws262.

Sloka, J. and Stefanelli, M. (2005) 'The mechanism of action of methylprednisolone in the treatment of multiple sclerosis', *Multiple Sclerosis*, 11, pp. 425–432.

Smith, K. J., Blakemore, W. F. and McDonald, W. I. (1979) 'Central remyelination restores secure conduction', *Nature*, 280(August), pp. 395–396.

Smith, R. and Koles, Z. (1970) 'Myelinated nerve fibers: computed effect of myelin thickness on conduction velocity', *American Journal of Physiology*, 219(5), pp. 1256–1258. doi: 10.1152/ajplegacy.1970.219.5.1256.

Snaidero, N., Möbius, W., Czopka, T., Hekking, Liesbeth H.P., *et al.* (2014) 'Myelin membrane wrapping of CNS axons by PI(3,4,5)P3-dependent polarized growth at the inner tongue', *Cell*, 156(1–2), pp. 277–290. doi: 10.1016/j.cell.2013.11.044.

Snaidero, N., Möbius, W., Czopka, T., Hekking, Liesbeth H.P., *et al.* (2014) 'Myelin Membrane Wrapping of CNS Axons by PI(3,4,5)P3-Dependent Polarized Growth at the Inner Tongue', *Cell*, 156(1–2), pp. 277–290. doi: 10.1016/j.cell.2013.11.044.

Sobel, R. A. *et al.* (1994) 'Immunolocalization of proteolipid protein peptide 103–116 in myelin', *Journal of Neuroscience Research*, 37(1), pp. 36–43. doi: 10.1002/jnr.490370106.

Sobel, R. A. and Ahmed, A. S. (2001) 'White matter extracellular matrix chondroitin sulfate/dermatan sulfate proteoglycans in multiple sclerosis', *Journal of Neuropathology and Experimental Neurology*, 60(12), pp. 1198–1207. doi: 10.1093/jnen/60.12.1198.

Sobottka, B. *et al.* (2011) 'CNS live imaging reveals a new mechanism of myelination: The liquid croissant model', *Glia*, 59(12), pp. 1841–1849. doi: 10.1002/glia.21228.

Sommer, I. and Schachner, M., 1981. Monoclonal antibodies (O1 to O4) to oligodendrocyte cell surfaces: An immunocytological study in the central nervous system. *Developmental Biology*, 83(2), pp.311-327.

Sorensen, A. *et al.* (2008) 'Astrocytes, but not olfactory ensheathing cells or Schwann cells, promote myelination of CNS axons in vitro', *Glia*, 56(7), pp. 750–763. doi: 10.1002/glia.20650.

Spassky, N. *et al.* (2002) 'Directional guidance of oligodendroglial migration by class 3 semaphorins and netrin-1', *Journal of Neuroscience*, 22(14), pp. 5992–6004. doi:

10.1523/jneurosci.22-14-05992.2002.

Spedden, E. and Staii, C. (2013) 'Neuron biomechanics probed by atomic force microscopy', *International Journal of Molecular Sciences*, 14(8), pp. 16124–16140. doi: 10.3390/ijms140816124.

Sperber, B. R. *et al.* (2001) 'A Unique Role for Fyn in CNS Myelination', *The Journal of Neuroscience*, 21(6), pp. 2039–2047. doi: 10.1523/jneurosci.21-06-02039.2001.

Spitzer, S. O. *et al.* (2019) 'Oligodendrocyte Progenitor Cells Become Regionally Diverse and Heterogeneous with Age', *Neuron*, 0(0), pp. 1–13. doi: 10.1016/J.NEURON.2018.12.020.

Srinivas, N., Maffuid, K. and Kashuba, A. D. M. (2018) 'Clinical Pharmacokinetics and Pharmacodynamics of Drugs in the Central Nervous System', *Clinical Pharmacokinetics*. Springer International Publishing, 57(9), pp. 1059–1074. doi: 10.1007/s40262-018-0632-y.

St Croix, C. M., Shand, S. H. and Watkins, S. C. (2005) 'Confocal microscopy: comparisons, applications, and problems.', *BioTechniques*, 39(6 Suppl). doi: 10.2144/000112089.

Stahn, C. *et al.* (2007) 'Molecular mechanisms of glucocorticoid action and selective glucocorticoid receptor agonists', *Molecular and Cellular Endocrinology*, 275, pp. 71–78. doi: 10.1016/j.mce.2007.05.019.

Stallcup, W. and Beasley, L. (1987) 'Bipotential glial precursor cells of the optic nerve express the NG2 proteoglycan', *The Journal of Neuroscience*, 7(9), pp. 2737–2744. doi: 10.1523/jneurosci.07-09-02737.1987.

Stefano, N. De *et al.* (1998) 'Axonal damage correlates with disability in patients with relapsing – remitting multiple sclerosis Results of a longitudinal magnetic resonance spectroscopy study', *Brain*, 121, pp. 1469–1477.

Steinhäser, C., Jabs, R. and Kettenmann, H. (1994) 'Properties of GABA and glutamate responses in identified glial cells of the mouse hippocampal slice', *Hippocampus*, 4(1), pp. 19–35. doi: 10.1002/hipo.450040105.

Sternberger, N. H. *et al.* (1978) 'Myelin Basic Protein Demonstrated Immunocytochemically in Oligodendroglia Prior to Myelin Sheath Formation Source : Proceedings of the National Academy of Sciences of the United States of America , Published by : National Academy of Sciences Stable URL ':, *Proceedings of the National Academy of Sciences*, 75(5), pp. 2521–

2524.

Sternberger, N. H. *et al.* (1979) 'Myelin-associated glycoprotein demonstrated immunocytochemically in myelin and myelin-forming cells of developing rat.', *Proceedings of the National Academy of Sciences*, 76(3), pp. 1510–1514. doi: 10.1073/pnas.76.3.1510.

Stevens, B. *et al.* (2002) 'Adenosine: A neuron-glial transmitter promoting myelination in the CNS in response to action potentials', *Neuron*, 36(5), pp. 855–868. doi: 10.1016/S0896-6273(02)01067-X.

Sun, T. *et al.* (1998) 'Pax6 influences the time and site of origin of glial precursors in the ventral neural tube', *Molecular and Cellular Neurosciences*, 12(4–5), pp. 228–239. doi: 10.1006/mcne.1998.0711.

Sun, L. O. *et al.* (2018) 'Spatiotemporal Control of CNS Myelination by Oligodendrocyte Programmed Cell Death through the TFEB-PUMA Axis', *Cell*. Elsevier Inc., 175(7), pp. 1811-1826.e21. doi: 10.1016/j.cell.2018.10.044.

Susuki, K. *et al.* (2013) 'Three mechanisms assemble central nervous system nodes of ranvier', *Neuron*, 78(3), pp. 469–482. doi: 10.1016/j.neuron.2013.03.005.

Svenningsen, Å. F. *et al.* (2003) 'Rapid method for culturing embryonic neuron-glial cell cocultures', *Journal of Neuroscience Research*, 72(5), pp. 565–573. doi: 10.1002/jnr.10610.

Sydor, A. M. *et al.* (2015) 'Super-Resolution Microscopy: From Single Molecules to Supramolecular Assemblies', *Trends in Cell Biology*. Elsevier Ltd, 25(12), pp. 730–748. doi: 10.1016/j.tcb.2015.10.004.

Syed, Y. A. *et al.* (2011) 'Inhibition of CNS Remyelination by the Presence of Semaphorin 3A', *Neurobiology of Disease*, 31(10), pp. 3719–3728. doi: 10.1523/JNEUROSCI.4930-10.2011.

Swire, M. and ffrench-Constant, C. (2019) 'Oligodendrocyte–neuron myelinating coculture', *Methods in Molecular Biology*, 1936, pp. 111–128. doi: 10.1007/978-1-4939-9072-6_7.

Swire, M. *et al.* (2019) 'Endothelin signalling mediates experience-dependent myelination in the CNS', *eLife*, 8, pp. 1–23. doi: 10.7554/eLife.49493.

Takebayashi, H. *et al.* (2002) 'The basic helix-loop-helix factor Olig2 is essential for the development of motoneuron and oligodendrocyte lineages', *Current Biology*, 12(13), pp. 1157–1163. doi: 10.1016/S0960-9822(02)00926-0.

Tang, D. G., Tokumoto, Y. M. and Raff, M. C. (2000) 'Long-term culture of purified postnatal oligodendrocyte precursor cells: Evidence for an intrinsic maturation program that plays out over months', *Journal of Cell Biology*, 148(5), pp. 971–984. doi: 10.1083/jcb.148.5.971.

Tarnowski, C. P. and Morris, M. D. (2001) 'Raman Spectroscopy and Microscopy', *Encyclopedia of Materials - Science and Technology*, pp. 7976–7983.

Taveggia, C. *et al.* (2008) 'Type III Neuregulin-1 promotes oligodendrocyte myelination', *Sixth Report on the World Nutrition Situation Geneva UNSCN DC AICR 4*, 56, pp. 284–293. doi: 10.1002/glia.

Tekki-Kessaris, N. *et al.* (2001) 'Hedgehog-dependent oligodendrocyte lineage specification in the telencephalon', *Development*, 128(13), pp. 2545–2554.

Temple, S. and Raff, M. C. (1985) 'Differentiation of a bipotential glial progenitor cell in single cell microculture', *Nature*, 313(5999), pp. 223–225. doi: 10.1038/313223a0.

Temple, S. and Raff, M. C. (1986) 'Clonal analysis of oligodendrocyte development in culture: Evidence for a developmental clock that counts cell divisions', *Cell*, 44(5), pp. 773–779. doi: 10.1016/0092-8674(86)90843-3.

Thomson, J. F. (1960) 'Physiological Effects of D2O in Mammals', *Annals of the New York Academy of Sciences*, 84(16), pp. 736–744. doi: 10.1111/j.1749-6632.1960.tb39105.x.

Thompson, R. E., Larson, D. R. and Webb, W. W. (2002) 'Precise Nanometer Localisation Analysis for Individual Fluorescent Probes', *Biophysical Journal*, 82(May), pp. 2775–2783. doi: 10.1016/S0006-3495(02)75618-X.

Timsit, S. *et al.* (1995) 'Oligodendrocytes originate in a restricted zone of the embryonic ventral neural tube defined by DM-20 mRNA expression', *Journal of Neuroscience*, 15(2), pp. 1012–1024. doi: 10.1523/jneurosci.15-02-01012.1995.

Tipping, W. J. *et al.* (2016) 'Stimulated Raman scattering microscopy: An emerging tool for drug discovery', *Chemical Society Reviews*. Royal Society of Chemistry, 45(8), pp. 2075–2089. doi: 10.1039/c5cs00693g.

Tipping, W. J. *et al.* (2017) 'Imaging drug uptake by bioorthogonal stimulated Raman scattering microscopy', *Chemical Science*. Royal Society of Chemistry, 8(8), pp. 5606–5615. doi: 10.1039/c7sc01837a.

Tomassy, G. S. *et al.* (2014) 'Distinct Profiles of Myelin Distribution Along Single Axons of Pyramidal Neurons in the Neocortex', *Science*, 344(6181), pp. 319–324. doi: 10.1126/science.1249766.

Traka, M. *et al.* (2015) 'Oligodendrocyte death results in immune-mediated CNS demyelination', *Nature Neuroscience*, 19(1), pp. 65–74. doi: 10.1038/nn.4193.

Trapa, P. E. *et al.* (2019) 'In vitro–in vivo extrapolation of key transporter activity at the blood–brain barrier *S*', *Drug Metabolism and Disposition*, 47(4), pp. 405–411. doi: 10.1124/dmd.118.083279.

Trapp, B. D. *et al.* (1997) 'Differentiation and Death of Premyelinating Oligodendrocytes in Developing Rodent Brain', *Journal of Cell Biology*, 137(2), pp. 459–468.

Trapp, B. D. *et al.* (1998) 'Axonal Transection in the Lesions of Multiple Sclerosis', *New England Journal of Medicine*, 338(5), pp. 278–285. doi: 10.1056/nejm199801293380502.

Tripathi, R. B. *et al.* (2010) 'NG2 Glia Generate New Oligodendrocytes But Few Astrocytes in a Murine Experimental Autoimmune Encephalomyelitis Model of Demyelinating Disease', *Journal of Neuroscience*, 30(48), pp. 16383–16390. doi: 10.1523/JNEUROSCI.3411-10.2010.

Tripathi, R. B. *et al.* (2011) 'Dorsally and ventrally derived oligodendrocytes have similar electrical properties but myelinate preferred tracts', *Journal of Neuroscience*, 31(18), pp. 6809–6819. doi: 10.1523/JNEUROSCI.6474-10.2011.

Tsai, H. H. *et al.* (2016) 'Oligodendrocyte precursors migrate along vasculature in the developing nervous system', *Science*, 351(6271), pp. 379–384. doi: 10.1126/science.aad3839.

Uchida, N. *et al.* (2012) 'Human neural stem cells induce functional myelination in mice with severe dysmyelination (Science Translational Medicine (2012) 4, (165er7))', *Science Translational Medicine*, 4(165). doi: 10.1126/scitranslmed.3005469.

Van Heyningen, P., Calver, A. R. and Richardson, W. D. (2001) 'Control of progenitor cell number by mitogen supply and demand', *Current Biology*, 11(4), pp. 232–241. doi: 10.1016/S0960-9822(01)00075-6.

Van Horssen, J. *et al.* (2006) 'Extensive extracellular matrix depositions in active multiple sclerosis lesions', *Neurobiology of Disease*, 24(3), pp. 484–491. doi: 10.1016/j.nbd.2006.08.005.

Van Horssen, J., Dijkstra, C. D. and De Vries, H. E. (2007) 'The extracellular matrix in multiple sclerosis pathology', *Journal of Neurochemistry*, 103(4), pp. 1293–1301. doi: 10.1111/j.1471-4159.2007.04897.x.

Vartanian, T., Fischbach, G. and Miller, R. (1999) 'Failure of spinal cord oligodendrocyte development in mice lacking neuregulin', *Proceedings of the National Academy of Sciences of the United States of America*, 96(2), pp. 731–735. doi: 10.1073/pnas.96.2.731.

Velez-Fort, M. *et al.* (2010) 'Postnatal Switch from Synaptic to Extrasynaptic Transmission between Interneurons and NG2 Cells', *Journal of Neuroscience*, 30(20), pp. 6921–6929. doi: 10.1523/jneurosci.0238-10.2010.

Vereyken, E. J. F. *et al.* (2009) 'An in vitro model for de- and remyelination using lysophosphatidyl choline in rodent whole brain spheroid cultures', *Glia*, 57(12), pp. 1326–1340. doi: 10.1002/glia.20852.

Viehover, A. *et al.* (2001) 'Neuregulin: An oligodendrocyte growth factor absent in active multiple sclerosis lesions', *Developmental Neuroscience*, 23(4–5), pp. 377–386. doi: 10.1159/000048721.

Viganò, F. *et al.* (2013) 'Transplantation reveals regional differences in oligodendrocyte differentiation in the adult brain', *Nature Neuroscience*. Nature Publishing Group, 16(10), pp. 1370–1372. doi: 10.1038/nn.3503.

Vinet, J. *et al.* (2010) 'Subclasses of oligodendrocytes populate the mouse hippocampus', *European Journal of Neuroscience*, 31(3), pp. 425–438. doi: 10.1111/j.1460-9568.2010.07082.x.

Vondran, M. W. *et al.* (2010) 'BDNF +/- mice exhibit deficits in oligodendrocyte lineage cells of the basal forebrain', *Glia*, 58(7), pp. 848–856. doi: 10.1002/glia.20969.

Wahlsten, D. (1984) 'Growth of the Mouse Corpus Callosum', *Developmental Brain Research*, 15, pp. 59–67.

Wake, H. *et al.* (2015) 'Nonsynaptic junctions on myelinating glia promote preferential myelination of electrically active axons.', *Nature communications*, 6, p. 7844. doi: 10.1038/ncomms8844.

Wake, H., Lee, P. R. and Fields, R. D. (2011) 'Control of local protein synthesis and initial

events in myelination by action potentials', *Science*, 333(September), pp. 1647–1652.

Wang, C., Rougon, G. and Kiss, J. Z. (1994) 'Requirement of polysialic acid for the migration of the O-2A glial progenitor cell from neurohypophyseal explants', *Journal of Neuroscience*, 14(7), pp. 4446–4457. doi: 10.1523/jneurosci.14-07-04446.1994.

Wang, H. *et al.* (2005) 'Coherent Anti-Stokes Raman Scattering Imaging of Axonal Myelin in Live Spinal Tissues', *Biophysical Journal*. Elsevier, 89(1), pp. 581–591. doi: 10.1529/biophysj.105.061911.

Wang, S. *et al.* (1998) 'Notch receptor activation inhibits oligodendrocyte differentiation', *Neuron*, 21(1), pp. 63–75. doi: 10.1016/S0896-6273(00)80515-2.

Waring, M. J. *et al.* (2015) 'An analysis of the attrition of drug candidates from four major pharmaceutical companies', *Nature Reviews Drug Discovery*. Nature Publishing Group, 14(7), pp. 475–486. doi: 10.1038/nrd4609.

Watkins, T. A. *et al.* (2008) 'Distinct Stages of Myelination Regulated by γ-Secretase and Astrocytes in a Rapidly Myelinating CNS Coculture System', *Neuron*. Elsevier Inc., 60(4), pp. 555–569. doi: 10.1016/j.neuron.2008.09.011.

Waxman, S. G. (1977) 'Conduction in Myelinated, Unmyelinated, and Demyelinated Fibers', *Archives of Neurology*, 34, pp. 585–589.

Webb, A. *et al.* (1995) 'Guidance of oligodendrocytes and their progenitors by substratum topography', *Journal of Cell Science*, 108(8), pp. 2747–2760.

Wegner, M. (2008) 'A matter of identity: Transcriptional control in oligodendrocytes', *Journal of Molecular Neuroscience*, 35(1), pp. 3–12. doi: 10.1007/s12031-007-9008-8.

Weil, M.-T. *et al.* (2019) *Transmission Electron Microscopy of Oligodendrocytes and Myelin*.

Weinshenker, B. G. *et al.* (1989) 'The natural history of multiple sclerosis: A Geographically based study. I. Clinical Course and Disability', *Brain*, 112, pp. 133–146.

Westphal, V. *et al.* (2008) 'Video-rate far-field optical nanoscopy dissects synaptic vesicle movement', *Science*, 320(5873), pp. 246–249. doi: 10.1126/science.1154228.

Wilson, H. C., Onischke, C. and Raine, C. S. (2003) 'Human Oligodendrocyte Precursor Cells In Vitro: Phenotypic Analysis and Differential Response to Growth Factors', *Glia*, 44(2), pp. 153–

165. doi: 10.1002/glia.10280.

Wolswijk, G. (1998) 'Chronic Stage Multiple Sclerosis Lesions Contain a Relatively Quiescent Population of Oligodendrocyte Precursor Cells', *Journal of Neuroscience*, 18(2), pp. 601–609.

Wolswijk, G. (2000) 'Oligodendrocyte survival, loss and birth in lesions of chronic-stage multiple sclerosis', *Brain*, 123, pp. 105–115. doi: 10.1093/brain/123.1.105.

Wong, A. W. *et al.* (2013) 'Oligodendroglial Expression of TrkB Independently Regulates Myelination and Progenitor Cell Proliferation', *Journal of Neuroscience*, 33(11), pp. 4947–4957. doi: 10.1523/JNEUROSCI.3990-12.2013.

Wood, P., Okada, E. and Bunge, R. (1980) 'The use of networks of dissociated rat dorsal root ganglion neurons to induce myelination by oligodendrocytes in culture', *Brain Research*, 196(1), pp. 247–252. doi: 10.1016/0006-8993(80)90732-5.

Wu, L. M. N. *et al.* (2012) 'Increasing internodal distance in myelinated nerves accelerates nerve conduction to a flat maximum', *Current Biology*. Elsevier Ltd, 22(20), pp. 1957–1961. doi: 10.1016/j.cub.2012.08.025.

Wyllie, D. J. A. *et al.* (1991) 'Activation of glutamate receptors and glutamate uptake in identified macroglial cells in rat cerebellar cultures', *Journal of Physiology*, 433, pp. 235–258.

Xiao, L. *et al.* (2016) 'Rapid production of new oligodendrocytes is required in the earliest stages of motor-skill learning', *Nature Neuroscience*, 19(9). doi: 10.1038/nn.4351.

Yang, J. *et al.* (2017) 'EGF enhances oligodendrogenesis from glial progenitor cells', *Frontiers in Molecular Neuroscience*, 10(April), pp. 1–10. doi: 10.3389/fnmol.2017.00106.

Ye, F. *et al.* (2009) 'HDAC1 and HDAC2 regulate oligodendrocyte differentiation by disrupting the B-catenin-TCF interaction', *Nature Neuroscience*. Nature Publishing Group, 12(7), pp. 829–838. doi: 10.1038/nn.2333.

Yuan, X. *et al.* (1998) 'A role for glutamate and its receptors in the regulation of oligodendrocyte development in cerebellar tissue slices', *Development*, 125(15), pp. 2901–2914.

Yuen, T. J. *et al.* (2013) 'Identification of endothelin 2 as an inflammatory factor that promotes central nervous system remyelination', *Brain*, 136(4), pp. 1035–1047. doi: 10.1093/brain/awt024.

Yeung, M. S. Y. *et al.* (2014) 'Dynamics of oligodendrocyte generation and myelination in the human brain', *Cell*, 159(4), pp. 766–774. doi: 10.1016/j.cell.2014.10.011.

Yeung, Maggie S.Y. *et al.* (2019) 'Dynamics of oligodendrocyte generation in multiple sclerosis', *Nature*. Springer US, 566(7745), pp. 538–542. doi: 10.1038/s41586-018-0842-3.

Yin, X. *et al.* (1997) 'CNP Overexpression Induces Aberrant Oligodendrocyte Membranes and Inhibits MBP Accumulation and Myelin Compaction', *Journal of Neuroscience Research*, 50, pp. 238–247.

Young, K. M. *et al.* (2013a) 'Oligodendrocyte dynamics in the healthy adult CNS: Evidence for myelin remodeling', *Neuron*. Elsevier Inc., 77(5), pp. 873–885. doi: 10.1016/j.neuron.2013.01.006.

Young, K. M. *et al.* (2013b) 'Oligodendrocyte dynamics in the healthy adult CNS: Evidence for myelin remodeling', *Neuron*. Elsevier Inc., 77(5), pp. 873–885. doi: 10.1016/j.neuron.2013.01.006.

Yuan, X. *et al.* (1998) 'A role for glutamate and its receptors in the regulation of oligodendrocyte development in cerebellar tissue slices.', *Development (Cambridge, England)*, 125(15), pp. 2901–14. Available at: http://www.ncbi.nlm.nih.gov/pubmed/9655812.

Yuen, T. J. *et al.* (2013) 'Identification of endothelin 2 as an inflammatory factor that promotes central nervous system remyelination', *Brain*, 136(4), pp. 1035–1047. doi: 10.1093/brain/awt024.

Zawadzka, M. *et al.* (2008) 'CNS-Resident Glial Progenitor / Stem Cells Produce Schwann Cells as well as Oligodendrocytes during Repair of CNS Demyelination', *Cell*, 6, pp. 578–590. doi: 10.1016/j.stem.2010.04.002.

Zhang, D. *et al.* (2013) 'Spectrally modulated stimulated Raman scattering imaging with an angle-to-wavelength pulse shaper', *Optics Express*, 21(11), pp. 13864–13874. doi: 10.1364/oe.21.013864.

Zhang, H. *et al.* (2004) 'A role for the polysialic acid - Neural cell adhesion molecule in PDGF-induced chemotaxis of oligodendrocyte precursor cells', *Journal of Cell Science*, 117(1), pp. 93–103. doi: 10.1242/jcs.00827.

Zhang, J. H., Chung, T. D. Y. and Oldenburg, K. R. (1999) 'A simple statistical parameter for use in evaluation and validation of high throughput screening assays', *Journal of Biomolecular Screening*, 4(2), pp. 67–73.

Zhang, Y. *et al.* (2007) 'Biometric and bioactive nanofibrous scaffolds from electrospun composite nanofibers', *International Journal of Nanomedicine*, 2(4), pp. 623–638. Available at: papers2://publication/uuid/1FF8AE9E-49BB-4350-AC6E-EB1A1F98D995.

Zheng, W., Thorne, N. and McKew, J. C. (2013) 'Phenotypic screens as a renewed approach for drug discovery', *Drug Discovery Today*. Elsevier Ltd, 18(21–22), pp. 1067–1073. doi: 10.1016/j.drudis.2013.07.001.

Zhou, Q. and Anderson, D. J. (2002) 'The bHLH transcription factors OLIG2 and OLIG1 couple neuronal and glial subtype specification', *Cell*, 109(1), pp. 61–73. doi: 10.1016/S0092-8674(02)00677-3.

Zhou, Q., Choi, G. and Anderson, D. J. (2001) 'The bHLH Transcription Factor Olig2 Promotes Oligodendrocyte Differentiation in Collaboration with Nkx2.2', *Neuron*, 31, pp. 791–807.

Zhu, H. and Barker, P. (2010) 'MR Spectroscopy and Spectroscopic Imaging of the Brain', *Methods in Molecular Biology*, pp.203-226.

Zonouzi, M. *et al.* (2011) 'Bidirectional plasticity of calcium-permeable AMPA receptors in oligodendrocyte lineage cells', *Nature Neuroscience*. Nature Publishing Group, 14(11), pp. 1430–1438. doi: 10.1038/nn.2942.

Zonouzi, M. *et al.* (2015) 'GABAergic regulation of cerebellar NG2 cell development is altered in perinatal white matter injury', *Nature Neuroscience*, 18(5), pp. 674–682. doi: 10.1038/nn.3990.

Zrzavy, T. *et al.* (2017) 'Loss of " homeostatic " microglia and patterns of their activation in active multiple sclerosis', *Brain*, 140, pp. 1900–1913. doi: 10.1093/brain/awx113.

Zuchero, J. B. *et al.* (2015) 'CNS Myelin Wrapping Is Driven by Actin Disassembly', *Developmental Cell*. Elsevier, 34(2), pp. 152–167. doi: 10.1016/j.devcel.2015.06.011.

Zumbusch, A., Holtom, G. R. and Xie, X. S. (1999) 'Three-dimensional vibrational imaging by coherent anti-stokes raman scattering', *Physical Review Letters*, 82(20), pp. 4142–4145. doi: 10.1103/PhysRevLett.82.4142.

SUPPLEMENTARY

Supplementary Data 2.1: Columbus 96-well Flat Culture Analysis Pipeline Example

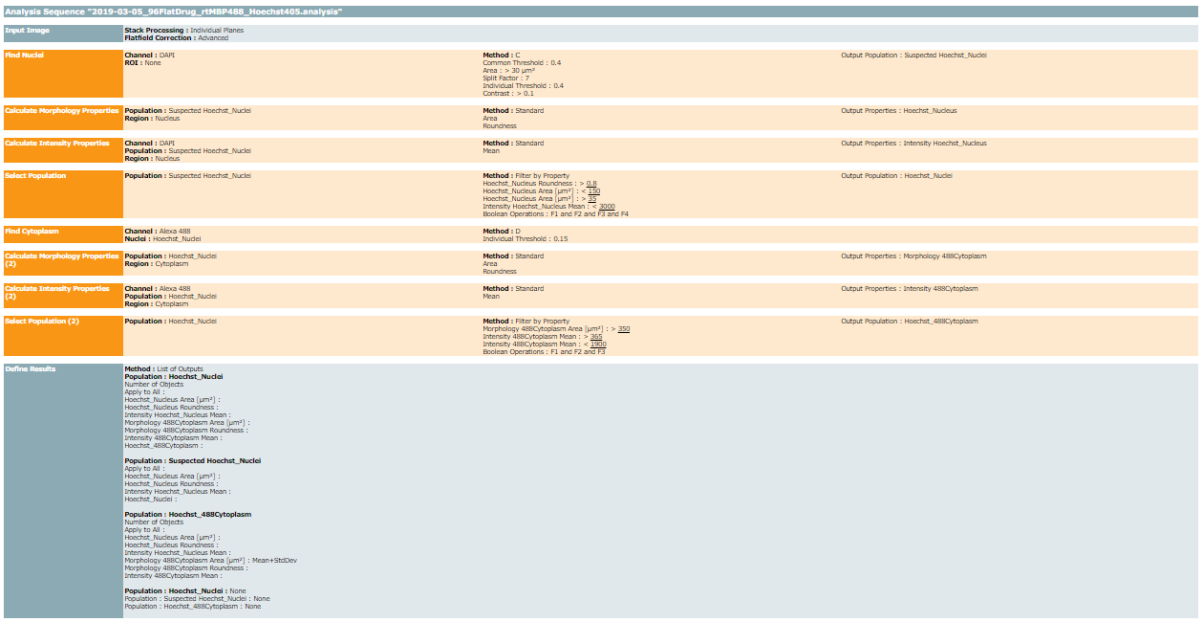

Supplementary Data 2.2: Leica SP8 MatrixScreener Imaging Stitching Script

```
macro "Making stacks [F1]"{

//Initialise macro

print("\\Clear");

setBatchMode(true);

print("***** Macro started *****");

//

var well;

var stitchDir;

//Source and target folders

dir1=getDirectory("Select Screen Folder");          //Folder containing all the wells data i.e. well--U00--V00, well--U00--V01
```

```
dir2=getDirectory("Select Save Folder");            //Folder for saving the stacks
listAll = getFileList(dir1);            //list all wells subfolder in dir1
//


//Mapping the well subfolders into an array wellList
print("Listing wells subfolders");
wellList = newArray();
for (n=0; n<listAll.length; n++){
        if (startsWith(listAll[n], "well--")){
        wellList = Array.concat(wellList, listAll[n]);
        }
}
Array.print(wellList);
//


//Processing well folder and the fields
for (m=0; m<wellList.length; m++){
        wellName=substring(wellList[m], 0,lengthOf(wellList[m])-1);
        print("**********************************");
        print("Processing well= "+wellName);
        fieldList=getFileList(dir1+wellList[m]);
        print("Processing fields:");
        Array.print(fieldList);
        processField(fieldList);
```

```
}


//Function for sorting folder and subfolder
function processField(fieldList) {
for (k=0; k<fieldList.length; k++) {
        print("Processing Field= "+dir1+wellList[m]+fieldList[k]);
        fieldPath=dir1+wellList[m]+fieldList[k];
        indexOfX=indexOf(fieldPath, "X");
        indexOfY=indexOf(fieldPath, "Y");
        fieldX=substring(fieldPath, indexOfX,indexOfX+3);
        fieldY=substring(fieldPath, indexOfY,indexOfY+3);
        intFieldX=parseInt(fieldX);
        intFieldY=parseInt(fieldY);
        processImages(fieldPath);
        }
}


function processImages(fieldPath){
listRename=getFileList(fieldPath);
for(i=0; i<listRename.length; i++){
        pathImage=dir1+wellList[m]+fieldList[k]+listRename[i];
        if (startsWith(listRename[i], "image--")){
                padZero(pathImage);
        }
```

```
}
listImages=getFileList(fieldPath);
for(j=0; j<listImages.length; j++){
	pathToImage=dir1+wellList[m]+fieldList[k]+listImages[j];
	if (startsWith(listImages[j], "image--")){
		open(dir1+wellList[m]+fieldList[k]+listImages[j]);
	}
}
	makeHyperstack();
	//stitchDir=dir2+well+File.separator;
	//print("Stitch directory= "+stitchDir);
	}
//run("Grid/Collection stitching", "type=[Grid: row-by-row] order=[Right & Up] grid_size_x=4 grid_size_y=3 tile_overlap=10 first_file_index_i=1 directory="+[stitchDir]+" file_names={i}.tif output_textfile_name=TileConfiguration.txt fusion_method=[Max. Intensity] regression_threshold=0.30 max/avg_displacement_threshold=2.50 absolute_displacement_threshold=3.50 compute_overlap computation_parameters=[Save computation time (but use more RAM)] image_output=[Fuse and display]");

//Pad zero for z position in file name
function padZero(pathImage){
indexOfZ=indexOf(listRename[i], "Z");
indexOfC=indexOf(listRename[i], "--C");
test=substring(listRename[i], indexOfZ,indexOfC);
if (lengthOf(test)<4) {
```

```
		//print(test);
		newName=substring(listRename[i],
0,indexOfZ+1 )+"0"+substring(listRename[i],indexOfZ+1,lengthOf(listRename[i]) );
		File.rename(dir1+wellList[m]+fieldList[k]+listRename[i],
dir1+wellList[m]+fieldList[k]+newName);
		}
}

//Create final hyperstack
function makeHyperstack(){
run("Images to Stack", "name=Stack title=[] use");
// Change channels & number of z-slice
run("Stack to Hyperstack...", "order=xyczt(default) channels=4 slices=100 frames=1
display=Color");
Stack.setChannel(1);
run("Grays");
Stack.setChannel(2);
run("Grays");
Stack.setChannel(3);
run("Grays");
//Stack.setChannel(4);
//run("Green");
well=substring(wellList[m], 0,lengthOf(wellList[m])-1);
File.makeDirectory(dir2+wellName);
//print(fieldX, fieldY);
```

```
indexOfX=indexOf(fieldX, "X");

indexOfY=indexOf(fieldY, "Y");

X=substring(fieldX, indexOfX+1,indexOfX+3);

Y=substring(fieldY, indexOfY+1,indexOfY+3);

intX=parseInt(X);

intY=parseInt(Y);

//print(intX,intY);

if (intX==0){

	tileNumber=1+Y;

}

if (intX==1){

	tileNumber=5+Y;

}

if (intX==2){

	tileNumber=9+Y;

}

if (intX>2){

	exit("Incorrect number of tiles !");

}

saveAs("tiff", dir2+File.separator+well+File.separator+"tile_"+tileNumber+".tif");

print(dir2+wellName+"_field_"+fieldX+"_"+fieldY+".tif"+" saved");

run("Close All");

}

setBatchMode(false);
```

```
print("****** DONE ******");
}

macro "Stitching Well [F2]"{
print("\\Clear");
setBatchMode(true);
dir1=getDirectory("Source directory");
list=getFileList(dir1);

for (i=0; i<list.length; i++){
        currentDir=list[i];
        print(currentDir);
        if (endsWith(currentDir, "/")){
                indexSlash=indexOf(currentDir,"/");
                name=substring(currentDir, 0,indexSlash);
                name=name+".tiff";
                print("final name ="+name);
                dir=dir1+currentDir;
               run("Grid/Collection stitching", "type=[Grid: row-by-row] order=[Right & Up] grid_size_x=4 grid_size_y=3 tile_overlap=10 first_file_index_i=1 directory="+dir+" file_names=tile_{i}.tif output_textfile_name=TileConfiguration.txt fusion_method=[Max. Intensity] regression_threshold=0.30 max/avg_displacement_threshold=2.50 absolute_displacement_threshold=3.50 compute_overlap computation_parameters=[Save computation time (but use more RAM)] image_output=[Fuse and display]");
```

```
                print("Saving file ="+dir1+currentDir+name);
                saveAs("tiff", dir1+currentDir+name);
                while (nImages>0) {
                        selectImage(nImages);
                        close();
                }
        }
}
print("***** DONE *****");
setBatchMode(false);
}
```

Supplementary Data 2.3: CARS Flat-Field Correction Script for Tile Scan Images

```
print("\\Clear");
setBatchMode(false);
tileX=getNumber("tiles in X", 13);
tileY=getNumber("tiles in Y", 13);

dir2=getDirectory("Saving raw tiles");
//dir3=getDirectory("Saving corrected tiles");
openImage=getImageID();
//run("Z Project...", "projection=[Average Intensity]");
averageID=getImageID();
for (i=0; i<tileY; i++){    //tiles in Y axis
```

```
	for(j=0; j<tileX; j++){  //tiles in X axis
		selectImage(averageID);
		x=j*511;  //pixels - can make more fancy by adding line to divide pixels by number of tiles inputed at start
		y=i*511;
		makeRectangle(x, y+1, 511, 511);
		run("Duplicate...", " ");
		saveAs("tiff", dir2+"tile"+"_X_"+i+"_Y_"+j+".tiff");
		close();
	}
}

listDir2=getFileList(dir2);
path=dir2+listDir2[0];
run("Image Sequence...", "open=path sort");
rawStackID=getImageID();
rawStacktitle=getTitle();
run("Z Project...", "projection=[Average Intensity]");
avgID=getImageID();
avgTitle=getTitle();
run("Gaussian Blur...", "sigma=20");
getStatistics(area, mean);
run("Calculator Plus", "i1="+rawStacktitle+" i2="+avgTitle+" operation=[Divide: i2 = (i1/i2) x k1 + k2] k1="+mean+" k2=0 create");
```

```
resultID=getImageID();

run("Make Montage...", "columns="+tileX+" rows="+tileY+" scale=1");

selectImage(avgID);

close();

selectImage(rawStackID);

close();
```

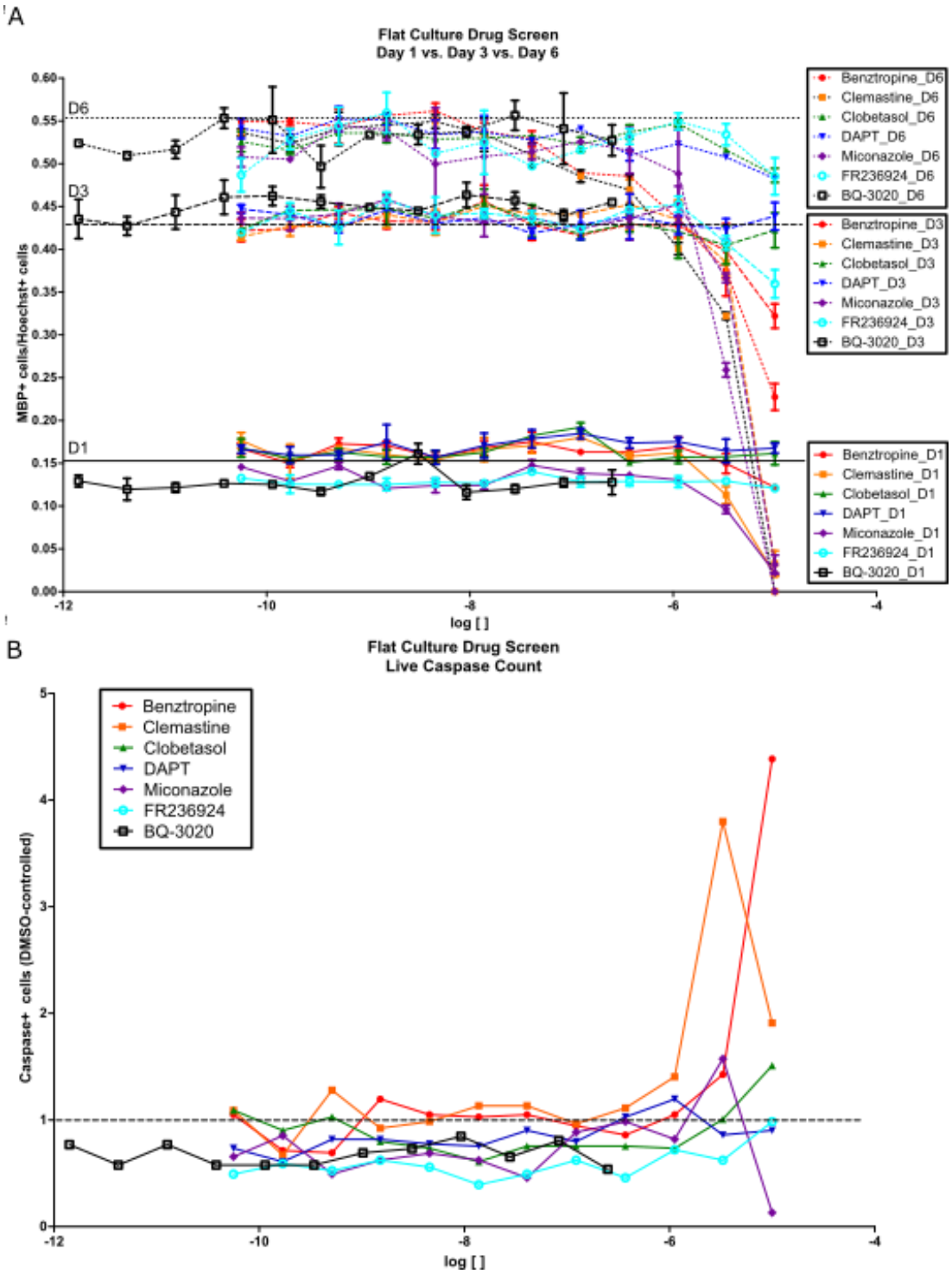

Supplementary Figure 3.1 Time-point MBP+ cells percentage and preliminary live caspase flat culture drug screen results

A+ B + C. (A) D1, (B) D3, and (C) D6 dose-response results of percentage of MBP+ cells over Hoechst+ cells. This experiment was performed using the same protocol for the flat culture drug screen experiments, but the cells were fixed 24 hours, 3 days, and 6 days after drug

addition, followed by staining, imaging on the Operetta, and analysis on Columbus. The D6 plates had half media changes (to prevent cells from drying out) with fresh drugs added at the same final concentration on day 3. The average percentage of MBP+ cells from total nuclei for the DMSO control are depicted with solid (D1), dashed (D3), and dotted (D6) lines. n = 1

D. Preliminary results from a live caspase cell viability experiment. The cells were plated and drugs added using the same protocol. On day 3, the cells were labelled for 30 minutes with Nucview® 488 Caspase-3/7 in DMSO (Biotium 10402) at 2.5µM, followed by 0.5x CellMask Deep Red plasma membrane stain (Thermo Fisher Scientific C10046) and Hoechst for 5 minutes, all in the same myelination media that they were plated in. They were then imaged on the Operetta with 7.5% CO_2 at 37°C using the 10x objective. Hoechst was quantified using Columbus, CellMask was excluded from quantification due to indistinct staining, and the NucView® counted by hand. The data was recorded in Excel and plotted on GraphPad Prism. n = 1

   Point of note 1: Clemastine at log[-5] had approximately 1000 Hoechst+ cells and Miconazole had approximately 2000 Hoechst+ cells at log[-5] and 4000 Hoechst+ cells at log[-5.48] compared to the DMSO control standard of between 5-6000 Hoechst+ cells. The lower ratio of Caspase+ cells at these concentrations are therefore due to the low presence of cells overall, rather than the low percentage of Caspase+ cells.

   Point of note 2: The number of caspase+ cells was extremely low, ranging from 0.25% to 9% of the total Hoechst+ cells. It is therefore difficult to draw any meaningful conclusions from this preliminary data.